Grid Current Control Methods for MV Wind Energy Conversion Systems

vorgelegt von
M.Sc. Hang Yin
ORCID: 0000-0002-8553-8015

von der Fakultät IV - Elektrotechnik und Informatik
der Technischen Universität Berlin
zur Erlangung des Akademischen Grades
Doktor der Ingenieurwissenschaften
- Dr.-Ing.-
genehmigte Dissertation

Promotionsausschuss:
Vorsitzender: Prof. Dr.-Ing. Julia Kowal
Gutachter: Prof. Dr.-Ing. Sibylle Dieckerhoff
Gutachter: Prof. Dr.-Ing. Uwe Schäfer
Gutachter: Prof. Dr.-Ing. Lijun Cai
Tag der wissenschaftlichen Aussprache: 31.08.2018

Berlin 2019

Dedicated to my parents

Preface

Foremost, I would like to express my deepest, sincere gratefulness to my supervisor, Prof. Sibylle Dickerhoff, for her professional and patient guidance during my PhD study time. Without her help and support, the doctoral research would be hard to accomplish. I do think that my thinking manner and research method which I learnt from her during my PhD study will be of great orientation for my career and through my future life.

Besides, I would like to give my sincere thanks in advance to my thesis reviewers, Prof. Uwe Schäfer and Prof. Lijun Cai for their insightful comments. Many thanks go to my colleagues in power electronics group at TU Berlin for their help during my PhD time, especially to Mr. Andrew The and Dr. Aris Gkountaras for their support and help. I would also like to thank my classmates, Dr. Zhiyong Dai and Dr. Nanfang Yang for their many times discussion on the research problems. And special thanks to the president of Global Energy Interconnection Research Institute Europe, Prof. Dr. Xianzhang Lei for his kind support and tremendous help. And thanks to Dr. Hui Zhang from the Abteilung für Bildungswesen der Botschaft der Volksrepublik China in der Bundesrepublik Deutschland for her kind support and care.

Additionally, I would like to thank China Scholarship Council (CSC) for the main financial support. And the Ph.D. project is partially supported by the Department of Power Electronics, Technische Universität Berlin, Germany and Deutschen Akademischen Austauschdienstes (DAAD, German Academic Exchange Service), who supported me for the Ph.D. degree completion grant. Acknowledgements are given to the mentioned institutions.

Last but not the least, I would like to thank my parents, Zhoumin Yin and Junye Wang and my wife, Xiaobing Fan for their constant support and concern. Especially, I would like to give a deep mourning to my beloved mother. Her sudden leave in March makes me know that Life is impermanent, and we should cherish all we have.

Hang Yin

May 08, 2018
Berlin, Germany

Abstract

Wind energy has been one of the most important renewable energies as an alternative to fossil energy. The power rating of a single wind turbine has been increasing during the past forty years. A megawatt level wind turbine has been a tendency, especially for offshore wind energy application. The current common solution is to make the two-level low voltage converter in parallel in order to achieve sufficient power rating. However, research has found that by employing medium voltage multilevel converters will reduce the cost of energy. Additionally, the grid converter is the only way to connect the renewable power generation to the power grid. Grid converter control strategies considering normal and abnormal operation have been one of most concerned points for renewable energy integration. Based on these issues, the Ph.D. project will focus on the grid converter control algorithms investigation.

In order to design the control and evaluate the performance of the proposed control algorithms, system modelling is necessary and an essential task at first. Including the DC-link capacitor, grid converter, LCL filter and PCC voltage, the modelling of these parts is built in chapter 3. Besides, one scaled experiment low voltage system setup is designed and introduced as well, which will be used for experimental verification. For the control of the grid converter with LCL filter, the current control strategy becomes more complex if compared to a grid converter with simple inductive filters. Although an LCL filter can greatly increase the attenuation for the high frequency range, it also brings new problems, such as resonance issues and which current should be adopted as the feedback current, grid current or converter side current. This is discussed in chapter 4 in detail. For overcoming the resonance problem, passive and active damping are discussed in this chapter as well. For evaluating the control performance or requiring the wind turbine behavior on different scenarios, the latest grid standards are also reviewed. Some suggestions on the grid code modifications are given as well for better regulating the next generation wind turbine to behave as a traditional synchronous generator. Thermal performance is an important aspect related to the system reliability, efficiency and lifetime. The loss calculation and temperature estimation method are introduced in the third section of chapter 4. Based on the previous study in part II, system design and evaluation of wind energy conversion system, grid converter control strategies are

investigated in part III, which includes three chapters, the state of the art grid converter control, model predictive control and backstepping control.

Voltage orientated control as the industrial solution for grid converter control has been developed and adopted for the past forty years, which is difficult to be improved without limitation. It is necessary to find another control to meet the technical challenges, e.g., switching frequency limitation. One requirement of the MV power control is to reduce the switching frequency to decrease the switching losses. Then the semiconductor reliability might be increased and the system efficiency is improved. Through the comparison, it has been proved that the proposed multiple steps model predictive control can achieve the lowest switching frequency without compromising the current quality. In order to reduce the sensors, one Luenberger observer is designed for estimating the grid current and capacitor voltage, which is needed for the active damping. It should be pointed out that for reducing the processor calculation burden, the observer is implemented with Xilinx System Generator in FPGA for experiments. In order to duel with the parameter mismatch, distorted grid voltage, and unbalanced grid faults, a non-linear control is proposed in chapter 7, which is a recursive Lyapunov-based method with high robustness. Finally, a conclusion is given at end of this Ph.D. thesis, and some interesting further research points are listed as well.

Zusammenfassung

Die Windenergie ist eine der wichtigsten erneuerbaren Energien als Alternative zur fossilen Energie. Die installierte Leistung einer einzelnen Windturbine ist seit den letzten 40 Jahren stetig gestiegen. Ein Megawatt Windturbinen sind insbesondere für Offshore Windparke heutzutage üblich. Eine Parallelschaltung von zwei 2LV-Niederspannungsumrichtern wird verwendet, um die benötigte Leistung zu decken. In der Forschung wurde aber herausgefunden, dass ein einziger Mittelspannung-Multilevelumrichter die Energiekosten senken kann. Zusätzlich bietet der Netzumrichter die einzige Möglichkeit, Erzeuger von erneuerbaren Energien mit dem Energieversorgungsnetz zu verbinden. Die Steuerung und Regelung von Netzumrichtern sowohl im Normalbetrieb als auch beim Fehlerfall werden zum Schwerpunkt bei der Integration von erneuerbaren Energiequellen. Diese Arbeit konzentriert sich auf die Untersuchung der Regelung von Netzumrichtern.

Damit die Regelung entworfen und das Verhalten der vorgeschlagenen Regelungsstrategien bewertet werden kann, ist eine Modellbildung des Systems notwendig und wichtig für den ersten Schritt. Die Komponenten des Systemmodells, u.a. der Zwischenkreiskondensator, der Netzumrichter, der LCL-Filter und die Netzanschlusspannungen werden im Kapitel 3 erläutert. Der Entwurf eines skalierten Niederspannungstestaufbaus zur experimentellen Verifizierung wird dazu noch vorgestellt. Die Verwendung eines LCL-Filters erschwert die Stromregelung des Netzumrichters im Vergleich zur Regelung mit einem einfachen L-Filter. Obwohl ein LCL-Filter die Dämpfung im HF-Bereich erheblich steigert, führt dieser auch neue Probleme ein, u.a. das Resonanzproblem und die Entscheidung, ob der Netzstrom oder der Umrichterstrom in der Stromregelschleife zurückgeführt werden soll. Diese Problematik wird in Kapitel 4 im Detail diskutiert. Die passive und aktive Dämpfung zum Lösen des Resonanzproblems werden ebenfalls in diesem Kapitel erklärt. Um die Regelverhalten des Systems bei verschiedenen Fällen zu bewerten, werden die aktuellsten Netzanschlussnormen auch überprüft. Mögliche Anpassungen der Normen werden vorgeschlagen, damit die neue Generation der Windturbine, die sich wie traditionelle Synchrongeneratoren verhalten sollen, besser reguliert werden kann. Das thermische Verhalten ist ein wichtiger Aspekt im Bezug auf die Systemzuverlässigkeit, Effizienz und Lebensdauer. Auf die Kalkulation der Verluste und

die Methode zur Schätzung der Temperatur wird im Abschnitt 3 des Kapitels 4 eingegangen. Aufbauend auf die Studie im Teil II „system design and evaluation of wind energy conversion system“ untersucht der Teil III dieser Arbeit die Regelstrategien von Netzumrichtern. Dieser besteht aus drei Kapiteln zum aktuellen Stand der Netzumrichterregelung, Modellprädiktiver Regelung und Backstepping Regelung.

Spannungsorientierte Regelung (VOC) als eine Industrielösung für die Netzumrichterregelung ist in den letzten 40 Jahren bereits entwickelt und angepasst worden, sodass Verbesserungen schwer ohne Einschränkungen durchzuführen sind. Es ist notwendig, andere Regelmethoden zu finden, die die technischen Anforderungen, z.B. die Einschränkung der Schaltfrequenz, erfüllen. Eine Voraussetzung für die Leistungsregelung in der Mittelspannungsebene ist die Schaltfrequenz zu reduzieren, um die Schaltverluste zu senken. Dadurch kann die Zuverlässigkeit der Halbleiter gesteigert und die Effizienz des Gesamtsystems verbessert werden. Durch einen Vergleich kann bestätigt werden, dass die vorgeschlagene Mehrschritt-modellprädiktive Regelung die niedrigste Schaltfrequenz erzielen kann, ohne die Stromverzerrung zu verschlechtern. Ein Beobachter von Luenberger zur Schätzung der Netzströme und der Kondensatorspannung wird verwendet, um die Anzahl der Sensoren zu reduzieren. Die geschätzten Größen werden für die aktive Dämpfung benötigt. Es ist wichtig zu erwähnen, dass zum Verringern der notwendigen Rechenleistung der Beobachter experimentell in FPGA mit einem Xilinx System Generator implementiert ist. Für die Bekämpfung von Parameterverschiebungen, verzerrten Netzspannungen und unsymmetrischen Netzfehlern wird im Kapitel 7 eine nichtlineare Regelung vorgestellt, die eine rekursive Methode mit hoher Robustheit nach Lyapunov darstellt. Am Ende dieser Arbeit wird eine Schlussfolgerung gegeben und einige interessante weiterführende Forschungsschwerpunkte werden aufgelistet.

Contents

List of Figures

List of Tables

List of Abbreviations

WECS	Wind Energy Conversion System
DFIG	Doubly Fed Induction Generator
PMSG	Permanent Magnet Synchronous Generator
SG	Synchronous Generator
NPC	Neutral Point Clamped
PWM	Pulse Width Modulation
SPWM	Sinusoidal Pulse Width Modulation
SVPWM	Space Vector Pulse Width Modulation
PF	Power Factor
FFT	Fast Fourier Transform
PCC	Point of Common Coupling
CSCF	Converter Side Current Feedback
GSCF	Grid Side Current Feedback
AD	Active Damping
PD	Passive Damping
TSO	Transmission System Operator
FRT	Fault Ride-through
HVRT	High Voltage Ride-through
LVRT	Low Voltage Ride-through
GCRs	Grid Connection Requirements
DPC	Direct Power Control
VOC	Voltage Oriented Control
THD	Total Harmonics Distortion
MPC	Model Predictive Control
MPDCC	Model Predictive Direct Current Control
SS-MPDCC	Single Step Model Predictive Direct Current Control
MS-MPDCC	Multiple Steps Model Predictive Direct Current Control
BSC	Backstepping Control

List of Symbols

f_{sw}	Switching Frequency
f_1	Fundamental Frequency
f_c	Carrier Frequency
f_r	Modulation Frequency
f_s	Sampling Frequency
ω_1	Fundamental Angular Frequency
T_s	Sampling Time
G_m	Gain Margin
P_m	Phase Margin
$G(s)$	Transfer Function in s Domain
$G(z)$	Transfer Function in z Domain
C_f	Filter Capacitance
p	Instantaneous Active Power
q	Instantaneous Reactive Power
P	Active Power
Q	Reactive Power
$f_{\overline{SW}}$	Average Frequency
η	Efficiency
P_{loss}	Power Losses
I_N	Nominal Current
λ_{sw}	Weighting Factors for Switch Commutation
λ_i	Weighting Factors for Current Track Error
λ_{npp}	Weighting Factors for Neutral Point Potential
δ	Boundary for Boundary Control

Part I

Preamble

This part is the preamble of the Ph.D. thesis, which includes two chapters. ***Chapter 1*** *is the introduction. It mainly introduces the background and current status of the wind energy technology. The trends and technical challenges are also addressed. The motivation and objective of the Ph.D. thesis are discussed at the end of the chapter. In* ***Chapter 2****, fundamentals of Medium Voltage Multi-level Converters are described. It mainly discusses the topologies of MV multi-level converters and its market overview. Additionally, as the bases, the MV semiconductors are classified. The state of the art market overview is given at the end.*

1 Introduction

This chapter first presents the background and current status of wind energy. It includes a short state-of-the-art of wind energy technology and an overview of wind turbine configurations, followed by the future development trends and the current technical challenges. Then, the motivation and objective of this thesis are discussed. For better understanding, the thesis structure is presented to show the whole research route at the end of this chapter.

1.1 Background and Current Status

Energy production and consumption have kept increasing as economies grow. The large-scale development and utilization of fossil energy have resulted in serious problems such as resource shortage, environmental pollution, and climate change. According to the BP Statistical Review of World Energy 2016 [1], the reserve of coal can be used for 114 years while the oil and natural gas can only be available 50.7 years and 52.8 years, respectively, if the current consumption rate is kept. Burning fossil fuels releases emissions such as

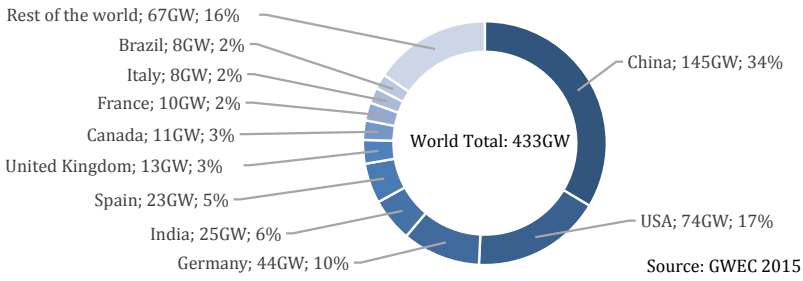

Figure 1.1: *Wind Power Cumulative Capacity Share by the End of 2017*

carbon dioxide, nitrogen oxides, which affect the global environment. How to fight the climate change, fossil fuel crisis and environmental pollution are becoming a big challenge for human beings. Renewable Energy is an alternative solution for this situation, such as photovoltaic (PV), wind energy, geothermal, biomass etc. Renewables mainly provide the energy in three important energy consumption areas, which are electricity generation, heating/cooling, and transportation. Many countries have made a specific plan for energy transition. In Germany, the government has formulated guidelines for an environmentally sound, reliable and affordable energy supply until 2050. The German government will seek to make renewables sharing 60% of gross final energy consumption by 2050. Especially the electricity generated by renewables will be increased to 80% by 2050 [2]. In November 18^{th}, 2015, UK decided to close all the coal-fired power stations by 2025 and restrict its use from 2023 [3]. According to REN 21, renewables have already provided an estimated 19.2% of global final energy consumption in 2014. By the end of 2015, 23.7% of global electricity comes from renewables [4]. Among the renewable energy resources, PV and wind are the most dominant ones and have been developed significantly in recent years. Solar PV installation has been increased to 227 GW by the end of 2015. The wind energy installation was increased dramatically in 2015. A record 63 GW was added in this year and leads to the total about 433 GW. The world share cumulative capacity by the end of 2017 is shown in figure 1.1. China installed a staggering 30.8 GW new capacity in 2015, which is almost half of the new installed capacity of 2015. According to the global weighted average levelized cost of electricity (LCOE) of projects commissioned in 2016, it was around USD 0.07/KWh for onshore wind, which is one of the most competitive sources of electricity available [4]. With the development of technology, e.g., larger power rating, maturer installation technology, the cost of onshore wind declines into the same range with new fossil fuel, which is around USD 0.045/KWh. Wind energy has a bright development prospect in the next decades.

1.1.1 State of the Art Wind Energy Technology

In the last thirty years, wind energy technology has been significantly developed and improved. Since the output wind power is proportional to the wind turbine swept area and in order to decrease the per unit cost, the commercial wind turbine size has been increased exponentially. The power rating has increased from several hundred kilowatt to megawatt. Now several 8 MW wind turbines are either in production or prototype state, e.g., V164-8.0 MW® from MHI Vestas Offshore Wind [5], AD 8-180 from Adwen, a joint venture between Gamesa and Areva [6] and SWT-8.0-154 from Siemens [7]. For example, the blade of V164-8.0 MW® is 80 m long and the swept area is 21.124 m^2. It can supply approximately 7500 European households [5].

Wind energy technology is a multidisciplinary studies, including meteorology, aerodynamics, materials, economical, mechanical and electrical engineering. It contains wind prediction, mechanical system, electrical system, information, communication and control technologies. From the perspective of electrical engineering, the electric generator and the power converter are the two main components in the wind energy conversion system (WECS) [8]. Power electronics technologies used in wind power generation have been changed dramatically, which take part in the wind energy system more deeply, from a soft start in the 80s to back-to-back (B2B) power conversion system since the 2000s [9]. The details of power converters in wind energy systems will be discussed in the next subsection. More power electronics taking part in the wind energy system, more flexible functions can be implemented.

With the development of onshore wind, the land resources are occupied to some extent. Due to the limited land resources and more wind on the sea, offshore wind is an alternative solution for the near future. However, the offshore wind generation is still in the early stage due its high cost and more technical challenges, e.g., installation in the deep sea (>30 m), or electricity transmission far from the coast (>80 km). By the end of 2017, 18.8 GW offshore wind was installed in the world, which is mostly located in Europe. Compared to onshore wind, offshore wind generation has a much higher potential in the next decades. In order to transfer the offshore wind energy to the coast, it is proved that high voltage direct current (HVDC) transmission is prior to high voltage alternative current (HVAC) transmission. Since the current wind farms are parallel AC connections, an offshore wind platform has to be built for power collection and conversion. As an alternative, a DC offshore wind farm might be a choice in the future [10, 11].

1.1.2 Overview of Wind Turbine Configurations

During the last three decades, the wind turbine configurations have changed dramatically. According to the state of the art technologies, there are mainly two different types of wind turbine configurations, which are Doubly Fed Induction Generator (DFIG) with partial scale power converter Wind Energy Conversion Systems (WECSs) [12, 13], Per-

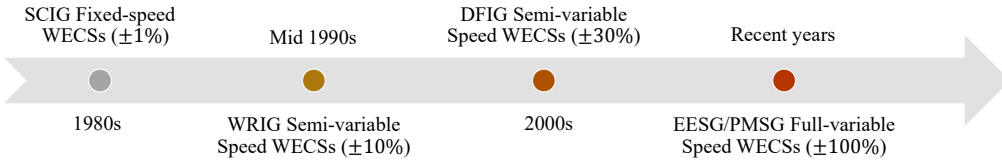

Figure 1.2: *The Development Process of Wind Turbine Time Line*

manent Magnet Synchronous Generator (PMSG) based full-scale B2B power converter WECSs [14–16]. It should be noted that DFIG WECSs has taken up to 50% of the market share. However, PMSG WECSs have an increasing share due to their fully adjustable speed range and better grid support compared to the former ones [12, 17].

Additionally, Squirrel Cage Induction Generator (SCIG) based full-scale B2B WECSs were also investigated in some publications and adopted for commercial products [18–20]. This SCIG configuration is different from the ones used in the 1980s, which were known as the first generation wind turbines. The disadvantages of this type have two aspects. One is the capacitor bank for reactive power compensation and the other one is the fixed speed which produces mechanical stress [9, 21]. Meanwhile, the SCIG based full-scale B2B WECSs are not very popular in the market either for two reasons. Compared to DFIG WECSs, SCIG needs full power converter which makes the system expensive. And SCIG WECSs are not able to be implemented with direct drive as PMSGs from the technical feasibility [17, 22]. The timeline of the development process is shown in figure 1.2 [8]. It should be noted that with the size and power rating increasing, especially for offshore wind, the PMSG with full B2B power converter WECSs are becoming attractive.

The Doubly-Fed Induction Generator based partial scale power converter WECS configuration is shown in figure 1.3, which has been used since the 2000s. Besides the rotor connected to the grid through the partial scale power converter (30% of the rated power), the stator is also connected to the grid directly, which makes this configuration more sensitive to the grid variation than full-scale power converter [23]. The advantage of this type compared to the fixed speed SCIG WECS is that it has ±30% adjustable speed range which improves the system efficiency. However, since the partial power converter is used, the system has limited Low Voltage Ride Through (LVRT) capability. Additionally, the rotor windings are connected to the power converter through slip rings and brushes. And it's known that the average lifetime of brushes is 6-12 months only, which leads the regular maintenance and limit this configuration in offshore application [8].

Compared to DFIG based WECSs, the SG based full B2B power converter WECSs have larger adjustable speed range and better LVRT compliance. The configuration is shown in figure 1.4. The generator type can be SCIG, EESG or PMSG. The gearbox can be removed by employing multipole PMSG. The extra cost of the full -scale power

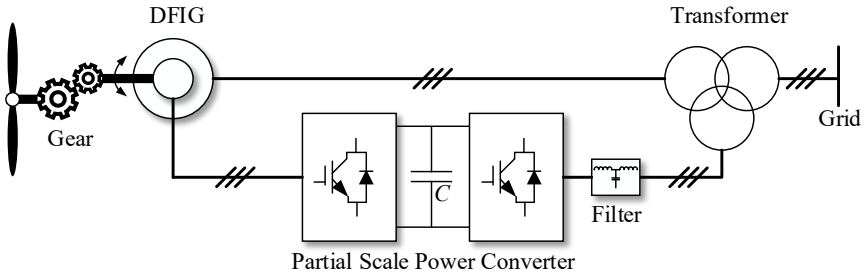

Figure 1.3: *DFIG based Partial Scale Power Converter WECS*

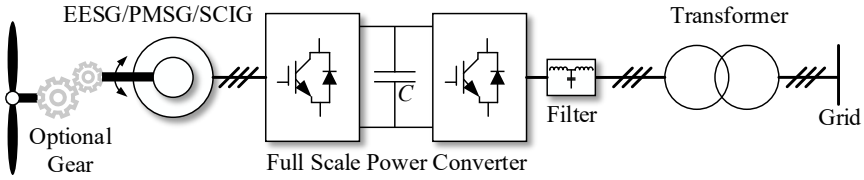

Figure 1.4: *EESG/PMSG/SCIG based Full Scale Power Converter WECS*

converter is around 7%-12% of the total wind turbine cost [24]. Among all the wind turbine configures, PMSG based full B2B power converter WECSs have the highest efficiency, which makes this type more attractive [8].

Some selected commercial MW level wind turbines (>5.0 MW) main parameters are shown in table 1.1, which are the top 10 wind turbine manufacturer in 2015 and main MW wind turbines manufactures. It can be found that most of them are used for the offshore application. The PMSG based full-scale power converter configuration is dominant in the offshore market. Both gear-box drive and direct drive have a share. For the power converter, it can be seen that parallel B2B two-level converter with low voltage (690 V) is the mainstream commercial configuration. Only a few models adopt MV power converter, e.g., the model AD 5-135 from Adwen. The three-level Neutral Point Clamped (NPC) with terminal voltage 3300 V is used in this model. With the power rating increasing, the number of power converter modules increase which makes the size, cost, and complexity increasing. In reference [25], detailed cost analyses of wind energy conversion system are conducted between commercial LV and MV wind technology. The conclusion is that using MV system can reduce 2.5% of the cost of energy.

Table 1.1: *Wind Turbine above* 5.0 MW *Parameter in Top 10 Wind Turbine Manufacturers of 2015 and Mainstream MW Wind Turbine Manufacturers*

Manufacture	Model Name	Offshore	Generator	Power Converter	Power Rating
MHI Vestas	V164	Yes	GE-PMSG	B2B -	8.0 MW
GE	Haliade* 150	Yes	DD-PMSG	B2B 900 V	6.0 MW
Siemens	SWT-6.0-154	Yes	DD-PMSG	Parallel B2B-2L 690 V	6.0 MW
Siemens	SWT-7.0-154	Yes	DD-PMSG	Parallel B2B-2L 690 V	7.0 MW
Siemens	SWT-8.0-154	Yes	DD-PMSG	Parallel B2B-2L 690 V	8.0 MW
Gamesa	G128	Yes	GE-PMSG	Parallel B2B-2L 690 V	5.0 MW
Gamesa	G132	Yes	GE-PMSG	Parallel B2B-2L 690 V	5.0 MW
Enercon	E-126	No	DD-EESG	Parallel B2B-2L 690 V (Common DC-link)	7.58 MW
United Power	UP6000-136	Yes	GE-DFIG	B2B 6600 V[1]	6.0 MW
Ming Yang	SCD	Yes	GE-PMSG	Parallel B2B-2L 690 V	6.0 MW
CSIC Haizhuang	H127	Yes	GE-PMSG	Parallel B2B-2L 690 V	5.0 MW
Adwen	AD 5-132	Yes	GE-PMSG	Parallel B2B-2L 690 V	5.0 MW
Adwen	AD 5-135	Yes	GE-PMSG	B2B-3L-NPC 3300 V (ABB ACS 800)	5.0 MW
Senvion	6.2M 126	Yes	GE-DFIG	Parallel B2B-2L 660 V	6.15 MW
Senvion	6.2M 152	Yes	GE-DFIG	Parallel B2B-2L 660 V	6.15 MW

1.2 Trends and Challenges

Based on the past three decades of development and current status, with the development of power electronics technology, computer science, and related technologies, there are several distinct trends regarding the wind energy technology. First, the single wind turbine in terms of power rating will increase continuously in the coming years. Currently, the largest wind turbine is 8.0 MW (Vestas 164), and several manufacturers have already announced 10 MW∼15 MW wind turbines. This will make the manufactures to reconsider what the suitable configurations and technologies are for the tens of MW level wind turbines including gearbox drive-train technologies, electric generators, power converters and grid code requirements. Second, the penetration of wind energy will take an important role in the future power system. With the development of renewable energy, especially wind and PV, the modern power system has been changed significantly. More and more power electronics are involved in the system, which causes the characteristics of traditional synchronous generator decreasing, e.g., rotational inertia and damping characteristics [26]. This might lead to the system stability decreasing. Third, after the WECS stability is guaranteed, the performance of WECSs needs to be improved to reduce the cost of energy, increase the lifetime, reduce the downtime and provide superior dynamic and steady state performance [8]. In general, advanced control of grid connected WECS is required to achieve high efficiency, high reliability and high power quality.

In order to meet the future development trends aforementioned, several emerging challenges and questions which need to be considered and solved are:

- *What are the challenges for the high penetration with renewable energy?*
  - *Is it possible to implement 100% renewable energy power generation?*
  - *How can the highly involved power converters support the future modern power system?*
  - *Are there any solutions to make the wind energy more competitive among the renewable energy resources?*
- *What are the challenges for the large-power MW level wind turbine technologies?*
  - *What are the suitable power converter configurations regarding losses, redundancy and reliability?*
  - *What control schemes can guarantee the WECS to meet the future stringent grid code and provide superior dynamic and steady state performance?*

All of these research questions have been discussed in many published papers. It should be noted that with the power rating increasing, the lightweight technologies will be also one important aspect of the future wind turbine technology.

1.3 Motivation and Objective

1.3.1 Project Motivation

In order to answer those challenging questions and try to find the possible solutions, much related research work have to be conducted. From the perspective of electrical engineering, especially from the power electronics aspect, the power converter topology selection and grid filter design and its control considering losses, dynamic and steady state performance, stability and power quality are several main problems for the wind energy conversion system.

With the continual increasing of a single wind turbine system, a suitable power converter topology and configuration is one of the most important issues in WECSs. In order to improve the system efficiency, a low switching frequency should be preferred. However, the reduced switching frequency might cause unsatisfied performance which does not comply with the grid code. In other words, one advanced control algorithm should be developed to meet these two requirements.

Based on these demands and motivation, the thesis structure can be derived, which will be discussed in next section.

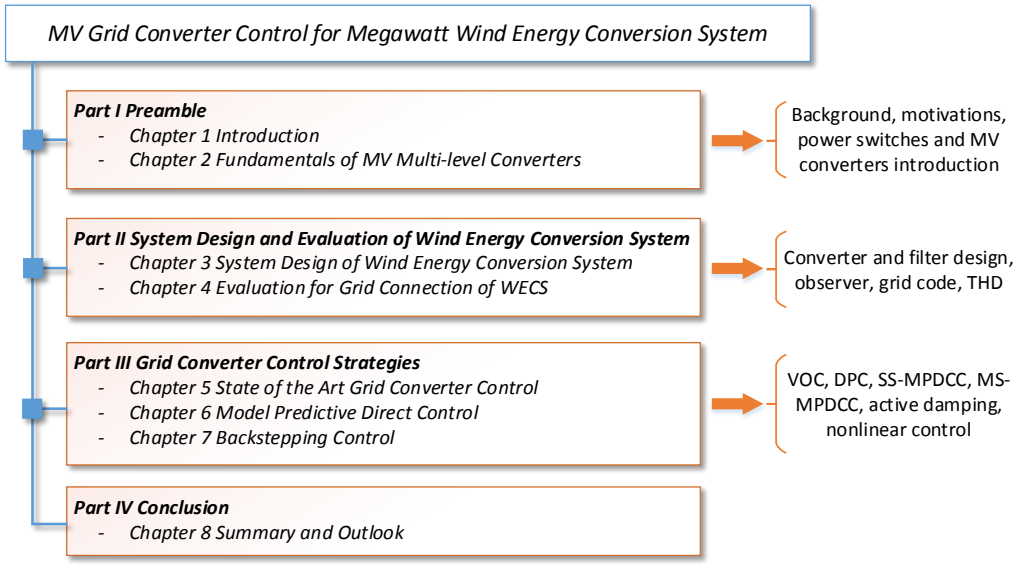

Figure 1.5: *Thesis Structure and Main Research Points in Each Part*

1.3.2 Thesis Objective and Outline

The objective of this thesis is to find an improved control scheme for grid converter control of MW level wind turbine power conversion system. In order to verify the proposed control scheme, one 5 MVA wind energy conversion system was designed for simulation and one 10 kVA test setup was built for experimental verification. The thesis outline is shown in figure 1.5.

The whole Ph.D. thesis is divided into four parts. Part I is the preamble of the thesis, which includes two chapters. Chapter 1 presents the background, current status, trends and challenges of wind energy technologies. Chapter 2 presents the fundamentals of MV multi-level converters, which includes the topologies and market overview of MV multi-level converters. As the bases, the MV semiconductors classification and market overview are also introduced in this chapter. Part II is the system design and evaluation of MW wind energy conversion systems, which also includes two chapters. Chapter 3 presents the structure overview of a MW wind energy conversion system. The grid converter and LCL filter design are illustrated in detail in this chapter. For the performance evaluation, the stability analysis is discussed for both grid side current feedback and converter side current feedback. What's more, the grid code and future trends are also introduced in this Chapter. Losses analysis as one of the important

[1]This model is in the prototype stage.

evaluation aspects is also discussed in this chapter. Based on the pre-study in Part I and Part II, the grid converter control strategies are investigated in Part III, which includes three chapters. Chapter 5 presents the state of the art grid converter control methods, which are well known as Voltage Orientated Control (VOC) and Direct Power Control (DPC). In this chapter, DPC is also improved reducing unnecessary switching transitions. Chapter 6 presents the model predictive control including Single Step Model Predictive Direct Current Control (SS-MPDCC) and Multiple Steps Model Predictive Direct Current Control (MS-MPDCC). In order to improve the performance concerning uncertainties and mismatch, a non-linear control method is introduced in Chapter 7. At end of this thesis is Part IV, which includes one chapter. Chapter 8 summarizes the whole thesis and gives an outlook for the future work.

2 Fundamentals of MV Multi-level Converters

This chapter focuses on the MV multi-level converter topologies and the MV semiconductors. First, the several classical multi-level converters are discussed, e.g., the three-level Neutral Point Clamped (NPC) converter, and the Flying Capacitor (FC) converter. Additionally, the latest market overview is also given for the multi-level converters. Semiconductors switches are the important components for the converters. A classification of MV semiconductors is given afterwards. As in the first part, the latest market overview about MV semiconductors is provided as well. At the end, a summary is given.

Table 2.1: *Voltage Class Classification of Low and Medium Voltages*

Regions/Countries	Standard	Low Voltage Class	Medium Voltage Class
Europe	IEC60038	230,400,690 V(<1000 V)	3.3,6.6,11,22,33 kV(<35 kV)
North Amercia	ANSI C84.1	208,120/240, 480,575 V(<600 V)	2.4,4.16,6.9,12.47, 13.8,21,34.5 kV(<35 kV)
China	GB-T156-2007	220,380,690 V(<1000 V)	3,6,10,20,35 kV(≤35 kV)

Before introducing the MV multi-level converters, it is necessary to know the definition of voltage class. The voltage class is not the same in different regions or countries. Table 2.1 shows the regional classification of low and medium voltage class adopted in Europe, North America and China [8, 27]. It can be seen that generally the voltage class below 1000 V is considered as low voltage (LV). Voltage class above 1 kV and below 35 kV is classified as medium voltage (MV). As discussed in subsection 1.1.2, most large wind power systems (>5.0 MW) in the market still utilize low voltage class (690 V). It has been proved that with the power rating increasing of a wind turbine, MV power converter has prior properties compared to LV power converter regarding cost and efficiency. Due to voltage limitation of semiconductors, there are two possibilities to implement a MV power converter, one is to connect the switches in series working as a single switch for a two-level converter, and the other one is multi-level converter. The two-level MV converter is shown in figure 2.1. Even though MV can be achieved by series switches, the output voltage still has two voltage levels which produces a higher THD compared to a multi-level converter.

2.1 Topologies of MV multi-level converters

Due to the high demand for large power systems, e.g., several megawatts, MV multi-level converters have been becoming an attractive solution in many applications in last several decades. Especially for the electrical drive in industrial applications, e.g., pipeline pumps, conveyors, wind tunnels, compressors and so on, MV multi-level converter has

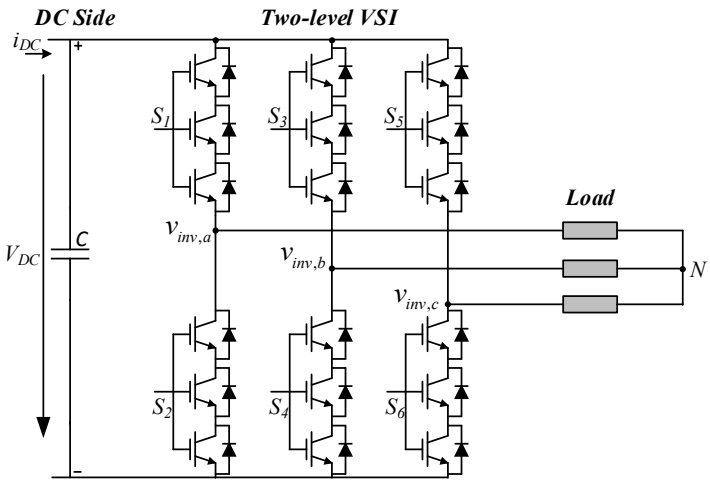

Figure 2.1: *Two-level Medium Voltage Power Converter*

been adopted frequently [28, 29]. The classification of the power converter is shown in figure 2.2. According to the dc-link energy storage components, power converters can be classified into current source and voltage source converter. Since voltage source converters (VSC) have higher market penetration and had more noticeable development over the last decades [28], this thesis only focuses on the VSC topology. The voltage source based power converters can be divided into two groups, one is the two-level converter, and the other is the multi-level converter. For the multi-level converter, it can be classified into four groups, i.e., Diode Clamped Converter (DCC), Flying Capacitor Converter (FCC), Cascaded H-bridge Converter (CHB) and Modular Multilevel Converter (MMC). All these four types will be discussed briefly in following subsections.

2.1.1 Diode Clamped Converter

Diode Clamped Converter (DCC) was first proposed by Nabae, Takahashi and Akagi in the early 1980s [30]. It is a three-level diode clamped converter, which is also known as three-level neutral point clamped (NPC) converter. The single phase three-level NPC converter circuit is shown in figure 2.3. Compared with two-level converter, the three-level NPC converter has two distinct advantages. First, each single switch only needs to bear half of the dc-link voltage, which makes it possible to implement MV applications with lower voltage switches. Second, the output of the phase to neutral voltage has three voltage levels ($V_{DC}/2, 0, -V_{DC}/2$), which reduces the output voltage harmonics distortion compared with the two-level converters. On the other hand, the three-level NPC has two problems which need to be considered. One is the neutral

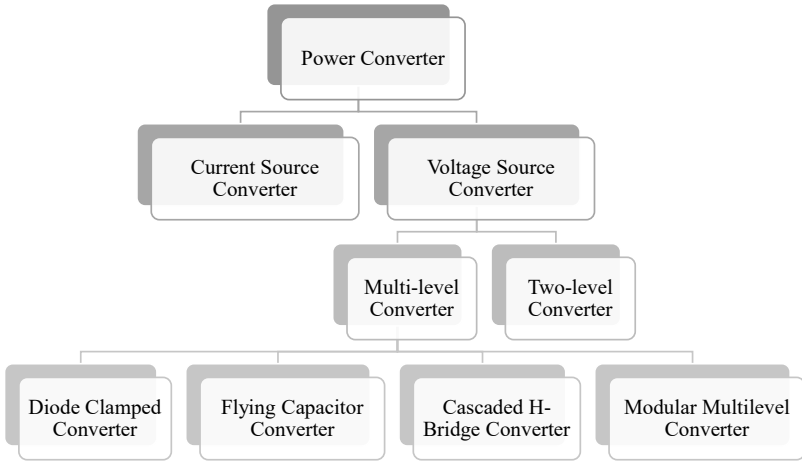

Figure 2.2: *Power Converter Classification*

point voltage balancing and the other is the uneven loss distribution between the outer switches (S_{11}, S_{14}) and the inner switches (S_{12}, S_{13}). The former one can be solved with proper redundant voltage vectors to balance the upper and lower capacitor voltage through the neutral point current i_{NP}, which has been discussed in many publications and solved in industry [31–35]. The later one is the inherent drawback of NPC converter. The three-level active NPC converter was proposed by T. Brückner and S. Bernet in 2001 [36] to overcome this problem. The two clamped diodes in the single phase are replaced by two active switches, which form an additional redundant switch to balance the uneven losses. With the additional active switches, better losses distribution and higher semiconductor utilization can be achieved [36, 37]. Compared to the two-level converters, three level converters need more control signals and calculation effort, but this has not been a problem with the fast development of computer technology. Three level NPC converters have been widely used in industry, especially in MV application (2.3-4.16 kV) [38–41]. Leading manufacturers offer a variety of converters, e.g., ABB PCS6000, which is an MV wind turbine converter using IGCT and three-level converter. More MV products will be discussed in section 2.2.

Besides the three-level NPC converter, the Diode Clamped Converter can be extended to four-level, five-level or more. The four-level and five-level diode clamped converter circuits are shown in figure 2.4. With the number of levels increasing, the single switch blocking voltage decreases, e.g., for five-level DCC, the single switch only needs to bear one quarter of the dc-link voltage. It can be noted that the clamped diodes blocking voltage are not the same for the level more than three. For example, from the figure 2.4b, it can be seen that if the switches $S_{15} - S_{18}$ turn on, D_{16} blocks

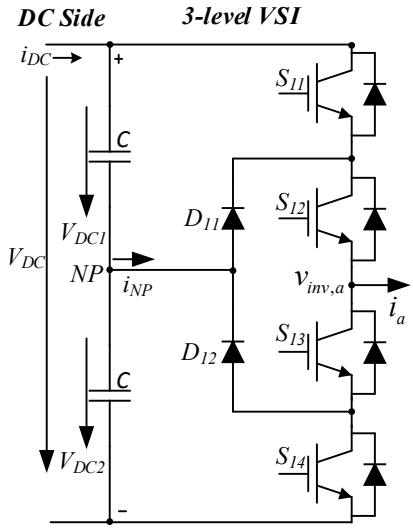

Figure 2.3: *Single-phase Three-level Neutral Point Clamped Converter*

$V_{DC}/4$, D_{14} blocks $V_{DC}/2$ and D_{12} blocks $3V_{DC}/4$. If same diodes are used in the converter, it means that multiple quantities should be used which is shown in the dashed box. If more voltage levels are required, the diodes quantities will increase dramatically ($(N_{level}-1)\cdot(N_{level}-2)$) and voltage balancing will be complex. This might be the reason that only three-level NPC typology is widely used in the industry.

2.1.2 Flying Capacitor Converter

Flying Capacitor Converter (FCC) is also known as capacitor clamped converter. The three-level, four-level and five-level FCC topologies are shown in figure 2.5 respectively. Taking three-level FCC as an example, which is shown in figure 2.5a, the only difference compared to figure 2.3 is that the two clamped diodes are replaced by one capacitor C_{11}. The output voltage $v_{inv,a}$ has three voltage levels. If the switches S_{11}, S_{12} turn on, the output voltage is $V_{DC}/2$. If the switches S_{13}, S_{14} turn on, the output voltage is $-V_{DC}/2$. For the output voltage zero, either the switches S_{11}, S_{13} or the switches S_{12}, S_{14} turn on. The clamped capacitor C_{11} is charged to $V_{DC}/2$. Figure 2.5c shows the five-level flying capacitor converter. Similar to the three-level converter, the clamped capacitor C_{11}, C_{12}, C_{13} are charged to $3V_{DC}/4$ in total. The clamped capacitor C_{14}, C_{15} are charged to $V_{DC}/2$ in total. The clamped capacitor C_{16} is charged to $V_{DC}/4$. If the switches $S_{11}, S_{12}, S_{13}, S_{14}$ turn on, the output voltage is $V_{DC}/2$. If the switches $S_{15}, S_{16}, S_{17}, S_{18}$ turn on, the output voltage is $-V_{DC}/2$. For the output voltage $V_{DC}/4$ and $-V_{DC}/4$, there are three combinations respectively while the five-level DCC only

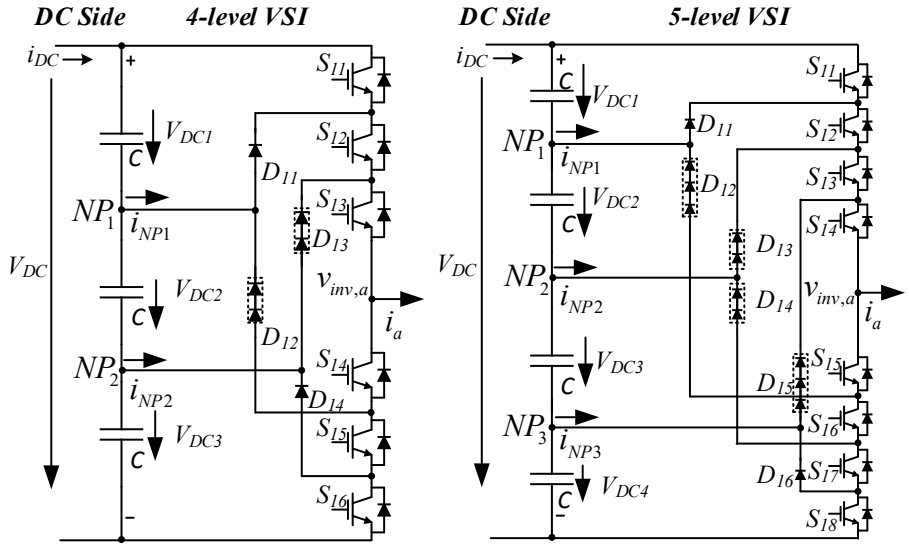

(a) Four-level *(b) Five-level*

Figure 2.4: *Single-phase Multi-level Diode Clamped Converter*

has one switching state with one combination. For zero output voltage, there are six combinations of switch states while the five-level DCC only has one switching states with one combination [29]. Switching combinations need to be selected considering the clamped capacitor voltage balancing. High expense of flying capacitor at low carrier frequency is another disadvantage of this topology [42].

2.1.3 Cascaded H-Bridge Converter

The Cascaded H-Bridge (CHB) converter topology is shown in figure 2.6, which was proposed by Hammond in 1993 [43,44]. It can be seen that cascaded H-bridge converter has no common dc-link, which is based on the series connection of single phase full bridge module. Each single-phase full bridge can generate at the output three voltage levels, $V_{DC}/2, 0, -V_{DC}/2$. The total phase to neutral voltage is the sum of the individual output voltages of each module. Taking the five-level CHB converter as an example, if V_{DC1} and V_{DC2} are $V_{DC}/4$, so the output voltage level can be $\pm V_{DC}/2$, $\pm V_{DC}/4$ and zero, which are five levels. If the quantity of single-phase full bridge is n, the output voltage level will be $2n+1$. The Cascaded H-Bridge converter can be easily extended to higher output voltage and power level (e.g. 13.8 kV, 30 MVA) [45]. The CHB converter has a major advantage, which is the high degree of modularity. This makes the topology easy to extend to high voltage and power, easy to replace and implement modular control

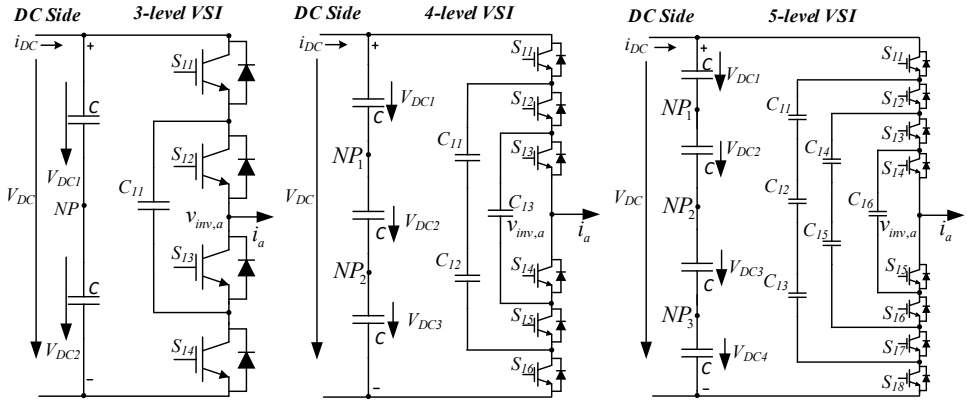

(a) Three-level *(b) Four-level* *(c) Five-level*

Figure 2.5: *Single-phase Multi-level Flying Capacitor Converter*

algorithms. However, one disadvantage is that this topology needs separate DC-links for each single phase full bridge. Usually, this can be achieved by using a transformer with multi-terminal windings on the secondary side and a rectifier. Reference [46] presents this topology for wind energy applications.

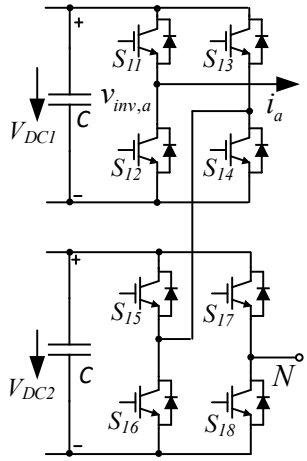

Figure 2.6: *Five-level Cascaded H-Bridge Converter*

2.1.4 Modular Multilevel Converter

The Modular multilevel converter (MMC) was proposed by Marquardt for HVDC applications in 2003 [47], and was first commercially used in the Trans Bay Cable project. MMC is an attractive topology for HVDC application and high power due to its several advantages, such as strictly modular, no AC-filters necessary, distributed dc-link capacitor and low switching frequency ($f_{sw} \approx 3f_1$) for a large number of modules. The three-phase modular multi-level converter is shown in figure 2.7. During the last ten years, MMC related issues have been investigated widely in the literatures. However, there are still several issues, e.g., circulating current suppression and capacitor voltage balancing. Reference [42] presents voltage balancing control of the multiple floating dc capacitors from theoretical and experimental verifications. Reference [48] presents MMC for back-to-back HVDC transmission system using phase-disposition sinusoidal pulse width modulation (PD-SPWM) strategy including capacitor voltage balancing. For the modulation, losses analysis and semiconductor requirement are presented in [49–52]. For a wind energy conversion system without transformer, which means the output voltage might need to be a medium voltage level network, e.g. 33 kV, the modular multilevel topology might be one attractive solution. Reference [53] presents modular multilevel converters in wind energy applications and proves that for a generator nominal frequency above grid frequency, it can achieve the best efficiency among the investigated topologies.

2.2 Market Overview MV Multilevel Converters

It has been more than three decades after multi-level converters were first introduced in the 1980s. For the high voltage application, MMC is becoming one attractive solution. For the medium voltage application, among the multilevel converters, three-level NPC converter is the most widely used for MV drives. Table D.1 shows an overview of mainstream MV multi-level converter manufacturers. It can be found that the most used topology is the three-level NPC VSC. Besides, CHB VSCs also have some market share. The power rating can be extended to dozens of megawatt, e.g., GE MV7000 can drive an 81 MW system. The voltage level range starts at 2.3 kV until 13.8 kV. The semiconductors adopted in MV application are dominated by IGBTs and IGCTs.

2.3 Overview of MV Semiconductors

The most common power semiconductors are diodes, thyristors and power transistors. According to the application voltage, they can be divided into low voltage (LV, <1000 V) and medium voltage (MV, >1000 V devices, e.g., 1.7, 2.5, 3.3, 4.5 and 6.5 kV). For the medium voltage power semiconductor switches, IGBTs and IGCTs cover almost all the market, which is illustrated in table D.1. This section will present the main characteristics of IGBTs and IGCTs.

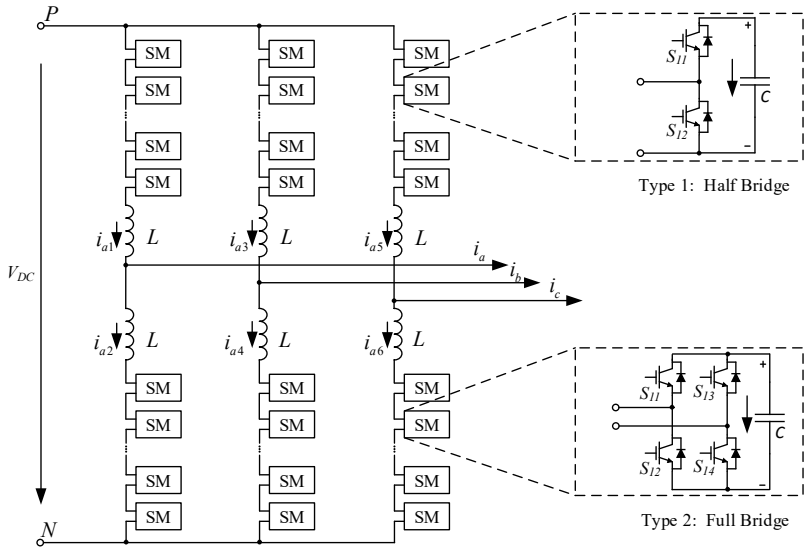

Figure 2.7: *Three-phase Modular Multi-level Converter*

2.3.1 Insulated Gate Bipolar Transistors (IGBTs)

The IGBT was first introduced in 1982 by J.Baliga from GE, with a symmetric blocking voltage of 600 V and 10 A (6 kVA) [54]. It combines the advantages of BJT and MOSFET (e.g., high input impedance, fast switching and low drive energy) to form a mixed device. The IGBT conduction drop voltage is small, which is generally 2 to 3 V (e.g. ABB 5SNA 1200G450350, $V_{CE,sat} = 2.6$ V). The IGBT has several advantages, such as a simple gate unit, snubberless operation, high speed switching for silicon devices and modular design with insulated baseplate [55]. In the market, there are several types, e.g., the traditional structure PT IGBT (Punch-through), NPT-IGBT (Non-punch-through) and FS-IGBT (Field-stop) [54, 56]. Current IGBTs have newer concepts, which include trench-gate IGBTs (Trench-Field-stop IGBT), injection-enhanced IGBTs. In recent years, SiC technology has been developed dramatically. Reference [57] presents comparative evaluation between a 15 kV SiC IGBT and a 15 kV SiC MOSFET. A transformer-less intelligent power substation with 15 kV SiC IGBTs is proposed in [58].

2.3.2 Integrated Gate-commutated Thyristors (IGCTs)

The IGCT was introduced in 1997 especially for high power and medium voltage applications. The structure of IGCT is similar to GTOs. The IGCT has unity turn-off current gain, which means for 4.5 kV, 3000 A IGCT, a negative 3000 A is needed for turn

off [54]. Namely extra low leakage inductance is necessary for IGCT to have a short duration variation and a very large di/dt (e.g., $3000\,\mathrm{A\,\mu s^{-1}}$). The common GTO gate has a stray inductance of around 30 nH, however, IGCT has only around 6 nH [55].

2.4 Market Overview of MV Semiconductors

The mainstream MV power semiconductors manufacturers and their products are shown in table D.2, which mainly include IGBTs and IGCTs. IGBTs have a larger market share than IGCTs. It can be noted that normally the voltage level is designed as 1.7, 2.5, 3.3, 4.5 and 6.5 kV. The maximum dc collector current I_C for 1.7 kV IGBT is 3600 A. Besides the module package of IGBTs, press-pack IGBTs are also offered by manufacturers, e.g., WESTCODE. Press-pack has several advantages, such as explosion free devices, higher thermal reliability and possible redundant converter design due to its short-circuit in failure [55]. Compared to IGBTs, thyristor-based IGCTs are only offered by a few manufacturers, e.g., ABB. The blocking voltage levels have 4.5, 5.5 and 6.5 kV. The current in the table D.2 for IGCTs is the maximum controllable turn-off current (I_{TGQM}). The maximum average on-state current (I_{TAVM}) for ABB 6.5 kV IGCT is 1290 A, which is much higher than the dc collector current for the same voltage level of a IGBT. Generally, the IGCTs have lower saturation voltage than IGBTs.

2.5 Summary

In this chapter, the fundamental MV multi-level converters are introduced. With the increasing demand for the power rating of a single converter, multi-level converters replacing the traditional two-level converter becomes an attractive solution for high power applications. Among a variety of multi-level converter topologies, diode clamped converter (DCC) is the most common for the low-level multi-level converter, i.e., three-level converters. Another topology, the cascaded H-bridge converter (CHB) due to its modular property is widely used for middle-level multi-level converter applications, e.g., nine-level for YASKAWA MV1000. The modular structure makes the system easy to maintain and enables redundant design, which makes the system more reliable. The Modular Multilevel Converter (MMC) was originally designed for high voltage applications. But by employing MMC, the grid converter of WECS can be extended to MV without a transformer (e.g., 33 kV), which can be directly connected to the PCC and might be an alternative for large wind turbine applications.

In the second part of this chapter, the most widely used full-controlled power semiconductors are introduced, i.e., Insulated Gate Bipolar Transistor (IGBT) and Integrated Gate-commutated Thyristor (IGCT). IGCTs are only available in press-pack package, while for IGBTs there are two types of packages, i.e., module and press-pack. Generally speaking, IGCTs can offer larger power rating compared to IGBTs.

Part II

System Design and Evaluation of Wind Energy Conversion System

Referring to Figure 1.5, the second part of the Ph.D. thesis includes two chapters. ***Chapter 3****, system design of wind energy conversion system, presents the detailed system parts modelling individually. For the experimental verification, a low voltage test bench is also designed and built.* ***Chapter 4****, evaluation of wind energy conversion system grid connections focuses on the evaluation criteria of one wind turbine system in terms of stability, efficiency and power quality.*

3 System Design of Wind Energy Conversion System

In this chapter, a megawatt level wind energy conversion system is presented. As described in the previous Chapter 1, the back-to-back direct driven PMSG based wind energy conversion system is selected as the investigation object. First, the MW system overview is shown. Following, the grid side key parts are discussed separately, including the grid side converter, LCL filter and grid modelling. Especially, one scaled low voltage 10 kVA test bench is designed for the experimental verification.

3.1 MW System Structure Overview

Based on the state of the art wind turbine technologies [9, 59], for a megawatt wind power system, PMSG based direct driven generator with multi-level medium voltage back-to-back converter is one attractive choice. Figure 3.1 shows the system structure,

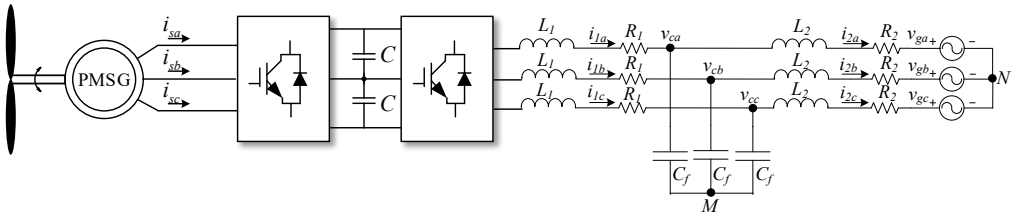

Figure 3.1: *MW Wind Power System Structure*

which mainly includes wind blades, PMSG, power converter and LCL filter without gearbox and transformer. The parameters based on reference [60] of the wind turbine and PMSG are shown in table 3.1a and table 3.1b respectively. The wind turbine rated apparent power is designed as 5 MVA. The maximum power tracking with field oriented control can be implemented in the generator side control. This thesis will focus on the grid side converter current control for grid code compliance.

Table 3.1: *MW Wind Turbine and PMSG Parameters [60]*

(a) *MW Wind Turbine*

Variables	Value
Rated power	5 MW
Rated rotor speed	14.8 rpm
Rotor diameter	116 m
Cut in wind speed	2.5 m s^{-1}
Cut out wind speed	25 m s^{-1}
Rated wind speed	11.8 m s^{-1}
Optimum tip speed ratio	7.61179
Maximum Power coefficient	0.4746

(b) *PMSG Parameters*

Variables	Value
Generator rated power	5 MW
Rated L-L voltage	3.3 kV
Power factor	0.95
Phase resistor Rs	50 mΩ
d-axis inductance	3.5218 mH
q-axis inductance	3.5218 mH
PM flux	10.1486 Wb
Number of pole pairs	118

Among the multi-level medium voltage power converters, three level (A)NPC has been the most prevalent topology in the industry, which is discussed in previous section 2.1. The power converter topology used in the MW system design is shown in figure 3.2, which is a back-to-back active NPC converter. Actually, when the active switches to the midpoint are turned off, and only the body diodes are used, then it becomes a NPC converter. Instead of a single inductor, LCL filter is more effective for medium voltage level, where the switching frequency is around 1 kHz. The detailed LCL filter design will be introduced in section 3.4.

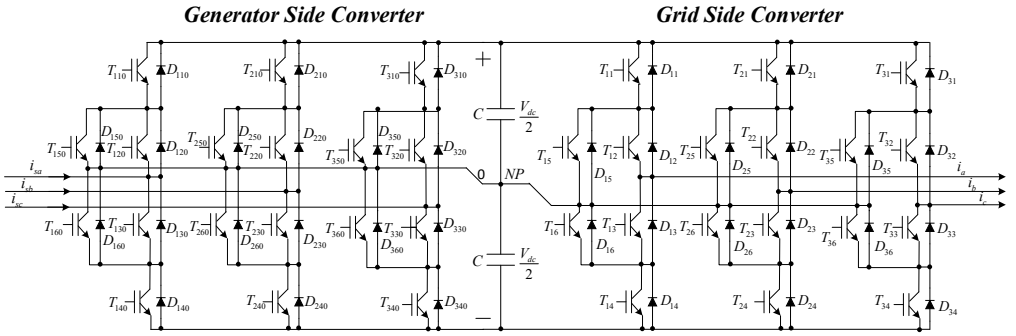

Figure 3.2: *Back-to-back Three Level (A)NPC Converter*

3.2 MV Grid Converter

As the basis, converter modelling should be done at first. The topology of a three-level NPC converter with L-filter connected to the grid is depicted in figure 3.3. Compared to the two-level converter, the three-level NPC converter has three states at the phase output to neutral (NP), which are positive, zero and negative. The switching states of one phase of the converter are given in table 3.2, where $S_{j1}, S_{j2}, S_{j3}, S_{j4} (j = a, b, c)$ indicate the states of the switches. The states of the three level NPC converter can be modelled through switching space vector with the switching functions $p_j(t)$. The switching space vector can be built as:

$$\mathbf{p}(t) = \frac{2}{3}(p_a(t) + \alpha p_b(t) + \alpha^2 p_c(t)) \tag{3.1}$$

$$p_j(t) = \begin{cases} 1 & \text{if } S_j = '+' \\ 0 & \text{if } S_j = '0' \\ -1 & \text{if } S_j = '-' \end{cases} \tag{3.2}$$

where $\alpha = e^{j2\pi/3}$. So the converter output voltage space vector can be achieved by:

$$\mathbf{v}(t) = \mathbf{p}(t)\frac{V_{dc}}{2} \tag{3.3}$$

where V_{dc} is the DC-link voltage. The voltage vector $\mathbf{v}(t)$ can be projected from the 3-phase system into the stationary $\alpha\beta$ frame or the rotating dq frame. The relation between them is presented in figure 3.4. The detailed transformation among the three frames is described in Appendix A of reference [61].

Using space vector representation, there are 27 switching states and hence there are 27 voltage vectors. However, only 19 voltage vectors differ from each other, as shown

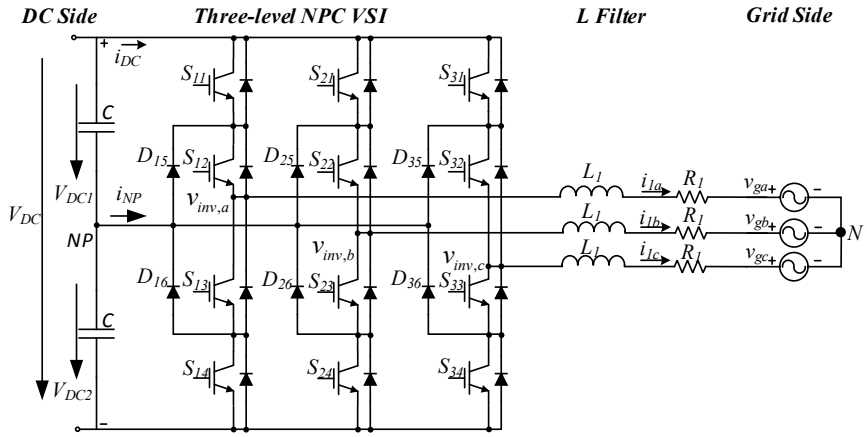

Figure 3.3: *Three-level NPC Converter Grid Connection with L Filter*

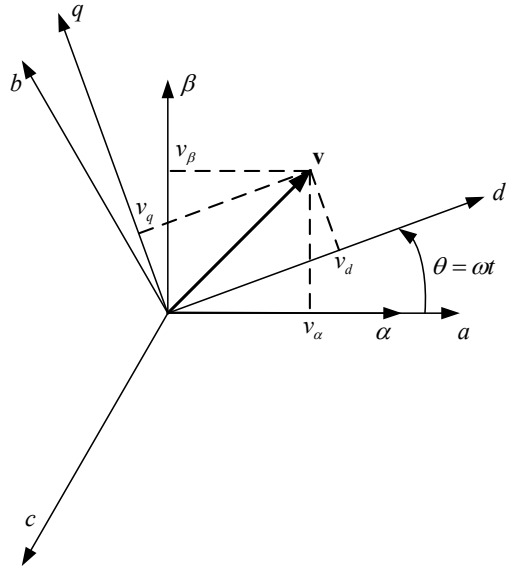

Figure 3.4: *Voltage Vector Projects into Stationary $\alpha\beta$ Frame and Rotating dq Frame*

in figure 3.5. The vectors are classified into four groups. There are six large voltage vectors ($|V_1| \sim |V_6| = 2V_{dc}/3$), six medium voltage vectors ($|V_{12}| \sim |V_{61}| = V_{dc}/\sqrt{3}$), twelve low voltage vectors ($|V_{01}| \sim |V_{06}| = V_{dc}/3$) and three zero voltage vectors.

Table 3.2: *Switching States of Single Phase NPC Converter*

S_{j1}	S_{j2}	S_{j3}	S_{j4}	S_j	$V_{ph,NP}$
1	1	0	0	+	$V_{dc}/2$
0	1	1	0	0	0
0	0	1	1	−	$-V_{dc}/2$

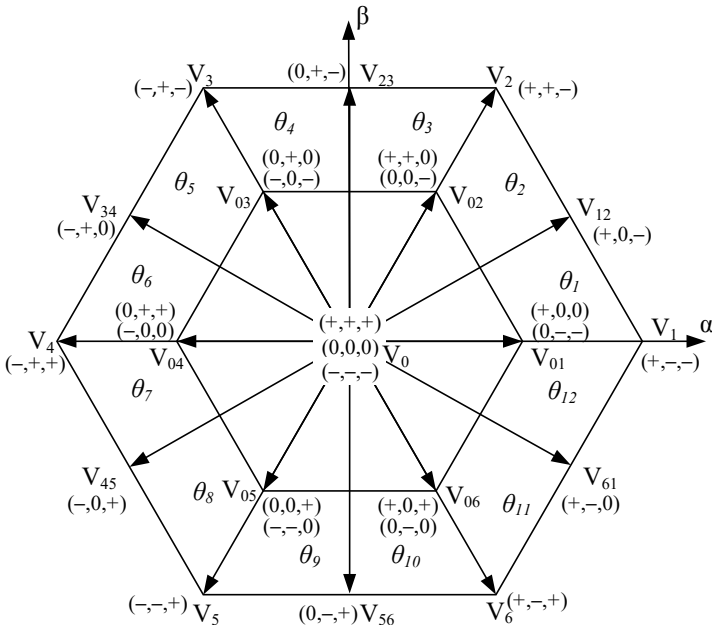

Figure 3.5: *Three level NPC Converter*

3.3 DC-link Capacitor

The DC-link capacitor as the bridge between the generator side and grid side converter takes a very important role in WECSs. The DC-link voltage ripple should be small enough for high quality control performance. Low frequency ripple, e.g., twice of the grid frequency when grid faults occur, require a larger capacitor. A smaller capacitor has fast response, but it might have higher voltage ripples and reduced lifetime. So the DC-link capacitor design is a trade-off between the voltage ripples and control response considering lifetime, footprint and cost. Considering these aspects, the DC-link capacitor can be designed according to the following equation [62, 63]:

$$C_{dc} = \frac{S}{V_{dc}^* \cdot \Delta v_{dc} \cdot 2 \cdot \min\{\omega_{e,grid}, \omega_{e,gen}\}} \tag{3.4}$$

where C_{dc} is the whole DC-link capacitor, and $C_{dc1}, C_{dc2} = C = 2C_{dc}$. S is the apparent converter power. V_{dc}^* is the nominal DC-link voltage. Δv_{dc} is the allowed voltage ripple (2% recommended in [64]). $\omega_{e,grid}$ and $\omega_{e,gen}$ represent the grid angular frequency and generator nominal electrical angular frequency, respectively. According to equation 3.4 and the parameters shown in table 3.1a and table 3.1b, the DC-link capacitor is designed as 7631 µF (5% voltage ripple).

3.4 LCL Filter

3.4.1 Modelling of LCL Filter

The diagram of the converter connected to grid through the LCL filter is shown in figure 3.6. According to Kirchhoff's voltage law the three-phase voltage equations under balanced condition can be obtained in abc frame. They are given by:

$$\begin{cases} L_2 \frac{di_{2k}}{dt} = -R_2 i_{2k} + v_{ck} - v_{gk} \\ C_f \frac{dv_{ck}}{dt} = i_{1k} - i_{2k} \\ L_1 \frac{di_{1k}}{dt} = -R_1 i_{1k} + v_{1k} - v_{ck} \end{cases} \tag{3.5}$$

where the subscript $k = a, b, c$ indicates the three phases. i_{1k} is the converter side current, i_{2k} is the grid side current, v_{ck} is the capacitor voltage in LCL filter, v_{1k} is the output voltage of the converter, and v_{gk} is the grid voltage. L_1,L_2 are the converter side and grid side inductances, respectively. R_1,R_2 are the resistances of the converter side and grid side inductors, respectively. C_f is the capacitance of the LCL filter.

The system shown in equation 3.5 can be simply written in the space state form:

$$\frac{d}{dt}x = A_m x + B_m u + E_m w \tag{3.6}$$

where the state variable vector is the combination of grid side current, capacitor voltage and converter side current in abc coordinates $x = [\ i_2 \quad v_c \quad i_1\ ]^T$. The input vector $u = v_1$ and the disturbance term $w = v_g$. The state matrix A_m, input matrix B_m and disturbance matrix E_m are given by:

$$A_m = \begin{vmatrix} -\frac{R_2}{L_2} & \frac{1}{L_2} & 0 \\ -\frac{1}{C_f} & 0 & \frac{1}{C_f} \\ 0 & -\frac{1}{L_1} & -\frac{R_1}{L_1} \end{vmatrix} \tag{3.7}$$

$$B_m = [\ 0 \quad 0 \quad \tfrac{1}{L_1}\ ]^T \tag{3.8}$$

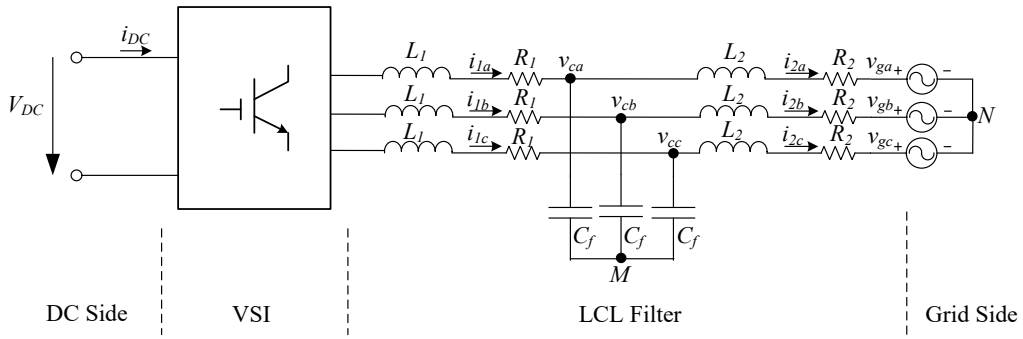

Figure 3.6: *Voltage Source Converter Grid Connection with LCL Filter*

$$E_m = \begin{bmatrix} -\frac{1}{L_2} & 0 & 0 \end{bmatrix}^T \tag{3.9}$$

3.4.2 Design of LCL Filter

In order to design the grid side inductor, it is necessary to analyse the forward transfer-admittance, which is the transfer function from converter phase voltage to grid current shown below:

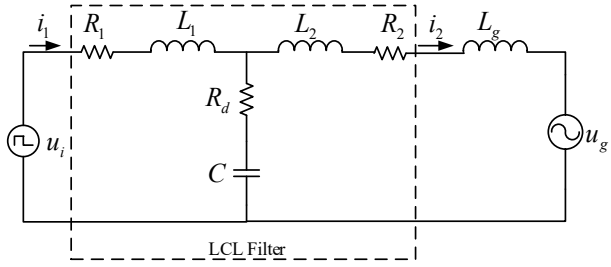

Figure 3.7: *LCL Filter Equivalent Circuit*

$$G(s) = \frac{I_2}{U_1} = \frac{R_d C s + 1}{L_1 L_2 C s^3 + k_2 s^2 + k_1 s + R_1 + R_2} \tag{3.10}$$

where $k_2 = [L_1(R_2+R_d)+L_2(R_1+R_d)]C$ and $k_1 = [L_1+L_2+(R_1R_2+R_1R_d+R_2R_d)C]$. If the inductor parasitic resistances R_1 and R_2 are neglected, equation 3.10 can be simplified:

$$G_1(s) = \frac{I_2}{U_1} = \frac{R_d C s + 1}{L_1 L_2 C s^3 + (L_1 + L_2) R_d C s^2 + (L_1 + L_2) s} \tag{3.11}$$

Table 3.3: *Base Value of PU System*

Variable	Symbol	Formula	Value	Unit
Power	P_b	-	5	MW
Voltage	V_b	-	3.3	kV
Frequency	f_b	-	50	Hz
Angular Frequency	ω_b	$2\pi f_b$	314.16	rad/s
Current	I_b	$P_b/V_b = \sqrt{3}I_N$	1515	A
Impedance	Z_b	V_b^2/P_b	2.178	Ω
Inductance	L_b	Z_b/ω_b	6.933	mH
Capacitance	C_b	$1/Z_b\omega_b$	1461	μ F

For convenience, the system base variables of the PU system are shown in table 3.3. The line-to-line voltage is selected as the base voltage V_b. The base current variable I_b equals P_b/V_b, which is actually the rated phase current. The base impedance Z_b, inductance L_b and capacitance C_b are V_b^2/P_b, Z_b/ω_b and $1/(Z_b\omega_b)$ respectively. The LCL filter design procedures are discussed as follows:

1. Converter side inductor design

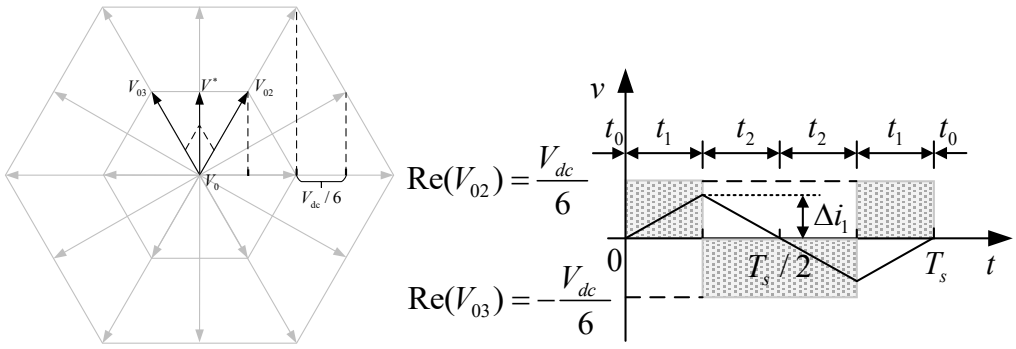

(a) *Vector Combination* ***(b)*** *Current Ripple*

Figure 3.8: *Three-level NPC Current Ripple for Worst Case*

The converter side inductor is designed in order to limit the ripple of the converter side current. There is a trade off between the ripple reduction and the inductor cost. The smaller the current ripple, the larger the inductor. From the industrial point of view, the current ripple can be chosen as 15% ∼ 25% of the rated current. For a two-level converter, the minimum converter side inductor can be calculated by the equation given

in reference [65]. It should be noted that the equation depends on the topology and modulation algorithm though. For the three-level converter (figure 3.8), the projection of the selected voltage vector at axis a, i.e., horizontal axis is the phase A voltage. It can be found that the range for phase A voltage is changing from $-2V_{DC}/3$ to $2V_{DC}/3$ with the step $V_{DC}/6$. For SVM, which is equivalent to SPWM with third harmonics injection, the composite voltage vector V^* can be implemented by adjacent voltage vectors and zero vectors, which is shown in figure 3.8a. The relation can be expressed as:

$$V_0 \cdot t_0 + V_{02} \cdot t_1 + V_{03} \cdot t_2 = V^* \cdot \frac{T_s}{2} \tag{3.12}$$

where $t_0 + t_1 + t_2 = T_s/2$. Assuming that the capacitor voltage is constant during one switching period, the maximum current ripple will occur when $t_0 = 0$ and the phase A voltage is crossing zero. So the peak voltage-second can be derived as:

$$L_1 \frac{di_1}{dt} = v_{L_1} \Rightarrow L_1 \Delta i_1 = v_{L_1} \Delta t = \frac{V_{dc}}{6} \cdot \frac{T_s}{4} \tag{3.13}$$

If the value 20% of the rated current is selected as the current ripple, the minimum inductance of the converter side can be estimated by [66]:

$$L_{1\,\min} = \frac{V_{dc}}{24 \Delta i_{1\,\max} f_s} \tag{3.14}$$

where $\Delta i_{1\,\max}$ is the peak current ripple and f_s is the switching frequency. Since the converter side current has to endure high frequency ripple current, and with high requirements for core material and the volume, typically the converter inductor is more expensive than the grid side inductor. From the cost point of view, a smaller the converter side inductor design is preferred.

The current ripple depends on DC link voltage V_{dc} and switching frequency f_s. For medium voltage and mega-watt level wind power application, the switching frequency range is normally around 1 kHz, which is smaller than the PV and low power wind application. In order to guarantee a symmetrical PWM output, the carrier wave ratio $N = f_c/f_r$ should be an odd and a multiple of three. For this case, $N = 21$ is selected for the LCL filter design, i.e., the switching frequency is 1050 Hz. Regarding the DC link voltage, theoretically there is a minimum voltage for normal operation of PWM converter, e.g., $V_{dc}/2 \geq V_{gm}$ (SPWM) and $V_{dc}/\sqrt{3} \geq V_{gm}$ (SVPWM). Here, V_{gm} is the amplitude of the grid phase voltage. For this reason and considering some margin, the DC link nominal voltage is selected as 6000 V. Based on the analysis above, the relationship between the maximum current ripple $\Delta i_{1\,\max}$ and converter side inductor L_1 can be found. It can be derived that if 20% of the rated current is selected as the current ripple, the minimum converter side inductor is 1.36 mH.

2. Shunt capacitor design

After the minimum converter side inductance is chosen, the shunt capacitor selection is a trade-off between reactive power installed in the capacitor and the converter side inductance. If the capacitor is too small, the inductor L_1 needs to be large enough in order to meet the attenuation requirement. At the same time, a large L_1 increases the cost significantly. However, a large capacitor means large reactive power, and a larger current flows through the converter, which makes relevantly more losses. As another aspect, the application should also be considered. Equation 3.15 shows the relation between the shunt capacitance and the base capacitance, where x represents the PU value. For low power and several kilohertz switching frequency, 2%-15% of the base capacitance C_b is typically used [65, 67, 68]. But for high power, e.g. mega-watt level, where the switching frequency is around one kilohertz, a capacitor in the range of 42%-45% of the base capacitance C_b is recommended [66, 69]. A value of 43% is considered in this work, which corresponds to a capacitance of 628 µF.

$$C_f = xC_b \tag{3.15}$$

3. Grid side inductor design

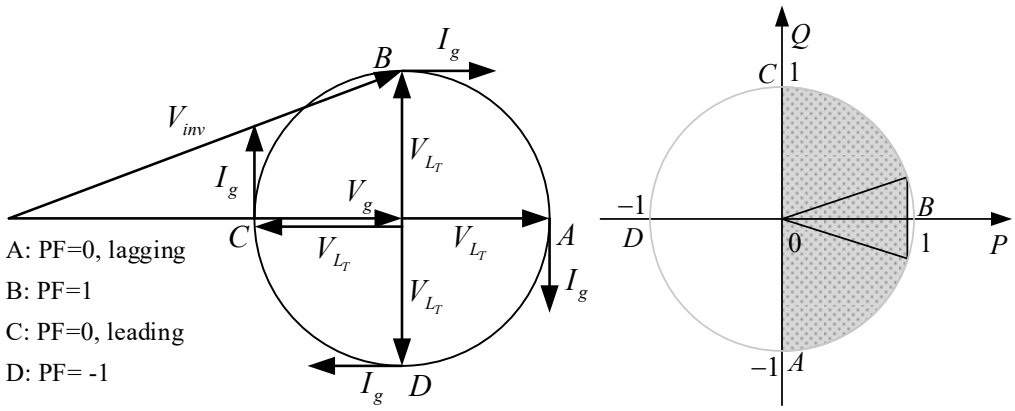

(a) Vector Diagram *(b) PQ Diagram*

Figure 3.9: *Vector Diagram and PQ Diagram*

The grid side inductor is mainly used to limit the high order harmonics. However, with the grid inductor increasing, the fundamental voltage drop becomes larger. From the vector diagram shown in figure 3.9a, it can be found that the operation point C ($PF = 0, leading$) needs the smallest inverter output voltage, while at the operation point A ($PF = 0, lagging$), the largest inverter output voltage is required. In reality, four quadrant full operation is not necessary, according to the PQ diagram shown in

figure 3.9b, where the inner triangle shows the normal range of operation with 5% reactive power injected/absorbed [61]. Assuming that the capacitor is ignored, the total inductance should comply with:

$$L_T = L_1 + L_2 \leq L_{\max\_op} \leq \frac{V_{dc}/2 - V_{gm}}{2\pi f_1 I_{gm}} \tag{3.16}$$

where $L_{\max\_op}$ is the maximum inductor limited by the pre-defined operation point, e.g., point A, V_{gm} and I_{gm} are the amplitude of the grid phase voltage and current respectively.

Under this condition, the grid inductor should be designed to comply with the grid code, e.g., IEEE 519-1992. The current harmonics limits of this grid code are shown in figure 3.10. One tested grid current harmonic distribution at $PF = 1$ is also analysed, which comply with the grid code. Detailed information on the grid code will be given in section 4.2.

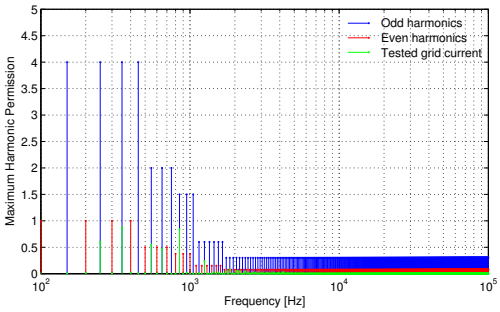

Figure 3.10: *Grid Code Standard IEEE 519-1992 (Current Harmonics)*

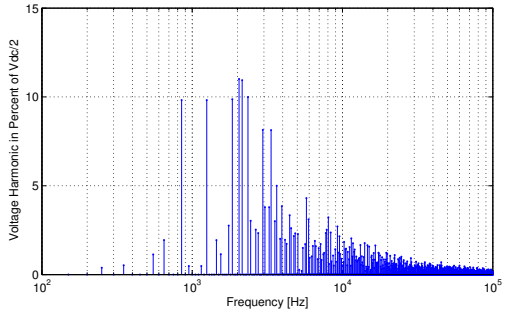

Figure 3.11: *Converter Phase Voltage FFT Analysis with $PF = 1$*

Assume L_T as a constant and $\alpha = L_1/L_T$, equation 3.11 can be written as:

$$G_1(s) = \frac{I_2}{U_1} = \frac{R_d C s + 1}{\alpha(1-\alpha)L_T^2 C s^3 + L_T R_d C s^2 + L_T s} \tag{3.17}$$

It can be easily proved that when $\alpha = 0.5$, namely $L_1 = L_2$, the filter has the best attenuation. But at the same time, the resonance frequency $f_{res,1}$ become the smallest, which may cause resonance problems. To avoid this, the resonance frequency of the LCL filter normally should be in the range of ten times the fundamental frequency and half of the switching frequency [66].

$$f_{res,1} = \frac{1}{2\pi}\sqrt{\frac{1}{\alpha(1-\alpha)L_T C}} \tag{3.18}$$

In order to get the optimal value of the grid inductor, several values of L_2 are compared in figure 3.12. According to the grid current limitation spectrum shown in figure 3.10 and the phase voltage spectrum shown in figure 3.11, a grid code transfer function can be defined as:

$$G_{grid\_code} = \frac{I_{g\_grid\_code}(s)}{V_{inv}(s)} > G_1(s) = \frac{I_2}{U_1} \tag{3.19}$$

Namely by employing the LCL filter, the forward transfer-admittance $G_1(s)$ should be below the grid code transfer function to comply with the grid code, which is shown in figure 3.12. Considering the filter size, weight and cost, $L_2 = 0.3\,\text{mH}$ is selected. It should be noted that damping is necessary for the filter.

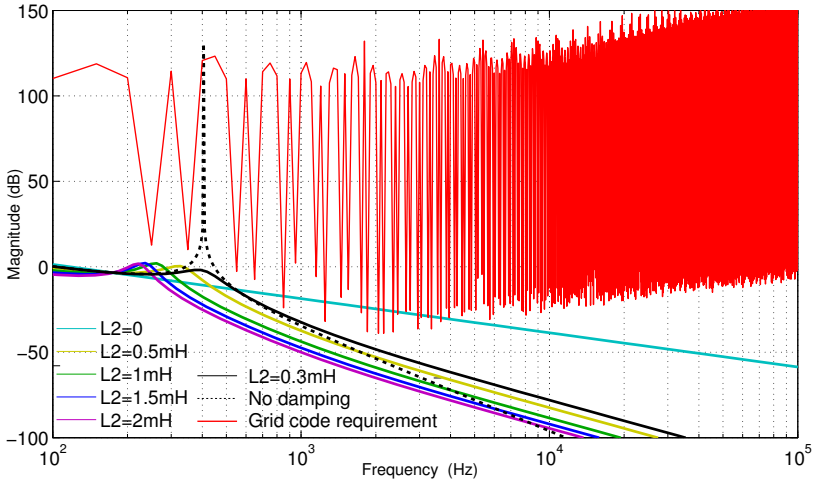

Figure 3.12: *Forward Trans-admittance with Different Grid Side Inductance*

Based on the design procedure aforementioned, the designed parameters of the LCL filter are summarised in table 3.4.

Table 3.4: *LCL Filter Parameters*

Component	PU Value	Real Value
L_1	0.196	1.36 mH
C_f	0.43	628 µF
L_2	0.04	0.3 mH
R_d	0.09	0.2 Ω

3.5 Modelling of PCC Voltage

For the balanced grid voltage, the positive sequence can be expressed as:

$$\begin{cases} v_a = V_m^+ \cos \omega t \\ v_b = V_m^+ \cos(\omega t - \frac{2\pi}{3}) \\ v_c = V_m^+ \cos(\omega t + \frac{2\pi}{3}) \end{cases} \tag{3.20}$$

where V_m^+ is the amplitude of the positive sequence of the grid voltage. By employing the Clarke transformation, it can be easily transferred to:

$$\begin{bmatrix} v_\alpha \\ v_\beta \end{bmatrix} = \frac{2}{3} T \begin{bmatrix} v_a \\ v_b \\ v_c \end{bmatrix} = V_m^+ \begin{bmatrix} \cos \omega t \\ \sin \omega t \end{bmatrix} \tag{3.21}$$

where

$$T = \begin{bmatrix} 1 & -1/2 & -1/2 \\ 0 & \sqrt{3}/2 & -\sqrt{3}/2 \end{bmatrix} \tag{3.22}$$

It can be found that:

$$\begin{cases} \frac{dv_\alpha}{dt} = -V_m^+ \omega \sin \omega t = -V_m^+ \omega v_\beta \\ \\ \frac{dv_\beta}{dt} = V_m^+ \omega \cos \omega t = V_m^+ \omega v_\alpha \end{cases} \tag{3.23}$$

3.6 Scaled Experimental Low Voltage System Setup

In order to verify the investigated control algorithms, a low voltage power conversion system is built. The original plan was to include a three phase three-level back-to-back (A)NPC converter, a 12-pulse three phase diode rectifier, an LCL filter, two transformers, a wind emulator and control system. The whole structure is shown in figure 3.13. However, it should be noted that the wind emulator in the left dashed frame was not built for final test. The right dashed rectangle frame indicates the converter metal cabinet. The main power conversion parts are installed in the cabinet for safety reasons. The 12-pulse diode rectifier is used for the DC-link charge. The wind emulator consists of an Induction Motor (IM) and an Electrically Excited Synchronous Generator (PMSG). The induction machine is controlled by a Siemens Sinamics 120 Converter, which can implement direct torque control to simulate the different wind profiles. The control system mainly includes a Wago Programmable Logic Controller (PLC) and a dSPACE SCALEXIO system. The former one is responsible for the DC-link charge and discharge, door system and the IM control. The latter one is in charge of the converter control, which includes PWM signal generation, Analog Digital Conversion (ADC) and error signal receiving. For human-computer interaction, e.g., reference value setting,

physical variables measurement, is implemented via dSPACE ControlDesk. A photo of the test bench is shown in figure A.1.

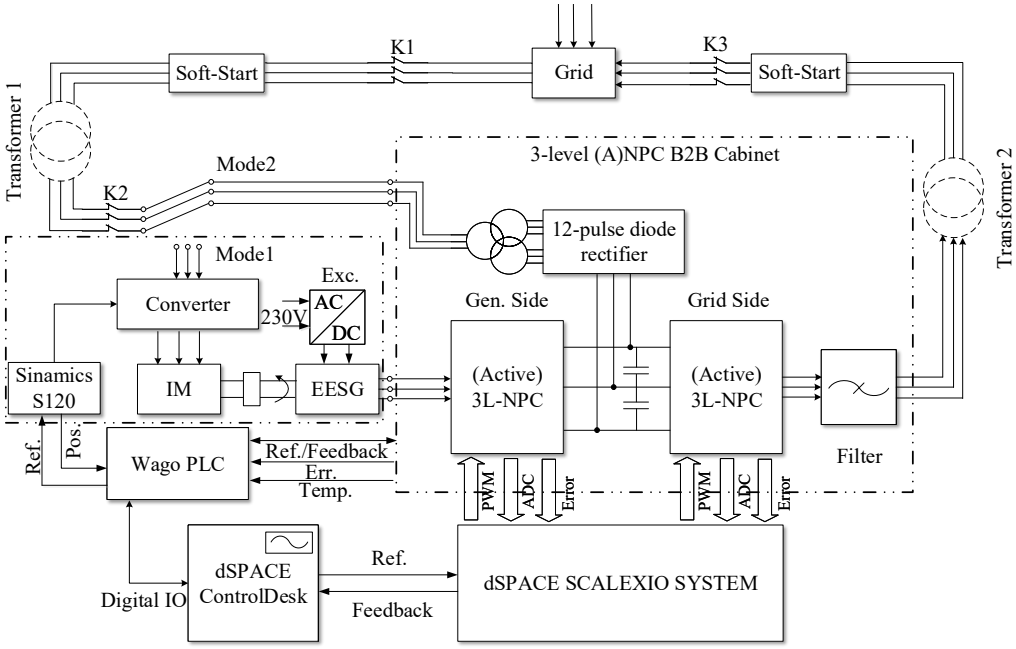

Figure 3.13: *10KVA Three Phase Three-level (A)NPC Back-to-back Power Conversion System*

3.6.1 Operation Modes

The original objective is to build a flexible setup in order to offer a large flexibility [70], which includes:

- 4-quadrant operation on both converter sides
- 2-level or 3-level converter operation including NPC and ANPC mode
- simulation of different source behaviours (wind, diesel, biomass)
- changing of machine task (motor/generator)
- grid integration and off-line operation mode
- implementation of various converter control algorithms

The converter test bench has two operation modes, which are:

- Mode 1: Back-to-back operation
- Mode 2: Diode rectifier and grid side converter operation

Operation mode 1, can fully simulate the full power conversion back-to-back wind turbine from the generator side to the grid connection. Being available in the power electronics group, an EESG is used to emulate the function of a PMSG. The excitation system is controlled by an AC/DC converter.

For operation mode 2, the power flows through the 12-pulse diode rectifier, the grid side converter and the LCL filter connecting to the grid. The generator side converter is not utilized. In this mode, the test bench is mainly used for grid converter control algorithm verification. For the grid converter control, the grid code must be fully considered to comply with, including the harmonics requirement and high/low voltage ride-through. This thesis will focus on the operation mode 2 to investigate the current control of the grid side converter.

3.6.2 Control System

The control system consists of two parts, a programmable logic controller (PLC) and a dSPACE Scalexio control system. While the PLC realizes overall control tasks as the startup sequence, fault handling and control of the drive train, the dSPACE system controls the back-to-back converter. More details can be found in appendix A.1.

1. Programmable Logic Controller

   A WAGO PLC (750-881) system is responsible for functional safety, charging and discharging of the dc link capacitors, temperature measurement, and drive train control. It consists of a single central controller which is supplemented by a touch-enabled display to deploy a versatile human-machine-interface (figure A.2a). The display can be used for monitoring both electrical and mechanical values as well as for powering on and controlling the test bench.

2. dSPACE SCALEXIO System

   The converters are controlled by the dSPACE SCALEXIO control system, which is integrated with the DS2655 FPGA Base Module and the DS2655M1 I/O Module. For example, for mode 1, the state-of-the art cascaded control schemes can be applied for the operation of the test bench. This means that on the generator side, field oriented control (FOC) is used. Under normal operation, the Maximum Power Point Tracking (MPPT) method, see e.g. [71, 72] is adopted to extract the maximum power from the wind turbine, giving the generator speed reference. Figure 3.14 depicts the outer speed and the inner current loop of the controller.

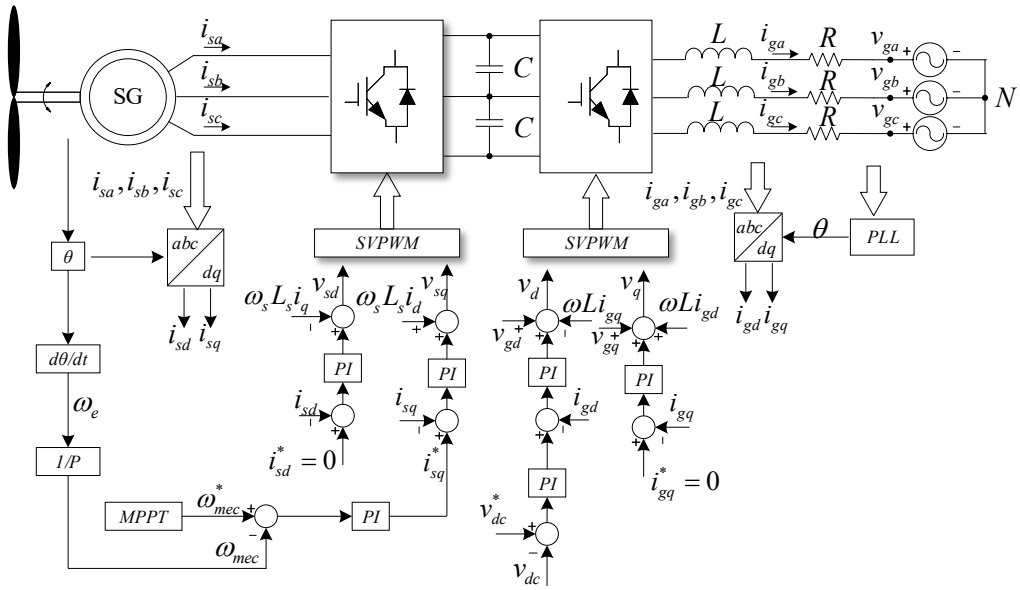

Figure 3.14: *Cascaded Control Scheme for the Back-to-back Converter*

On the grid side, voltage orientated control (VOC) operating in a synchronous dq reference frame is implemented [73]. Since MPPT is used for the generator, the grid side converter is responsible for the dc link voltage control. All controllers could be classical PI controllers designed according to the "modulus optimum" for the current loops and the "symmetrical optimum" for the dc voltage.

3.6.3 Power Converter

The scaled back-to-back converter consists of a generator side rectifier and a grid side inverter in IGBT technology applying 1.2 kV semiconductor devices [74]. Four 4700 µF / 450 V electrolytic capacitors in series are used for the DC link. Each converter is realized as a 3-level Active Neutral Point Clamped Converter (ANPC) which comprises additional active switches compared to the NPC, as shown in Figure 3.2. Choosing an appropriate PWM scheme, each converter can be operated either as a 2-level converter, a 3-level NPC converter or as a 3-level ANPC converter with an optimized loss distribution. Figure A.4a depicts the IGBT modules, drivers and heat sinks of the converter.

3.6.4 LCL Filter

As mentioned before, the LCL filter is the bridge between the converter and the grid. The megawatt level LCL filter design was illustrated in subsection 3.4. For the low voltage test bench, LCL filter components are selected in order to match the PU value shown in table 3.4 as close as possible. Based on the available devices, the selected components are shown in table 3.5.

Table 3.5: *LCL Filter Parameter for 10KVA Test Bench*

Component	PU Value	Real Value
L_1	0.161	8.2 mH
C_f	0.118	23.5 µF
L_2	0.149	7.6 mH
R_d	0.3	5 Ω

3.7 Summary

In this chapter, the design of the electrical part of a 5 MVA wind turbine is addressed. It includes a PMSG, the back-to-back three-level converter and the LCL filter. The modelling of the grid converter, LCL filter, and the grid are described, respectively. In addition, the design of an LCL filter is given step by step for medium voltage and megawatt level.

Finally, the low voltage system setup is designed and built in the laboratory. The main parts of the setup, i.e., control system, power converter, and LCL filter are discussed in detail. The system design is the basis for the further research.

4 Evaluation for Grid Connection of WECS

This chapter addresses the evaluation methods of a wind turbine system. For the power system, the stability, power quality and efficiency are the basic three aspects. Stability is the most important one. Power quality is a complex issue, which includes line interruptions, flicker, phase unbalance, distortion [75]. Around the world, different countries have different grid codes to achieve the required quality. Guaranteeing stability and power quality, efficiency can be considered further for decreasing losses and performance improvement. For a single wind turbine electrical system, the same aspects can be analysed, and will be discussed in this chapter.

4.1 Stability Analysis

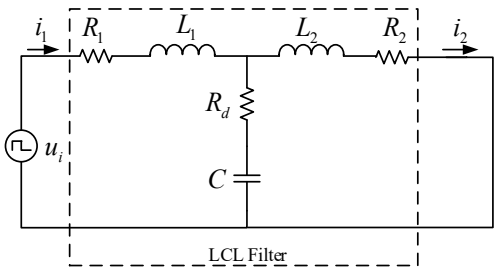

Figure 4.1: *Simplified LCL Filter Equivalent Circuit for Stability Analysis*

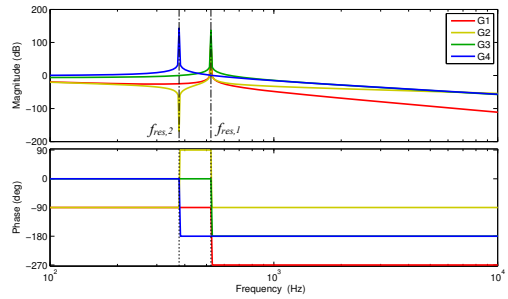

Figure 4.2: *LCL Filter Transfer Function Bode Plot*

The main goal of the grid side converter is the independent control of active and reactive power injected to the grid, which means the voltage source converter is controlled as a current source. Normally, the internal control loop is the current control loop. A good current controller design is essential for the system stability. Since the LCL filter is used for the grid connection and introduces resonance problems into the system, it is necessary to analyse the relevant transfer functions. Figure 3.7 can be simplified with an assumption that the grid voltage only contains a fundamental component, which can be seen as a short circuit with zero impedance when performing the stability analysis and harmonics analysis. The simplified circuit is shown in figure 4.1. In the frequency domain, there are four transfer functions to be considered. For the worst case, the inductor parasitic resistances R_1 and R_2 are neglected. The converter voltage to the grid current transfer function $G_1(s)$ is shown in equation 3.11. The other three are given below. Here, U_c is the sum voltage of R_d and C.

$$G_2(s) = \frac{I_1}{U_1} = \frac{L_2Cs^2 + R_dCs + 1}{L_1L_2Cs^3 + (L_1 + L_2)R_dCs^2 + (L_1 + L_2)s} \tag{4.1}$$

$$G_3(s) = \frac{U_c}{U_1} = \frac{L_2R_dCs^2 + L_2s}{L_1L_2Cs^3 + (L_1 + L_2)R_dCs^2 + (L_1 + L_2)s} \tag{4.2}$$

$$G_4(s) = \frac{I_2}{I_1} = \frac{R_dCs + 1}{L_2Cs^2 + R_dCs + 1} \tag{4.3}$$

The bode plots of transfer function G_1, G_2, G_3, G_4 without damping ($R_d = 0$) are shown in figure 4.2. Two resonance frequencies can be found:

$$f_{res,1} = \frac{1}{2\pi}\sqrt{\frac{L_1 + L_2}{L_1L_2C}} \tag{4.4}$$

$$f_{res,2} = \frac{1}{2\pi}\sqrt{\frac{1}{L_2C}} \tag{4.5}$$

where it is obvious that $f_{res,1} > f_{res,2}$, since $L_1 + L_2 > L_1$. For the test setup described in subsection 3.6, the resonance frequencies are $f_{res,1} = 522.76\,\text{Hz}$ and $f_{res,2} = 376.60\,\text{Hz}$.

Compared to a simple inductive filter, the LCL filter has two options to design the internal current loop, the converter side current feedback (CSCF) and the grid side current feedback (GSCF). In the literature, both methods are used. In references [76–79], the CSCF is adopted with or without additional damping, while in references [80–85], the GSCF is fully studied. In addition, several references also compare the two methods. In reference [86], the discrete root loci are analysed with different ratio of resonance frequency and control frequency. It is concluded that the GSCF is superior to the CSCF since the former could be stable without any damping. On the contrary, the reference [87] shows that the CSCF is more stable due to the unique inherent damping characteristic of the LCL filter. The conclusion is drawn that the GSCF has no such inherent damping. However, there is no time delay considered in this paper. Actually, the time delay caused by the ADC, computation, and pulse width modulation (PWM) generation is inevitable, which should be considered in the stability analysis. Reference [88] conducts the stability analysis of both CSCF and GSCF methods considering time delay. A comprehensive overview of the previous papers is given, which illustrates why different conclusions have been drawn in before.

The stability depends on the ratio of resonance frequency and control frequency and the feedback current, and time delay. The detailed analysis will be given for the MV designed system.

4.1.1 Grid Side Current Feedback Control

Since the original objective of the grid converter is to control the active power and reactive power, it is natural to select the grid current as the controlled variable. Moreover, the grid code has specific requirements on the grid current harmonics. So the direct grid current control should be considered as a priority. Reference [86] shows that if the resonance frequency is less than half and above one quarter of the control frequency, the system is stable without damping for grid side current feedback control. A similar conclusion is drawn in reference [81], the grid side current inherent damping effect is only available when the resonance frequency is above one-sixth of the system sampling frequency. In order to observe the stability of the designed system, the open loop transfer function block diagram in s-domain is shown in figure 4.3, where $G_c(s)$ is the controller. $G_d(s)$ represents the total time delay, and k_{PWM} is the gain of the PWM, which is one here. For Voltage Oriented Control (VOC), a simple PI controller is adopted:

$$G_c(s) = k_p(1 + \frac{1}{\tau s}) \tag{4.6}$$

where k_p is the proportional parameter and τ is the time constant. The PI controller is designed according to the modulus optimum (MO) method. Here $k_p = L_T/(3T_s)$, $\tau = L_T/R_T$, and $L_T = L_1 + L_2$, $R_T = R_1 + R_2$. T_s is the sampling time. For the time delay block, λT_s ($\lambda = 1.5$) is estimated here, so

$$G_d(s) = \frac{1}{\lambda T_s s + 1} \tag{4.7}$$

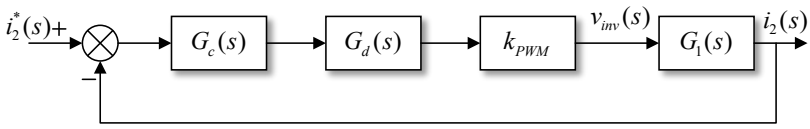

Figure 4.3: *Grid Side Current Feedback Control Block Diagram in S-domain*

So the open loop transfer function in s-domain can be achieved as:

$$G_{opg}(s) = k_{PWM}G_c(s)G_d(s)G_1(s) \tag{4.8}$$

Since the controller will be implemented in the digital system, the transfer function is transformed into z-domain, which is shown in figure 4.4. So the open loop and close loop transfer function can be obtained as:

$$G_{opg}(z) = G_c(z)G_g(z) \tag{4.9}$$

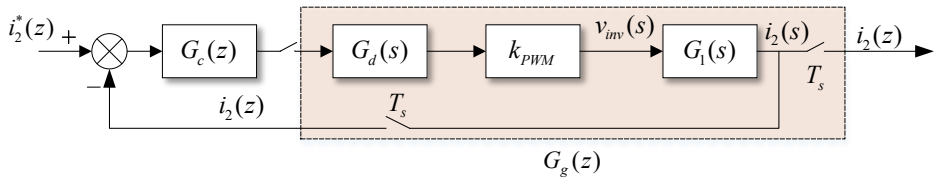

Figure 4.4: *Grid Side Current Feedback Control Block Diagram in Z-domain*

$$G_{clg}(z) = \frac{G_c(z)G_g(z)}{1 + G_c(z)G_g(z)} \tag{4.10}$$

where $G_g(z)$ is the discrete part of delay, PWM generator and forward admittance $G_1(s)$ from inverter side voltage $v_{inv}(s)$ to grid current $i_2(s)$. From equation 4.10, the system zeros ('o') and poles ('x') can be obtained, which are shown in figure 4.5. It can be noted that without damping ($R_d = 0$), the system poles are already outside of the unit circle, which means the system is not stable. With increasing the damping resistor value, the system poles move to the inside of the unit circle, which means the system becomes stable.

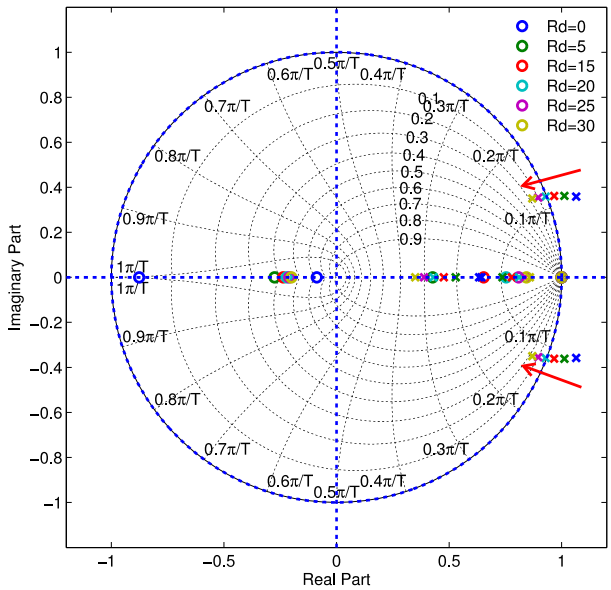

Figure 4.5: *GSCF Close Loop Root Locus with R_d Varying*

In conclusion, if the GSCF control is adopted for the designed system, it is not stable without damping and with $1.5T_s$ delay considered. The system can be stable if the damping resistor increases. It can be noted that the minimum value of the damping resistor is $20\,\Omega$ according to figure 4.5.

4.1.2 Converter Side Current Feedback Control

Besides the GSCF control, CSCF control is the second option. In order to reduce the cost and the quantities of the sensors, normally the converter side current is measured since for an industrial converter, the current sensors are installed in its hardware, which is also used for protection [76, 77]. Similar to GSCF, the single current loop diagram in the s-domain is shown in figure 4.6. So the open loop transfer function in s-domain can be achieved as:

$$G_{opi}(s) = k_{PWM} G_c(s) G_d(s) G_2(s) \tag{4.11}$$

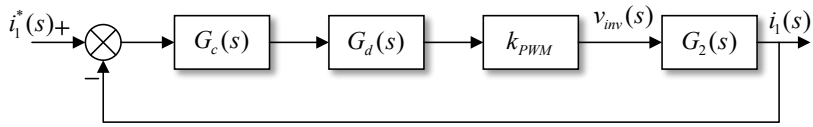

Figure 4.6: *Converter Side Current Feedback Control Block Diagram in S-domain*

The CSCF control loop diagram in z-domain is shown in figure 4.7, where the grid side current branch $G_g(z)$ is also drawn, and $G_i(z)$ is the discrete part of delay, PWM generator and self admittance $G_2(s)$ from inverter side voltage $v_{inv}(s)$ to inverter current $i_1(s)$.

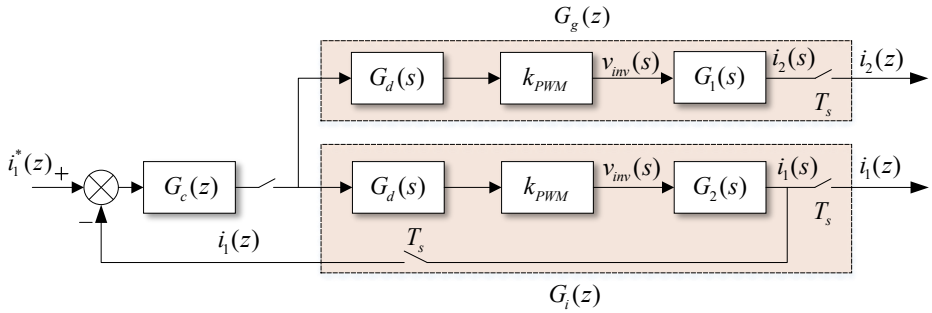

Figure 4.7: *Converter Side Current Feedback Control Block Diagram in Z-domain*

So the open loop and close loop transfer function can be obtained as:

$$G_{opi}(z) = G_c(z)G_i(z) \tag{4.12}$$

$$G_{cli}(z) = \frac{G_c(z)G_i(z)}{1 + G_c(z)G_i(z)} \tag{4.13}$$

From equation 4.13, the zeros and poles of CSCF control system can be obtained and drawn in z-plane shown in figure 4.8. Compared to GSCF, the poles of CSCF are all inside of the unit circle even without any damping ($R_d = 0$). With the damping resistance increasing, the poles move close to the origin which means the transient response attenuates faster with the larger damping factor.

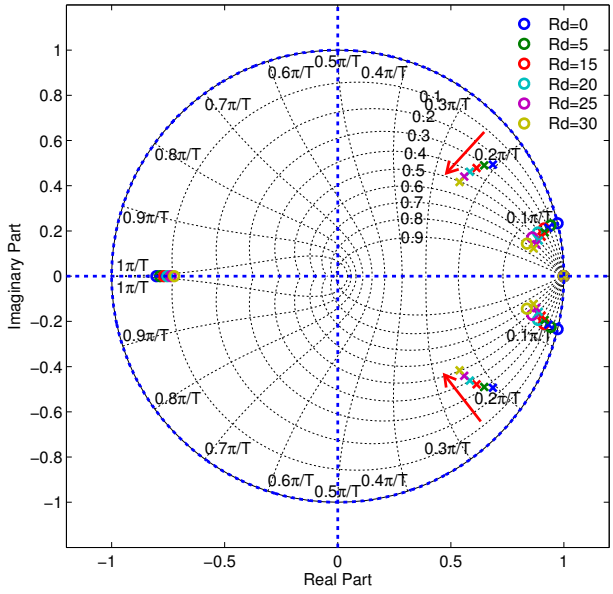

Figure 4.8: *CSCF Close Loop Root Locus with R_d Varying*

Comparing the two methods, it can be concluded that CSCF is better than the GSCF for the designed system. This also complies with the conclusion given in reference [88], which is shown in table 4.1. For the designed system, the resonance frequencies $f_{res,1} = 522.76\,\text{Hz} < \frac{1}{9}f_s = 1.11\,\text{kHz}$, which is located in the optimal range of CSCF with $\lambda = 1.5$. Here f_s is the sampling frequency.

Table 4.1: *Stable Range Considering Sampling Frequency and Resonance Frequency [88]*

Method	λ	Stable Range	Optimal Range
CSCF	1	$f_{res} < \frac{1}{4}f_s$	$f_{res} < \frac{1}{6}f_s$
	1.5	$f_{res} < \frac{1}{6}f_s$	$f_{res} < \frac{1}{9}f_s$
GSCF	1	$\frac{1}{4}f_s < f_{res} < \frac{1}{2}f_s$	$\frac{1}{3}f_s < f_{res} < \frac{1}{2}f_s$
	1.5	$\frac{1}{6}f_s < f_{res} < \frac{1}{2}f_s$	$\frac{2}{9}f_s < f_{res} < \frac{4}{9}f_s$

4.1.3 Passive Damping

As mentioned in the previous section, in order to achieve larger stable margin and suppress the resonances, a damping solution should be adopted. The simplest method is to add resistors in the system. There are several ways to implement this, which are shown in figure 4.9.

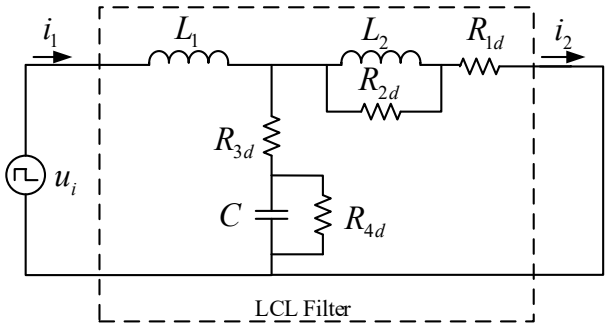

Figure 4.9: *Location of Passive Damping Resistor*

It should be noted that parasitic resistances are neglected here. The resistors $R_{1d}, R_{2d}, R_{3d}, R_{4d}$ represent four different passive damping methods, which will be discussed as following.

1. Damping resistor with grid inductor in series
   $(R_{1d} \neq 0, R_{2d} = \infty, R_{3d} = 0, R_{4d} = \infty)$

   In this case, the forward admittance from converter voltage to grid current transfer function is:

$$G_{p1}(s) = \frac{I_2}{U_1} = \frac{1}{L_1 L_2 C s^3 + L_1 R_{1d} C s^2 + (L_1 + L_2)s + R_{1d}} \tag{4.14}$$

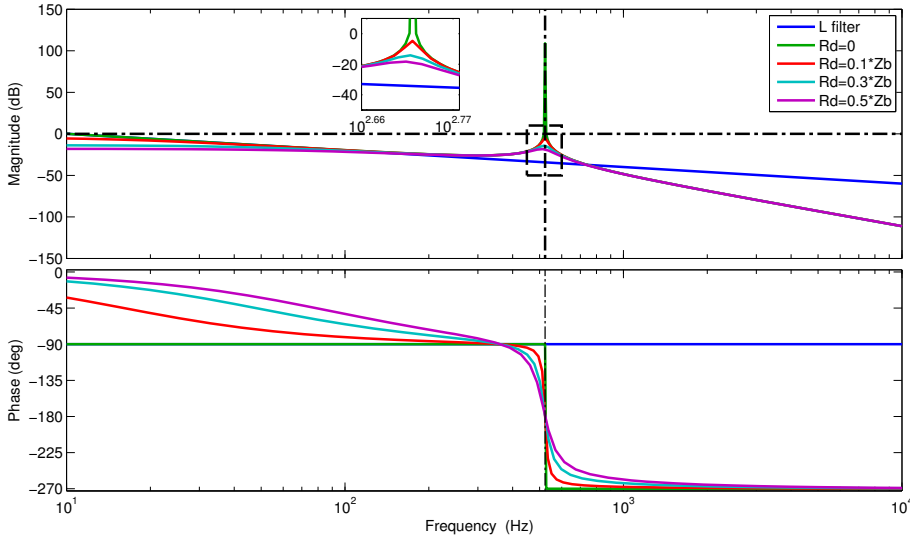

Figure 4.10: *Damping Resistor with Grid Inductor in Series*

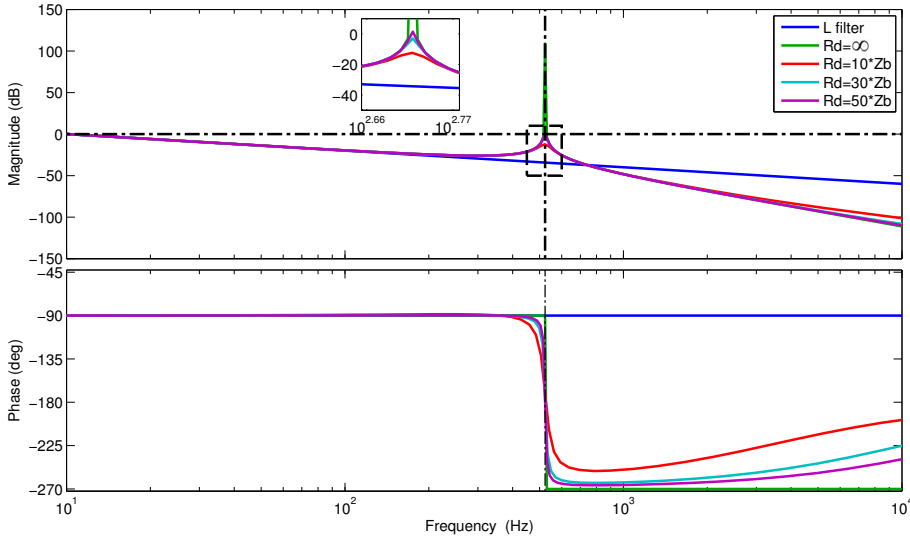

Figure 4.11: *Damping Resistor Parallel with Grid Inductor*

where the damping resistor, R_{1d}, is installed in series with grid inductor. The bode plot is shown in figure 4.10. It can be noted that with increasing damping resistance the resonance peak is suppressed. The attenuation characteristic for high frequency is the same as in the undamped case. However, for the low frequency range, the transfer ratio (magnitude) from converter voltage to grid current decreases, which will affect the control system steady state performance. From the magnitude figure, with 10% of base impedance(Z_b), the resonance peak can be suppressed below zero dB. In order to achieve enough gain margin($> 6\,\mathrm{dB}$), the resistance has to be increased further, which will cause higher losses. Compared to a damping resistor in parallel with the capacitor, the resistance in this case is 10 times higher.

2. Damping resistor in parallel with grid inductor
   ($R_{1d} = 0, R_{2d} \neq \infty, R_{3d} = 0, R_{4d} = \infty$)

   In this case, the passive damping resistor is installed in parallel with the grid inductor. The transfer function of the forward admittance is:

$$G_{p2}(s) = \frac{I_2}{U_1} = \frac{L_2 s + R_{2d}}{L_1 L_2 R_{2d} C s^3 + L_1 L_2 s^2 + (L_1 + L_2) R_{2d} s} \tag{4.15}$$

   where R_{2d} is the damping resistor. With decreasing damping resistance, the resonance peak is suppressed significantly, see figure 4.11. It can be noted that with R_{2d} equal to 10 times of the base impedance(Z_b), a sufficient gain margin can be obtained. However, the attenuation characteristic for high frequency decreases. Therefore, this method is seldom adopted for industry applications.

3. Damping resistor with capacitor in series
   ($R_{1d} = 0, R_{2d} = \infty, R_{3d} \neq 0, R_{4d} = \infty$)

   For this case, the damping resistor is installed in series with the capacitor. The transfer function of forward admittance is:

$$G_{p3}(s) = \frac{I_2}{U_1} = \frac{R_{3d} C s + 1}{L_1 L_2 C s^3 + (L_1 + L_2) R_{3d} C s^2 + (L_1 + L_2) s} \tag{4.16}$$

   where R_{3d} is the damping resistor. The bode plot is shown in figure 4.12. With a small resistance, e.g. 1% of the base impedance (Z_b), the resonance is already suppressed. The transfer ratio (magnitude) for the low frequency range is the same as in the undamped case. For the high frequency range, the attenuation characteristic does not show an obvious change. Compared to a damping resistor with grid inductor in series, this case uses a much smaller (10 times) resistance, which will generate relevantly less losses. This method is a good alternative solution for passive damping.

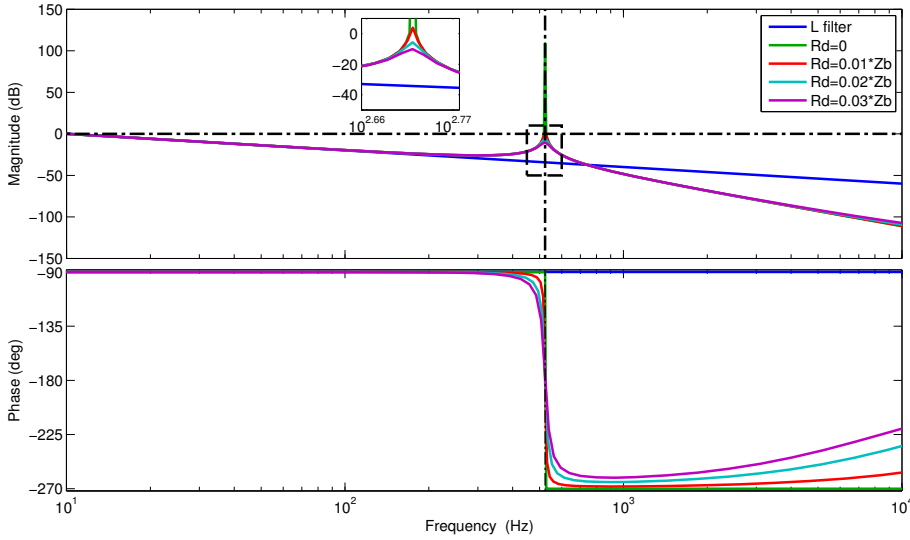

Figure 4.12: *Damping Resistor with Capacitor in Series*

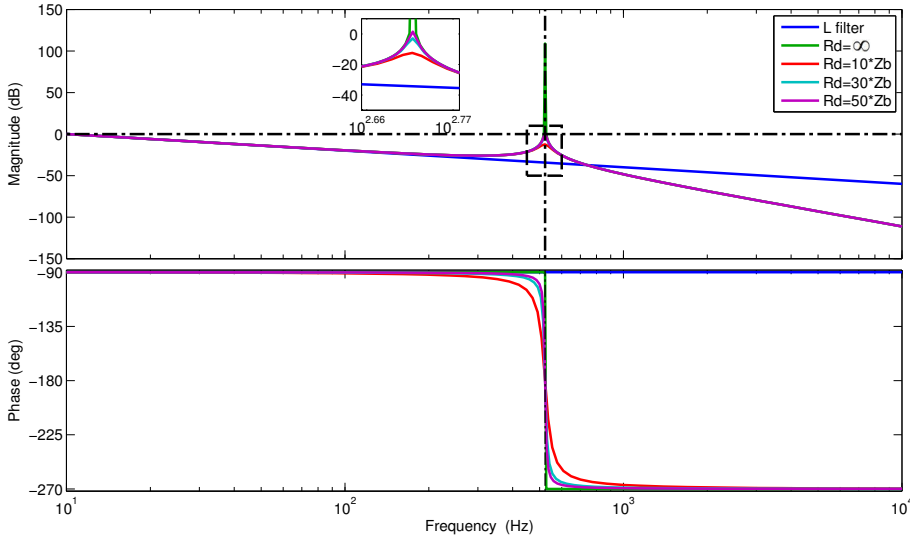

Figure 4.13: *Damping Resistor in Parallel with Capacitor*

4. Damping resistor in parallel with capacitor
   ($R_{1d} = 0, R_{2d} = \infty, R_{3d} = 0, R_{4d} \neq \infty$)

   In this case, the damping resistor is installed in parallel with the capacitor. The transfer function of the forward admittance is:

$$G_{p4}(s) = \frac{I_2}{U_1} = \frac{R_{4d}}{L_1 L_2 R_{4d} C s^3 + L_1 L_2 s^2 + (L_1 + L_2) R_{4d} s} \tag{4.17}$$

   where R_{4d} is the damping resistor. The bode plot is shown in figure 4.13. The characteristic for both low frequency range and high frequency range are the same as in the undamped case, which is a big advantage of this method. However, in order to get sufficient gain margin, the resistance has to decrease to 10 times of the base impedance(Z_b). Due to the parallel structure, with the resistance decreasing, the losses increase. If the losses can be reduced for to an acceptable value, it will be the best method to solve the resonance problem.

In conclusion, from the aspects of control performance, filter attenuation characteristic, damping characteristic and power losses, the damping resistor with capacitor in series is a good solution, and commonly adopted for industry applications.

4.1.4 Active Damping

Even though the passive damping can supply sufficient damping for the control loop, it leads to higher losses which may be considerable. In medium- and high voltage applications they may be larger than 1% of the nominal power [87]. The passive damping using a damping resistor with capacitor in series will definitely compromise the attenuation effectiveness in the high frequencies range. So the damping implementation without losses becomes a special issue for the LCL filter control. Since a positive resonance peak occurs at the resonance frequency, simply if another negative peak can be added at the same frequency, which can eliminate the positive peak, the problem will be solved. Actually, this can be implemented through changing the control structure. This method is called active damping (AD). Filters based AD [89, 90], e.g. notch filter or low-pass filter are proposed in [89]. Filter based AD can be implemented without additional current or voltage sensors compared with multi-loop control AD. Multi-loop control also can damp resonances, e.g., [82, 91]. Besides these two methods, based on the passive damping, the virtual resistance (VR) concept was first proposed in [92]. Compared to the filter based AD and multi-loop control AD, the VR concept has the advantage that the active damping can be implemented through adding a damping component in the current reference, which means the internal control structure is not changed. It is convenient for modulation-less control structures, unlike the filter-based AD and multi-loop control which are generally based on PWM modulation voltage reference.

Similar to the passive damping, the active damping resistor can be placed at different locations. It can be located either in series to or in parallel with the grid inductor or capacitor of the filter [92]. Here, the two options, which are in series to and in parallel with the capacitor will be discussed in detail. The other two options can be analysed in the same way. As shown in figure 4.6, the converter current is considered as feedback loop variable. If the damping resistor is in series to the capacitor, the system control structure can be depicted as in figure 4.14.

The dashed line with R_d in 4.14a represents the damping components. Through equivalent reconfiguration, the structure can be transformed to 4.14b. Assuming that the converter side current reference $i_1^*(s) = i_1(s)$, the damping components can be added to the reference, which is:

$$i_{1d}^*(s) = i_1^*(s) + R_d C s * i_c(s) \tag{4.18}$$

where $i_c(s)$ indicates the capacitor current, and $i_{1d}^*(s)$ indicates the modified reference after considering the damping component. The modified control structure is shown in figure 4.14c. The capacitor current can be obtained via an additional current sensor or state observer. Finally, the simplified system control diagram is shown in figure 4.14d, where the $G_{20}(s)$ indicates the self admittance transfer function of pure LCL filter without any damping, which is $G_2(s)$ in equation 4.1 with $R_d = 0$. The block $G_{1c}(s)$ represents the transfer function from $v_{inv}(s)$ to capacitor current $i_c(s)$, which is:

$$G_{1c}(s) = \frac{I_c}{U_1} = \frac{L_2 C s}{L_1 L_2 C s^2 + (L_1 + L_2)} \tag{4.19}$$

From the structure shown in figure 4.14d, the open loop transfer function can be derived as:

$$G_{op,ads} = \frac{G_c(s) G_d(s) G_{20}(s)}{1 - R_d C s \cdot G_{1c}(s) G_c(s) G_d(s)} \tag{4.20}$$

where the subscript of $G_{op,ads}$ indicates open loop of active damping with resistor in series to the capacitor. In order to investigate the effect of the damping resistor value for the system control performance, the open loop bode plot with different resistor values is shown in figure 4.15. In the bode plot, the undamped case and passive damping are also shown for comparison. With the passive damping ($R_d = 5\,\Omega$), the resonance peak of the resonance frequency $f_{res,1}$ is suppressed significantly. The active damping can also suppress the resonance peak, but the stability margin decreases. For example, at the same value ($R_d = 5\,\Omega$), the magnitude frequency response of AD has a similar characteristics as the PD. However, the phase frequency response is different in the high frequency range, the phase margin decreases significantly. The larger the resistor value, the more the phase margin loses. So the AD with resistor in series to the capacitor can provide the damping effect, but the system stability becomes worse.

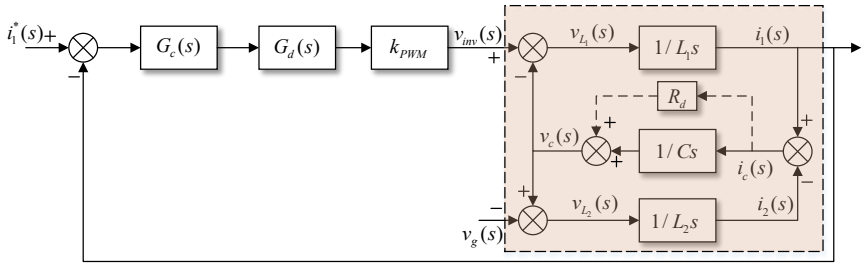

(a) *Virtual Resistor in Series to Capacitor*

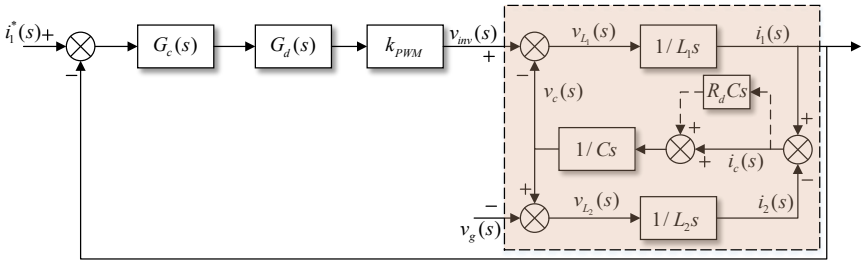

(b) *Reconfiguration of Structure*

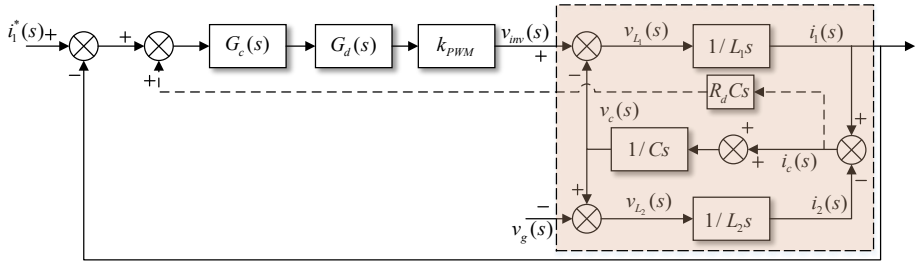

(c) *Equivalent Structure with Assuming* $i_1^*(s) = i_1(s)$

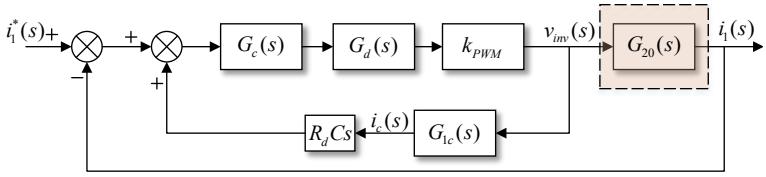

(d) *Simplified Equivalent Structure*

Figure 4.14: *Active Damping using Virtual Resistor in Series to Capacitor of LCL Filter*

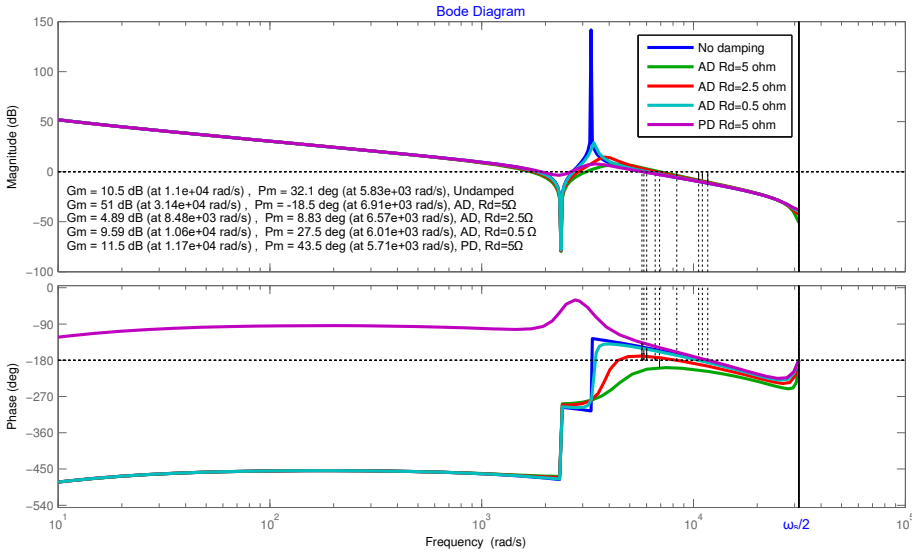

Figure 4.15: *Bode Plot of Virtual Damping Resistor in Series to Capacitor*

For the active damping with a resistor in parallel with the capacitor, the control diagram is shown in figure 4.16. Similarly, the dashed line in figure 4.16a represents the damping component. The term $i_c(s)$ represents the sum of currents through the damping resistor and the capacitor. It is again assumed that the converter side current reference $i_1^*(s) = i_1(s)$, so the damping components can be added in the reference, which is:

$$i_{1d}^*(s) = i_1^*(s) - \frac{1}{R_d} \cdot v_c(s) \tag{4.21}$$

where $v_c(s)$ indicates the capacitor voltage, and $i_{1d}^*(s)$ indicates the modified reference after considering the damping component. The modified control structure is shown in figure 4.16b. The simplified equivalent structure is shown in figure 4.16c. The block $G_{1v}(s)$ represents the transfer function from $v_{inv}(s)$ to capacitor voltage $v_c(s)$, which is:

$$G_{1v}(s) = \frac{U_c}{U_1} = \frac{L_2}{L_1 L_2 C s^2 + (L_1 + L_2)} \tag{4.22}$$

From the structure shown in figure 4.16c, the open loop transfer function can be derived as:

$$G_{op,adp} = \frac{G_c(s) G_d(s) G_{20}(s)}{1 + (1/R_d) \cdot G_{1v}(s) G_c(s) G_d(s)} \tag{4.23}$$

where the subscript of $G_{op,adp}$ indicates open loop of active damping with resistor in parallel to the capacitor. In order to investigate the effect of the damping resistor value on the system control performance, the open loop bode plot with different resistances is shown in figure 4.17. In both cases, AD and PD, the attenuation ratio for both low and high frequency range is identical to the undamped case, which is also consistent with 4 of passive damping discussed in section 4.1.3. The resonance peak during active damping is suppressed in the same way as during passive damping applying the same resistance. A smaller resistance leads to better damping, but it should be noted that if the resistance is too small, the system will not be stable.

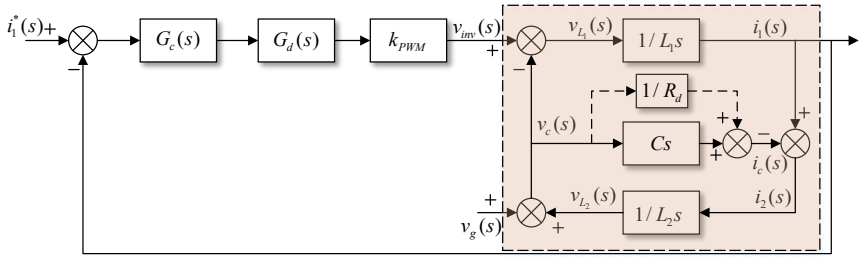

(a) *Virtual Resistor in Parallel with Capacitor*

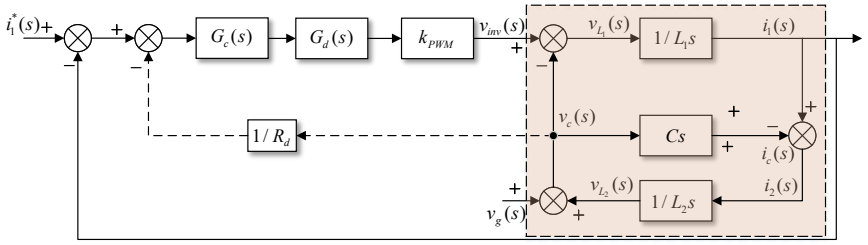

(b) *Equivalent Structure with Assuming* $i_1^*(s) = i_1(s)$

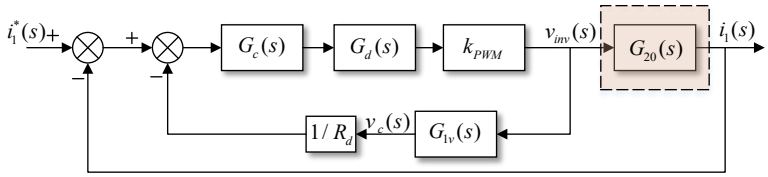

(c) *Simplified Equivalent Structure*

Figure 4.16: *Active Damping with Virtual Resistor in parallel with the capacitor of LCL Filter*

In conclusion, compared to the AD with the resistor in series to the capacitor, the parallel damping has some advantages. The damping effect can be implemented without

compromising the system control performance. Equation 4.21 further indicates that the modified reference does not contain any differential term which is helpful for digital implementation. So parallel this active damping method will be adopted in this thesis for further investigation.

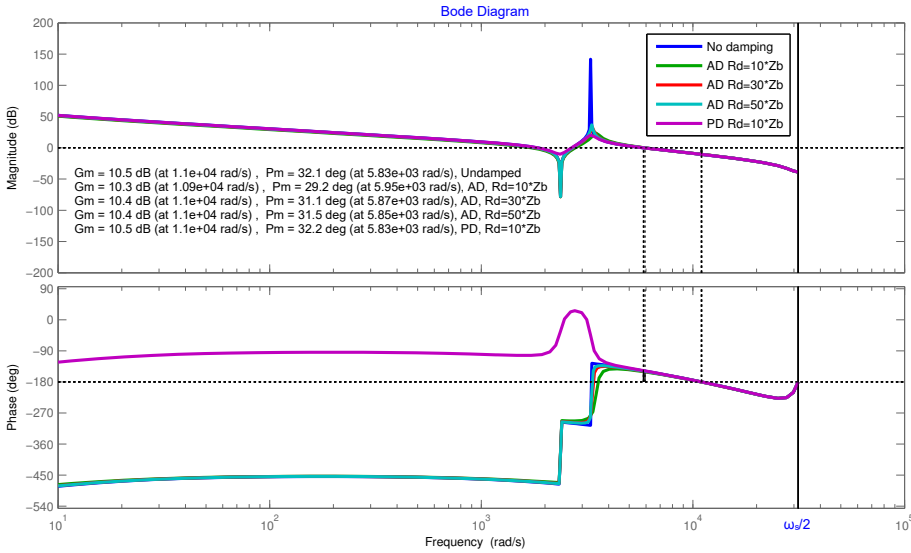

Figure 4.17: *Bode Plot of Damping Resistor in Parallel with Capacitor*

4.2 Grid Integration Standards

Renewable energy technologies have vigorously developed all over the world, and wind power generation has taken an important role in the whole power system. In order to guarantee stability, reliability and power quality, wind power generation should meet the requirements for grid connection, so-called grid codes. An overview of grid codes for wind power integration in different countries around the year 2000 can be found in reference [93]. Grid codes are very complex documents. The most important requirements from a wind-farm connection perspective are:

- Voltage and frequency variations
- Active power control and frequency control
- Reactive power control or power factor control and voltage control
- Fault ride-through and reactive current injection

- Power quality.

4.2.1 Current Status of Grid Code

With increasing penetration of renewable energy, most countries have published their own grid codes. Regarding the type of renewables, technical regulations are normally released by the Transmission System Operators (TSOs) or relevant organizations. Table D.3 shows the latest grid codes for wind power generation in different countries and the EU. Most countries have already updated the grid codes in the past two years in order to adapt to the high penetration of wind power generation.

In Germany, the wind power capacity has reached 45 GW, which can supply half of the electricity consumption (peak 80 GW). The renewable energy has covered 32.5% percent of power consumption in 2015 [94]. Especially on 23 August, 2015, between 1pm and 2pm, 83.2 percent of all power demand was covered by renewables. It is therefore necessary to revise previous regulations to guarantee, that the new power system is stable. In January 2015, the new grid code, "VDE-AR-N 4120, Technical requirements for the connection and operation of customer installations to the high voltage network" (TAB high voltage) was released to replace the Transmission Code 2007 and SDLWindV 2009[1]. New equipment must meet the new grid code at least after a transition period of two years, i.e. January 2017. The new grid code has enhanced requirements on the static voltage control (reactive power control) and dynamic grid support during grid faults. In addition, also new is a certification process, which can be used to prove and verify compliance with the requirements. Finally, for the first time, processes and timetables are defined which clarify responsibilities between all parties involved [95].

In China, the wind power capacity has reached 145 GW, and newly installed capacity in 2015 is 31 GW, which is almost 50 percent of the new installation in 2015 all over the world [96]. However, the wind power generation only covers 3.32 percent of the electricity sector. According to the National Bureau Of Energy in China, the average operating capacity of wind farms was only 1728 hours, and 33.9 TWh of wind electricity was curtailed. Based on this, China does not have the same challenge as in Germany currently. The grid code, "Technical rule for connecting the wind farm to power system" (GB/GB/T 19963-2011), was released in 2011 and has replaced the previous one, GB/Z 19963-2005. In this version, more advanced requirements are given for the active power control and voltage control under grid faults, e.g. low voltage ride-through.

4.2.2 Fault Ride-through

When a grid fault happens, according to the Grid Code, wind power plants should fulfil the Fault Ride-through (FRT) requirements, which contains High Voltage Ride-through (HVRT) and Low Voltage Ride-through (LVRT). Generally, a grid voltage

[1]SDLWindV 2009 represents the Ordinance on System Services by Wind Energy Plants (System Service Ordinance – SDLWindV)

dip will emerge due to grid faults. The voltage dips depend on the position of grid faults [97]. The grid faults can be classified into two main categories, symmetrical faults and unsymmetrical faults [98]. Symmetrical faults are commonly caused by a three phase short circuit. They are no phase shifts between three phases, and the same grid voltage drop. Unsymmetrical faults are generally caused by one or two-phase shorted to ground or to each other. They guarantee an unbalanced grid voltage drop and phase shifts between the phases.

Figure 4.18 shows the voltage limit of FRT according to the grid connection requirements (GCRs) for wind turbine systems published by VDE in 2015 [95]. The black solid line presents the limit for symmetrical grid faults, i.e. three-phase short circuits. The wind power plants should not disconnect if the line-to-line voltage is between the two solid black curves. The grey line presents the limit for unsymmetrical grid faults. For constructional reasons, power generating plants shall not disconnect from the grid during a single-phase fault, which is not considered here [95]. During a grid fault, the grid side converter has to inject reactive current to support the grid. Figure 4.19 shows the relation between the voltage variation and required reactive current. The additional reactive current Δi_B shall be proportional to the voltage deviation Δu ($\Delta i_B = k \cdot \Delta u$), where k is the amplification factor.

Normally the system control algorithms consist of two parts, normal operation and grid fault operation. At normal operation, the Maximum Power Point Tracking (MPPT) method is adopted for the generator side converter to extract the maximum power from the wind turbine, e.g., [71,99]. The generator speed reference is given by MPPT method. The outer control loop is the speed loop, and the inner loop is the current loop. For the grid side converter, voltage oriented control is used [100]. DC link voltage reference is set previously. The outer control loop is the dc voltage loop. During normal operation, reactive power injected to the grid equals zero. At grid fault operation, the MPPT control module will be disabled. Active power and reactive power references should be set according to the grid code. The system control algorithm is described in Figure 5.7. When grid voltage dips occur, the grid side converter should be controlled to inject reactive current, which will help the grid voltage to recover. Many investigations have been conducted to how to control the wind power system converter to meet the grid codes under grid faults [16, 101, 102].

4.2.3 Suggestions on Grid Code Modifications

With the development of renewables, the power system will definitely change. New grid codes and relevant analysis and control methodology have to be created. Here the Virtual Synchronous Generator Concept is discussed for the future grid code.

With increasing renewable power generation, the traditional synchronous generator (SG) disappears from the power system gradually, and power converters take a more important role. As a result, system inertia and damping are becoming weak, since the power converter does not contain physical inertia as a SG. As is well known, the two

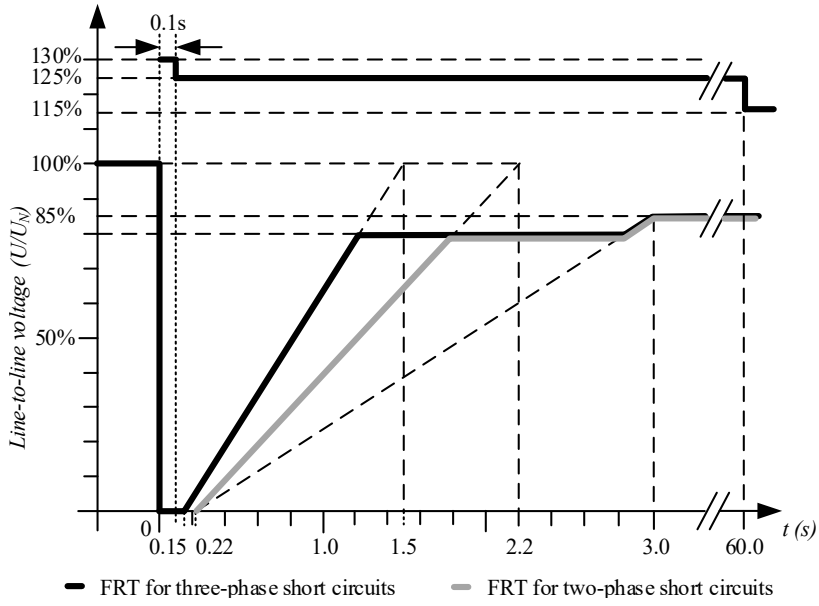

Figure 4.18: *Voltage Limit Curve of Fault Ride-through (FRT) Requirement for Wind Turbine [95]*

characteristics, inertia and damping from traditional SG play a crucial role in the power system regarding stability. Actually, in the grid code from Spain, 'Technical Requirements For Wind Power and Photovoltaic Installations and Any Generating Facilities Whose Technology Does Not Consist on A Synchronous Generator Directly Connected to The Grid', inertia emulation has already been mentioned [61, 103]. A PD controller is used for inertia emulation. The control structure is shown in figure 4.20, where Δf is the frequency variation as input, and ΔP_d is the active power variation as output. The gain K_d should be adjustable from zero to 15 seconds, and with the speed of derivative response that at least the $\Delta P = 0.05PU$ should be increased in 50 ms. In order to inject or absorb active power up to 10% of the nominal apparent power at least for 2 s, the facility must have its own energy storage system. The detailed requirements can be found in reference [103]. It is further recommended that the power generation unit should have the ability to damp or reduce the power oscillations for frequencies between 0.15 and 2 Hz [103].

It can be found that the trend is artificially to create these two characteristics, inertia and damping, which are gradually decreasing with the development of renewables in the power system. This concept is called Virtual Synchronous Generator (VSG) and was first mentioned in the VSYNC project. It started in October 2007 under the 6^{th} EU

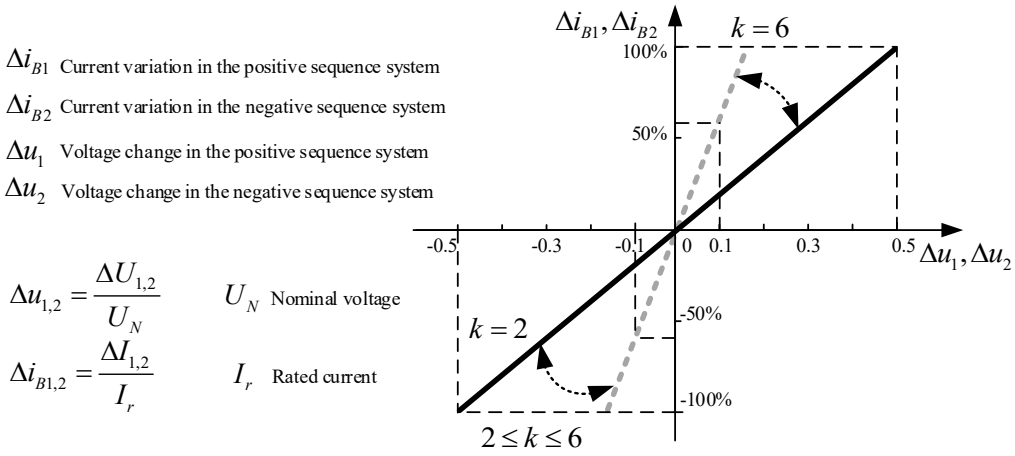

Figure 4.19: *Voltage Support Curve of Fault Ride-through (FRT) Requirement for Wind Turbine [95]*

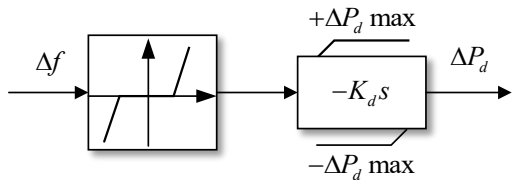

Figure 4.20: *Inertia Emulation Recommended in Grid Code of Spain [103]*

Research Framework Program [104]. A virtual inertia can be implemented using short term energy storage and a power converter with a proper control algorithm [26]. A simple diagram of the VSG is shown in figure 4.21. It can be noted that the only external part compared to the traditional structure is the energy storage, which is used for absorbing or injecting active power to the grid for short time.

4.3 Loss Analysis and Temperature Estimation

For evaluation of a wind turbine performance, besides stability and power quality, system efficiency is another important aspect. The power converter is an important part, which contributes to the losses. The semiconductor losses are the main part, containing conduction losses and switching losses.

The losses depend on the junction temperature. The switching frequency and the output power are limited by the thermal constraints [74, 105]. So the junction temper-

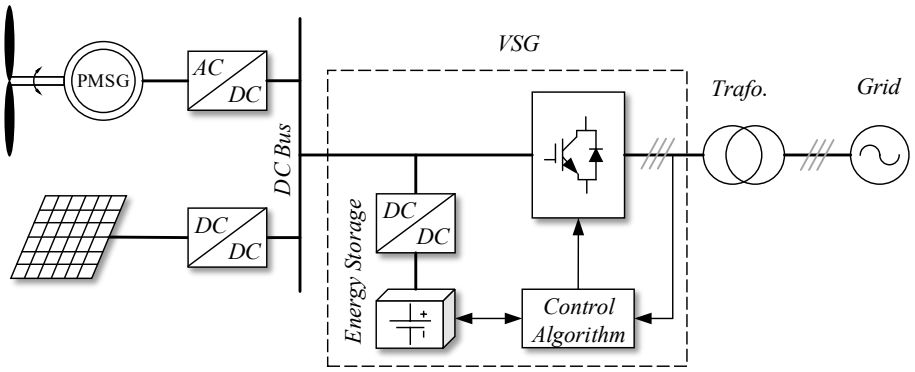

Figure 4.21: *Virtual Synchronous Generator Concept*

ature is a very important parameter, in general it can affect:

1. The maximum switching frequency and system losses
2. The reliability and lifetime
3. The cooling system design

A more detailed analysis on conduction losses, switching losses and the temperature estimation can be found in appendix C.

4.4 Summary

This chapter describes the evaluation aspects for the wind turbine system, which includes stability analysis, power quality and loss analysis. Stability is a prerequisite and the most important issue. Since an LCL filter is used, the system current feedback has two possibilities, grid side current feedback and converter side current feedback. The stability analysis for both cases is conducted. For the LCL filter, both active damping and passive damping methods are analysed. In order to comply with the grid code, a latest grid code collection is made for countries or areas with high penetration of renewables. The new requirements are highlighted, e.g. fault ride-through and reactive power injection.

Part III

Grid Converter Control Strategies

In the third part of the Ph.D. thesis, the grid converter control strategies are presented. This part includes three chapters. ***Chapter 5****, state of the art grid converter control, describes the basic voltage orientated control for the grid converter of wind turbines. A second state of the art control, the direct power control (DPC) which is used in drive applications is developed and optimized for the grid converter. In order to improve the overall performance, e.g. converter efficiency, power quality and LVRT ability, a new control algorithm should be developed.* ***Chapter 6****, model predictive direct control, discusses the model based predictive direct control. Besides the single step prediction, a multiple steps prediction is proposed for the grid converter control to realize low switching frequency for loss reduction. The multiple steps model predictive control can achieve around* 500 Hz *while complying with the grid code on harmonics. In* ***Chapter 7****, a novel nonlinear Lyapunov based controller is presented, so called backstepping control. It can handle unsymmetrical grid faults with excellent performance. At the same time, backstepping control has a very good robustness considering uncertainties and parameter mismatch.*

5 State of the Art Grid Converter Control

The inner current control is the core control, which takes a very important role for the control performance. In this chapter, the state of the art current control algorithm for grid connected converters is presented. Derived from direct torque control (DTC), the direct power control has been researched in many literatures, which is developed and improved with improved switching table adopted for the grid converter control

application.

5.1 Historical Overview of Grid Converter Control

The objective of power converter control is to supply the voltages, currents or frequency needed for the loads and to comply with the requirements in terms of dynamic and steady state performance from the respective standards and load demands. Pulse Width Modulation is the basic technique for modern converter control, which was first used in 1964 [106]. Later in 1968 and 1972, indirect and direct vector control were invented by K. Hasse and F. Blaschke, respectively [107, 108]. The vector control has been considered as one immortal invention for electrical drives, which is the fundamental to modern converter control and three-phase motor control. For grid converter control, the vector control is adapted as voltage oriented control (VOC). It will be briefly described in the next subsection. The classification of converter control algorithms is shown in figure 5.1, where they are categorized in four groups. Compared to other advanced control, e.g., sliding mode, fuzzy logic, etc., predictive control has been paid much more attention especially in power electronics due to the development of fast computation devices. It is the only one advanced control methodology which has made a significant impact on industrial control, e.g., process industry. Considering that the predictive control has many variations, it is classified as an own group here. The first two groups can be considered as classical control methods. Actually, the hysteresis control-direct current control is the simplest current regulation scheme, which was used for electrical drives in the late 70s [109]. It contains three independent two level hysteresis controllers for three phase current control, and is directly implemented in abc frame. Reference [110] presents the comparison of hysteresis, ramp comparison and predictive control in 1985. A general review of current regulation methods of PWM inverters are presented in 1993 [111], which includes on-off hysteresis regulator, linear regulator and predictive regulator. In 1998, the comparison of current control techniques for active filter applications is described in reference [112].

Direct torque control (DTC) was first published by Isao Takahashi and Toshihiko Noguchi in 1984 [113]. Later in 1986, a similar idea so-called direct self control (DSC) was patented by Manfred Depenbrock [114]. In the same year, Takahashi and Noguchi also published DTC in IEEE Transaction on Industry Application [115]. Another control method, direct power control (DPC) derived from DTC is often used for power converters in the power grid. It was first introduced by T. Ohnishi in 1991 [116]. DPC and its improvement will be discussed in section 5.3.

More historical background can be found in reference [117]. Finite control set (FCS) MPC is one branch of predictive control, which uses the discrete model of load and converter to predict the future switch vector to minimize a defined cost function without modulation. Reference [118] presented this idea in 2004. Generalized predictive control (GPC) differs from FCS-MPC, which allows solution of the optimization analytically

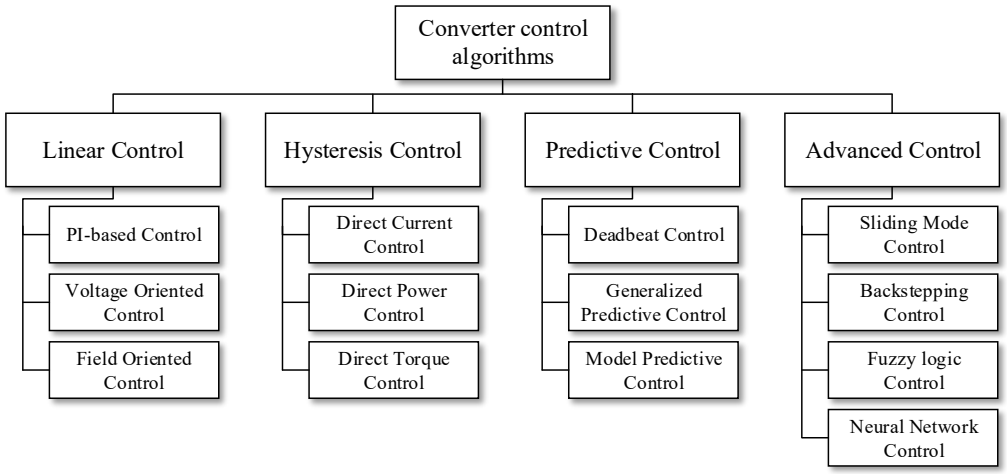

Figure 5.1: *Power Converter Control Algorithms Classification*

when the system is linear and no constraints and a modulation is needed for most GPC [119]. MPC will be investigated in Chapter 6.

For the unconventional control methods, due to the complexities, most of them are not paid much attention in real industrial application. However, with the power system becoming more complex with unknown parameters or more uncertainties, these methods may take more important role in the future due to their remarkable properties of robustness, accuracy and easy tuning. The basic principles of sliding mode control (SMC) can be found in several references [120–123]. In order to move a step further in the advanced control for power converter control, the backstepping control will be described in Chapter 7.

5.2 Voltage Oriented Control

As described in the previous subsection, voltage oriented control is derived from field oriented control. It has been invented and developed for almost fifty years. Nowadays, VOC is used in industrial power converter control. It is definitely the state of the art method and dominates the market for three phase grid converter control. The basic idea is to control the current in a rotating dq frame with a PI controller. The VOC control diagram for the three-level NPC converter with LCL-filter is shown in figure 5.2, where v_{ga}, v_{gb}, v_{gc} are the three phase grid voltages, and i_{ga}, i_{gb}, i_{gc} are the three phase grid side currents. i_{1a}, i_{1b}, i_{1c} are the three phase converter side currents. The current feedback can be implemented with either converter side current or grid side current. It has been proved that converter side current feedback (CSCF) is better than grid side

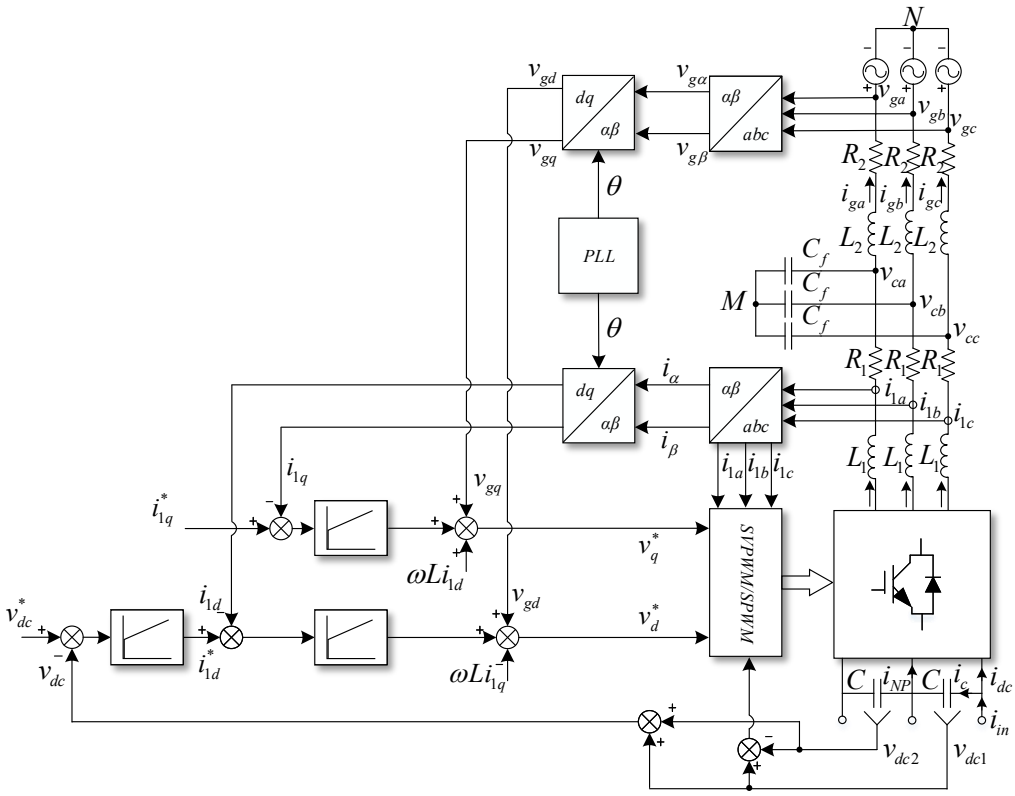

Figure 5.2: *Voltage Oriented Control for Grid Converter with LCL-filter*

current feedback (GSCF) regarding stability in section 4.1. So here CSCF will be used for the current control loop. The control structure contains two loops. The outer loop is the DC voltage loop, and the inner is the current loop. The grid voltage angle is obtained through a phase locked loop (PLL). The essence of VOC is to let the grid voltage vector align the d-axis so that its components in q-axis are zero. According to the instantaneous power theory, the active power and reactive power of the system can be calculated as:

$$\begin{cases} p = \frac{3}{2}(v_{gd}i_{gd} + v_{gq}i_{gq}) \\ q = \frac{3}{2}(v_{gq}i_{gd} - v_{gd}i_{gq}) \end{cases} \tag{5.1}$$

where v_{gd}, v_{gq} and i_{gd}, i_{gq} are the three phase grid voltage and grid current in dq frame. Assuming that the three phase grid voltage is balanced and the d-axis is aligned with

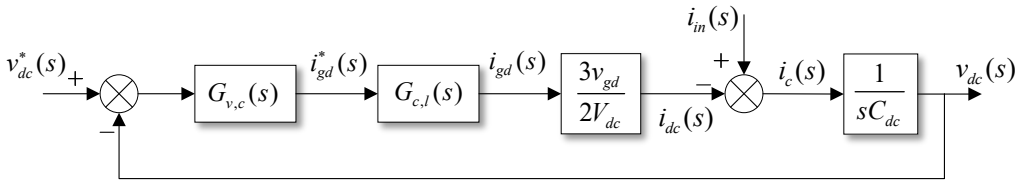

Figure 5.3: *DC link Voltage Control Loop*

the grid voltage vector, $v_{gq} = 0$, equation 5.1 can be simplified as:

$$\begin{cases} p = \frac{3}{2} v_{gd} i_{gd} \\ q = -\frac{3}{2} v_{gd} i_{gq} \end{cases} \tag{5.2}$$

where the active power and reactive power can be controlled by the d- and q-axis grid current. Since the converter side current is controlled, in order to achieve unity power factor, the q-axis component reference i^*_{1q} should not be set to zero. For LCL-filter capacitor reactive power compensation, $Q_c = -1.5 v^2_{gd} \omega_1 C_f$, where the ω_1 represents the fundamental angular frequency. So the q-axis component reference $i^*_{1q} = -2Q_c/(3v_{gd})$. In figure 5.2, assuming that the previously injected current is $i_{in}(t)$, $i_{NP} \approx 0$ and neglecting losses, since $C_{dc} dv_{dc}/dt = i_c$ and $i_{dc} = i_{in} - i_c$, it can be achieved:

$$p = v_{dc} i_{dc} = \frac{3}{2} v_{gd} i_{gd} \tag{5.3}$$

$$i_{dc} = \frac{3 v_{gd} i_{gd}}{2 v_{dc}} \tag{5.4}$$

where C_{dc} is the dc-link capacitor, $C_{dc} = 0.5C$.

Assuming that $v_{dc} = V_{dc}$ in the steady state, the voltage control loop can be obtained according to figure 5.3. $G_{v,c}(s)$ represents the voltage controller, which can be a classical PI control. Here it can be expressed as:

$$G_{v,c}(s) = k_{pv}(1 + \frac{1}{\tau_v s}) \tag{5.5}$$

k_{pv} is the proportional parameter and τ_v is the integral time constant. $G_{c,l}(s)$ represents the current control closed-loop transfer function, according to equation 4.11. The PI controller for current control is designed according to the modulus optimum method. So the $k_{pi} = L_T/(3T_s)$, $\tau_i = L_T/R_T$ (see equation 4.6). T_s is the sampling time. According to the current open loop and close loop transfer function with assuming $T_s \ll \tau_i$, $G_{c,l}(s)$ can be derived as:

$$G_{c,l}(s) = \frac{1}{1 + 3T_s s} \tag{5.6}$$

Assuming that $V_{dc} \approx \sqrt{3} v_{gd}$ (the DC link voltage cannot be lower than this value in order to allow current controllability [61], for SPWM, $V_{dc} \approx 2 v_{gd}$), the voltage control open loop transfer function can be obtained as:

$$G_{ov}(s) = \frac{\sqrt{3} k_{pv} (\tau_v s + 1)}{2 \tau_v C_{dc} s^2 (3T_s s + 1)} \tag{5.7}$$

The PI controller can be tuned following the symmetrical optimum method [61,124]. The controller's parameters are:

$$\begin{cases} k_{pv} = \frac{C_{dc}}{2\sqrt{3} a T_s} \\ \\ \tau_v = 3a^2 T_s \end{cases} \tag{5.8}$$

where

$$a = \frac{1 + \cos\psi}{\sin\psi} \tag{5.9}$$

where ψ represents the phase margin at the crossover frequency of the open loop transfer function. The crossover frequency $\omega_c = 1/(3aT_s)$. If the phase margin is given by 45°, the parameter $a = 2.4$, $k_{pv} = 0.12 C_{dc}/T_s$ and $\tau_v = 17.28 T_s$ [125]. The bandwidth can be estimated as:

$$f_{b,v} \approx \frac{\omega_c}{2\pi} = \frac{1}{6\pi a T_s} \approx \frac{1}{50 T_s} = \frac{f_s}{50} \tag{5.10}$$

where f_s represents the system sampling frequency.

5.3 Direct Power Control

Besides the voltage oriented control, another feasible method is Direct Power Control (DPC), which is derived from direct torque control [126]. DTC has been extensively used by ABB in their commercial MV drives, e.g., ACS880. Like DTC, DPC has no internal current loop. Based on a switching table, DPC uses an instantaneous voltage vector to control active and reactive power directly. Reference [127] gives an experimental comparison of VOC and DPC techniques for two-level converters, whereas reference [128] compares virtual flux DPC and VOC for two level converters based on simulations. Several references have investigated DPC control with the NPC controlled as a rectifier [129–131].

The control structure is given in figure 5.4. It mainly consists of an instantaneous active power and reactive power estimation, the hysteresis controller and a switching table. Compared to VOC control, there is no current loop, and no dq-transformation

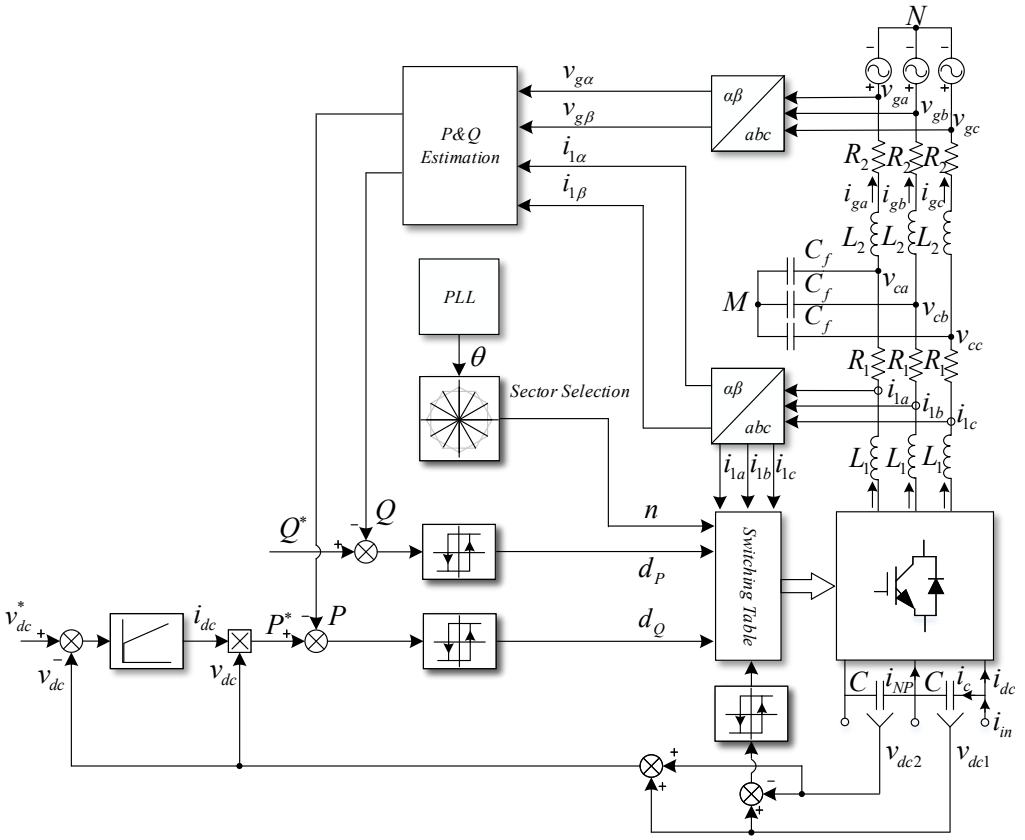

Figure 5.4: *Direct Power Control for Grid Converter with LCL-filter*

to the synchronous rotating reference frame (SRF), which saves calculation resources. The detailed design for the hysteresis controller will be discussed in the following subsections. In order to improve the performance, a modified switching table considering the switching transitions and reactive power control is also described.

5.3.1 Hysteresis Controller Design

Hysteresis control is nonlinear, but easy to implement. Generally, the hysteresis controller has only two states to adjust the controlled variables. According to [126], the outputs d_P, d_Q of the hysteresis controller are defined as follows, which are also depicted in figure 5.5.

$$d_{P(k)} = \begin{cases} 1 & P_{ref} - P > H_P \\ d_{P(k-1)} & -H_P < P_{ref} - P < H_P \\ 0 & P_{ref} - P < -H_P \end{cases} \tag{5.11}$$

$$d_{Q(k)} = \begin{cases} 1 & Q_{ref} - Q > H_Q \\ d_{Q(k-1)} & -H_Q < Q_{ref} - Q < H_Q \\ 0 & Q_{ref} - Q < -H_Q \end{cases} \tag{5.12}$$

Here k and $k-1$ represent the time instant. With the active and reactive power references P_{ref}, Q_{ref}, the estimated active power P and reactive power Q, and the hysteresis bands H_P, H_Q, one can determine the outputs d_P, d_Q. The relation between the hysteresis controller's output and the desired variation of active and reactive power is shown in table 5.1. A change of the switching states occurs, if the estimated power is above or below the reference value plus/minus the hysteresis band. If between two sampling instances k the power stays within the boundaries, the output will not change.

For low frequencies the LCL-filter can be approximated by an L-filter, so the instantaneous active and reactive power can be estimated as [132]:

$$\begin{cases} p = \frac{3}{2}(v_{g\alpha} i_{1\alpha} + v_{g\beta} i_{1\beta}) \\ \\ q = \frac{3}{2}(v_{g\beta} i_{1\alpha} - v_{g\alpha} i_{1\beta}) \end{cases} \tag{5.13}$$

where $i_{1\alpha}$ and $i_{1\beta}$ are the alpha-beta components of converter side current. Similar to VOC, in order to achieve unity power factor, the reactive power of the LCL-filter has to be compensated. Here, the reactive power reference is $Q_c = -1.5 v_{gd}^2 \omega_1 C_f$.

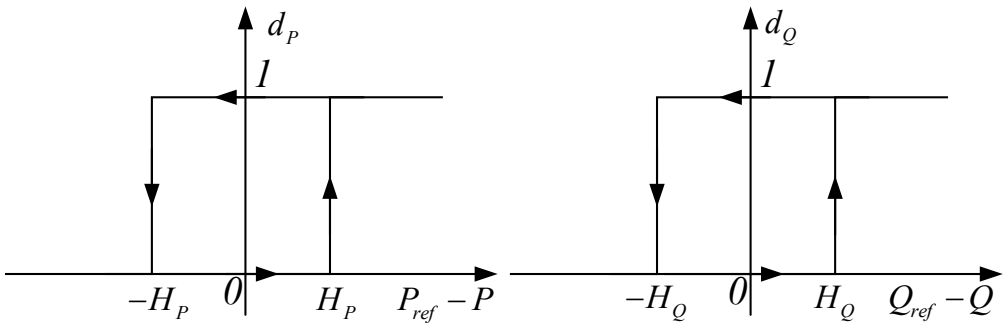

(a) Hysteresis Controller of Active Power *(b) Hysteresis Controller of Reactive Power*

Figure 5.5: *Hysteresis Controller of Active and Reactive Power*

Table 5.1: *States of the Hysteresis Controller and Desired Power [133]*

d_P	d_Q	Index	Desired effect on active power	Desired effect on reactive power
0	0	0	(decrease)↓	(decrease)↓
0	1	1	(decrease)↓	(increase)↑
1	0	2	(increase)↑	(decrease)↓
1	1	3	(increase)↑	(increase)↑

5.3.2 Conventional Switching Table

The topology of a three-level NPC converter connected to the grid through an L filter is depicted in figure 3.3. According to the KCL and KVL, it can be obtained:

$$L_1 \frac{di_{1k}}{dt} + R_1 i_{1k} = v_{inv,k} - v_{gk},\ k = a, b, c \tag{5.14}$$

$$C_{dc} \frac{dv_{dc}}{dt} = i_{dc} - \frac{1}{u_{dc}} \left(\sum_{k=a,b,c} v_{inv,k} \cdot i_{1k} \right) \tag{5.15}$$

Based on equations 5.14 and 5.15, neglecting the parasitic resistance and assuming that the difference between grid voltage and inverter voltage is constant during the sampling time step Ts, the converter model can be simplified to equation 5.16. Here, $\overrightarrow{i_1}$, $\overrightarrow{v}_{inv}$ and $\overrightarrow{v}_g$ are the grid current space vector, inverter voltage vector and grid voltage vector. Transformed into SRF, equation 5.1 and equation 5.2 show that d- and q-axis components of the current determine the active and reactive power, if the q-component of the grid voltage v_q is zero. The projections of $\Delta\overrightarrow{i_1}$ upon the rotating reference frame determine the d- and q-axis components of the grid current change, which therefore define the variation of ΔP and ΔQ as shown in 5.17.

$$L_1 \frac{d\overrightarrow{i_1}}{dt} \approx \overrightarrow{v}_{inv} - \overrightarrow{v}_g \Rightarrow \Delta\overrightarrow{i_1} \approx \frac{T_s}{L_1}(\overrightarrow{v}_{inv} - \overrightarrow{v}_g) = \frac{T_s}{L_1}\Delta\overrightarrow{v} \tag{5.16}$$

$$\begin{cases} \Delta P \propto \Delta i_d \\ \Delta Q \propto -\Delta i_q \end{cases} \tag{5.17}$$

Since the space vectors $\Delta\overrightarrow{i_1}$ and $\Delta\overrightarrow{v}$ are collinear according to equation 5.16, the projections of vector $\Delta\overrightarrow{v}$ upon the d-q-axes have the same effect on the active and reactive power as $\Delta\overrightarrow{i_1}$.

Figure 5.6 exemplarily shows the different converter voltage vectors and their effects on active and reactive power in case the grid voltage vector is in sector θ_1. In figure

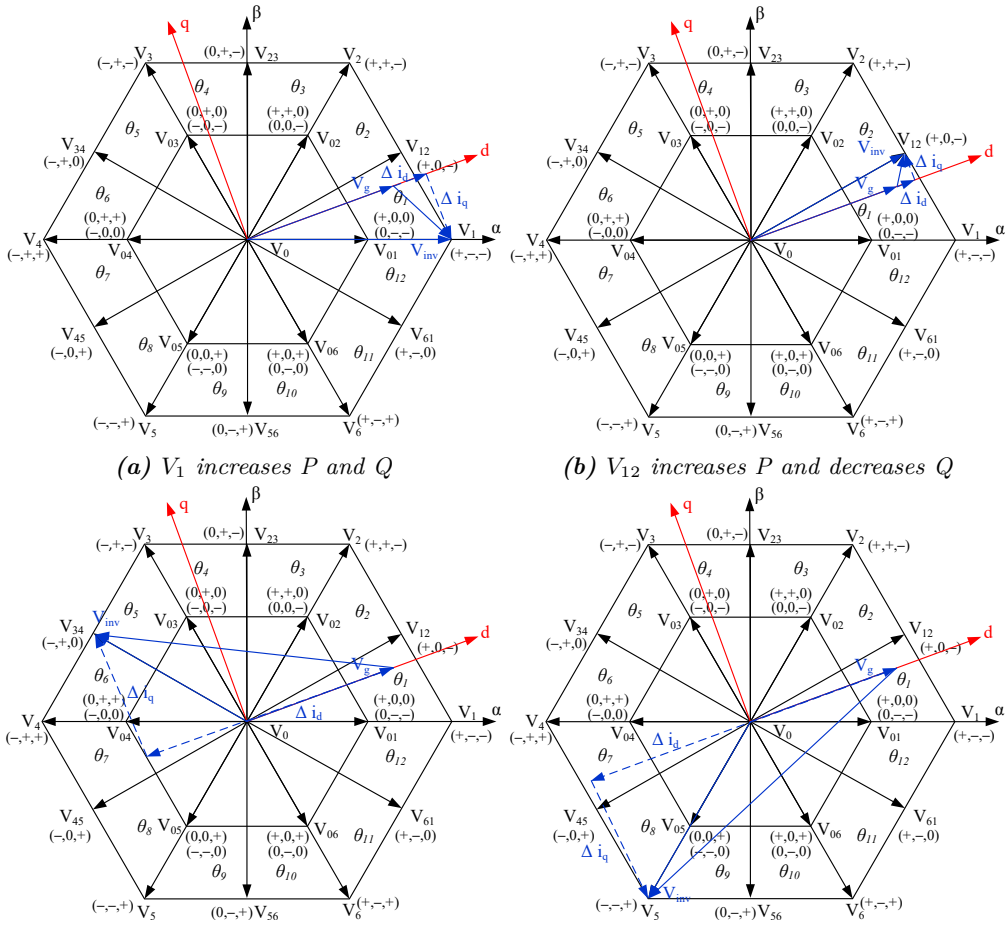

(a) V_1 *increases* P *and* Q *(b)* V_{12} *increases* P *and decreases* Q

(c) V_{34} *decreases* P *and* Q *(d)* V_5 *decreases* P *and increases* Q

Figure 5.6: *Desired variation of active and reactive power selecting* V_1, V_{12}, V_{34}, V_5 *when* V_g *is in sector* θ_1

5.6a, the voltage vector V_1 $(+,-,-)$ is selected. For this inverter voltage vector, the projection upon the d-axis is positive, while the projection upon the q-axis is negative. Hence, vector V_1 will force both active and reactive power to increase. In figure 5.6b, the medium voltage vector V_{12} is selected. This time, both, the projections of $\Delta\overrightarrow{v}$ upon the d-axis and the q-axis are positive. Consequently, the medium voltage vector V_{12} forces the active power to increase and the reactive power to decrease. According to this rule, a fundamental switching table (see table 5.2) without using the small vectors

($V_{01} \sim V_{06}$) has been derived in reference [134]. It should be noted that this switching table is not optimized for the minimization of switching actions. Switching table 5.2 can be also called fast-switching-table. It should be noted that d- and q- axis components are only used to develop the switching table, but are not used in the DPC control itself.

Table 5.2: *Fundamental Switching Table for Three-level Converter (ST1)*

d_P	d_Q	Index	θ_1	θ_2	θ_3	θ_4	θ_5	θ_6	θ_7	θ_8	θ_9	θ_{10}	θ_{11}	θ_{12}
0	0	0	V_{34}	V_4	V_{45}	V_5	V_{56}	V_6	V_{61}	V_1	V_{12}	V_2	V_{23}	V_3
0	1	1	V_5	V_{56}	V_6	V_{61}	V_1	V_{12}	V_2	V_{23}	V_3	V_{34}	V_4	V_{45}
1	0	2	V_{12}	V_2	V_{23}	V_3	V_{34}	V_4	V_{45}	V_5	V_{56}	V_6	V_{61}	V_1
1	1	3	V_1	V_{12}	V_2	V_{23}	V_3	V_{34}	V_4	V_{45}	V_5	V_{56}	V_6	V_{61}

In order to balance the neutral point voltage, a modified switching table using the low voltage vectors is derived, see table 5.3. Only the six low voltage vectors (V_{01}-V_{06}) and the six medium voltage vectors (V_{12}-V_{61}) can influence the neutral point voltage, with each low voltage vector having two switching possibilities. The basic idea is to calculate the neutral point current i_{NP} (see figure 5.4) choosing one of the low voltage vectors and the voltage error Δv_{dc} between v_{dc1} and v_{dc2}. Then, according to the sign of i_{NP} and Δv_{dc}, it is decided to apply the chosen low voltage vector or to select the other one.

Table 5.3: *Switching Table with Neutral Point Voltage Control (ST2)*

d_P	d_Q	Index	θ_1	θ_2	θ_3	θ_4	θ_5	θ_6	θ_7	θ_8	θ_9	θ_{10}	θ_{11}	θ_{12}
0	0	0	V_{02}	V_{02}	V_{03}	V_{03}	V_{04}	V_{04}	V_{05}	V_{05}	V_{06}	V_{06}	V_{01}	V_{01}
0	1	1	V_{01}	V_{01}	V_{02}	V_{02}	V_{03}	V_{03}	V_{04}	V_{04}	V_{05}	V_{05}	V_{06}	V_{06}
1	0	2	V_{12}	V_2	V_{23}	V_3	V_{34}	V_4	V_{45}	V_5	V_{56}	V_6	V_{61}	V_1
1	1	3	V_1	V_{12}	V_2	V_{23}	V_3	V_{34}	V_4	V_{45}	V_5	V_{56}	V_6	V_{61}

Since the switching frequency of DPC is not constant, in order to compare this control scheme with VOC, an equivalent switching frequency is introduced to achieve comparable switch load for the semiconductors. VOC of the NPC converter is based on a PWM scheme where the outer IGBTs switch with a regular pattern. The switching frequency is fixed. However, for DPC, the IGBT turning on and off has no regular pattern, since it depends on the switching table. The equivalent switching frequency is calculated by equation 5.18. Here T_1 is the fundamental grid period, which is 0.02 s. The number of the pulses N_{pulses} can be influenced by the hysteresis controller bands and system sampling frequency.

$$f_{\overline{SW}} = \frac{N_{pulses}}{T_1} = \frac{N_{pulses}}{0.02s} \tag{5.18}$$

5.3.3 Improved Switching Table

By employing the switching table 5.3, the switching transitions are reduced significantly. It means that unnecessary switching actions are eliminated, which decreases the average switching frequency. However, the reactive power control performance has a ripple in some operation points due to the limited voltage vector candidates. This can be improved either by multi-level hysteresis controller or dividing the $\alpha\beta$ plane into more sectors. In order to improve the reactive power control performance, a switching table with 24 sectors is derived shown in table 5.4. The simulation verification of the modified switching table is shown in figure 5.21. It can be found that the reactive power has a smaller ripple in figure 5.21d (ST3) compared to figure 5.20d (ST2).

Table 5.4: *Improved Switching Table with Neutral Point Voltage Control (ST3)*

d_P	d_Q	Index	θ_1	θ_2	θ_3	θ_4	θ_5	θ_6	θ_7	θ_8	θ_9	θ_{10}	θ_{11}	θ_{12}
0	0	0	V_{02}	V_{02}	V_{02}	V_{03}	V_{03}	V_{03}	V_{03}	V_{04}	V_{04}	V_{04}	V_{04}	V_{05}
0	1	1	V_{01}	V_{01}	V_{01}	V_{01}	V_{02}	V_{02}	V_{02}	V_{02}	V_{03}	V_{03}	V_{03}	V_{03}
1	0	2	V_{12}	V_{12}	V_2	V_{23}	V_{23}	V_{23}	V_3	V_{34}	V_{34}	V_{34}	V_4	V_{45}
1	1	3	V_1	V_{12}	V_{12}	V_{12}	V_2	V_{23}	V_{23}	V_{23}	V_3	V_{34}	V_{34}	V_{34}
d_P	d_Q	Index	θ_{13}	θ_{14}	θ_{15}	θ_{16}	θ_{17}	θ_{18}	θ_{19}	θ_{20}	θ_{21}	θ_{22}	θ_{23}	θ_{24}
0	0	0	V_{05}	V_{05}	V_{05}	V_{06}	V_{06}	V_{06}	V_{06}	V_{01}	V_{01}	V_{01}	V_{01}	V_{02}
0	1	1	V_{04}	V_{04}	V_{04}	V_{04}	V_{05}	V_{05}	V_{05}	V_{05}	V_{06}	V_{06}	V_{06}	V_{06}
1	0	2	V_{45}	V_{45}	V_5	V_{56}	V_{56}	V_{56}	V_6	V_{61}	V_{61}	V_{61}	V_1	V_{12}
1	1	3	V_4	V_{45}	V_{45}	V_{45}	V_5	V_{56}	V_{56}	V_{56}	V_6	V_{61}	V_{61}	V_{61}

5.4 VOC Results

The principle control scheme is shown in figure 5.2, which mainly consists of a PLL, PI decoupled controllers for the grid current's d- and q-axis component and modulation. Generally, there is also a voltage loop to control the DC link voltage. Especially for NPC control, the neutral point voltage control should be also implemented.

5.4.1 Simulation Scenario Design

The main objective of this thesis is to design a proper controller for a medium voltage wind turbine grid converter application. For this reason, all the simulation results in this

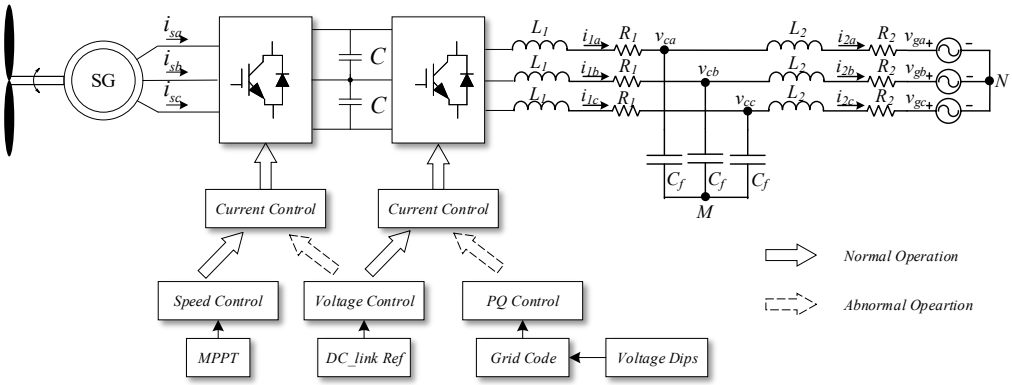

Figure 5.7: *Wind Energy Conversion System Control Strategy under Normal and Abnormal Operation*

Table 5.5: *System Parameters*

Description	Symbol	MV value	LV value	PU value
Rated DC-link Voltage	V_{dc}	6000 V	750 V	2.227/2.296
DC-link Capacitance	C_{dc}	7.631 mF	1.175 mF	5.214/5.906
Rated Power	P	5 MVA	10 kVA	1.000
Rated Output Voltage	V	3300 V	400 V	1.225
Grid Current	I_2	874.8 A	14.43 A A	0.707
Grid Frequency	f_1	50 Hz	50 Hz	1.000
Converter Side Inductance	L_1	1.36 mH	8.2 mH	0.196/0.161
Converter Side Resistance	R_1	6.534 mΩ	0.05 Ω	0.003
Grid Side Inductance	L_2	0.3 mH	7.6 mH	0.04/0.149
Grid Side Resistance	R_2	6.534 mΩ	0.05 Ω	0.003
Filter Capacitance	C_f	628 µF	23.5 µF	0.43/0.118

thesis are achieved for the 5 MVA system. The system parameters used in simulation are given in the MV value column given in table 5.5, and the PU base values are in table 3.3. In the following subsections the steady state and the transient performance of VOC and DPC control under normal and abnormal operation will be presented. Both operation modes are explained as follows, see also figure 5.7. In order to assess the converter efficiency and device stress, a thermal analysis is also conducted by PLECS thermal modelling.

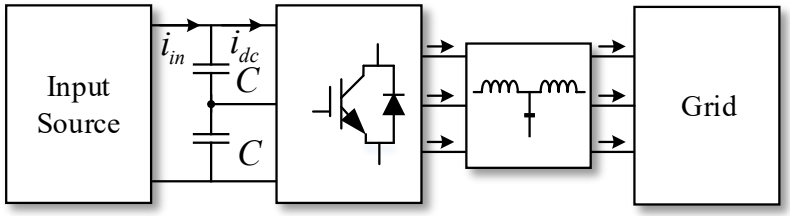

Figure 5.8: *Simulation Model under Study*

Normal Operation For normal operation, the generator side converter works in MPPT mode and the DC-link voltage is controlled by the grid side converter. The injected active power is decided by the generator and the reactive power injected into the grid is zero, which means that unity power factor is achieved. Two cases are defined for controller verification both in steady state and transient.

- Case 1: nominal operation point
- Case 2: active power drops to 0.5 PU and reactive power keeps zero

Since the grid side converter control is focused in this thesis, the generator side is modelled as controlled current source providing the input power shown in figure 5.8.

Abnormal Operation For abnormal operation, e.g., LVRT, the generator side should not work in MPPT mode any more and take over the task of DC-link voltage control. The injected active and reactive power of the grid side converter to the grid will be decided by the requirement of the grid code. The input source is modelled as constant voltage source. It should be noted that the neutral point voltage balancing is still implemented in the grid side controller. In order to verify the performance under LVRT conditions, two cases with symmetrical grid fault are defined.

- Case 3: Three-phase grid voltage drops to 0.7 PU
- Case 4: Three-phase grid voltage drops to 0.5 PU

5.4.2 VOC under Normal Operation

The simulation is conducted with PLECS®. The control parameters of the VOC are given in table 5.6. The sampling time T_s is 80 µs. The PI controllers are designed according to the modulus optimum (MO). Considering anti-windup, the back calculation coefficient K_b is set to 1.36 for the MV application. The proportional coefficient $K_p = L_T/T_s$, where $L_T = L_1 + L_2$. The integral coefficient $K_i = K_p/\tau_i$, where $\tau_i = L_T/R_T$,

and $R_T = R_1 + R_2$. The damping resistor is kept to the designed value shown in table 3.4.

Table 5.6: *VOC Control Parameter*

Description	Symbol	MV value	LV value	PU value
Sampling Frequency	f_s	12.5 kHz	12.5 kHz	2500
Carrier Frequency	f_c	1.05 kHz	1.05 kHz	21
Dead Time	t_d	-	2 µs	-
Proportional Coefficient	K_p	8.95	65.8	-
Integral Coefficient	K_i	54.5	400	-
PI Output Saturation	L_{upper}, L_{lower}	3000 V	375 V	1.11/1.15
Anti-Windup	K_b	1.36	10	-
Damping Resistor	R_d	0.196 Ω	5 Ω	0.09/0.31

Steady State Case 1, the steady state performance of VOC at nominal operation point is shown in figure 5.9. The pure sinusoidal PCC grid voltage without harmonics is shown in Figure 5.9a, the converter current in figure 5.9b, and its FFT analysis in figure 5.9c. The harmonics spectrum has specific distribution characteristics. Around 2100 Hz it has obvious sideband harmonics, which is two times of the carrier frequency for the NPC converter due to the neutral point voltage control. It also can be found that there are some low order harmonics which is caused by the low carrier frequency. The corresponding harmonics can be found in the FFT analysis of the three phase converter side voltage (figure 5.9i). The grid current is shown in figure 5.9d and its FFT analysis is shown in figure 5.9e. It can be seen that the grid current has very good steady state performance. Due to the LCL filter, the THD of the grid current has been decreased to 3.8%, which is well below the requirement of the grid code. It also can be noted that the high order harmonics around the switching frequency have been attenuated significantly. Furthermore, the low order harmonics around the resonance frequency have been increased compared to the converter side current due to the resonance problem. However, the harmonics amplitude is below 2.5%, which also complies with the grid code requirements. Since the converter side current is controlled, its dq components are shown in figure 5.9f. It can be found that both d-axis and q-axis component are regulated very well. In order to obtain unity power factor on the grid side, the q-axis component reference is set to non-zero ($i_q \approx \sqrt{2}V_{g,ph}\omega C_f$). The grid side active and reactive power are shown in figure 5.9g. Unity power factor is achieved. However, due to the 5^{th} and 7^{th} low harmonics in the grid current, the reactive power has a ripple. The switching frequency of VOC is fixed, which mainly depends on the modulation carrier frequency. The switches in the NPC converter are only switched in one half period while kept off in the other half period. So using the average frequency

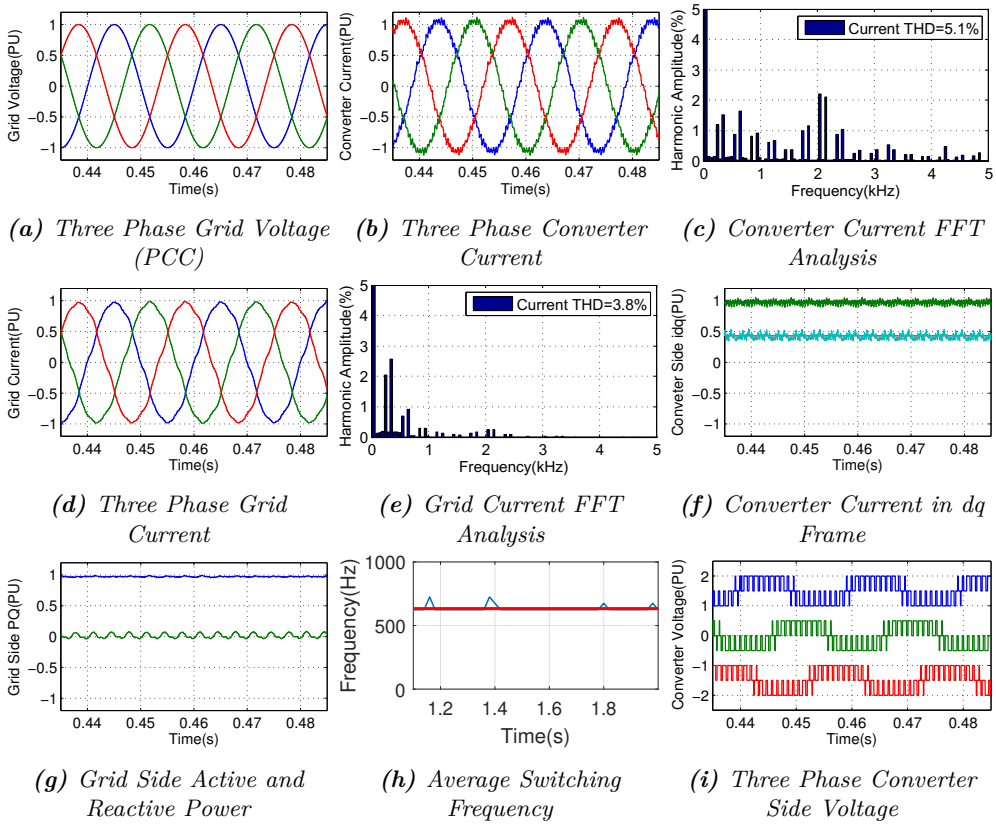

(a) Three Phase Grid Voltage (PCC) *(b) Three Phase Converter Current* *(c) Converter Current FFT Analysis*

(d) Three Phase Grid Current *(e) Grid Current FFT Analysis* *(f) Converter Current in dq Frame*

(g) Grid Side Active and Reactive Power *(h) Average Switching Frequency* *(i) Three Phase Converter Side Voltage*

Figure 5.9: *Voltage Oriented Control under Nominal Operation Point*

definition given in equation 5.18, the average frequency of VOC shown in figure 5.9h is around 633 Hz. The three phase converter side voltage is depicted in figure 5.9i.

Figure 5.10 shows the steady state DC-link voltage during normal operation. The DC-link voltage is well controlled and the steady state error is 0.1%. In order to get sufficient DC-link balancing, the hysteresis band for the neutral point control is set to 1% of half the DC-link voltage, i.e., $3000\,\mathrm{V} \times 1\% = 30\,\mathrm{V}$. Figure 5.10b shows the error of $v_{dc1} - v_{dc2}$ is well controlled. Correspondingly, the variations of upper and lower capacitor voltage (v_{dc1} and v_{dc2}) are limited within 0.5% of half the DC-link voltage, i.e., $3000\,\mathrm{V} \times 0.5\% = 15\,\mathrm{V}$, which is show in figure 5.10c.

Transient The transient performance is an important aspect of a controller. Case 2, active power drops to 0.5 PU and reactive power keeps zero is investigated, and the

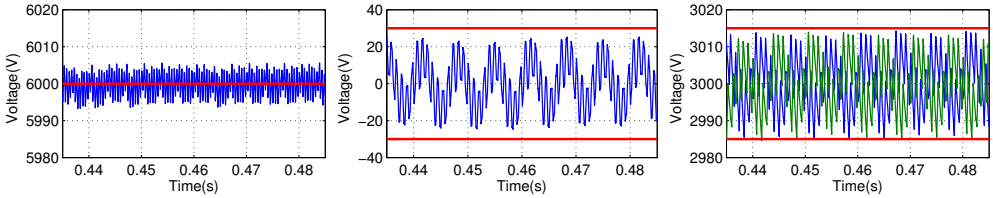

(a) *DC-link Voltage* ***(b)*** $v_{dc1} - v_{dc2}$ ***(c)*** v_{dc1} *and* v_{dc2}

Figure 5.10: *DC-link Voltage Performance of VOC under Nominal Operation Point*

results are summarized in figure 5.11. The three phase converter side current as shown in figure 5.11a is well regulated in different operation points. At time 0.7 s, the d-axis current reference i_d is set to 0.5 and the q-axis current reference is kept unchanged. It can be seen clearly in figure 5.11c that the d-axis component has a step at 0.7 s and the q-axis component remains the same. Due to the decoupling term in the VOC current controller, the d- and q-axis components can be controlled independently. The three phase grid current is shown in figure 5.11b. The transient process is well regulated. Due to the lower current reference, the steady state current becomes a bit worse than the nominal operation point. The grid side active power and reactive power are shown in figure 5.11d. The rising time of grid side active power is around 4.3 ms. The DC-link tracking performance is shown in figure 5.11e. There is around 1.6% undershoot and around 23 ms rising time. The capacitor voltage difference is shown in figure 5.11f. It can be found that the DC-link capacitor voltage difference is well controlled within 1% of half DC-link voltage.

5.4.3 VOC under Abnormal Operation

Case 3, three-phase grid voltage dropping to 0.7 PU is defined to verify the fault-handling of the controller. According to the Voltage Support Curve of the Fault Ride-through (FRT) Requirement for Wind Turbines (figure 4.19), 60 percent of the rated current should be injected to the grid as reactive current. The active power injected to the grid should depend on the generated power by the wind turbines. In the worst case, the pitch control of the wind turbine does not have enough time to be activated, so as much active power as possible should be injected as much as possible. In order to avoid over current, active current should comply with:

$$i_{d,ref} \leq \sqrt{I_b^2 - i_{q,ref}^2} \tag{5.19}$$

where I_b is the base current, $i_{q,ref}$ is the required reactive current calculated through the grid voltage dip, and $i_{d,ref}$ is the injected active current. For VOC control, the

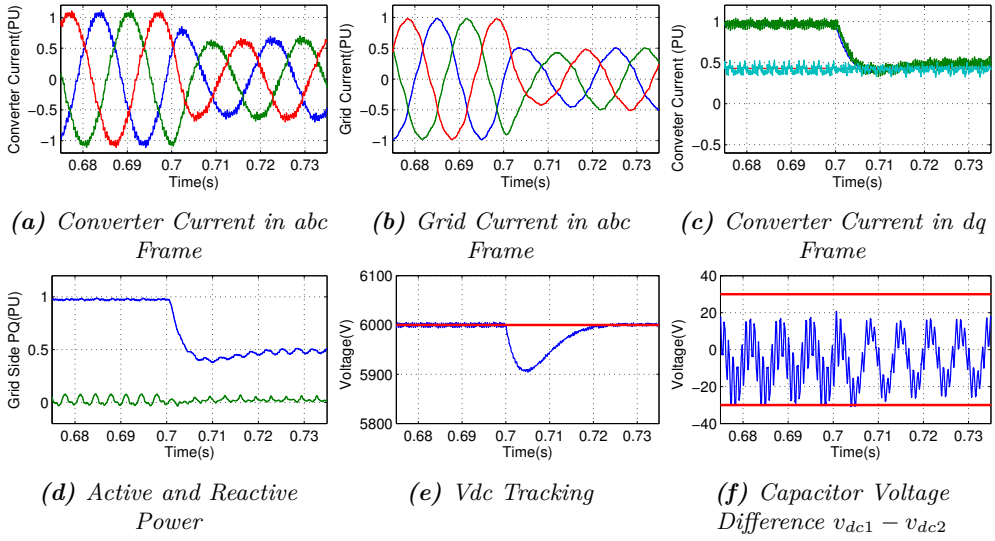

(a) Converter Current in abc Frame *(b) Grid Current in abc Frame* *(c) Converter Current in dq Frame*

(d) Active and Reactive Power *(e) Vdc Tracking* *(f) Capacitor Voltage Difference $v_{dc1} - v_{dc2}$*

Figure 5.11: *VOC Case 2 Active Power Drops to* 0.5 PU *and Reactive Power Keeps Zero*

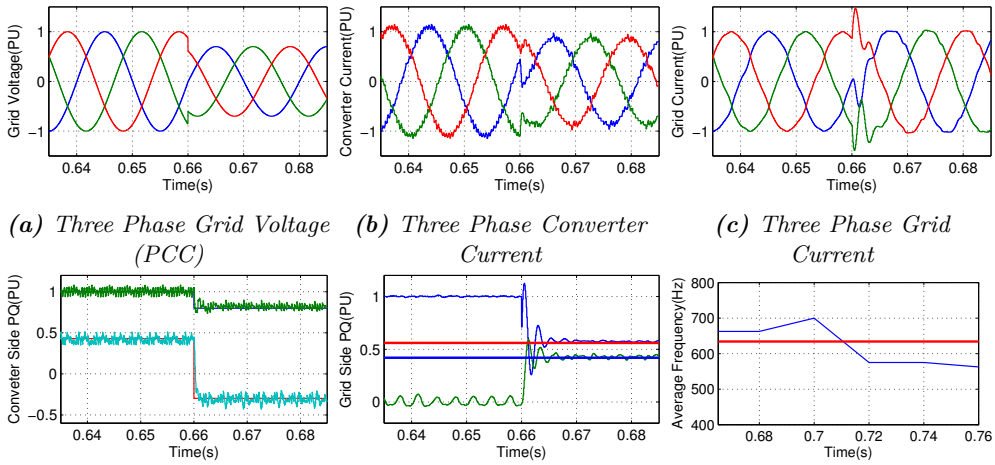

(a) Three Phase Grid Voltage (PCC) *(b) Three Phase Converter Current* *(c) Three Phase Grid Current*

(d) Converter Side Current in dq Frame *(e) Grid Side Active and Reactive Power* *(f) Average Switching Frequency*

Figure 5.12: *VOC Case 3 Three-phase grid voltage drops to* 0.7 PU

active power and reactive power can be calculated by equation 5.2. For case 3, the active power P^*_{ref} and reactive power Q^*_{ref} should be 0.56 PU and 0.42 PU.

The simulation results are given in figure 5.12. The grid voltage drops to 0.7 PU at 0.66 s, see figure 5.12a. According to the grid code, the grid side inverter should inject 0.6 PU reactive current to support the grid. In the worst case, the active current should be the maximum value 0.8 PU. The converter side current tracking is shown in figure 5.12d. It is clear that the active current reference $i_{d,ref}$ is set to 0.8 PU and the reactive current reference $i_{q,ref}$ is set from 0.43 PU to -0.3 PU in order to inject the required reactive current and compensate the capacitor reactive power. The rising time of the i_d response is 0.2 ms and for the i_q response is 0.87 ms. Figure 5.12e shows the injected active and reactive power to the grid. Due to the existing capacitor, the grid side has a slower response compared to the converter side. Considering the dynamic performance of active power, the rising time is 1.2 ms and the settle time is 8.4 ms. The overshoot of grid side active power is 46%. For reactive power, the rising time is around 0.7 ms, and the overshoot is around 40%. The average switching frequency in LVRT case 3 is around 634 Hz, which is almost the same as in the normal operation. The neutral point control does not generate more switching actions during the LVRT operation mode.

5.4.4 VOC Thermal Analysis

The basics of loss calculation and temperature estimation has been presented in the previous section 4.3. In order to compare fairly and focus on the analysis of the grid side current controller performance, a constant dc-link voltage is considered, and only the current loop is analysed. It should be noted that the neutral point voltage balancing control is still implemented in the grid side converter.

Loss Analysis The loss analysis is conducted under two conditions, first at different operation points and second with different switching frequencies at nominal operation point in order to achieve comparable conditions with the DPC method, which is presented in subsection 5.6.

For the first type, the loss distribution of the power switching devices for different wind speeds, and for LVRT is shown in figure 5.13. Aside from the nominal operation point, two normal operation points with wind speed at $10\,\mathrm{m\,s^{-1}}$ and $8\,\mathrm{m\,s^{-1}}$ are also investigated. Especially $10\,\mathrm{m\,s^{-1}}$ is the annual average offshore wind speed investigated. In order to analysis the loss distribution during LVRT, the LVRT case with 0.3 PU voltage drop is designed. Figure 5.13a shows the loss distribution for semiconductors in one arm at nominal operation. It can be clearly seen that the outer IGBT T_1 generates most losses stress among all the components. The inverse diodes of the IGBTs are less stressed, especially the inner IGBT's inverse diodes. With decreasing the active power injection, the total losses are becoming smaller. The switching losses of the outer IGBTs are decreased significantly, which can be seen from figure 5.13a, 5.13b and 5.13c.

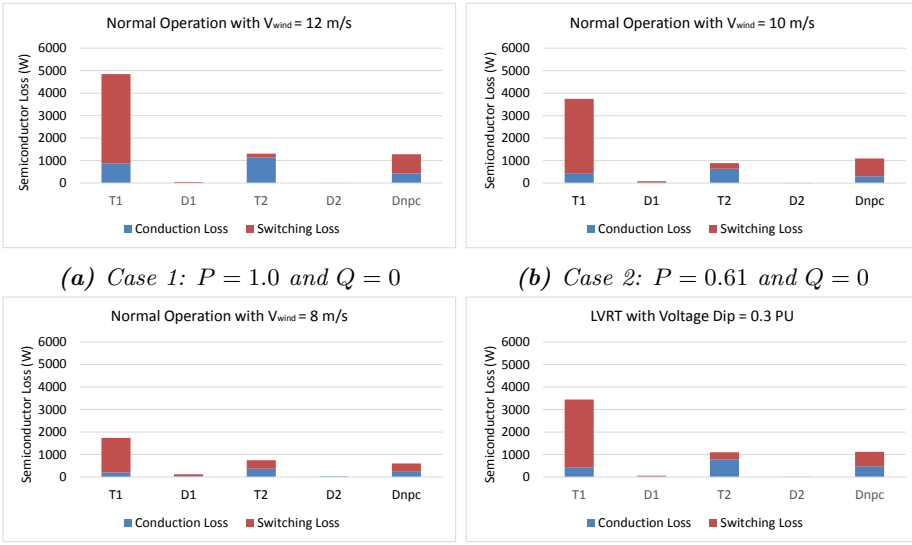

(a) Case 1: $P = 1.0$ and $Q = 0$

(b) Case 2: $P = 0.61$ and $Q = 0$

(c) Case 3: $P = 0.31$ and $Q = 0$

(d) Case 4: $P = 0.56$ and $Q = 0.42$

Figure 5.13: *Losses Analysis under Different Operation Points with VOC*

The loss distribution trends to be more balanced. The loss distribution under LVRT operation is shown in figure 5.13d. It does not change much and the most stressed device is still the outer IGBT T_1.

Temperature Estimation For large power converters, the semiconductor components are usually installed on separate heatsinks, which ensures a good thermal decoupling of the devices. For the simulation, the cooling water temperature is assumed as 37 °C [74]. The temperature distribution of the power switching devices for different operation points are shown in figure 5.14. Corresponding to the loss distribution shown in figure 5.13, the average junction temperature of the outer IGBT T_1 has the highest value, while the IGBT inverse diodes have relatively low temperatures. With decreasing active power, the temperature of IGBT T_1 decreases gradually.

5.4.5 VOC Experimental Results

In order to verify the VOC control, grid connection experiments were conducted with the low voltage test bench described in subsection 3.6. Mode 2 is used for experimental verification. The DC-link is powered by a 12-pulse diode rectifier. Due to the voltage drop at the input transformer, the DC-link can not be maintained at 750 V. For this reason, the grid voltage is adjusted to around 215 V also for the other control schemes

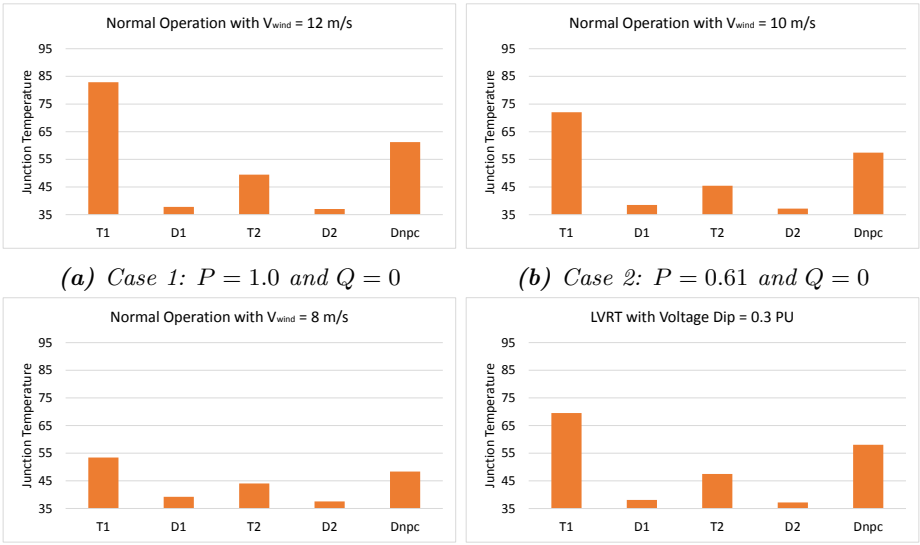

(a) *Case 1:* $P = 1.0$ *and* $Q = 0$ ***(b)*** *Case 2:* $P = 0.61$ *and* $Q = 0$

(c) *Case 3:* $P = 0.31$ *and* $Q = 0$ ***(d)*** *Case 4:* $P = 0.56$ *and* $Q = 0.42$

Figure 5.14: *Average Junction Temperature under Different Operation Points with VOC*

presented in this thesis. All the system parameters are scaled down with keeping the PU value as far as possible. The system parameters are summarised in table 5.5, the control parameters are given in table 5.6. The steady state and transient performance are discussed as following.

Steady State Figure 5.15 shows the results for the VOC under nominal operation. The three phase grid voltage is shown in figure 5.15a, which contains the 3^{rd} and 5^{th} order harmonics. The converter current is shown in figure 5.15c. It can be found from an FFT analysis (figure 5.15d) that the VOC has a very clear harmonics distribution, which should be distributed at the switching frequency and its multiples. Actually the carrier frequency is set to 1050 Hz. By employing the LCL filter, the high order harmonics are greatly attenuated. The three phase grid current is shown in figure 5.15e, which is slightly distorted at the amplitude due to the 5^{th} order harmonics (see 5.15f). The converter side current in dq frame is shown in figure 5.15g. The d-axis component is controlled to its reference value 20.4 A. The q-axis component is controlled to its reference value 2.4 A to compensate the reactive power of the LCL filter. The converter side active and reactive power are shown in figure 5.15h. The active power is slightly smaller than 10 kW due to the lower grid voltage setting, which has been discussed in

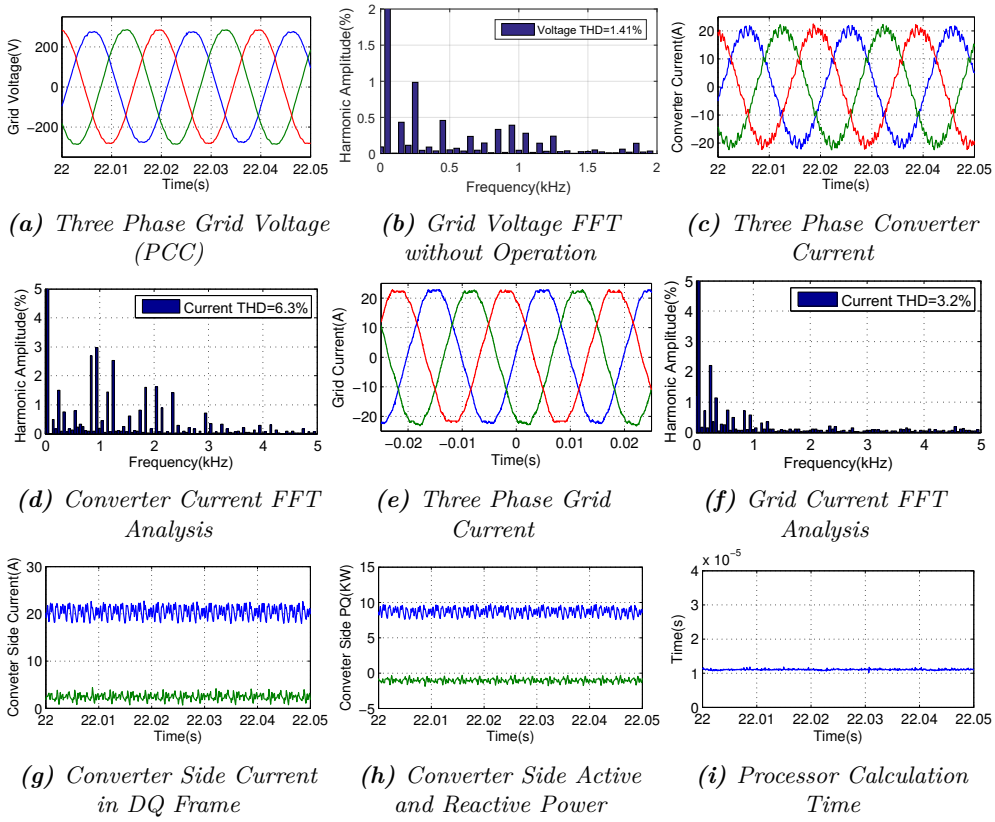

(a) Three Phase Grid Voltage (PCC)

(b) Grid Voltage FFT without Operation

(c) Three Phase Converter Current

(d) Converter Current FFT Analysis

(e) Three Phase Grid Current

(f) Grid Current FFT Analysis

(g) Converter Side Current in DQ Frame

(h) Converter Side Active and Reactive Power

(i) Processor Calculation Time

Figure 5.15: *Experimental Results of VOC at* 10 kW

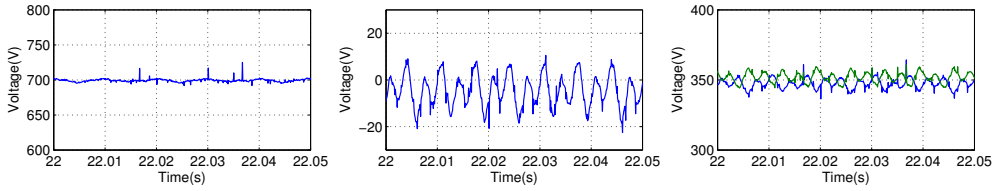

(a) DC-link Voltage

(b) $v_{dc1} - v_{dc2}$

(c) v_{dc1} *and* v_{dc2}

Figure 5.16: *Experimental DC-link Voltage measurement of VOC at* 10 kW

subsection 5.5.4. Figure 5.15i shows the calculation time of the main routine, which is around 11 µs. The DC-link voltage is shown in figure 5.16. Due to the voltage drop of

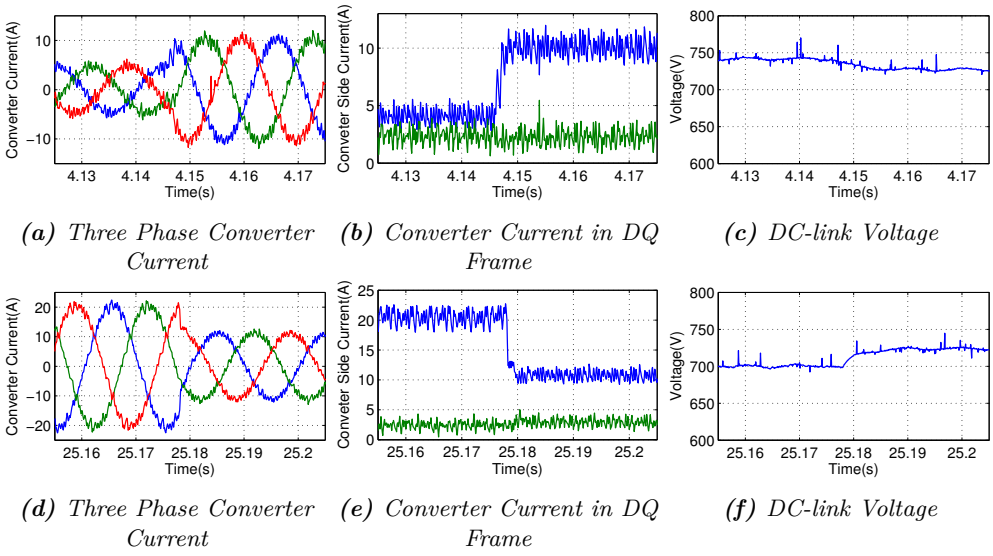

(a) *Three Phase Converter Current* ***(b)*** *Converter Current in DQ Frame* ***(c)*** *DC-link Voltage*

(d) *Three Phase Converter Current* ***(e)*** *Converter Current in DQ Frame* ***(f)*** *DC-link Voltage*

Figure 5.17: *Experimental Transient Performance of VOC for Active Power from 2 to step* 5 kW *and from 10 to* 5 kW

the input transformer, the DC-link voltage has dropped to 700 V. The neutral point voltage is maintained in the range of 5.7% of half the DC-link voltage.

Transient The results for the dynamic performance of the VOC method are shown in figure 5.17. Active power steps from 2 to 5 kW and from 10 to 5 kW are conducted while the reactive power is kept constant. Figure 5.17b shows the changes of active power is from 2 to 5 kW. The rising time is around 2.3 ms. Due to the decoupling term, the d-axis and q-axis components are controlled separately. For the active power step from 10 to 5 kW, the falling time is around 1.8 ms.

5.5 DPC Results

5.5.1 DPC under Normal Operation

The nominal operation point is first selected for the DPC control validation. Since the hysteresis controller is adopted for DPC, a higher sampling frequency is necessary to obtain a sufficient response. The average switching frequency depends on the sampling frequency and hysteresis controller bands. The sampling frequency is set at 125 kHz. In order to limit the switching frequency below 1 kHz, the hysteresis bands both H_P and H_Q for active and reactive power are set to 375 kW(PU=0.075). Considering the

state of art technology, for simplicity and comparison with VOC, the passive damping is adopted for the resonance damping. Here a damping resistor is selected as $R_d = 0.87\,\Omega$ ($PU = 0.4$).

Steady State Case 1, nominal operation is set for DPC control validation. The control structure has been discussed in previous subsection 5.3, figure 5.4. Figure 5.18 shows the steady state performance of DPC under nominal operation. The three phase grid voltage (PCC) in figure 5.18a has no distortion. The converter side current is shown in figure 5.18b. It can be noted that even without internal current loop, the converter side current is still well controlled. The FFT analysis of the converter side current is shown in figure 5.18c. It is obvious that the spectrum has not harmonics of a specific order as the VOC method, but it distributes around the frequency bands. The total harmonics distortion (THD) is 6.3%. However, it can be seen that the maximum amplitude range is located around 1 kHz with the amplitude 2.4%. Similar to the VOC method, harmonics exist around the sidebands of switching frequency and multiples, so it can be concluded that the average frequency of DPC under the given condition should be around 1 kHz. This is proved through figure 5.18h where the average switching frequency is 932 Hz. The three phase grid side current is shown in figure 5.18d. After the LCL filter, the high order harmonics are attenuated greatly. It can be seen from the FFT analysis that the high order harmonics, especially above the 13^{th} order harmonics, are suppressed and attenuated effectively. Due to the existing of 5^{th} and 7^{th} order harmonics in the converter side current, even though the resonance issue is definitely suppressed, the low order harmonics are not well attenuated. Especially the 5^{th} order harmonic is amplified from 2.1% to 2.9%. However, the THD of the grid side current is 4.8%, which is below the grid code requirement (5%) (IEEE519). For individual order harmonics both odd and even, the spectrum also complies with the grid code requirement according to figure 3.10. The low order harmonics suppression can be solved with a selective individual order filter or general suppression methods. The latter will be discussed in Chapter 7. The active power and reactive power of the converter are directly controlled using the hysteresis controller. They are kept within their limits. It can be seen in Figure 5.18f. The reactive power reference is not zero. In order to obtain a unity power factor on the grid side, reactive power of the capacitor has to be compensated ($Q_c \approx -3V_{g,ph}^2 \omega C_f$). The grid side active and reactive power are shown in figure 5.18g, which indicates that the unity power factor is achieved successfully. The converter side voltage is shown in figure 5.18i. Compared to the fastest switching table (5.2), the switching table (5.3) can reduce unnecessary switching transitions. The switching transitions directly changing in between positive and negative half of the DC-link voltage have been largely eliminated, which reduces the voltage stress of the switches.

During normal operation, the grid side converter should be in charge of the DC-link voltage control, while the generator side works in MPPT mode. Figure 5.19 shows the

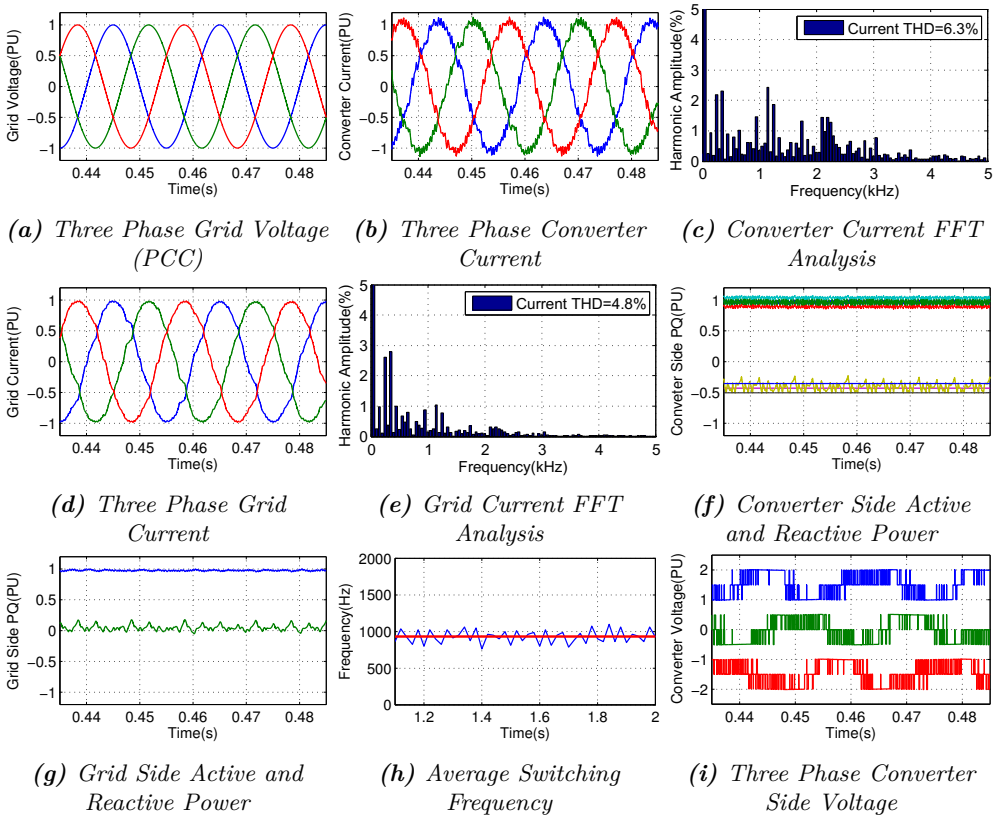

(a) *Three Phase Grid Voltage (PCC)*

(b) *Three Phase Converter Current*

(c) *Converter Current FFT Analysis*

(d) *Three Phase Grid Current*

(e) *Grid Current FFT Analysis*

(f) *Converter Side Active and Reactive Power*

(g) *Grid Side Active and Reactive Power*

(h) *Average Switching Frequency*

(i) *Three Phase Converter Side Voltage*

Figure 5.18: *Direct Power Control under Nominal Operation Point*

steady state performance of the DC-link voltage. The voltage reference is set to 6000 V. It can be found that the DC-link voltage is well controlled and the steady state error is 0.3%. Since the three-level NPC converter is used, the neutral point voltage balancing is an important task. In order to get sufficient DC-link balancing and limit the switching frequency as low as possible, the hysteresis band for the neutral point control is set to 5% of half the DC-link voltage, i.e., $3000\,\mathrm{V} \times 5\% = 150\,\mathrm{V}$. Figure 5.19b shows the error ($v_{dc1} - v_{dc2}$) is well controlled. Correspondingly, the variations of upper and lower capacitor voltage (v_{dc1} and v_{dc2}) are limited within 2.5% of half the DC-link voltage, i.e., $3000\,\mathrm{V} \times 2.5\% = 75\,\mathrm{V}$, which is shown in figure 5.19c.

Transient In order to test the DPC under different operation conditions, case 2, active power dropping to 0.5 PU and reactive power keeping zero is analysed for transient

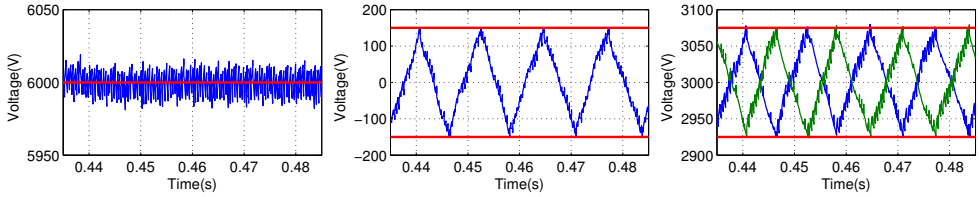

(a) DC-link Voltage *(b)* $v_{dc1} - v_{dc2}$ *(c)* v_{dc1} *and* v_{dc2}

Figure 5.19: *DC-link Voltage Control of DPC during Nominal Operation*

control verification.

The simulation results are shown in figure 5.20. At 0.7 s, the active power reference drops to 0.5 PU. It can be seen that the converter side current response (5.20a) is very fast and well regulated. The active and reactive power response are shown in figure 5.20c. Both active and reactive power are controlled well in the hysteresis bands (PU=0.075). Since the active power reference is given by the output of the voltage loop, which is not a regular step change, it is not easy to find the rising time of the active power. The grid current response given in figure 5.20b is slower than the converter current dynamics. The grid side active and reactive power are shown in figure 5.20d. The settling time to 5% error band is around 0.018 s, which is caused not only by the large capacitor of the filter, but also the voltage loop. The DC-link voltage tracking is shown in figure 5.20e. It can be found that there is around 1.8% overshoot and the rising time is around 0.012 s, which are reasonable for the voltage loop. Generally, the outer loop should be ten times slower than the internal loop. During the dynamic process, the neutral point voltage is well controlled in the band of 5% of half the DC-link voltage.

It should be noted that the reactive power has large variations compared to the active power by employing ST2 in nominal operation, which is analysed in subsection 5.3.3. The reactive power exceeds its boundaries some times (figure 5.20c), which produces the variations in the grid side reactive power (figure 5.20d). By using the improved switching table ST3, this problem can be solved. The case 2 with ST3 is shown in figure 5.21. However, the switching frequency has been increased slightly under the same conditions compared to ST2, which is 1156 Hz (>932 Hz with ST2 in nominal operation).

5.5.2 DPC under Abnormal Operation

As calculated in subsection 5.4.3, the injected active power P^*_{ref} and reactive power Q^*_{ref} should be 0.56 PU and 0.42 PU. The results of case 3 are shown in figure 5.22. The grid voltage drops to 0.7 PU at 0.660 s. In order to reduce the switching frequency as much as possible, switching table ST2 is adopted for this case. The converter side active power and reactive power are shown in figure 5.22d. It can be noted that the active and reactive power are controlled very fast. The rising time for both active and

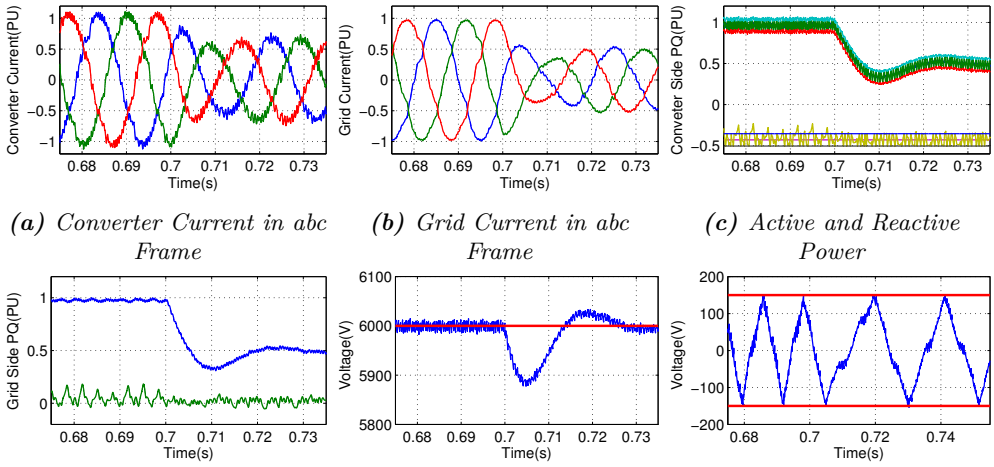

(a) *Converter Current in abc Frame*

(b) *Grid Current in abc Frame*

(c) *Active and Reactive Power*

(d) *Active and Reactive Power*

(e) *DC-link Tracking*

(f) *Capacitor Voltage Difference* ($v_{dc1} - v_{dc2}$)

Figure 5.20: *DPC Case 2 Active Power Drops to* 0.5 PU *and Reactive Power Keeps Zero with ST2*

reactive power references are 0.49 ms and 0.76 ms. It can be further noted that the error band is narrower after the grid voltage dip. The reason for this is that in order to achieve the same current ripple range, the hysteresis controller band has to be reduced by the factor $\delta = V_{lvrt}/V_{nominal}$. Figure 5.22b shows the converter side current. The current ripple is in the same range as in normal operation. The grid side current and power tracking performance are shown in figure 5.22c and 5.22e. Since the maximum apparent current is adopted, the grid side current amplitude is still one PU value. The THD in LVRT operation is 2.6%, and the related average switching frequency is around 767 Hz. The grid active power has peak drop at 0.660 s, which is caused by the grid voltage drop. The rising time of active and reactive power for grid side are 1.28 ms and 0.86 ms, which is very fast and can support the grid immediately.

Case 4, three-phase grid voltage dropping to 0.5 PU is further investigated. Since the d-axis of the grid voltage is reduced to half of the nominal voltage, it will cause the grid voltage vector to be shorter than the low voltage vectors ($|V_{01}| \sim |V_{06}| = V_{dc}/3$), i.e.,

$$v_{gd} = 0.5V_{LL} \cdot \sqrt{2}/\sqrt{3} = 1347\,\mathrm{V} < |V_{01}| = V_{dc}/3 = 2000\,\mathrm{V} \tag{5.20}$$

Namely, if the same low voltage vectors from ST2 are still used, they will cause the wrong power change. For example, when the voltage vector $\vec{V}_g$ is in sector θ_1, if the low voltage vector V_{02} is selected for reducing the active power and reactive power, it

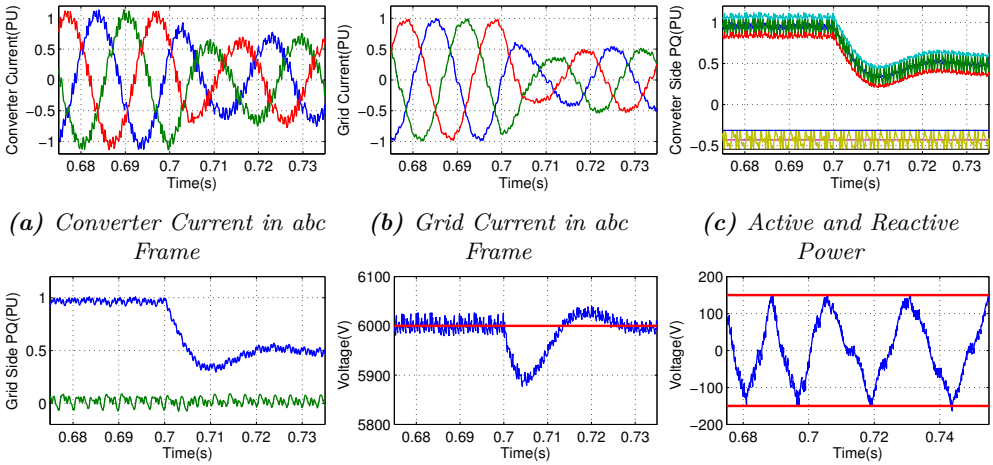

(a) Converter Current in abc Frame

(b) Grid Current in abc Frame

(c) Active and Reactive Power

(d) Active and Reactive Power

(e) DC-link Tracking Performance

(f) Capacitor Voltage Difference ($v_{dc1} - v_{dc2}$)

Figure 5.21: *DPC Case 2 Active Power Drops to* 0.5 PU *and Reactive Power Keeps Zero with ST3*

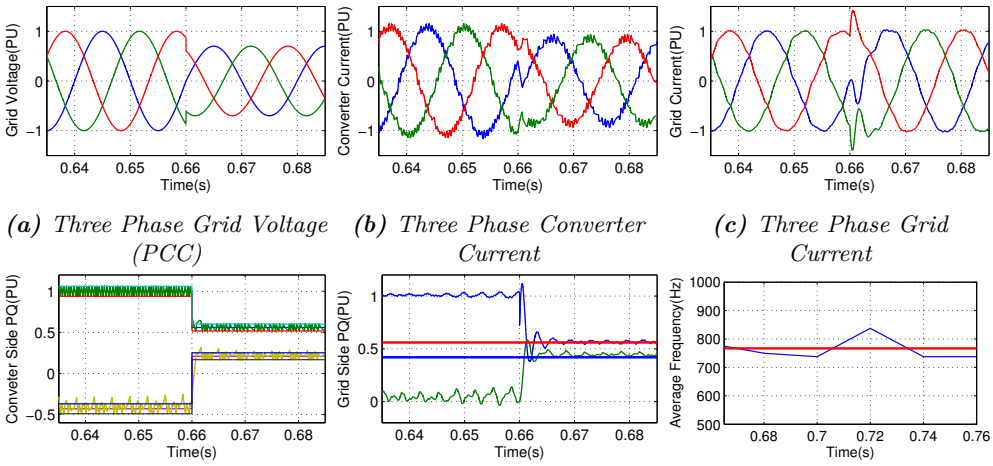

(a) Three Phase Grid Voltage (PCC)

(b) Three Phase Converter Current

(c) Three Phase Grid Current

(d) Converter Side Active and Reactive Power

(e) Grid Side Active and Reactive Power

(f) Average Switching Frequency

Figure 5.22: *DPC Case 3 Three-phase Grid Voltage Drops to* 0.7 PU

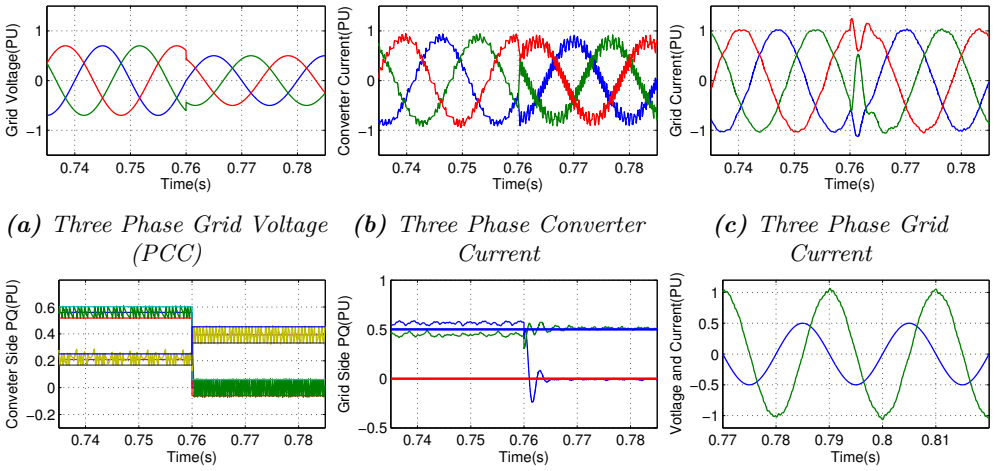

(a) *Three Phase Grid Voltage (PCC)*

(b) *Three Phase Converter Current*

(c) *Three Phase Grid Current*

(d) *Converter Side Active and Reactive Power*

(e) *Grid Side Active and Reactive Power*

(f) *Grid Side Phase A Voltage and Current*

Figure 5.23: *DPC Case 4 Three-phase Grid Voltage Drops to* 0.5 PU

will increase the active power instead, which can be understood by figure 5.6. So for this reason, the switching table ST1 is used. Since ST1 is a fast switching table, the switching frequency will be slightly higher than in case 3. In order to limit the switching frequency, the hysteresis band is reset to the normal value. It can be found that the active and reactive power error band is larger than in case 3 (figure 5.23d). This will also cause the converter side current ripple to increase (figure 5.23b). However, the steady state performance (figure 5.23c) is not becoming worse. The THD of the grid current is 1.9%. The rising time of active and reactive power on the converter side are 0.35 ms and 0.29 ms, respectively. The grid side power and reactive power are well controlled indirectly, see figure 5.23e. In the end, the power factor should be zero, since all the current is injected to the grid as reactive current. Figure 5.23f shows the phase A grid voltage and current.

5.5.3 DPC Thermal Analysis

Loss Analysis Similar to VOC, the thermal analysis for DPC is also conducted for two variation types. First, the performance is analysed in different operation points, which are normal operation with wind speed $12\,\mathrm{m\,s^{-1}}$, $10\,\mathrm{m\,s^{-1}}$, $8\,\mathrm{m\,s^{-1}}$ and LVRT with 0.3 PU voltage drop. Second, the performance is analysed for different controller parameters for nominal operation, which is mainly the hysteresis band parameter.

Figure 5.24a shows the loss distribution for each power semiconductor of one arm of

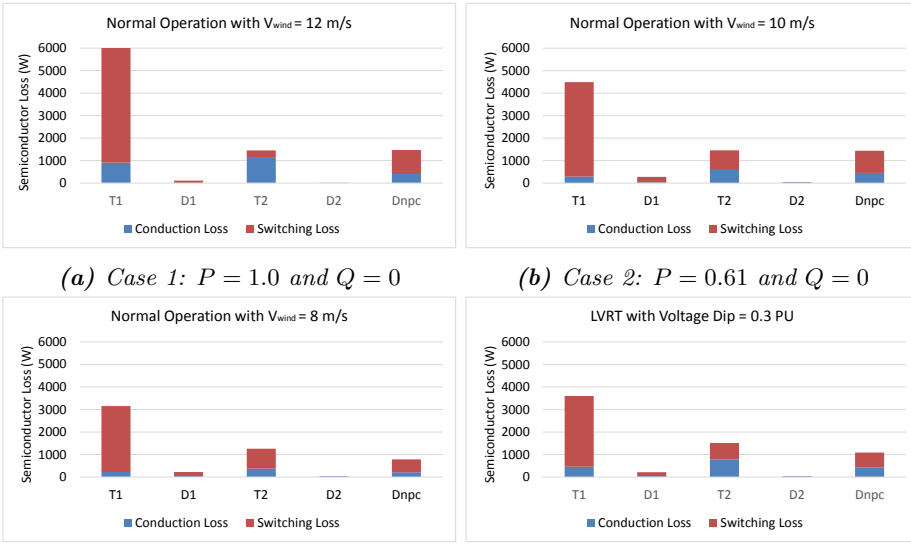

(a) Case 1: $P = 1.0$ and $Q = 0$

(b) Case 2: $P = 0.61$ and $Q = 0$

(c) Case 3: $P = 0.31$ and $Q = 0$

(d) Case 4: $P = 0.56$ and $Q = 0.42$

Figure 5.24: *Losses Analysis under Different Operation Points with DPC*

the three phase three-level NPC converter at nominal operation point. Similar to VOC, the uneven distribution exists. The outer IGBT is the most stressed switch, while the most unstressed devices are the inverter diodes. The neutral diode is moderately stressed.

The second type of the loss analysis is conducted with changing the hysteresis band at nominal operation point. The results are shown in table 5.7. It can be found that the average switching frequency calculated by equation 5.18 decreases when the hysteresis band increases. In order to limit the losses, the average switching frequency is controlled to be below 1000 Hz. For example, when the hysteresis band is set to 0.06 for both active and reactive power controller, the average switching frequency is around 916 Hz. The THD of the grid side current is around 2.42%. The total converter losses including conduction losses and switching losses for all semiconductors devices is around 59.58 kW, so that the efficiency of the converter is 98.81% without filter losses. When the switching frequency is reduced to 503 Hz, the THD of the grid side current is around 9.66%, which already exceeds the grid code requirement. It can be concluded that DPC can not achieve a satisfying grid current quality with the designed LCL filter, which is not sufficient to damp the harmonics produced by DPC method around 500 Hz. There are two possible reasons. One is that the LCL filter is designed for space vector modulation, and the other one is that the DPC method has a wider spectrum with more low-frequency

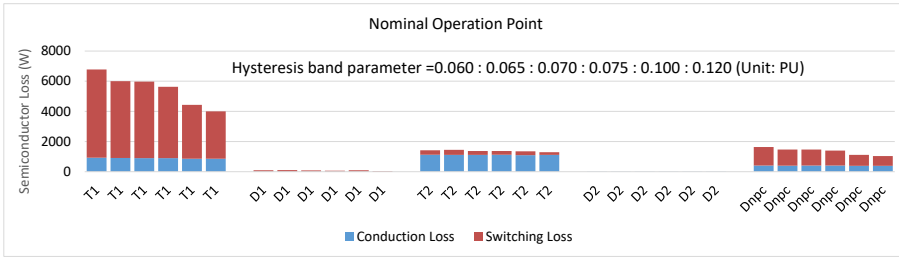

Figure 5.25: *Loss Distribution under Different Control Parameters at Nominal Operation Point with DPC*

harmonics.

Table 5.7: *DPC Control Performance with different Hysteresis Band*

H_P, H_Q (PU)	$f_{\overline{SW}}$ (Hz)	THD (%)	P_{loss} (kW)	η (%)
0.06	916	2.42	59.58	98.81
0.065	812	3.70	54.28	98.91
0.07	789	6.45	53.43	98.93
0.075	738	6.81	50.86	98.98
0.1	578	7.39	42.04	99.16
0.12	503	9.66	38.23	99.24

Additionally, the loss distribution for each semiconductor in one phase arm for the six different hysteresis control parameters are shown in figure 5.25. There are three conclusion points. First, the conduction losses of the semiconductors are the same, which indicates that the conduction losses are mostly decided by the operation point. Second, the loss distribution of three level NPC with DPC control is unequal as expected for NPC, and will decrease the overall switch utilization. Third, as also expected the switching losses decrease with increasing the hysteresis controller band.

Temperature Estimation Similar to VOC, the temperature distribution of the power switching devices at different operation points with DPC are shown in figure 5.26. Corresponding to the loss distribution in figure 5.24, the average junction temperature of the outer IGBT T_1 has the highest temperature, while the IGBT inverse diodes have a relatively low temperature. With the active power decreasing, the temperature of IGBT T_1 decreases gradually. For the LVRT case 4, the average junction temperature is similar to case 2. The average junction temperature at norminal operation point and

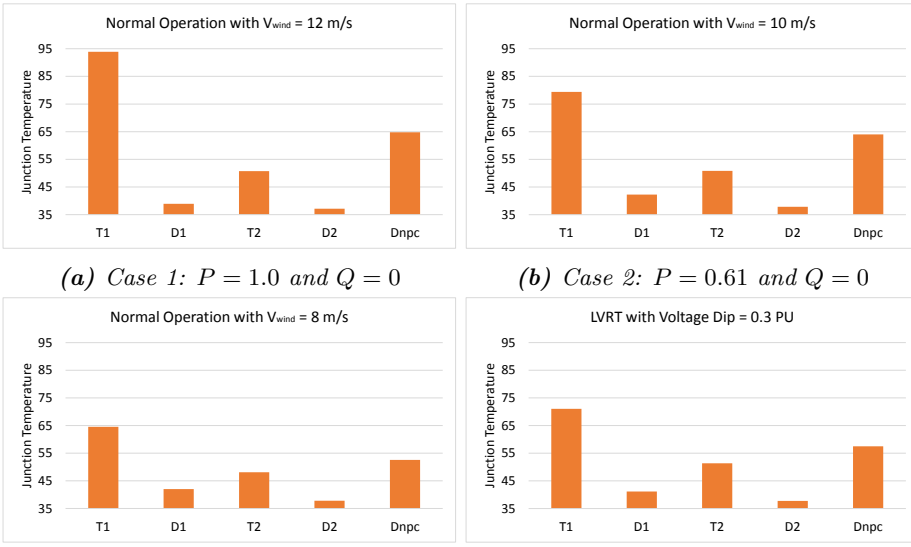

(a) Case 1: $P = 1.0$ and $Q = 0$ *(b) Case 2: $P = 0.61$ and $Q = 0$*

(c) Case 3: $P = 0.31$ and $Q = 0$ *(d) Case 4: $P = 0.56$ and $Q = 0.42$*

Figure 5.26: *Average Junction Temperature under Different Operation Points with DPC*

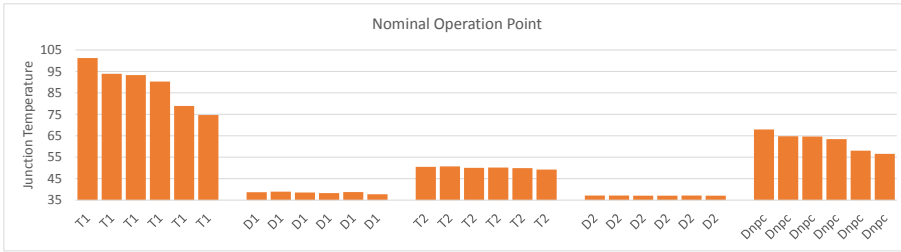

Figure 5.27: *Average Junction Temperature for Different Control Parameters at Nominal Operation Point with DPC*

different control parameters according to table 5.7 is shown in figure 5.27. The maximum junction temperature of IGBT T_1 appears when the hysteresis controller bands H_P and H_Q are set as 0.06, which is 93 ℃ and below the maximum junction operating temperature 125 ℃ [135].

5.5.4 DPC Experimental Results

In order to verify the DPC operation, experiments are conducted with the LV test setup as well. The control parameters are summarized in table 5.8. As discussed previously, the DPC needs a sufficient high sampling frequency to guarantee its performance. So for hardware implementation, the hysteresis controller and switching table reading are implemented in the FPGA for fast sampling time and reducing the CPU calculation effort. The minimum sampling time of ADCs for the FPGA model in the dSPACE SCALEXIO system is 500 ns. The sector detection is implemented in the CPU processor with a sampling time of 40 µs. So the system sampling is 25 kHz for the experiments. 2 µs is adopted as the dead time.

Table 5.8: *DPC Control Parameter*

Description	Symbol	MV value	LV value	PU value
Sampling Frequency	f_s	125 kHz	25 kHz	2500/500
Dead Time	t_d	-	2 µs	-
Hysteresis Band	H_P, H_Q	375 kW	500 W	0.075/0.05
Damping Resistor	R_d	0.87 Ω	5 Ω	0.4/0.31

Steady State The experimental results with ST2 at operation point 5 kW are shown in figure 5.28. The three phase grid voltage is not an ideal waveform but contains some low order harmonics. Figure 5.28b shows the FFT analysis of the grid voltage at TU Berlin. It can be found that there are around 0.8% 5^{th} and 7^{th} order harmonics which can cause unfavourable control issues especially if an LCL filter with low resonance frequency is used. The converter side current is indirectly controlled, figure 5.28c, and its FFT analysis is given in figure 5.28d. Due to the variable switching frequency, the harmonics distribute over a wide frequency range. The three phase grid currents are shown in figure 5.28e. From the FFT analysis of the grid current, it can be found that the high order harmonics are effectively suppressed by the LCL filter. However, it is obvious that there are 5^{th} and 7^{th} order harmonics existing in the grid current, caused by the nonlinear grid voltage and amplification of these harmonics by the chosen LCL filter. This can be solved by individual harmonics filter or general harmonic suppression using Backstepping Control (BSC) (chapter 7). The converter side active and reactive power are directly controlled (figure 5.28g). Both P and Q are well regulated by the hysteresis controller. The average frequency is shown in figure 5.28h, which is around 2.1 kHz[1]. The average frequency is calculated by counting the switching pluses divided by 20 ms. Since most functional modules are implemented in FGPA, the calculation effort of the

[1]The blue lines depict the counting values. Only the maximum values represent the real frequency.

processor is greatly reduced. The average turnaround time is around 10 µs. The DC-link voltage is clamped by a 12-pulse diode rectifier and can not be controlled. Figure 5.29 shows the DC-link voltage, which drops to 720 V due to the input transformer voltage drop. The neutral point voltage is controlled in the error range 5% of half the DC-link voltage.

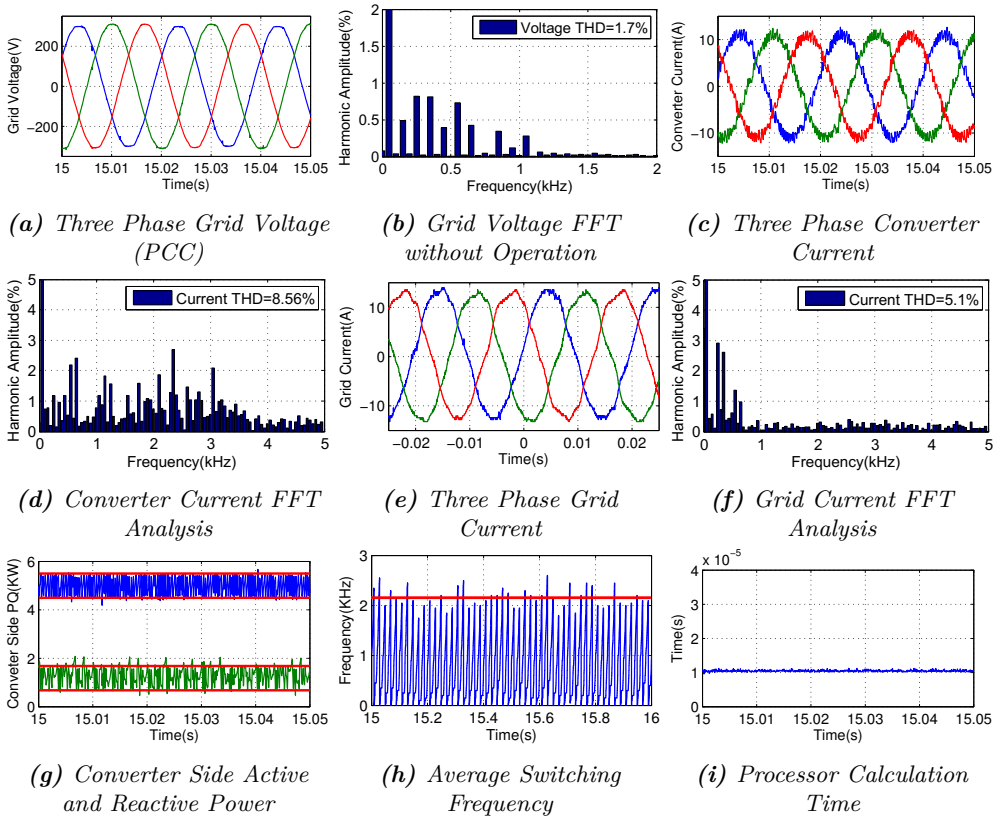

(a) Three Phase Grid Voltage (PCC)

(b) Grid Voltage FFT without Operation

(c) Three Phase Converter Current

(d) Converter Current FFT Analysis

(e) Three Phase Grid Current

(f) Grid Current FFT Analysis

(g) Converter Side Active and Reactive Power

(h) Average Switching Frequency

(i) Processor Calculation Time

Figure 5.28: *Experimental Results of DPC at* 5 kW

Transient In order to verify the dynamic performance of DPC, several different steps are conducted. Figure 5.30 shows the system response for an active power step from 2 to 5 kW and from 5 to 1 kW. Both cases are controlled very fast. Figure 5.30b shows that the active and reactive power are decoupled. The active power rising time is around 1.8 ms. When the active power becomes large, the reactive power control performance declines, which is already discussed in subsection 5.3.3. With the current increase, the

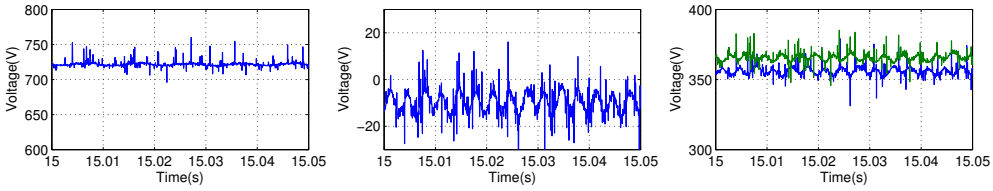

(a) DC-link Voltage *(b)* $v_{dc1} - v_{dc2}$ *(c)* v_{dc1} *and* v_{dc2}

Figure 5.29: *Experimental DC-link Voltage Performance of DPC at* 5 kW

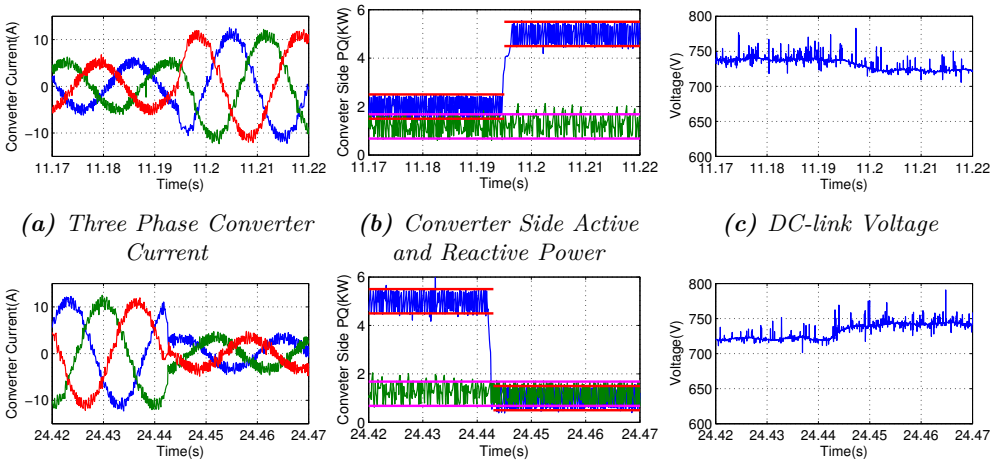

(a) Three Phase Converter Current *(b) Converter Side Active and Reactive Power* *(c) DC-link Voltage*

(d) Three Phase Converter Current *(e) Converter Side Active and Reactive Power* *(f) DC-link Voltage*

Figure 5.30: *Experimental Transient Performance of DPC during active power step from 2 to* 5 kW *and from 5 to* 1 kW

DC-link voltage drops. The results for the active power step from 5 to 1 kW are shown in figure 5.30d, 5.30e and 5.30f. The rising time is around 0.79 ms, which is faster than during step up, because the maximum output power increasing per sampling time is limited by the physical system and switching table.

5.6 Comparison of VOC and DPC

Steady State Comparing VOC (figure 5.9) and DPC (figure 5.18) during nominal operation, the grid current FFT analysis, average switching frequency, and three phase converter voltage are shown in figure 5.31. Even damped by the LCL filter, the fre-

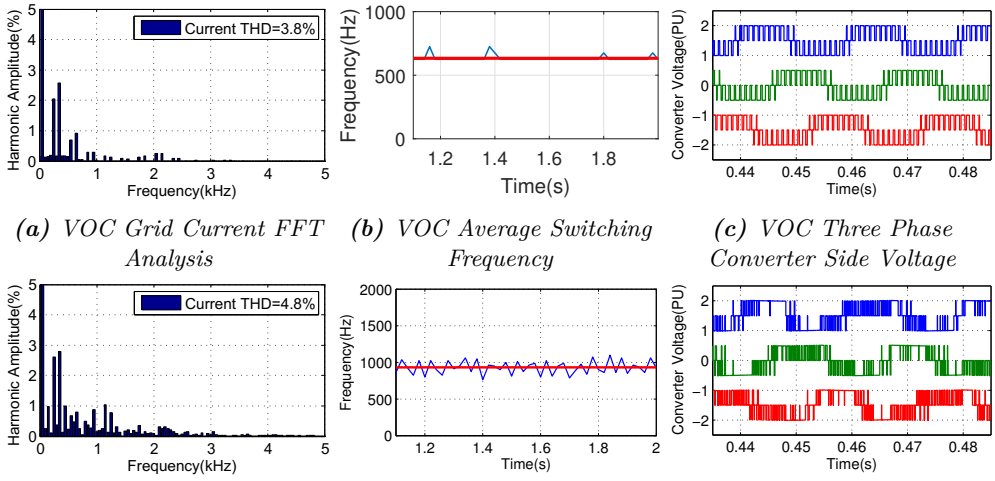

(a) VOC Grid Current FFT Analysis *(b) VOC Average Switching Frequency* *(c) VOC Three Phase Converter Side Voltage*

(d) DPC Grid Current FFT Analysis *(e) DPC Average Switching Frequency* *(f) DPC Three Phase Converter Side Voltage*

Figure 5.31: *Comparison of VOC and DPC at Nominal Operation Point*

quency spectrum of DPC is still more distributed over the frequency band. The average frequency of VOC is below the DPC average frequency. The loss analysis of VOC and DPC are shown in figure 5.32a and figure 5.32d respectively. The VOC generates less losses than DPC because of the lower switching frequency. Selected results for VOC at the nominal operation point and different switching frequencies are given in table 5.9. Compared with DPC, VOC achieves better current quality considering THD for the same average switching frequency. It can be noted that for the same average switching frequency, the converter has the same level of losses and efficiency.

In order to evaluate the characteristics of both control algorithms, further data are summarized in table 5.10. Comparing the steady state performance regarding the THD and switching frequency at different operation points, it can be noted that at the same operation point, VOC has better performance than DPC considering the THD.

Transient The control difference between VOC and DPC for the transient case 2 and LVRT case 3 are shown in figure 5.32. Here $i_{con,dq}$ represents converter side current in dq frame, and p_{con}, q_{con} represent converter side active power and reactive power. Table 5.11 presents the rising time of DPC, and VOC in different operation points. The converter side (CS) and grid side (GS) results are summarized respectively. It can be noted that DPC reacts much faster than VOC in normal operation. However, in abnormal operation, from the studied case 3, DPC and VOC have comparable dynamic

Table 5.9: *VOC and DPC Control Performance with Different Switching Frequency under Nominal Operation Point*

Method	$f_{\overline{SW}}$ (Hz)	THD (%)	P_{loss} (kW)	η (%)
VOC	787	1.69	54.91	98.90
	769	2.02	54.94	98.90
	617	3.5	43.96	99.12
DPC	789	6.45	53.43	98.93
	738	6.81	50.86	98.98
	578	7.39	42.04	99.16

Table 5.10: *Steady State Performance Comparison of DPC and VOC*

Operation Point	DPC			VOC		
	$f_{\overline{SW}}$ (Hz)	THC (% I_N)	η (%)	$f_{\overline{SW}}$ (Hz)	THC (%I_N)	η (%)
$P = 1.00, Q = 0$	812	3.7	98.91	617	3.5	99.12
$P = 0.61, Q = 0$	1024	3.1	99.08	745	2.1	99.30
$P = 0.31, Q = 0$	937	1.5	99.35	550	1.8	99.59
$P = 0.56, Q = 0.42$	694	2.4	99.23	575	1.5	99.31

performance.

Two conclusions can be drawn:

1. At the same operation point, VOC has a better steady state performance both in THD and switching frequency.

2. For the reference step, DPC has a much higher dynamic performance than the VOC method.

5.7 Summary

In this chapter, the state-of-the-art grid converter control algorithms, voltage oriented control and direct power control are investigated. First, a historical overview of grid converter control is presented. Voltage oriented control derived from field oriented control is well adopted for power converter control since the 60's. Direct power control derived from direct torque control has been used for power converter control since the

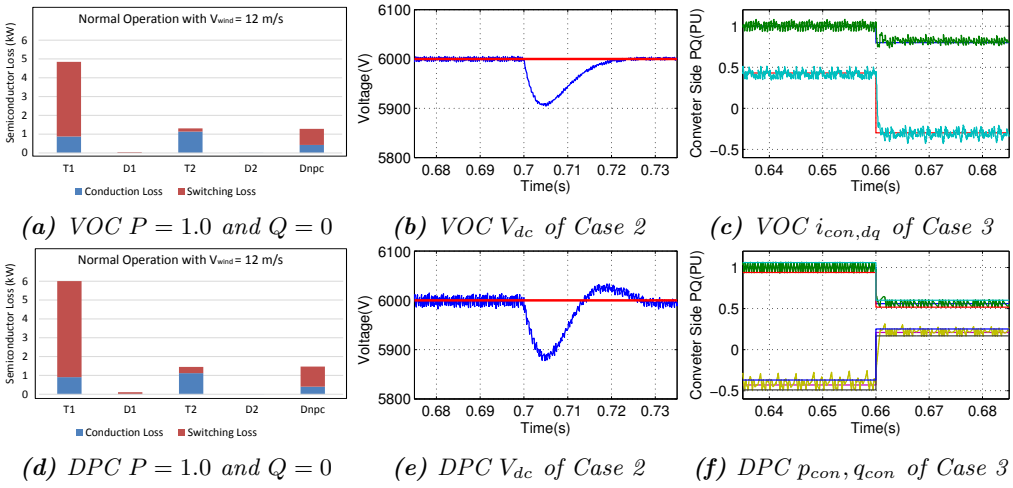

(a) VOC $P = 1.0$ and $Q = 0$ *(b) VOC V_{dc} of Case 2* *(c) VOC $i_{con,dq}$ of Case 3*

(d) DPC $P = 1.0$ and $Q = 0$ *(e) DPC V_{dc} of Case 2* *(f) DPC p_{con}, q_{con} of Case 3*

Figure 5.32: *Comparison of VOC and DPC (Simulation)*

Table 5.11: *Rising Time Comparison of DPC and VOC (Unit:ms)*

Operation Mode	Case Study	DPC		VOC	
		CS	GS	CS	GS
Abnormal	Case 3 P/d-axis	0.49	1.28	0.2	1.2
	Case 3 Q/q-axis	0.76	0.86	0.87	0.7
Normal	Case 2 DC-link Voltage	12		23	

80's. A detailed DPC control design processes including hysteresis control design and switching table development are illustrated in this chapter.

Both simulation and experiments were conducted to verify VOC and DPC methods. Since the objective of this thesis is to design a converter control for a MV application, the simulation was studied for a 5 MVA system. Experiments were conducted with a scaled-down LV test setup (10 kVA) with almost same PU values. Both simulation and experiments proved the correctness of the VOC and DPC method design.

At the end, a comparison of VOC and DPC is given. The DPC can improve the dynamic performance significantly compared to the VOC method. However, the switching frequency was not decreased for the same operation point compared to the VOC method. So in order to improve the efficiency of the power conversion system, other control methods must be investigated, which can decrease the switching frequency but keep the steady state and dynamic performance at the same time.

6 Model Predictive Direct Control

The previous chapter has presented the state-of-the-art control algorithms, VOC and DPC. An improved switching table for DPC is introduced in Chapter 5. However, it is difficult to improve the performance of the classic VOC. Model predictive control (MPC) has been used in the process industries, pulp and paper industries since 1970s, where the sampling period is long enough for the calculation of the controller [117]. However, nowadays, with the development of digital processor ability, it is possible to implement MPC for power system converter control. Therefore, MPC is emerging as an attractive control method for grid connected power converter control.

This chapter will introduce the MPC of a grid converter in the power system. First of all, section 6.1 gives the classification of MPC methods and presents the method used in this thesis. Afterwards, the single step and multiple steps prediction are investigated in section 6.2 and 6.3, respectively. In order to verify the proposed multiple steps MPC algorithm, first, a 5MVA wind turbine grid converter with medium voltage is simulated, which is shown in section 6.4. Then, experimental verification is provided in section 6.5 applying the scaled 10 kVA test bench. A comparison between the two methods for single step and multiple steps is introduced in section 6.6. At the end, a summary is given.

6.1 Benchmarking of Model Predictive Control

6.1.1 Model-based Predictive Control

Model predictive control is one of the model-based predictive methods, which consists of deadbeat control (DBC) and generalized predictive control (GPC). The common idea is to use a dynamic model to predict the controlled variables of the system, and select the optimal manipulated variables for an optimization criterion [119].

For deadbeat control, the optimization criterion is to reach the reference value at the next sampling instant by using the selected manipulated variables, e.g. the voltage vector of the voltage source converter control. Generally, a modulator is needed for deadbeat control to generate the switching signals [136]. The advantage of this method is its fast dynamic, while the disadvantage is that it is difficult to incorporate the non-linearities and constraints of the system [137].

Another well-known predictive control is the generalized predictive control, which was first introduced by Clarke [138–140]. Compared with deadbeat control, GPC belongs to the multiple steps prediction methods of model predictive control, which is also called "long-range model predictive control". During each sampling interval, a set of future control variables are generated. However, the first element is applied as manipulated variable (system input) [141]. When the system is linear and without constraints, GPC provides an explicit control method that can be easily implemented [119]. However, it will become much more complicated when considering the system constraints,

which have to be considered in practical applications.

6.1.2 Model Predictive Direct Control

Unlike DBC or GPC, MPC has a cost function as the optimization criterion, which is easily incorporated with multiple constraints. The control design is very simple and intuitive. For MPC, it can be classified according to different criteria. Table 6.1 shows the classification of model-based predictive control depending on the control principle and prediction steps. Both control schemes with and without modulator can be found, which cause either fixed or variable switching frequency. For the model-based predictive control without modulator, the name "model predictive direct control" is used, or "finite control set model predictive control (FCS-MPC)". In this case, the switching frequency is variable, which means that the spectrum of converter output voltage/current distributes in the whole frequency band. Considering the number of prediction steps, model-based predictive control can be divided into two groups, single step prediction (Np=1) and multiple steps prediction (Np>1). Here, Np is the number of prediction steps. Generally speaking, the multiple steps prediction can achieve better performance than the single step prediction. However, the calculation load increases exponentially, which is a big challenge for the digital processors.

Table 6.1: *Classification of Model-based Predictive Control*

	with modulator	without modulator
Np=1	-Dead Beat Control	-Single Step Model Predictive Direct Current Control -Single Step Model Predictive Direct Power Control
Np>1	-Generalized Predictive Control	-Multiple Steps Model Predictive Direct Current Control -Multiple Steps Model Predictive Direct Power Control

In the past decades, model predictive direct control (MPDC) has drawn much attention in the academic community. For three phase inverter control, it was first proposed in reference [118]. References [142–146] present model predictive direct current control for the power converters, while references [147–149] cover model predictive direct torque control for the induction machine control. For a grid converter with LCL filter, reference [150] proposes a cost function with constraints for a specific current

spectrum adopting model predictive direct current control, which is used to suppress resonances [151]. Reference [152] introduces model predictive direct power control for active front-end rectifiers (AFEs). The latest overview of model predictive direct control is presented in [153], where the different power converters using model predictive control are summarized, e.g. two-level, three-level neutral point clamped, or modular multilevel converter. Additionally, different control variables can be selected for different applications, e.g. current, neutral point voltage, torque, flux, active power, reactive power and switching frequency etc. The latest publications about predictive control can be found in the special section on "predictive control in power converters and electrical drives"-part I and part II [154, 155].

MPDC has developed significantly in the past decade. There are mainly two directions, single step prediction and multiple steps prediction. Mainly two representative research groups have conducted in depth research on MPDC. One is the Department of Electrical Engineering from the Universidad Técnica Federico Santa Maria in Valparaiso Chile, who has investigated a simple and powerful method to control power converters [143]. It has been applied in three-level NPC converters [144], three-level active NPC converters [156], multilevel cascaded H-bridge inverters [146], and for UPS applications [157], as well as for active and reactive control in grid-tied multilevel converter applications [158] and torque control of induction machines [148].

The second one is the Department of Information Technology and Electrical Engineering (D-ITET, Departement Informationstechnologie und Elektrotechnik) from ETH Zürich, where the well-known DPC method was developed and improved with online optimization instead of off-line switching tables [147, 149, 159, 160]. The same prediction method was adopted for direct current control for multi-level converters [161, 162]. The developed MPDC uses multiple steps prediction. The major benefit of this control method is its superior performance in terms of the switching frequency. Namely, for the same level THD, multiple steps MPDC can achieve a lower switching frequency, which is a very important point for medium voltage power converter or drives. However, with the increasing of prediction steps, the calculation effort increases exponentially. For example, for three-level neutral pointed clamped converters, there are 27 voltage vectors. If every vector is evaluated during each interval time, for three steps prediction, there will be $27^3 = 19683$ model calculations, which is not possible to finish during the normal sampling period for power control and drives (e.g., $T_s = 100\mu s$). Multiple steps model predictive direct control proposes a switching horizon for evaluation of each possible or predefined voltage vector and extrapolates the voltage vector candidates for achieving more prediction steps [159]. In section 6.3, the details of this method will be discussed.

6.2 Single Step Model Predictive Direct Current Control

The model-based predictive control of a three-phase inverter with an LCL filter was first mentioned in reference [163], in which a piecewise affine (PWA) model was used to get

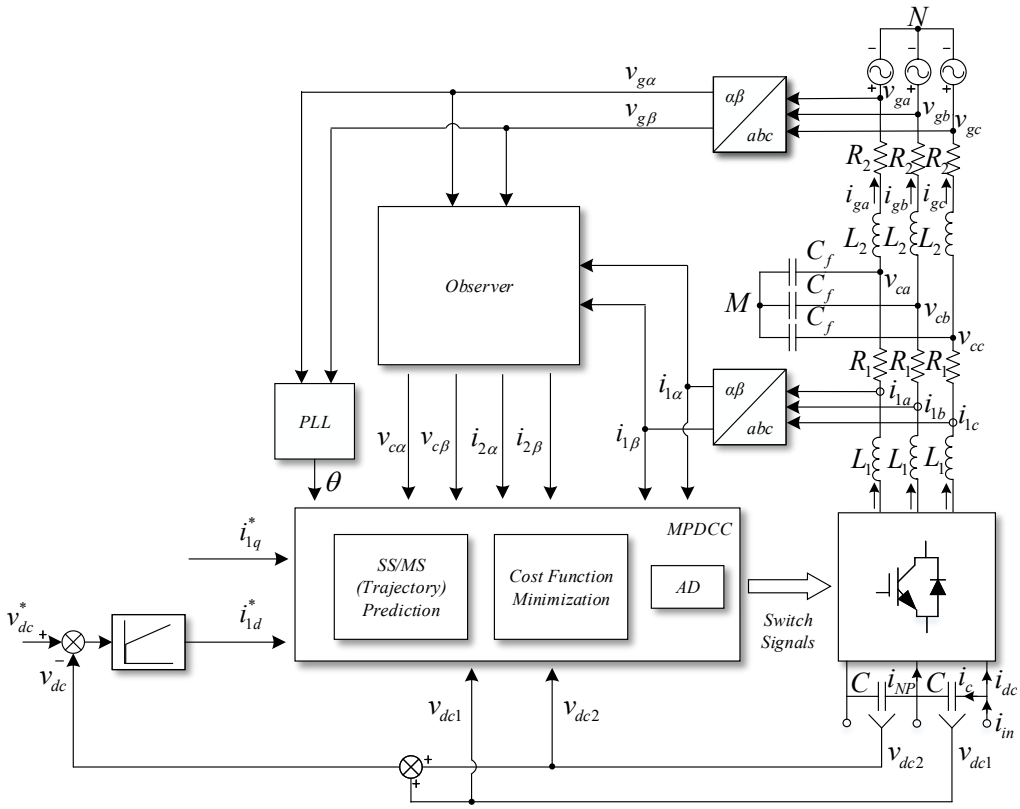

Figure 6.1: *Model Predictive Direct Current Control for Grid Converter with LCL-filter*

a more accurate prediction compared to the zero order hold model. This is not a direct method, though, since it uses PWA approximation, which is an improvement of PWM modulation. Model predictive direct control was first used to control the current of a grid connected converter with LCL filter in 2009 [151].

As discussed before, due to the LCL-filter, there are two currents that could be measured. From the point of view of converter over-current protection, it is necessary to install the current sensors on the converter side. In order to reduce the number of transducers and cost, only converter side current transducers are considered in this thesis. The system diagram of Single Step Model Predictive Direct Current Control is shown in figure 6.1. It mainly contains two loops, the outer loop voltage loop and the

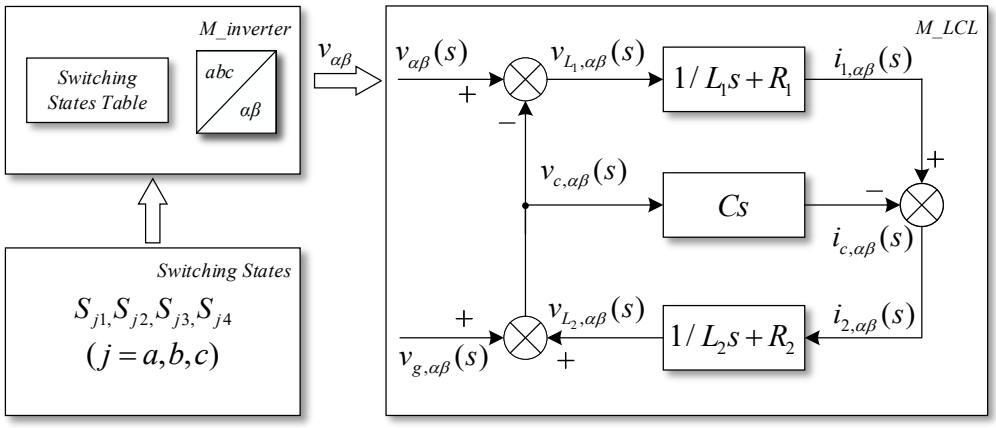

Figure 6.2: *Internal Model of the Controller*

inner loop current loop. Since active damping needs to be implemented in dq frame, the grid angle is also needed for the internal controller. Details will be discussed in the following subsections.

6.2.1 System Modelling

For model predictive control, the system model is essential and the core for prediction. It consists of modelling of the converter, LCL filter and grid. The internal model is used to predict the trajectory of the converter side current. According to the system model (equation 3.5), an internal model diagram is shown in figure 6.2. The state space representation is given in equation 6.1:

$$\begin{cases} \dot{x}(t) = Ax(t) + Bu(t) \\ y(t) = Cx(t) + Du(t) \end{cases} \tag{6.1}$$

The state variable vector is chosen as in equation 6.2, where i_1 is the converter side current, i_2 is the grid side current, v_c is the capacitor voltage, and grid voltage or point of common coupling (PCC) voltage is indicated as v_g. The subscript α and β represent the components of the $\alpha\beta$ coordinates.

$$x = \begin{bmatrix} i_{1\alpha} & i_{1\beta} & i_{2\alpha} & i_{2\beta} & v_{c\alpha} & v_{c\beta} & v_{g\alpha} & v_{g\beta} \end{bmatrix}^T \tag{6.2}$$

The input variable vector is defined in equation 6.3, where v_α and v_β represent the converter output voltage.

$$u = \begin{bmatrix} v_\alpha & v_\beta \end{bmatrix}^T \tag{6.3}$$

The output variable vector is defined as:

$$y = \begin{bmatrix} i_{1\alpha} & i_{1\beta} \end{bmatrix}^T \tag{6.4}$$

The matrices (A,B,C and D) of the system are shown in equation 6.5-6.8. The symbol indications are consistent with chapter 3.

.

$$A = \begin{vmatrix} -R_1/L_1 & 0 & 0 & 0 & -1/L_1 & 0 & 0 & 0 \\ 0 & -R_1/L_1 & 0 & 0 & 0 & -1/L_1 & 0 & 0 \\ 0 & 0 & -R_2/L_2 & 0 & 1/L_2 & 0 & -1/L_2 & 0 \\ 0 & 0 & 0 & -R_2/L_2 & 0 & 1/L_2 & 0 & -1/L_2 \\ 1/C_f & 0 & -1/C_f & 0 & 0 & 0 & 0 & 0 \\ 0 & 1/C_f & 0 & -1/C_f & 0 & 0 & 0 & 0 \\ 0 & 0 & 0 & 0 & 0 & 0 & 0 & -w_1 \\ 0 & 0 & 0 & 0 & 0 & 0 & w_1 & 0 \end{vmatrix} \tag{6.5}$$

$$B = \begin{vmatrix} 1/L_1 & 0 & 0 & 0 & 0 & 0 & 0 & 0 \\ 0 & 1/L_1 & 0 & 0 & 0 & 0 & 0 & 0 \end{vmatrix}^T \tag{6.6}$$

$$C = \begin{vmatrix} 1 & 0 & 0 & 0 & 0 & 0 & 0 & 0 \\ 0 & 1 & 0 & 0 & 0 & 0 & 0 & 0 \end{vmatrix} \tag{6.7}$$

$$D = \begin{vmatrix} 0 & 0 \\ 0 & 0 \end{vmatrix} \tag{6.8}$$

Considering the implementation of the control in the digital processor, the continuous time representation of the internal model (6.1) needs to be transferred to discrete time representation. For a linear time invariant (LTI) continuous system, e.g., $\dot{x}(t) = Ax(t) + Bu(t)$, the solution under the condition of $x(t_0)$ and $u(t)$ is [164]:

$$x(t) = \Phi(t - t_0)x(t_0) + \int_{t_0}^{t} \Phi(t - \tau)Bu(\tau)d\tau \tag{6.9}$$

Assume the sampling time is T_s, and $t_0 = kT_s$, so $x(t_0) = x(kT_s) = x(k)$. Assume $t = (k + 1)T_s$, so $x(t) = x[(k + 1)T_s] = x(k + 1)$. And during $t \in [k, k + 1]T_s$, $u(t) = u(kT_s) = constant$, the solution (equation 6.9) can be transformed to:

$$x(k + 1) = \Phi[(k + 1)T_s - kT_s]x(k) + \int_{kT_s}^{(k+1)T_s} \Phi[(k + 1)T_s - \tau]Bd\tau u(k) \tag{6.10}$$

Through some intermediate steps and substitutions, the discrete system state equation is derived [164]:

$$x(k+1) = \Phi(T_s)x(k) + \int_0^{T_s} \Phi(\tau)Bd\tau u(k) \tag{6.11}$$

where $\Phi(T_s) = e^{AT_s}$. e^{At} is the matrix exponential function. Thus

$$e^{AT_s} = I + AT_s + \frac{1}{2!}A^2T_s^2 + \frac{1}{3!}A^3T_s^3 + ... + \frac{1}{k!}A^kT_s^k = \sum_{k=0}^{\infty}\frac{1}{k!}A^kT_s^k \tag{6.12}$$

Considering a high sampling frequency ($f_s = 10kHz$) and simplification, only the first two items $I + ATs$ are used and the higher order items are neglected. Actually this is equivalent with the simple discrete forward-euler method. The discrete time representation is shown in equation 6.13. The matrices (A_d, B_d, C_d and D_d) can be calculated according to equation 6.14-6.17.

$$\begin{cases} x(k+1) = A_dx(k) + B_du(k) \\ y(k) = C_dx(k) + D_du(k) \end{cases} \tag{6.13}$$

$$A_d = I + AT_s \tag{6.14}$$

$$B_d = T_sB \tag{6.15}$$

$$C_d = C \tag{6.16}$$

$$D_d = D \tag{6.17}$$

6.2.2 Cost Function and Weighting Factor

The cost function is the evaluation criteria which is used to select the optimal voltage vector for the control objective. The objective of model predictive direct current control is to control the current tracking the given reference. The converter side current i_1 is controlled, and the cost function is expressed in orthogonal coordinates ($\alpha\beta$):

$$g = \left|i_{1\alpha}^*(k+1) - i_{1\alpha}^P(k+1)\right| + \left|i_{1\beta}^*(k+1) - i_{1\beta}^P(k+1)\right| \tag{6.18}$$

where $i_{1\alpha}^*(k+1)$ and $i_{1\beta}^*(k+1)$ are the components in $\alpha\beta$ coordinates of the converter side current reference. The $i_{1\alpha}^P(k+1)$ and $i_{1\beta}^P(k+1)$ represent the predicted converter side current, which can be achieved through the internal model(6.13). The state variables in equation 6.2 need to be measured. In order to reduce the measurement sensors and cost, an observer is necessary. It will be introduced in subsection 6.2.3. For simplicity, we can assume that the reference values at time instant $k+1$ do not change significantly

during one sampling period. Namely $i_1^*(k+1) = i_1^*(k)$ can be used for the cost function. This causes one sampling delay for the reference tracking, which will deteriorate the system performance when the system period is large. In order to achieve an accurate reference value at time instant $k+1$, the reference prediction method is introduced in subsection 6.2.4.

When the cost function consists of different controlled variables, e.g., current, voltage or switching frequency, weighting factors are necessary for balancing the importance of each variable and making them comparable among each other. For three-level NPC converters in medium voltage applications, besides the neutral point voltage balancing, the switching frequency should be kept in a low range to achieve low switching losses. So the aforementioned cost function (equation 6.18) can be improved to:

$$g = \frac{\lambda_i}{|i_1^*|^2} G_1 + \frac{\lambda_{dc}}{|v_{dc\_link}^*/2|^2} G_2 + \frac{\lambda_{sw}}{N_P} n_{sw} \tag{6.19}$$

$$G_1 = \left|i_{1\alpha}^* - i_{1\alpha}^P\right|^2 + \left|i_{1\beta}^* - i_{1\beta}^P\right|^2 \tag{6.20}$$

$$G_2 = \left|v_{dc1}^* - v_{dc1}^P\right|^2 + \left|v_{dc2}^* - v_{dc2}^P\right|^2 \tag{6.21}$$

where v_{dc1} and v_{dc2} represent the DC-link top and bottom capacitor voltage, v_{dc_link} is the total DC-link link voltage. Namely, $v_{dc\_link} = v_{dc1} + v_{dc2}$. N_P is the number of prediction steps, which means for single step prediction, $N_P = 1$, and for multiple steps prediction, $N_P > 1$. λ_i, λ_{dc} and λ_{sw} are the weighting factor of current, DC link voltage and commutation number. In order to tune the weighting factor, normalization is recommended. After the normalization, the range of each item is in the same level generally, which makes the parameter tuning more convenient.

6.2.3 Observer Design

Except for the system state variables i_1 and v_g, the state variables can not be achieved directly, and have to be acquired by an observer. In order decrease the system order of the observer and simplify the observer design, the grid voltage can be considered as disturbance $w(t)$, and system 6.1 can be written as:

$$\begin{cases} \dot{x}(t) = A_o x(t) + B_o u(t) + P_o w(t) \\ y(t) = C_o x(t) + D_o u(t) \end{cases} \tag{6.22}$$

where the system state variables do not contain the grid voltage. Then the system is modelled as:

$$A_o = \left| \begin{array}{cccccc} -R_1/L_1 & 0 & 0 & 0 & -1/L_1 & 0 \\ 0 & -R_1/L_1 & 0 & 0 & 0 & -1/L_1 \\ 0 & 0 & -R_2/L_2 & 0 & 1/L_2 & 0 \\ 0 & 0 & 0 & -R_2/L_2 & 0 & 1/L_2 \\ 1/C_f & 0 & -1/C_f & 0 & 0 & 0 \\ 0 & 1/C_f & 0 & -1/C_f & 0 & 0 \end{array} \right| \tag{6.23}$$

$$B_o = \left| \begin{array}{cccccc} 1/L_1 & 0 & 0 & 0 & 0 & 0 \\ 0 & 1/L_1 & 0 & 0 & 0 & 0 \end{array} \right|^T \tag{6.24}$$

$$P_o = \left| \begin{array}{cccccc} 0 & 0 & -1/L_2 & 0 & 0 & 0 \\ 0 & 0 & 0 & -1/L_2 & 0 & 0 \end{array} \right|^T \tag{6.25}$$

$$C_o = \left| \begin{array}{cccccc} 1 & 0 & 0 & 0 & 0 & 0 \\ 0 & 1 & 0 & 0 & 0 & 0 \end{array} \right| \tag{6.26}$$

$$D_o = \left| \begin{array}{cc} 0 & 0 \\ 0 & 0 \end{array} \right| \tag{6.27}$$

Utilizing the observability criterion, it can be obtained:

$$rank \begin{pmatrix} C_o \\ C_o A_o \\ \vdots \\ C_o A_o^5 \end{pmatrix} = 6 \tag{6.28}$$

which means that the system (6.22) is observable, and an observer can be designed as:

$$\begin{cases} \dot{\hat{x}} = A_o \hat{x} + B_o u + P_o w - L\left(\hat{y} - y\right) \\ \hat{y} = C_o \hat{x} \end{cases} \tag{6.29}$$

Equation (6.29) can be expressed further to:

$$\begin{aligned} &\dot{\hat{x}} = A_o \hat{x} + B_o u + P_o w - L\left(\hat{y} - y\right) \\ &= A_o \hat{x} + B_o u + P_o w - LC_o\left(\hat{x} - x\right) \\ &= (A_o - LC_o)\hat{x} + B_o u + P_o w + Ly \end{aligned} \tag{6.30}$$

where $(A_o - LC_o)$ is the system matrix of the observer, matrix dimension of L is 6×2. In order to guarantee the observer working correctly, under whatever the initial condition $\hat{x}(t_0)$ and $x(t_0)$ are, it is necessary to meet:

$$\lim_{x \to \infty} (\hat{x} - x) = 0 \tag{6.31}$$

Employing equation (6.22) and (6.29), the state equation of states error $x - \hat{x}$ is:

$$\begin{aligned} &\dot{x} - \dot{\hat{x}} = (A_o x + B_o u + P_o w) - [A_o \hat{x} + B_o u + P_o w - L(\hat{y} - y)] \\ &= A_o(x - \hat{x}) + LC_o(\hat{x} - x) \\ &= (A_o - LC_o)(x - \hat{x}) \end{aligned} \tag{6.32}$$

The solution of equation (6.32) is:

$$x - \hat{x} = e^{(A_o - LC_o)(t - t_0)} [x(t_0) - \hat{x}(t_0)] \tag{6.33}$$

when $x(t_0) = \hat{x}(t_0)$, then $x \equiv \hat{x}$. Since the system (6.22) is observable, there must be a matrix L, which enables eigenvalues of $(A_o - LC_o)$ in the left-half of the s-plane. So the observer system is asymptotically stable, and the states error $(x - \hat{x})$ will attenuate to zero in the steady state. The parameters of the matrix can be designed based on the zero-pole displacement method. Generally, the response of observer is three to ten times faster than the feedback system [164].

6.2.4 Current Reference Prediction

In the cost function (6.18), the future current reference at time instant $k + 1$ needs to be known. For single step prediction and high sampling frequency applications, it is possible to assume $i_1(k + 1) = i_1(k)$. However, in the application of multiple steps prediction (section 6.3), or low sampling frequency, this assumption is not accurate. For sinusoidal wave form, it is easy to estimate the future reference with the help of vectorial representation. For example, the current reference vector $\mathbf{i}^*$ can be described by its magnitude I^* and angle θ:

$$\mathbf{i}^*(k) = I^*(k) e^{j\theta(k)} \tag{6.34}$$

For a symmetrical three-phase power system and in the steady state, the angle θ at the time instant $k + 1$ can be calculated as:

$$\theta(k + 1) = \theta(k) + \omega T_s \tag{6.35}$$

where T_s is the time sampling period, and ω is the angular speed of the voltage vector. According to equation (6.34) and (6.35), and with the assumption that the magnitude keeps constant, the current reference vector i^* at time instant $k + 1$ can be calculated as:

$$\begin{aligned} &\mathbf{i}^*(k + 1) = I^*(k + 1) e^{j\theta(k+1)} \\ &= I^*(k) e^{j[\theta(k) + \omega T_s]} \\ &= \mathbf{i}^*(k) e^{j\omega T_s} \end{aligned} \tag{6.36}$$

similarly, the current reference vector I^* at time instant $k + 2$ can be calculated as:

$$\mathbf{i}^*(k + 2) = \mathbf{i}^*(k) e^{2 * j\omega T_s} \tag{6.37}$$

The calculation of the current reference at time instant $k+1$ and $k+2$ is illustrated in figure 6.3, which is only a schematic diagram. Actually for $f = 50Hz$ sinusoidal wave, when $T_s = 100\mu s$, the angle change in one step is only $\omega T_s = 1.8$ degree.

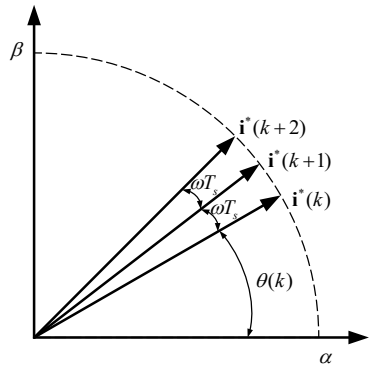

Figure 6.3: *Current Reference Prediction*

6.2.5 Time Delay Compensation

For model predictive direct control, the whole control algorithm is implemented in the digital signal processor, e.g., DSP, or FPGA. During each time interval, analog digital conversion, evaluation of the admissible voltage vectors and some other tasks need to be executed, which needs calculation time. Namely, it is not possible to apply the optimal vector at the starting point.

As shown in figure 6.4, it is supposed that the calculation time is more than 2/3 of the sampling period T_s. At the time instant t_k, the optimal voltage vector is applied, e.g., V_1. The output values at the time instant t_{k+1} are estimated, and the admissible voltage vectors at time instant t_{k+2} are evaluated. In figure 6.4, three voltage vectors are evaluated, V_1, V_2 and V_3. It is obvious that vector V_2 can achieve the least current error at time instant t_{k+2}. So V_2 is selected which will be used at the time instant t_{k+1}. Therefore at least two prediction steps are needed for model predictive direct current control with time delay compensation. In the first step, the optimal voltage selected in the previous step is applied. In the second step, the admissible voltage vectors should be evaluated and the optimal value should be selected according to the cost function [145].

6.3 Multiple Steps Model Predictive Direct Current Control

In the previous section, single step MPC is described step by step, from the basic system modelling, cost function and weighting factor design, to the necessary observer design,

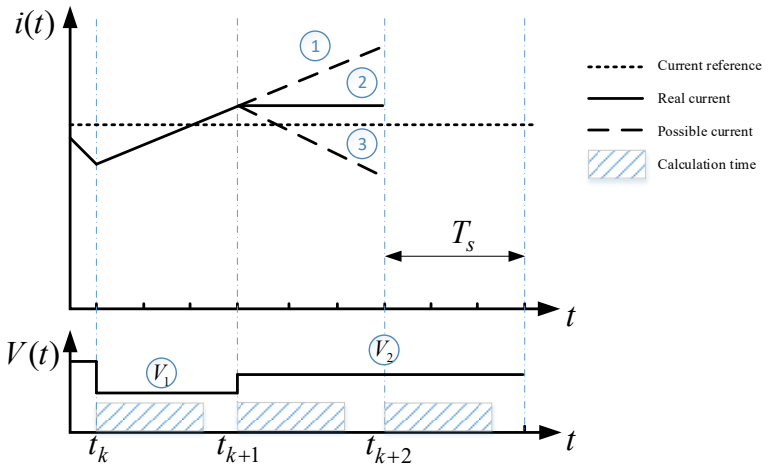

Figure 6.4: *Model Predictive Direct Current Control with Delay Compensation*

current reference prediction and time delay compensation. All these design stages are the core of the model predictive control and also the foundation of multiple steps MPC. In this section, at first, a short overview of the multiple steps MPC is given, and the challenges are discussed. Afterwards boundary control and linear extrapolation will be described. An improved method is proposed for the optimal voltage vector evaluation compared to the classical multiple steps prediction.

6.3.1 Overview and Challenges

Multiple steps MPDC was first used with direct torque control of electrical drives [159]. Later, theoretical analysis and experimental results for this method are given in reference [147, 149]. References [165, 166] present the multiple steps model predictive control for current control of electrical drives. Especially in reference [166], the multiple steps MPDC is compared with single step MPDC, SVM and optimal pulse patterns (OPP) on the steady state performance, e.g., switching frequency and THD. Using long prediction horizons, e.g., ($N = 10$), the THD of the grid current can be reduced more than 20% compared to single step prediction at the same switching frequency [166]. The transient performance is similar to single step control [166].

Undoubtedly, the computation effort for multiple step prediction is a big challenge for implementation of such a scheme. A simple solution is to increase the sampling period T_s, but this deteriorate the system performance or even to becoming unstable. Besides the predictive steps, the computation complexity also depends on the converter topology and optimization methods. Once the controlled object is decided, the topology of the converter is fixed. The only thing what we can improve is the optimization method,

which is also the core of model predictive control. From the literature [167], generally there are three strategies to keep the computation effort low, which are moving window blocking, extrapolation and the event-based horizon strategy. Extrapolation without the enumeration of all admissible voltage vectors is used in this thesis.

Multiple steps MPDC is a good alternative due to its prior switching optimization for low switching frequency in MV applications. The resonance problem of LCL filters has to be solved carefully. References [151,168,169] propose different methods to overcome the resonance problems. The overall procedure of Multiple Steps Model Predictive Direct Current Control is similar to Single Step MPDCC (figure 6.1). The only difference is that multiple steps control needs to predict several trajectories, which are used for candidate sequences selection according to the cost function.

6.3.2 Multiple Steps Control Scheme

For the single step MPDC, during every sampling interval, all the possible voltage vectors are evaluated and the optimal voltage vector is applied. This process is repeated every single step. However, for the multiple steps MPDC, during every sampling interval, the prediction should be conducted with multiple steps instead of one step. One can do the same evaluation as for a single step scheme, which means that all the possible voltage vectors are evaluated. However, it is not possible to implement this in a real digital processor unit, since the number of evaluations increases exponentially. To decrease the computation effort, linear extrapolation is adopted in this thesis. The multiple steps MPDCC scheme mainly comprises the following steps:

1. Obtain and update the state variables both from sensor measurement or observers at time instant k. Apply the previous optimal voltage vector for time delay compensation (illustrated in 6.2.5).

2. Evaluate all possible voltage vectors or predefined voltage vector matrix (shown in 6.41 and B.1) from time instant $k+1$ for N_s steps, which is the switching horizon.

3. Afterwards, one preliminary voltage vector sequence during the switching horizon is formulated, $[\mathbf{u}^i(k)\ \mathbf{u}^i(k+1)\cdots\mathbf{u}^i(k+N_s-1)]$, $i \in \boldsymbol{I}_c$. Here $\mathbf{u}(k)$ is the voltage vector at time instant k, and $\boldsymbol{I}_c$ represents all the possible voltage vector sequence set.

4. Employing boundary control (illustrated in 6.3.3), the candidate voltage vector sequence can be selected, $[\mathbf{u}^j(k)\ \mathbf{u}^j(k+1)\cdots\mathbf{u}^j(k+N_s-1)]$, $j \in \boldsymbol{J}_c \subseteq \boldsymbol{I}_c$. Here $\boldsymbol{J}_c$ represents the candidate voltage vector sequence set.

5. The candidate voltage vector sequence will be linearly extrapolated until exceeding the predefined boundary (illustrated in 6.3.4). The extrapolation horizon N_e may be different for different candidate sequences. So the expression N_e^j represents the individual extrapolation horizon for the candidate sequence j.

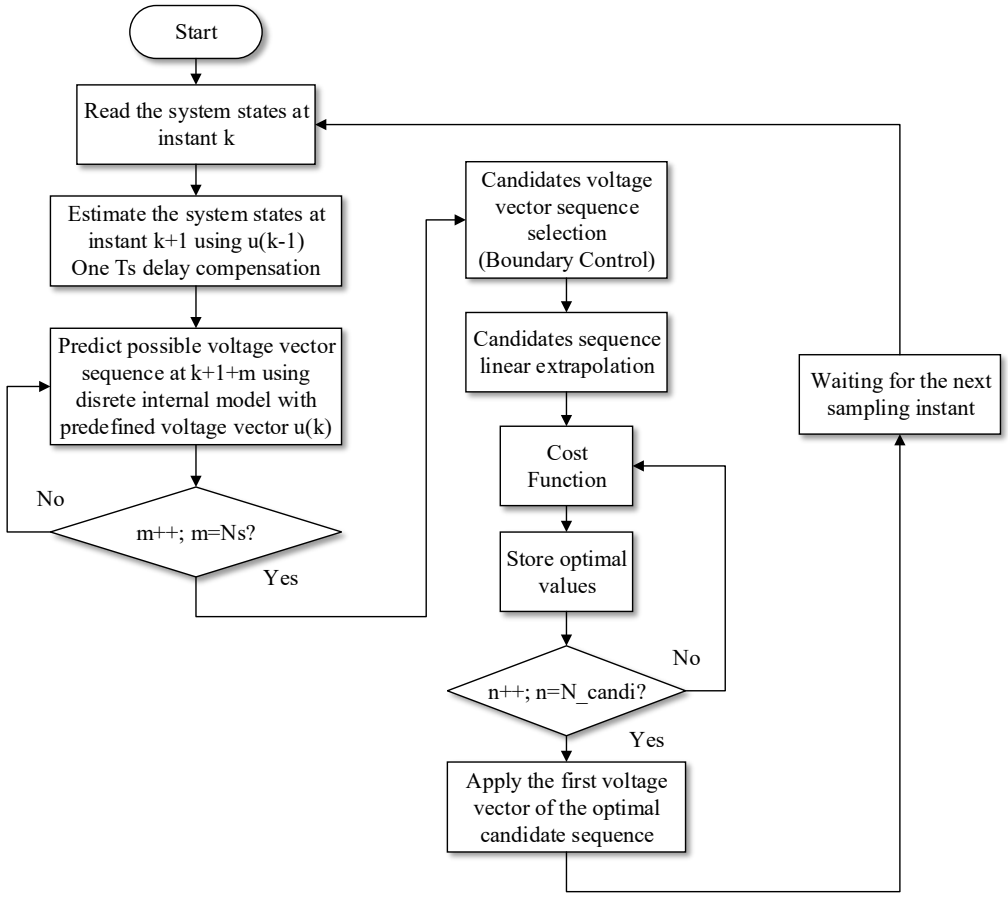

Figure 6.5: *Model Predictive Direct Current Control with Delay Compensation*

6. Finally the candidate sequence with extrapolation is achieved, which is shown in equation (6.38). Here, the final prediction horizon is $N_p = N_s + N_e$.

$$U^j(k) = [\mathbf{u}^j(k)\ \mathbf{u}^j(k+1) \dots \mathbf{u}^j(k+N_s-1) \dots \mathbf{u}^j(k+N_p^j-1)] \tag{6.38}$$

7. Employing the improved cost function (6.39), all the candidate voltage vector sequences are evaluated and the optimal voltage vector sequence, $U^{opt}(k)$ is selected. The first voltage vector $u^{opt}(k)$ is applied and step 1 is repeated. This idea is from the receding horizon control [170]. The flowchart of the controller is shown in figure 6.5, where m and n are counting variables. N_candi represents the quantity

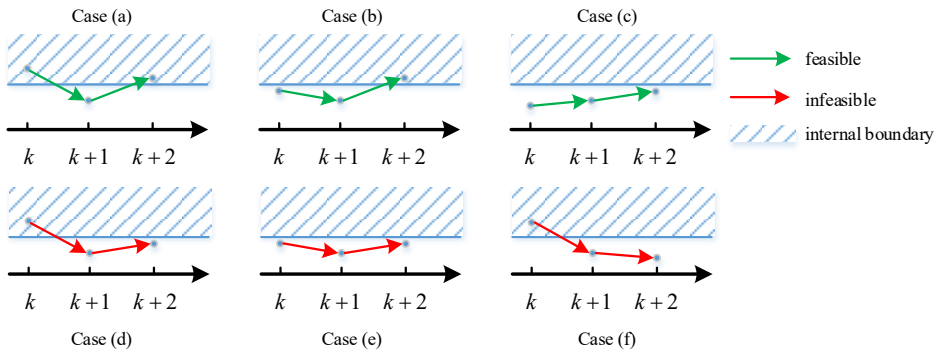

Figure 6.6: *Output Trajectory with Boundary Control for* $N_s = 2$

of candidate voltage vector sequences.

6.3.3 Boundary Control

In order to get the candidate voltage vector sequence $U^j(k)$, a feasibility selection is conducted according to the boundary, which can be implemented in all three coordinates, abc, $\alpha\beta$ or dq. For a three-phase symmetrical system, the components become constant in dq, which is easier to explain. The feasibility criteria can be divided into two types [171]:

I The predicted current at the last step of the switching horizon N_s is inside the boundary.

II The predicted current at every step of the switching horizon N_s trends towards the boundary instead of departing from the boundary.

As long as one of them is met, the voltage vector sequence can be regarded as a candidate sequence. An example with $N_s = 2$ is shown in figure 6.6. Case(a), (b) and (c) are feasible, while case (d), (e) and (f) are not. Case (a) and (b) belong to type I. No matter whether the output at the previous time instant is inside of the boundary or not, it is feasible if the output at the last step is inside of the boundary. Case (c) belongs to type II which means that case (c) trends to the boundary.

6.3.4 Linear Extrapolation

Utilizing the boundary control, the voltage vector sequence candidates can be selected, which comply with one of the two feasible types. To implement multiple steps MPDC, the linear extrapolation is adopted [171]. From the first step of the extrapolation horizon N_e, the prediction is conducted without all voltage vectors evaluations. The last

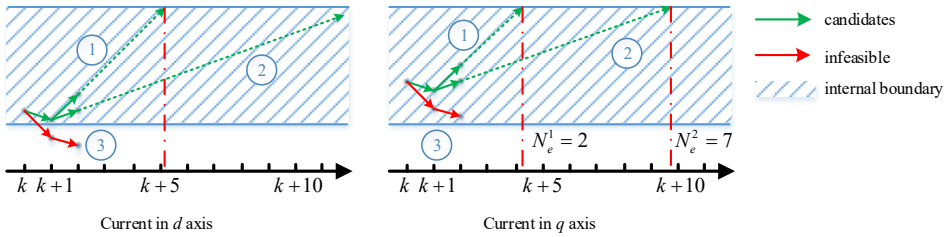

Figure 6.7: *Output Trajectory with Linear Extrapolation*

voltage vector of $[\mathbf{u}^j(k)\ \mathbf{u}^j(k+1)\cdots\mathbf{u}^j(k+N_s-1)]$ will be used to achieve the output trajectory through the internal prediction discrete model equation (6.13). This extrapolation process is repeated until the output exceeds the boundary. The extrapolation horizon N_e^j is defined as the number of prediction steps of the extrapolation process, and the superscript j indicates that the extrapolation horizon may be different with respect to different voltage sequence candidates. Figure 6.7 shows the linear extrapolation taking the example, where there are three voltage vector sequences during the switching horizon $N_s = 2$. However, only sequence 1 and 2 are candidates according to the feasibility criterion. Using the linear extrapolation, the output components are extended linearly until exceeding the boundary. It can be noticed that sequence 1 has extrapolation horizon $N_e^1 = 2$ and the sequence 2 has the extrapolation horizon $N_e^2 = 7$ respectively. Together with the switching horizon $N_s = 2$, the final prediction horizon for sequence 1 and 2 are $N_p^1 = 4$ and $N_p^2 = 9$, respectively. Since for the extrapolation steps the evaluation is not conducted, the computation effort is kept at a low level.

6.3.5 Optimal Voltage Vector Evaluation

After the boundary control and linear extrapolation, the candidate sequence is obtained. The optimal voltage sequence will be selected according to the optimization criteria. The improved cost function with current error consideration is proposed for robustness enhancement. The cost function is shown again below:

$$\begin{aligned} g^j = \lambda_{sw} \cdot \tfrac{1}{N_s} \sum_{n=1}^{N_s} ||\mathbf{u}^j(k+n) - \mathbf{u}^j(k+n-1)||_1 + \\ \lambda_i \cdot \tfrac{1}{N_p^j} \sum_{n=1}^{N_p^j} [(|i^{j*}(k+n) - i^{jp}(k+n)|^2)/I_b^2] + \\ \lambda_{npp} \cdot \tfrac{1}{N_p^j} \sum_{n=1}^{N_p^j} (|v_{npp}(k+n)|^2/V_b^2) \end{aligned} \tag{6.39}$$

where

λ_{sw}	:	weighting factors for switch commutation.
λ_i	:	weighting factors for current track error.
λ_{npp}	:	weighting factors for neutral point potential.
N_p^j	:	prediction steps of candidate sequence j.
N_s	:	switching horizon.
$\|\mathbf{u}\|_1$	:	1-norm of vector $\mathbf{u}$.
v_{npp}	:	neutral point potential defined as $(vdc2 - vdc1)/2$

The adjustable parameters in the cost function are three weighting factors. When the weighting factor λ_i, $\lambda_{npp} = 0$ and taking the example in figure 6.7, the optimization analysis is shown in table 6.2. Without the extrapolation, there are only 2 switching steps and the corresponding cost expressions would have been 0.5 and 1. So the controller would have selected $U^1(k)$ with index $i = 1$. While with the extrapolation, the cost $g^1 = 1/4$ and $g^2 = 2/9$, the voltage sequence $U^2(k)$ would have been selected. From the long time perspective, $U^2(k)$ is superior to $U^1(k)$ with respect to the switching frequency. Actually this is the reason why multiple steps prediction has the advantage of keeping the switching frequency at a low level with acceptable total harmonics distortion.

Table 6.2: *Evaluation with Cost Function*

Index i	Prediction Steps N_p^i	Switching transition N_c	Cost g^i
1	4	1	1/4
2	9	2	2/9
3	-	-	-

6.4 Multiple Steps MPDCC Simulation Results

To verify the proposed multiple steps model predictive direct current control, the medium voltage 5 MVA system from chapter 5 is simulated. The system parameters are given in table 5.5.

In order to decrease the computation effort, the admissible voltage vectors to be evaluated are optimized instead of evaluating 27 voltage vectors every step. The predefined switching transition is shown in the matrix 6.41. The second column $\begin{bmatrix} 0 & 1 & \cdots & 26 \end{bmatrix}^T$ represents the optimal voltage vector number at the last time instant. The first column number represents the valid elements of the present row, which is the quantity of the admissible voltage vector plus one.

The remaining columns are the possible voltage vectors. Take the first row as an example:

$$M_{sc}(1,:) = [\ 13 \quad 0 \quad 3 \quad 5 \quad 7 \quad 9 \quad 11 \quad 13 \quad 16 \quad 18 \quad 20 \quad 22 \quad 24 \quad 26\ ] \tag{6.40}$$

where "0" represents the optimal voltage vector is V_0, and the possible voltage vectors for evaluation are $V_3, V_5, V_7, V_9, V_{11}, V_{13}, V_{16}, V_{18}, V_{20}, V_{22}, V_{24}, V_{26}$, which are 12 vectors all together. The three-level voltage vector numbering is shown in figure 6.8. The number "13" means there are only 13 elements valid. In the row sixteen, there are only five voltage vectors $V_4, V_5, V_{13}, V_{16}, V_{26}$, which need to be evaluated if the $V_{k-1} = 15$. So row sixteen has only 6 valid elements. The other elements "0" are invalid. Employing this matrix, the maximum evaluation steps for $N_s = 2$ is 121 instead of $27^2 = 729$, which saves a lot of computation effort.

$$M_{sc} = \left|\begin{array}{cc|cccccccccccc|}
13 & 0 & 3 & 5 & 7 & 9 & 11 & 13 & 16 & 18 & 20 & 22 & 24 & 26 \\
4 & 1 & 4 & 8 & 12 & 0 & 0 & 0 & 0 & 0 & 0 & 0 & 0 & 0 \\
4 & 2 & 6 & 10 & 14 & 0 & 0 & 0 & 0 & 0 & 0 & 0 & 0 & 0 \\
10 & 3 & 0 & 5 & 6 & 13 & 14 & 16 & 17 & 25 & 26 & 0 & 0 & 0 \\
7 & 4 & 1 & 5 & 13 & 15 & 16 & 26 & 0 & 0 & 0 & 0 & 0 & 0 \\
10 & 5 & 0 & 3 & 4 & 7 & 8 & 15 & 16 & 18 & 19 & 0 & 0 & 0 \\
7 & 6 & 2 & 3 & 7 & 16 & 17 & 18 & 0 & 0 & 0 & 0 & 0 & 0 \\
10 & 7 & 0 & 5 & 6 & 9 & 10 & 17 & 18 & 20 & 21 & 0 & 0 & 0 \\
7 & 8 & 1 & 5 & 9 & 18 & 19 & 20 & 0 & 0 & 0 & 0 & 0 & 0 \\
10 & 9 & 0 & 7 & 8 & 11 & 12 & 19 & 20 & 22 & 23 & 0 & 0 & 0 \\
7 & 10 & 2 & 7 & 11 & 20 & 21 & 22 & 0 & 0 & 0 & 0 & 0 & 0 \\
10 & 11 & 0 & 9 & 10 & 13 & 14 & 21 & 22 & 24 & 25 & 0 & 0 & 0 \\
7 & 12 & 1 & 9 & 13 & 22 & 23 & 24 & 0 & 0 & 0 & 0 & 0 & 0 \\
10 & 13 & 0 & 3 & 4 & 11 & 12 & 15 & 23 & 24 & 26 & 0 & 0 & 0 \\
7 & 14 & 2 & 3 & 11 & 24 & 25 & 26 & 0 & 0 & 0 & 0 & 0 & 0 \\
6 & 15 & 4 & 5 & 13 & 16 & 26 & 0 & 0 & 0 & 0 & 0 & 0 & 0 \\
8 & 16 & 0 & 3 & 4 & 5 & 6 & 15 & 17 & 0 & 0 & 0 & 0 & 0 \\
6 & 17 & 3 & 6 & 7 & 16 & 18 & 0 & 0 & 0 & 0 & 0 & 0 & 0 \\
8 & 18 & 0 & 5 & 6 & 7 & 8 & 17 & 19 & 0 & 0 & 0 & 0 & 0 \\
6 & 19 & 5 & 8 & 9 & 18 & 20 & 0 & 0 & 0 & 0 & 0 & 0 & 0 \\
8 & 20 & 0 & 7 & 8 & 9 & 10 & 19 & 21 & 0 & 0 & 0 & 0 & 0 \\
6 & 21 & 7 & 10 & 11 & 20 & 22 & 0 & 0 & 0 & 0 & 0 & 0 & 0 \\
8 & 22 & 0 & 9 & 10 & 11 & 12 & 21 & 23 & 0 & 0 & 0 & 0 & 0 \\
6 & 23 & 9 & 12 & 13 & 22 & 24 & 0 & 0 & 0 & 0 & 0 & 0 & 0 \\
8 & 24 & 0 & 11 & 12 & 13 & 14 & 23 & 25 & 0 & 0 & 0 & 0 & 0 \\
6 & 25 & 3 & 11 & 14 & 24 & 26 & 0 & 0 & 0 & 0 & 0 & 0 & 0 \\
8 & 26 & 0 & 3 & 4 & 13 & 14 & 15 & 25 & 0 & 0 & 0 & 0 & 0
\end{array}\right| \tag{6.41}$$

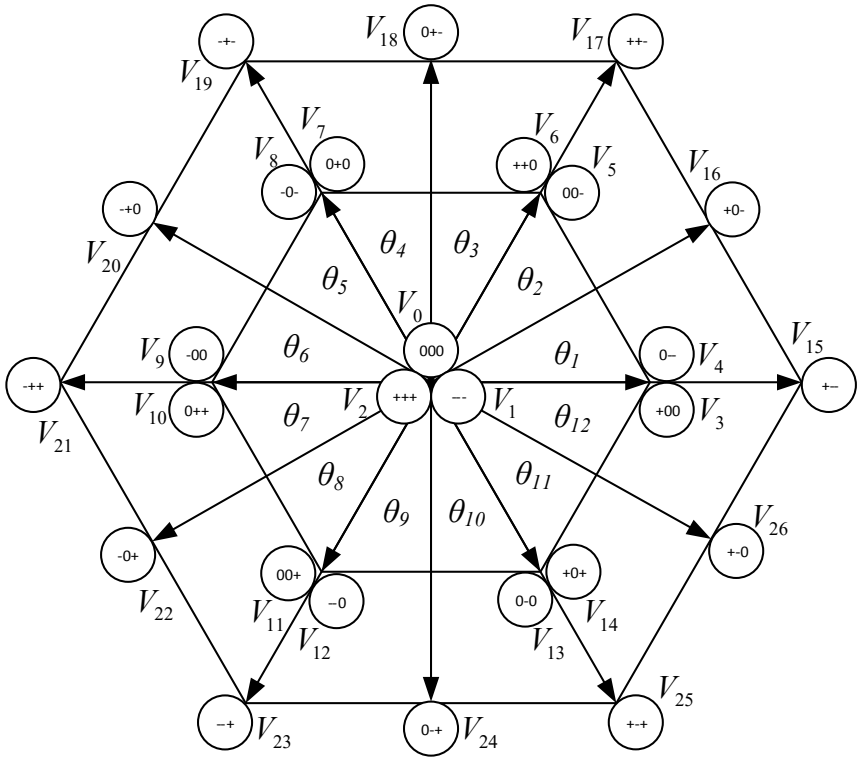

Figure 6.8: *Three-level Voltage Vector Numbering*

6.4.1 Performance under Normal Operation

For normal operation and the steady state performance verification, the nominal operation point is selected at first. Considering hardware limitations, $N_s = 2$ is selected to test the function of the proposed control strategy. In order to understand the principle of the scheme, three types of control strategy variants are discussed in the following. For this purpose, two constant dc voltage sources and ideal grid voltage are assumed.

1. Strategy with boundary control and linear extrapolation

   In figure 6.9, the simulation results of multiple steps MPDCC are presented. The grid voltage is a pure sinusoidal wave without any low order harmonics. Figure 6.9b shows the converter side current. Using the FFT analysis, figure 6.9c shows that there are some harmonics around the frequency at 1 kHz, most amplitudes are below 4%. Considering the grid code IEEE 519-1992 [172], the converter side current THD obviously exceeds the 5% current distortion limit. Employing the LCL filter, the grid

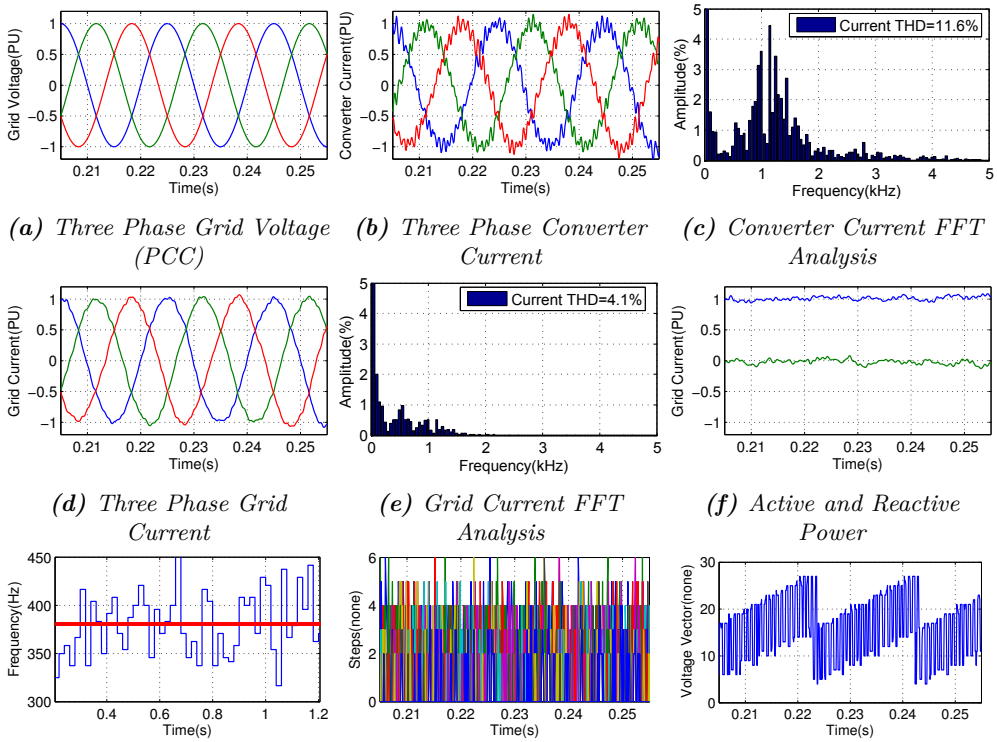

(a) *Three Phase Grid Voltage (PCC)*

(b) *Three Phase Converter Current*

(c) *Converter Current FFT Analysis*

(d) *Three Phase Grid Current*

(e) *Grid Current FFT Analysis*

(f) *Active and Reactive Power*

(g) *Average Switching Frequency*

(h) *Prediction Horizon* $N_p = N_s + N_e$

(i) *Selected Optimal Voltage Vector*

Figure 6.9: *Multiple Steps MPDCC at Nominal Operation Point*

current is shown in figure 6.9d, which is smoother than converter side current. Most high order harmonics are greatly attenuated. Figure 6.9e shows the grid side current FFT analysis, which complies with the requirements of the grid code. The THD of the grid side current is around 4.1% with the average switching frequency 380.65 Hz, figure 6.9g. The big advantage of multiple steps MPDCC is that an acceptable current quality can be achieved with a very low switching frequency. Figure 6.9f shows the active and reactive power injected into the grid. For the nominal case, active power 5 MVA, and reactive power 0 var is verified. From the figure 6.9h, it can be found that the prediction horizon is extended up to six steps. Since the switching horizon is fixed, $N_s = 2$, the extrapolation horizon N_e is up to 4. The optimal voltage vector selected during the displayed simulation time is shown in figure 6.9i.

2. Strategy without boundary control[2]

   In order to observe the function of the boundary control, the control strategy without boundary control is verified. The simulation results are shown in figure 6.10. The average frequency decreased to 348.23 Hz. Correspondingly the grid current harmonics increased slightly. The THD of the grid current is 4.5%. The quantity of feasible voltage vector sequence candidates is shown in figure 6.10g, which is significantly increased to the range of 49 to 85, while the candidates quantity of the original control strategy with boundary control is up to about 20 (figure 6.10h). Namely, the calculation effort for the extrapolation strategy is four times larger than for the control strategy with boundary control. So the boundary control function helps to save computation effort in general.

3. Strategy without linear extrapolation

   To understand the function of the extrapolation method, the results without linear extrapolation are shown in figure 6.11. The prediction horizon N_p is fixed to two (figure 6.11f), which contains only the switching horizon N_s, since the extrapolation horizon N_e is zero. It can be noted that the average frequency increases to 497.75 Hz. Correspondingly, the THD of the grid current decreases to 3.8%. Therefore, the linear extrapolation concept can help decreasing the average switching frequency, which is also consistent with the original idea of using extrapolation.

From the above discussion, it can be concluded that boundary control and linear extrapolation are the two main core parts of multiple steps MPDCC strategy. Without the boundary control, the quantity of voltage vector sequences needed to be extrapolated will increase significantly, which increases the calculation effort. Without the extrapolation, keeping the other conditions and parameters unchanged, the average frequency will obviously increase which causes higher losses of the converter.

Steady State Steady state case 1 discussed in subsection 5.4.1 is simulated using MS-MPDCC. The results are shown in figure 6.12 and figure 6.13. The converter side current is shown in figure 6.12b and its FFT analysis in figure 6.12c. Like the DPC method, the harmonics distribution has no characteristic spectrum since there is no modulator. The average frequency is about 427 Hz, see figure 6.12g. Employing the LCL filter, the grid side current is smoother than the converter side current (figure 6.12d). It can be found that the grid current has some low harmonics due to the low switching frequency or resonance issue. However, the harmonic components and the THD (3.8%) are well below the grid code requirement. The well controlled grid side active and reactive power are shown in figure 6.12f. Figure 6.12h shows the prediction

[2]It should be noted that the boundary control for extrapolation is still used to calculate the extrapolation horizon N_e.

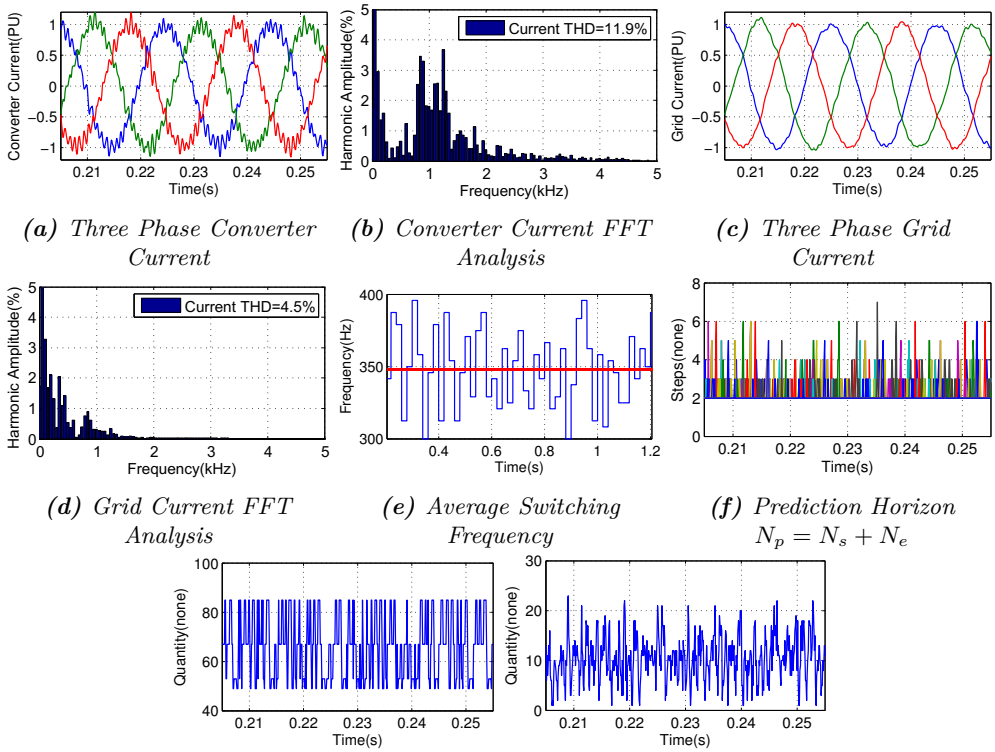

(a) Three Phase Converter Current

(b) Converter Current FFT Analysis

(c) Three Phase Grid Current

(d) Grid Current FFT Analysis

(e) Average Switching Frequency

(f) Prediction Horizon $N_p = N_s + N_e$

(g) Candidates Quantity without Boundary

(h) Candidates Quantity with Boundary

Figure 6.10: *Multiple Steps MPDCC without Boundary Control*

horizon, which has the maximum of 8 steps. With the grid voltage angle rotating, the optimal vector (6.12i) for every control step is also repeated periodically.

The voltage loop results are presented in figure 6.13. Compared to the DPC voltage control (figure 5.19), the MS-MPDCC method can achieve a better neutral voltage balancing with a lower switching frequency.

Transient In order to test the dynamic performance of the MS-MPDCC and for comparison with DPC and VOC, the same case 2, in which active power reference drops to 0.5 PU and reactive power keeps zero, is analysed. The results of the MS-MPDCC are shown in figure 6.14. Since the converter side current is controlled directly, it is necessary to verify the tracking performance. Therefore, the converter side current in abc and dq frame are shown in figure 6.14a and figure 6.14c respectively. It can be

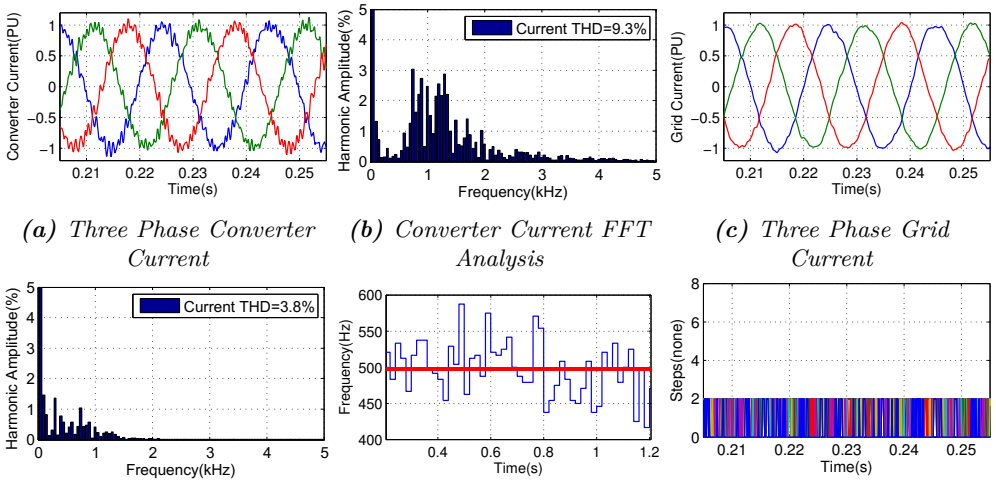

(a) Three Phase Converter Current

(b) Converter Current FFT Analysis

(c) Three Phase Grid Current

(d) Grid Current FFT Analysis

(e) Average Switching Frequency

(f) Prediction Horizon $N_p = N_s + N_e$

Figure 6.11: *Multiple Steps MPDCC without Linear Extrapolation*

noted that the current is regulated very well and the d- and q-axis component are decoupled. The three-phase grid current (figure 6.14b) has more harmonics in this new operation point. However, the total current harmonic distortion (TCH) is around 4.3% according to IEC-61400-21. It is also found that the average switching frequency for the new operation point is around 378 Hz. The grid current can be improved with variable active damping resistor. The active power and reactive power injected to the grid are shown in figure 6.14d. The rising time for active power is about 3.5 ms. The active power drop to 0.5 PU at 0.7 s, causes a voltage drop in the DC-link voltage (figure 6.14e). The DC-link voltage returns to the nominal value (6000 V) quickly. The rising time of the DC-link is about 14.6 ms and there is around 1.5% undershoot. The upper and lower capacitor voltages are shown in figure 6.14f. For a very short time the voltages are outside of the boundary which is acceptable.

6.4.2 Performance under Abnormal Operation

LVRT operation, case 3 and case 4 described in subsection 5.4.1 are adopted for MS-MPDCC verification. First, case 3, three-phase grid voltage drops to 0.7 PU at 0.66 s is shown in figure 6.15. The converter current amplitude after grid voltage drop has a slow response till recovering to the nominal value, which also causes the same response of the grid side current. Analysing the converter side current in dq frame, it can be found that the d-axis component has slow dynamics, while the q-axis reacts quickly.

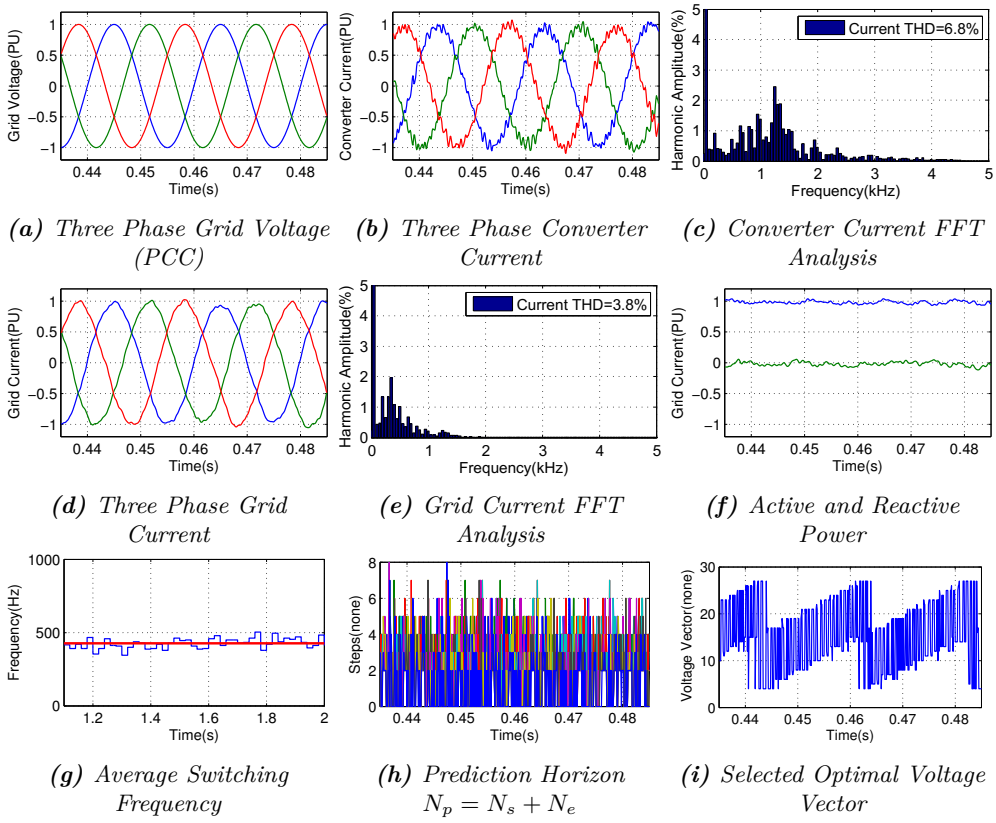

(a) Three Phase Grid Voltage (PCC) *(b) Three Phase Converter Current* *(c) Converter Current FFT Analysis*

(d) Three Phase Grid Current *(e) Grid Current FFT Analysis* *(f) Active and Reactive Power*

(g) Average Switching Frequency *(h) Prediction Horizon $N_p = N_s + N_e$* *(i) Selected Optimal Voltage Vector*

Figure 6.12: *MS-MPDCC at Nominal Operation with Voltage Loop*

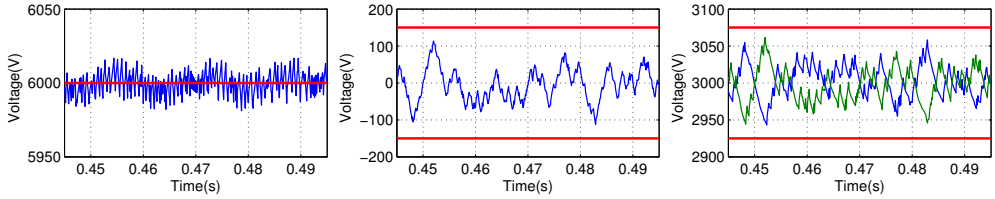

(a) DC-link Voltage *(b) $v_{dc1} - v_{dc2}$* *(c) v_{dc1} and v_{dc2}*

Figure 6.13: *DC-link Voltage Performance of MS-MPDCC at Nominal Operation*

The falling times for both components are around 27 ms and 1.3 ms respectively. The reason for this phenomenon is that the grid voltage drop causes a jump of the d-axis

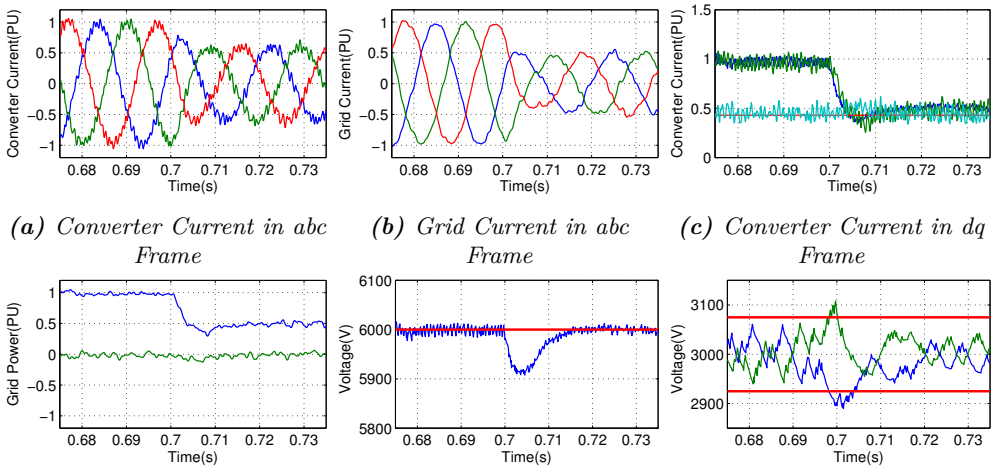

(a) *Converter Current in abc Frame*

(b) *Grid Current in abc Frame*

(c) *Converter Current in dq Frame*

(d) *Active and Reactive Power*

(e) *Vdc Tracking*

(f) *Capacitor Voltage v_{dc1} and v_{dc2}*

Figure 6.14: *MS-MPDCC Case 2 Active Power Drops to* 0.5 PU *and Reactive Power Is Zero*

component of the filter capacitor voltage v_{cd}. Since the active damping is implemented by a high-pass filter to extract the high frequency components of v_{cd} and v_{cq}, this step is also extracted and makes a huge damping voltage, which is shown in figure 6.15f. It can be noted that the damping voltage extracted from v_c stays in the range of $\pm 100\,\mathrm{V}$. However, when the grid voltage dip happens, the d-axis component of damping voltage reaches $-1000\,\mathrm{V}$, which will generate a huge damping current (equation 4.21). Due to the high-pass filter, it will take some time for recovery. This can be solved by adding a saturation, the results are shown in figure 6.16. The prediction horizon and average frequency are shown in figure 6.15g and 6.15h. The prediction horizon becomes larger than in normal operation while the average frequency (461 Hz) keeps the same level.

Figure 6.16 shows the results of case 3 with an active damping current limitation. It can be found that the d-axis component of the active damping voltage is limited to $-300\,\mathrm{V}$. The three-phase converter and grid current are well controlled. The d-axis component of the converter side current reaction is much faster than before. The rising time of d- and q-axis components are around 3.2 ms and 1.2 ms. The rising time of the grid side active and reactive power, are around 5.1 ms and 0.9 ms, which shows the good tracking performance.

Case 4, three-phase grid voltage drops to 0.5 PU, is also simulated. The results are shown in figure 6.17. It can be seen that the grid voltage drops to 0.5 PU at 0.76 s. The converter side current is well regulated, both d- and q-axis components have fast

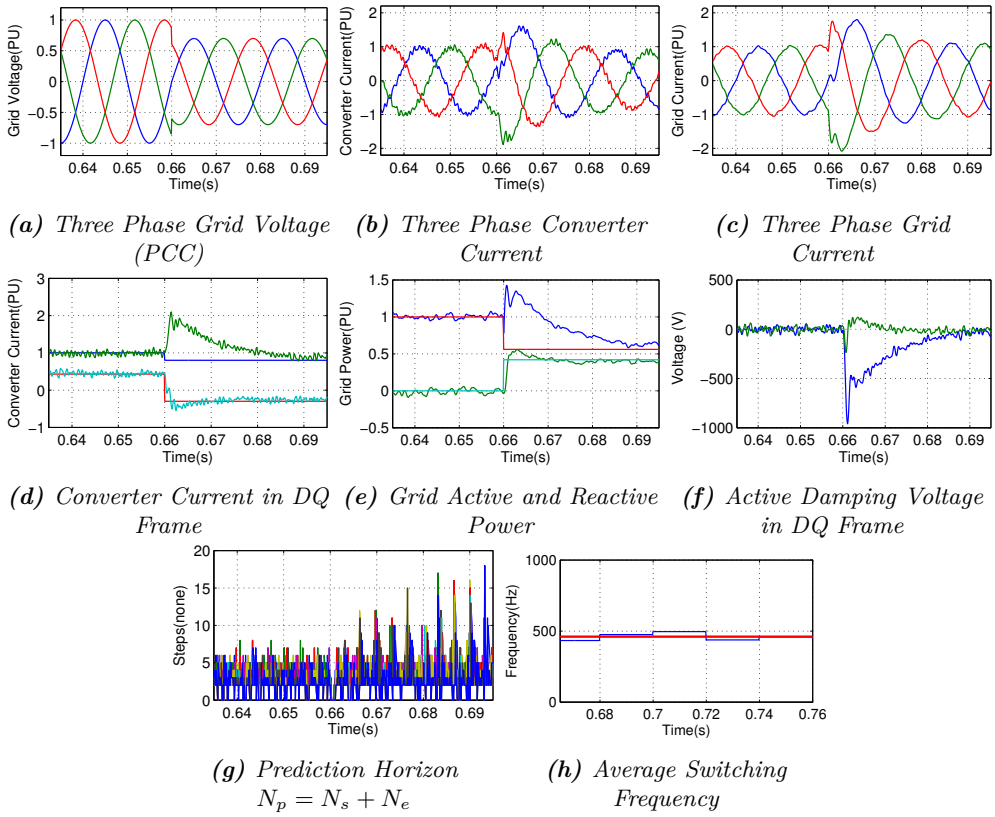

(a) *Three Phase Grid Voltage (PCC)*

(b) *Three Phase Converter Current*

(c) *Three Phase Grid Current*

(d) *Converter Current in DQ Frame*

(e) *Grid Active and Reactive Power*

(f) *Active Damping Voltage in DQ Frame*

(g) *Prediction Horizon* $N_p = N_s + N_e$

(h) *Average Switching Frequency*

Figure 6.15: *MS-MPDCC Case 3 Three-phase Grid Voltage Drops to* 0.7 PU

dynamic performance. The rising times are 2.2 ms and 1.4 ms. The grid side active and reactive power tracking is shown in figure 6.17e. The active power injected to the grid is zero while the reactive power is 0.5 PU. Actually the reactive current is 1.0 PU. The rising time for both active and reactive power are 2 ms and 1.1 ms, respectively. During the LVRT case 4, the average switching frequency is around 408 Hz.

6.4.3 Thermal Analysis

Similar to DPC and VOC, a thermal analysis is conducted for the MS-MPDCC method. The loss analysis during different operation points is shown in figure 6.18. There are four operation points, i.e., wind speed $12\,\mathrm{m\,s^{-1}}$, $10\,\mathrm{m\,s^{-1}}$, $8\,\mathrm{m\,s^{-1}}$, and LVRT with 0.3 PU voltage dip. Compared to DPC (figure 5.24) and VOC (figure 5.13), MS-MPDCC has the lowest switching losses considering the same operation point and same type of semi-

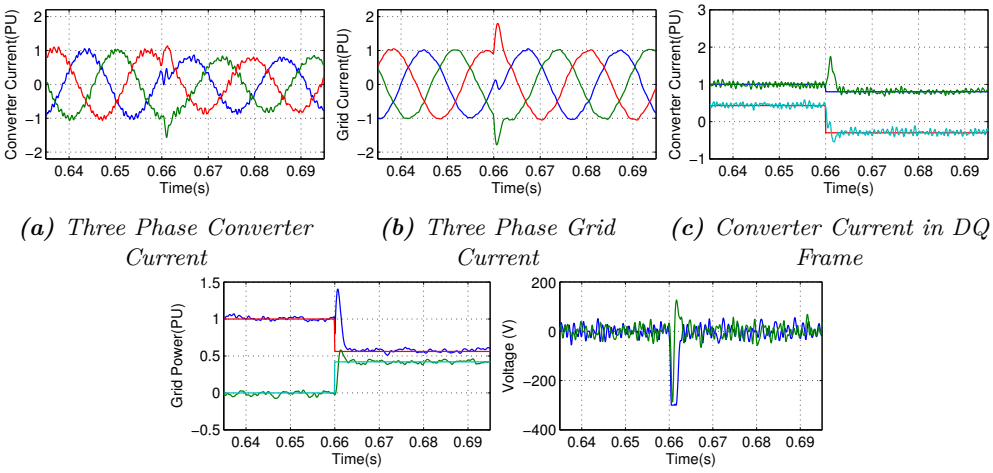

(a) *Three Phase Converter Current*

(b) *Three Phase Grid Current*

(c) *Converter Current in DQ Frame*

(d) *Grid Active and Reactive Power*

(e) *Active Damping Voltage in DQ Frame*

Figure 6.16: *MS-MPDCC Case 3 Three-phase grid voltage drops to* 0.7 PU *with Active Damping Current Limitation*

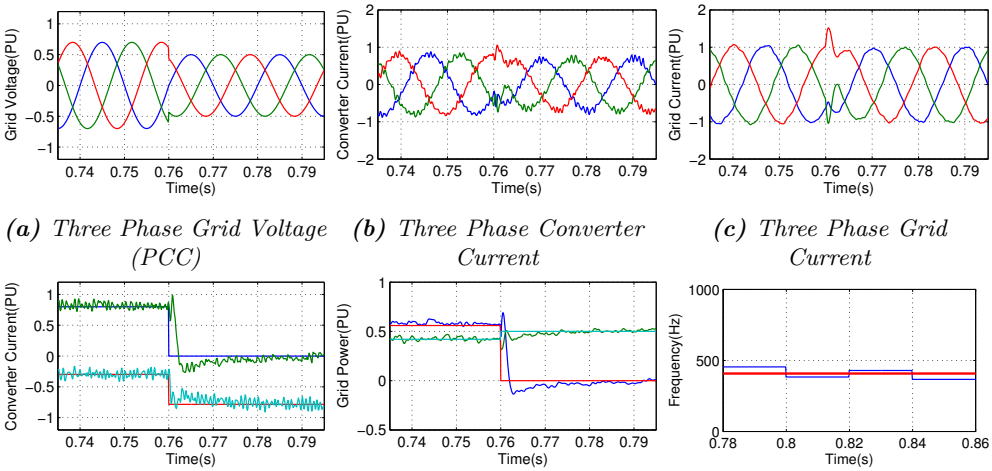

(a) *Three Phase Grid Voltage (PCC)*

(b) *Three Phase Converter Current*

(c) *Three Phase Grid Current*

(d) *Converter Current in DQ Frame*

(e) *Grid Active and Reactive Power*

(f) *Average Switching Frequency*

Figure 6.17: *MS-MPDCC Case 4 Three-phase Grid Voltage Drops to* 0.5 PU

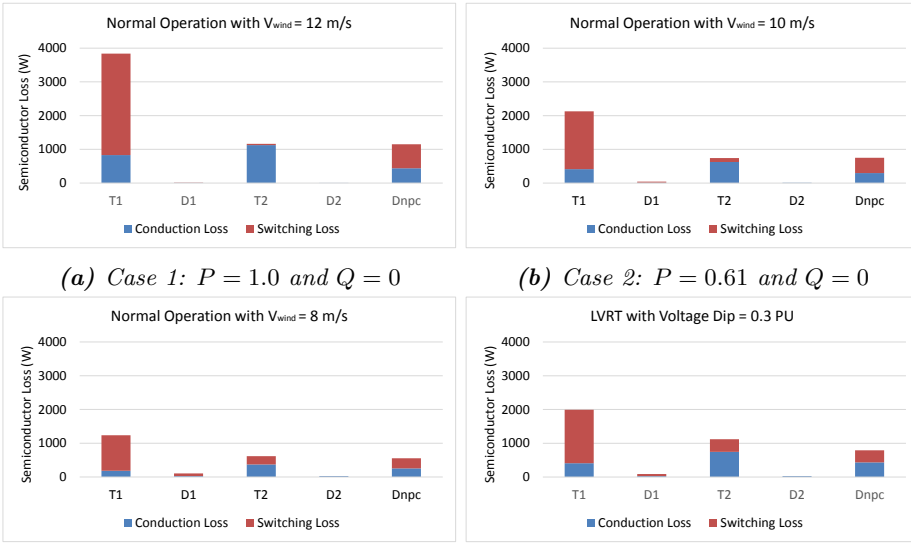

(a) Case 1: $P = 1.0$ and $Q = 0$

(b) Case 2: $P = 0.61$ and $Q = 0$

(c) Case 3: $P = 0.31$ and $Q = 0$

(d) Case 4: $P = 0.56$ and $Q = 0.42$

Figure 6.18: *Losses Analysis at Different Operation Points with MS-MPCDCC*

conductors. For example, for the nominal operation point, $P = 1.0$ and $Q = 0$, the switching losses of outer switch T_1 for DPC, VOC and MS-MPDCC are around 6 kW, 5 kW and 4 kW respectively. For inner switch T_2 and neutral diode D_{npc} the same relations can be found. The total switching losses of case 1 for these three methods are 39.62 kW, 30.26 kW and 22.60 kW, respectively. The total conduction losses remain almost the same for the same operation point, which are 14.66 kW, 14.67 kW and 14.38 kW, respectively. The data are summarized in table 6.3. Compared to the state of art VOC, the MS-MPDCC can improve the power converter efficiency up to 0.14%, which may lead to a profit for the whole wind farm.

Table 6.3: *DPC, VOC and MS-MPDCC Comparison for Nominal Operation Point*

Method	$f_{\overline{SW}}$ (Hz)	THD (%)	P_{CL} (kW)	P_{SL} (kW)	P_{loss} (kW)	η (%)
DPC	812	3.70	14.66	39.62	54.28	98.91
VOC	617	3.50	14.64	29.32	43.96	99.12
MS-MPDCC	439	3.60	14.38	22.60	36.98	99.26

However, it can be noted that the uneven losses distribution still exists, i.e., MS-

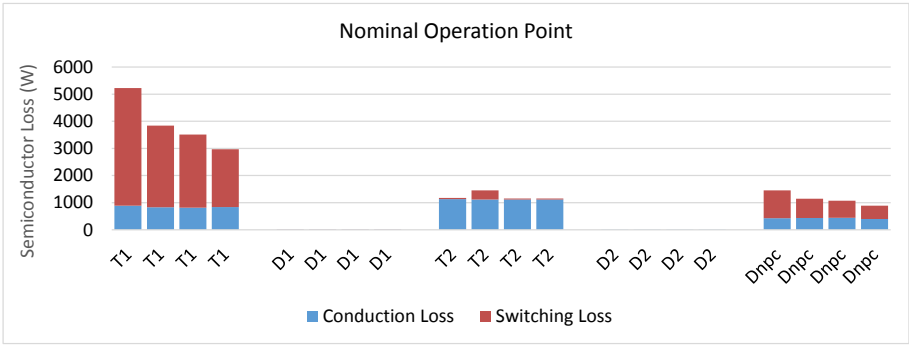

Figure 6.19: *Loss Distribution at Different Control Parameters and Nominal Operation Point with MS-MPDCC*

MPDCC method does not improve the unbalances. Also, the LVRT operation does not differ visibly compared to DPC or VOC. For different control parameters, variations of the switching weighting factor and the boundaries, the loss distribution at nominal operation point with MS-MPDCC is shown in figure 6.19. It can be found that most switching losses are generated by the outer switch and neutral point diode. Employing new generation semiconductors just for these two types of devices in three-level NPC converter might be an alternative solution for balancing the losses and improving the system efficiency. The four cases with different control parameters are shown in table 6.4. With the increasing of the weighting factor λ_{sw}, the average switching frequency decreases. The corresponding average junction temperature of each semiconductor type for the four operation points according to figure 6.18 are shown in figure 6.20. Compared to DPC (figure 5.26) and VOC (figure 5.14), MS-MPDCC has the lowest temperature considering the same operation point and same type of semiconductor. For example, for the nominal operation point, the average junction temperature of outer switch T_1 for these three control method are around 95℃, 85℃and 75℃respectively. The same relation can be found for the other semiconductors.

Table 6.4: *MS-MPDCC Performance with different Control Parameters*

Boundary (PU)	λ_{sw}	λ_i	λ_{npp}	$f_{\overline{SW}}$ (Hz)	THD (%)	P_{loss} (kW)	η (%)
0.20	0.03	0.62	0.35	593	2.61	47.20	99.06
0.20	0.13	0.72	0.15	439	3.60	36.98	98.26
0.20	0.15	0.70	0.15	390	4.3	34.47	99.31
0.22	0.40	0.45	0.15	338	4.6	30.13	99.40

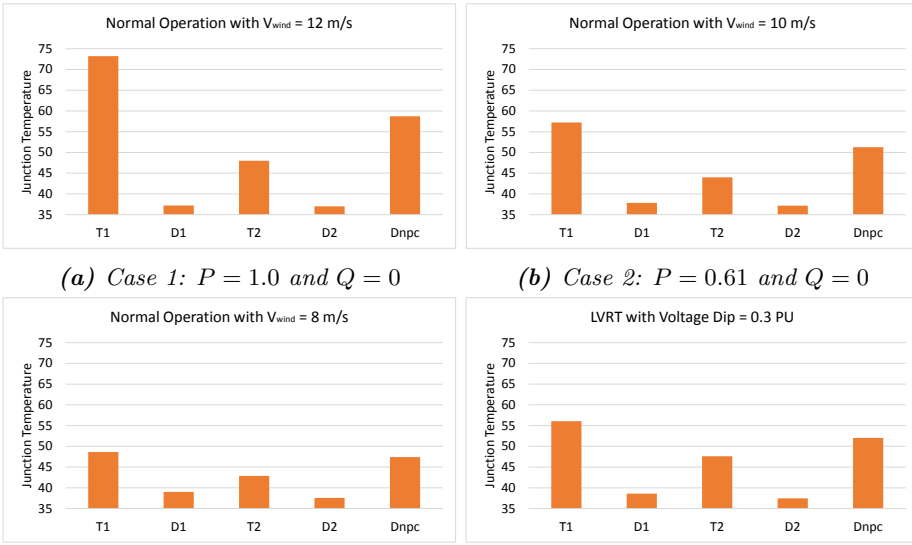

(a) Case 1: $P = 1.0$ and $Q = 0$

(b) Case 2: $P = 0.61$ and $Q = 0$

(c) Case 3: $P = 0.31$ and $Q = 0$

(d) Case 4: $P = 0.56$ and $Q = 0.42$

Figure 6.20: *Average Junction Temperature under Different Operation Points with MS-MPCDCC*

6.5 Multiple Steps MPDCC Experimental Results

In order to verify the principle of the multiple steps MPDCC further, the scaled down system setup with 10 kVA described in Chapter 3 is used for the experimental validation. Due to the processing power limitation of the hardware platform, the strategy with switching horizon $N_s = 2$ and extrapolation is adopted. The sampling period T_s is 100 μs. The internal control parameters are kept consistent with the simulation, which are summarized in table 6.5.

6.5.1 Steady State Performance

In order to present the advantages of linear extrapolation, figure 6.21 shows the experimental results of MS-MPDCC at nominal operation point with $N_e = 0$ first. The converter current is well regulated. Like DPC, MPC has a variable switching frequency, the FFT analysis of converter current has no obvious characteristic frequency but spreads across all the frequency bands. The grid current and its FFT analysis are shown in figure 6.21c and figure 6.21d respectively. The high order frequency harmonics are filtered noticeably while there is a clear 7^{th} order harmonic caused by the LCL filter. The THD of the grid current is around 3.2%. The grid side active and reactive power are shown

Table 6.5: *Control Parameters*

Description	Symbol	Value	Unit
Control variable	i_1	-	-
Control sequence	{S,S,E}	-	-
Sampling Period	T_s	100	μs
Reduced Switching Matrix	Yes	-	-
Switching Horizon	N_s	2	-
Control Boundary	B	0.2	PU
Current Weighting Factor	λ_i	0.825	-
Switching Weighting Factor	λ_{sw}	0.175	-
Normalization of Current	I_b	20.41	A
AD Virtual Resistance for MV	R_{vr}	0.45	PU
AD Virtual Resistance for LV	R_{vr}	1.56	PU
AD HP-filter factor	α	0.99	-

in 6.21e. Unity power factor is achieved. The observed and the measured converter side currents (figure 6.21f) show that the designed Luenberger Observer works very well. In order to reduce the calculation effort of the processor, the observer is implemented in the FPGA. Figure 6.21g shows the observed converter current from CPU and FPGA. Since extrapolation is not implemented, the average switching frequency is kept around 1200 Hz. The processor calculation time is around 35 µs (figure 6.21i). The measured DC-link voltage in figure 6.22 shows that the neutral point voltage is kept to 5.6% of the half the DC-link voltage.

The experimental results of MS-MPDCC at nominal operation with extrapolation are summarized in figure 6.23. The average switching frequency is reduced to be lower than 500 Hz. The calculation time is increased to around 50 µs due to the additional extrapolation calculation. Figure 6.23j shows the vector sequence candidates. It should be noted that in order to limit the calculation effort the reduced switching matrix B.1 is adopted. The prediction steps are shown in figure 6.23k. The basic switching horizon is 2 and the extension horizon can reach 7, so the maximum total prediction steps can be up to 9.

6.5.2 Transient Performance

In order to analyse the dynamic performance of the MS-MPDCC methods, several different steps are conducted. Two cases are shown in figure 6.25, which are startup and active power change from 10 to 5 kW. Figure 6.25a shows the startup converter side current. It should be noted that the observed system status variables are not correct before starting. So if the incorrect observed values are fed to the system, the system will

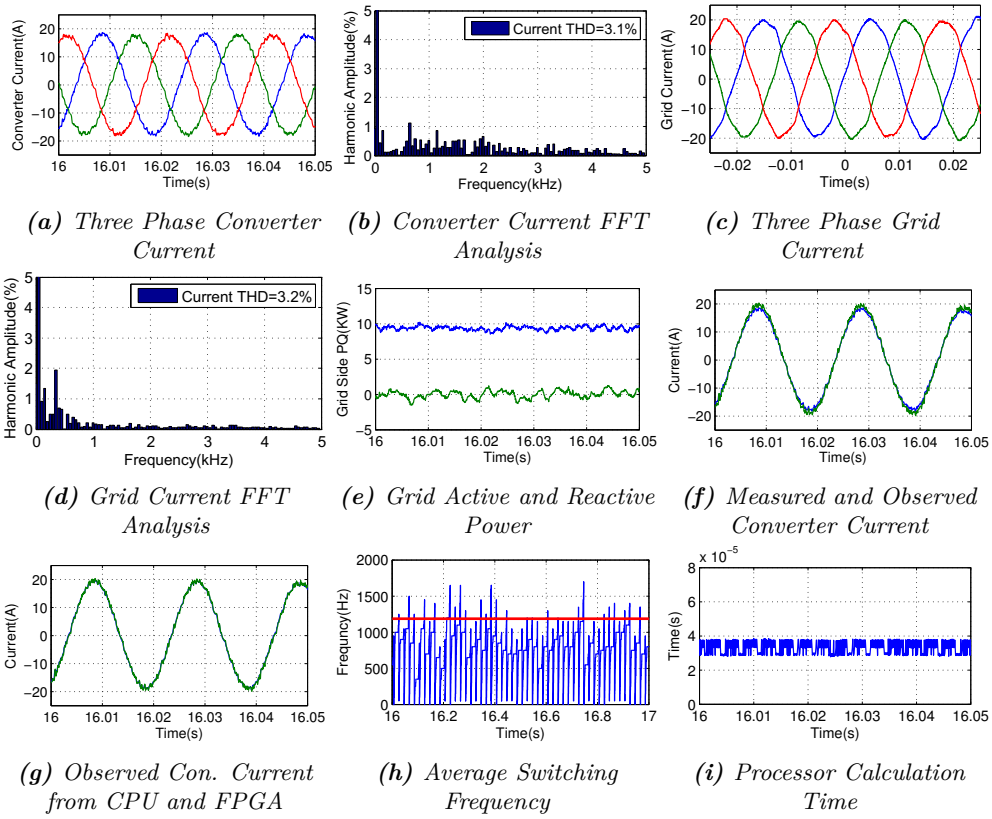

(a) Three Phase Converter Current *(b) Converter Current FFT Analysis* *(c) Three Phase Grid Current*

(d) Grid Current FFT Analysis *(e) Grid Active and Reactive Power* *(f) Measured and Observed Converter Current*

(g) Observed Con. Current from CPU and FPGA *(h) Average Switching Frequency* *(i) Processor Calculation Time*

Figure 6.21: *Experimental Results of MS-MPDCC at* 10 kW *with* $N_e = 0$

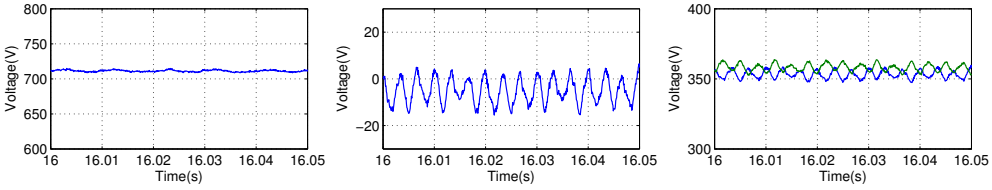

(a) DC-link Voltage *(b)* $v_{dc1} - v_{dc2}$ *(c)* v_{dc1} *and* v_{dc2}

Figure 6.22: *Experimental DC-link Voltage Performance of MS-MPDCC at* 10 kW *with* $N_e = 0$

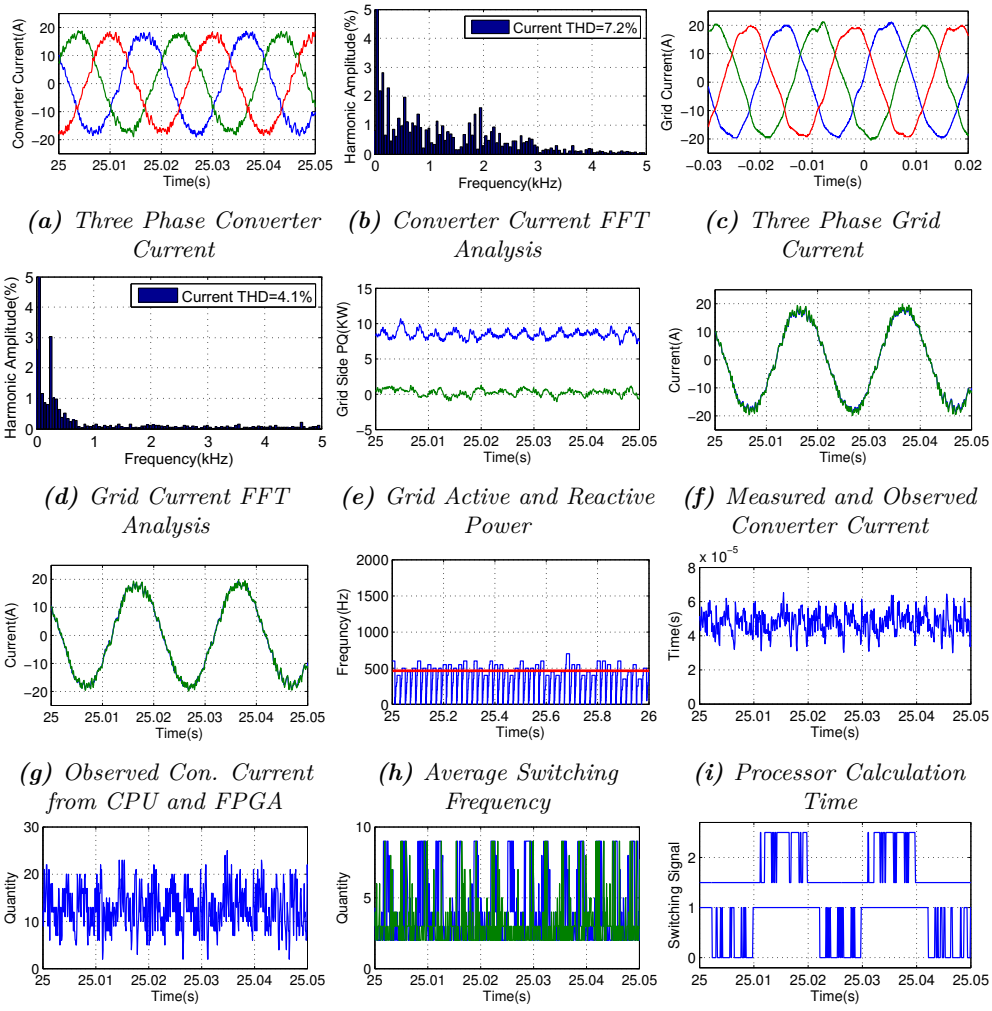

(a) *Three Phase Converter Current*

(b) *Converter Current FFT Analysis*

(c) *Three Phase Grid Current*

(d) *Grid Current FFT Analysis*

(e) *Grid Active and Reactive Power*

(f) *Measured and Observed Converter Current*

(g) *Observed Con. Current from CPU and FPGA*

(h) *Average Switching Frequency*

(i) *Processor Calculation Time*

(j) *Vector Sequence Candidates*

(k) *Prediction Step* $N_p = N_s + N_e$

(l) *Switching Signal on S11 and S12*

Figure 6.23: *Experimental Results of MS-MPDCC at* 10 kW *with Extrapolation*

not start up normally. In the experiments, the filter capacitor voltage is replaced by the grid voltage, and the grid current is replaced by the converter current for 200 µs during the startup. Afterwards, the real observed capacitor voltage and grid current are fed to the system. The rising time of the startup current is around 2.5 ms. It is interesting

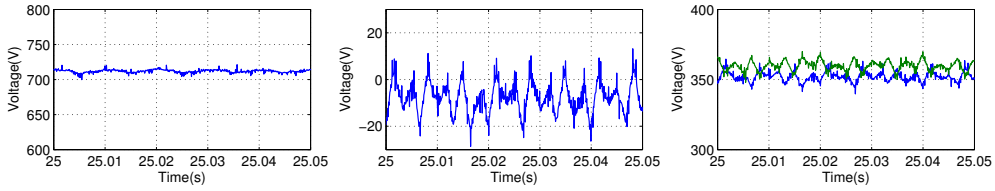

(a) DC-link Voltage *(b) $v_{dc1} - v_{dc2}$* *(c) v_{dc1} and v_{dc2}*

Figure 6.24: *Experimental DC-link Voltage Performance of MS-MPDCC at* 10 kW *with Extension*

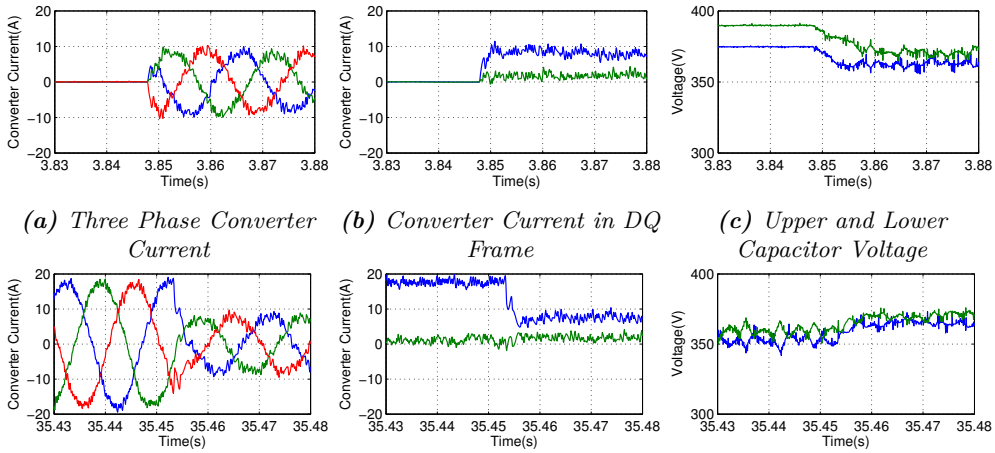

(a) Three Phase Converter Current *(b) Converter Current in DQ Frame* *(c) Upper and Lower Capacitor Voltage*

(d) Three Phase Converter Current *(e) Converter Current in DQ Frame* *(f) Upper and Lower Capacitor Voltage*

Figure 6.25: *Experimental Transient Performance of MS-MPDCC at Startup and Active Power Step from 10 to* 5 kW

to find that the upper and lower capacitor voltage are not balanced before starting, which might be caused by a parameter mismatch in the used 12-pulse diode rectifier or the input transformer. For the step down, the active power is changed from 10 to 5 kW, see figure 6.25d, 6.25e and 6.25f. The falling time is around 2.1 ms. The dynamic performance of MS-MPDCC satisfies the general requirement of converter control.

6.6 Comparison of Single Step and Multiple Steps Prediction

In order to find the advantages of multiple steps prediction, the comparison between the single step and multiple steps MPC is discussed in this section. The multiple

steps prediction with the control sequence {S,S,E} ($N_s = 2$) is adopted to compare to the single step MPDC , which is actually equivalent with the control sequence {S} ($N_s = 1$), but without extrapolation. In order to find the essential differences, the simulation conditions and the studied cases are kept as simple as possible. So two constant individual voltage sources are assumed for this simulation comparison.

6.6.1 Steady State Performance Comparison

The results of the single step MPDCC at the nominal operation point are given in figure 6.26. In order to compare with multiple steps MPDCC shown in figure 6.9, two case studies are designed:

I Keep i_2 THD, average switching frequency comparison

II Keep average switching frequency, i_2 THD comparison

Case I in figure 6.26 indicates that when the grid current THD is 4.2%, which is consistent with figure 6.9, the average switching frequency is 736.35 Hz, which is much larger than the one with multiple steps (380.65 Hz). The results of case II is not shown here, since the system has already gone out of operation. With the switching frequency 380.65 Hz, the system with SS-MPDCC can not work properly. The steady state performance with different switching frequencies for SS-MPDCC is shown in table 6.6. As expected, with the decreasing of the switching frequency, the THD of the grid current increases. When the average switching frequency reaches 560.71 Hz, the THD of grid current i_2 exceeds the requirement of 5%. For comparison, the steady state performance with different switching frequencies for MS-MPDCC is shown in table 6.7. Here, δ_i represents the current boundary. For a comparable THD, the switching frequency of the MS-MPDCC is decreased by 40% to 50% compared to the SS-MPDCC, which improves the system efficiency shown in table 6.8.

Table 6.6: *Single Step MPDCC Steady State Performance*

λ_{sw}	λ_i	$f_{sw}^{ave}[Hz]$	$i_2, THD[\%]$
0.00	1.00	949.34	3.5
0.01	0.99	736.35	4.2
0.02	0.98	560.71	5.8
0.03	0.97	516.94	11.2

6.6.2 Transient Performance Comparison

For the transient performance comparison, one case is simulated for both SS-MPDCC and MS-MPDCC, which is:

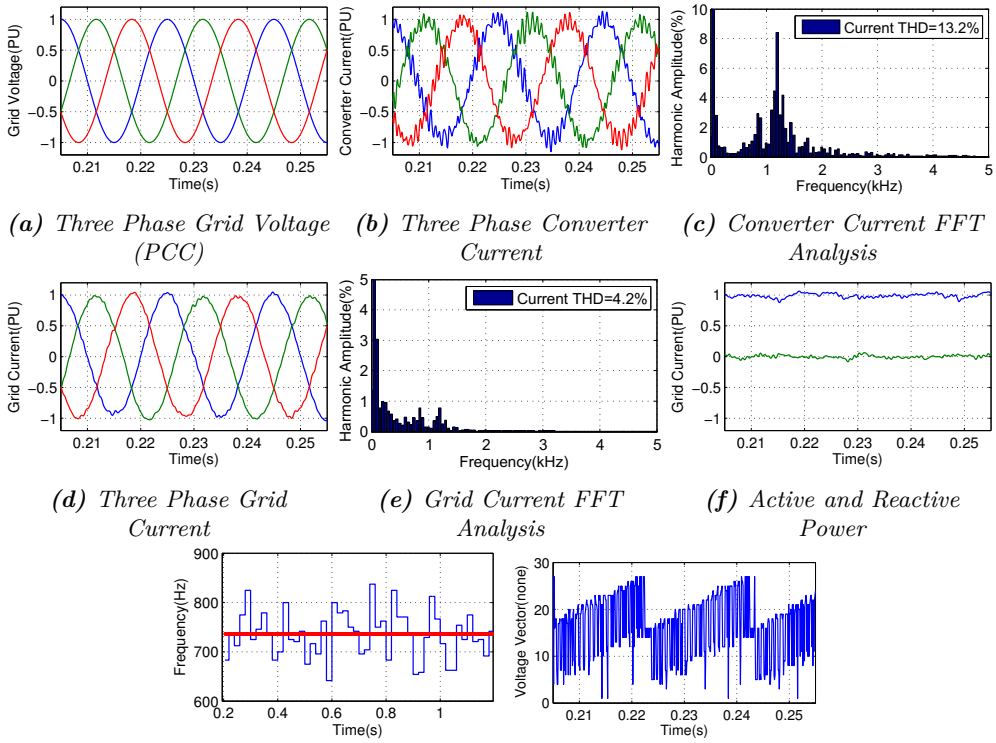

(a) Three Phase Grid Voltage (PCC) *(b) Three Phase Converter Current* *(c) Converter Current FFT Analysis*

(d) Three Phase Grid Current *(e) Grid Current FFT Analysis* *(f) Active and Reactive Power*

(g) Average Switching Frequency *(h) Selected Optimal Voltage Vector*

Figure 6.26: *Single Steps MPDCC at Nominal Point Operation*

Table 6.7: *Multiple Steps MPDCC Steady State Performance*

$\delta_i[PU]$, boundary	λ_{sw}	λ_i	$f_{sw}^{ave}[Hz]$	$i_2, THD[\%]$
0.2	0.1	0.9	472.71	3.4
0.2	0.3	0.7	342.25	4.3
0.2	0.4	0.6	327.28	6.3
0.2	1.00	0.00	289.96	8.0

- Case A: Active Power drops to 0.5 PU and reactive power is zero.

Case A for MS-MPDCC is shown in figure 6.27. The active power reference drops to 0.5 PU at 0.205 s. In order to observe the dynamic process more clearly, the currents

Table 6.8: *SS- and MS-MPDCC Performance Comparison*

$i_2, THD[\%]$ SS/MS	$f_{sw}^{ave}[Hz]$ SS/MS	f_{sw}^{ave} reduction[%] (SS-MS)/SS
3.5/3.4	949.34/472.71	50.2
4.2/4.3	736.35/342.25	53.5
5.8/6.3	560.71/327.28	41.6

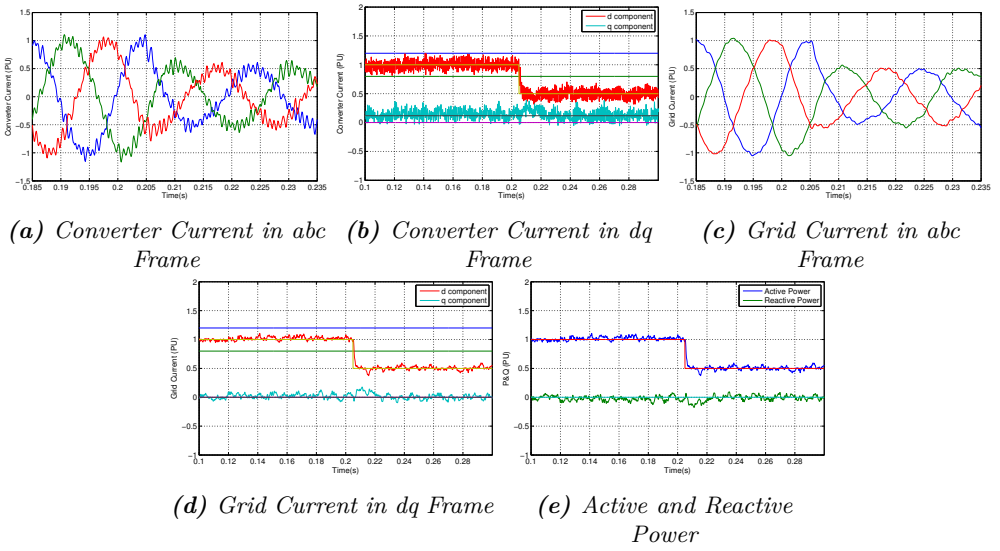

(a) *Converter Current in abc Frame* ***(b)*** *Converter Current in dq Frame* ***(c)*** *Grid Current in abc Frame*

(d) *Grid Current in dq Frame* ***(e)*** *Active and Reactive Power*

Figure 6.27: *MS-MPDCC Case A-Active Power Drops to* 0.5 PU *and Reactive Power Is Zero*

of both sides, converter side and grid side are shown in abc frame and dq frame. From the figure 6.27b, it can be noted that the converter side current is well limited in the boundary, which is 0.2 PU in this case. It also can be found that the q component is not zero ($i_{1q,ref} = 0.118$ PU), which is caused by the reactive compensation of the filter capacitor. The dynamic of i_{1d} is quite fast, and the falling time is around 2.2 ms. With the LCL filter, the high order harmonics are greatly attenuated. The three phase grid current is shown in figure 6.27c. According to figure 6.27d, the rising time (3.5 ms) becomes a little larger than for the converter side current due to the large capacitance of the LCL filter. The active power and reactive power in figure 6.27e should have the same dynamic as the grid side current, if the grid voltage is an ideal sinusoidal wave according to equation 5.2.

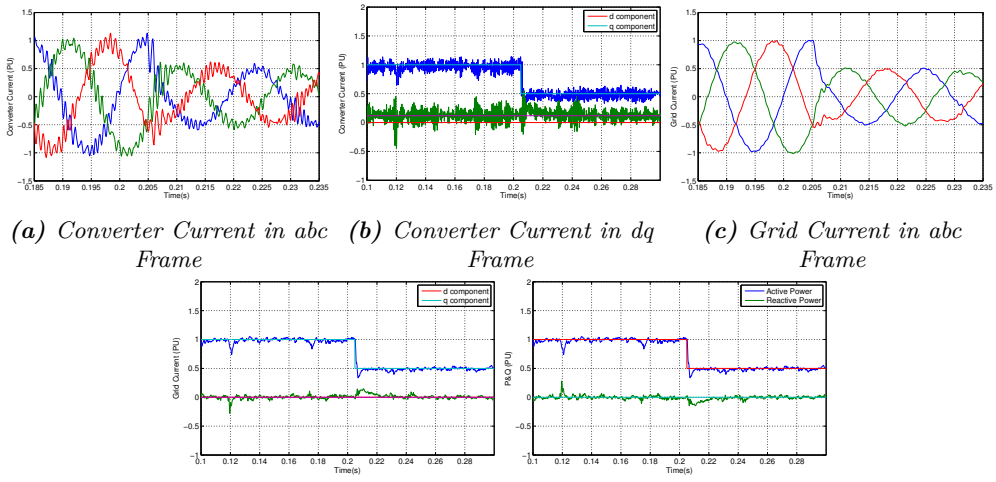

(a) Converter Current in abc Frame *(b) Converter Current in dq Frame* *(c) Grid Current in abc Frame*

(d) Grid Current in dq Frame *(e) Active and Reactive Power*

Figure 6.28: *Case A-Active Power Drops to* 0.5 PU *and Reactive Power Is Zero for SS-MPDCC*

The results for single step MPDCC for case A are shown in figure 6.28. Compared with multiple steps prediction, the single step method has a faster dynamic performance. In summary, no matter in which case, the rising time t_{r1} of converter current and the rising time t_{r2} of grid current for single step MPDCC are generally smaller than the ones using the multiple steps method. However, both performances are acceptable.

Table 6.9: *Rising Time of Direct Axis Component Comparison* (t_{r1}/t_{r2})

Methods	Case A[ms]	Case B[ms]
SS-MPDCC	0.3/1.6	1.3/1.8
MS-MPDCC	2.2/3.5	2.5/2.6

6.7 Summary

Model based predictive control methods are studied in this chapter. First, the classification of model predictive control is discussed. Among them, model predictive direct control is a promising method, which is quite suitable for converter control due to the inherent limited switching states. As the basis of the multiple steps method, single step

model predictive direct current control is presented step by step, which consists of system modelling, cost function formulation, current reference prediction and time delay compensation. In order to decrease the cost and improve the reliability of the system, a full state Luenberger observer is designed.

As the core of this chapter, the multiple steps MPDCC is presented in detail. By employing the concept of receding horizon, multiple steps MPDCC is designed for the MW level MV application. Since a low switching frequency can be achieved, which is around 400 Hz, the switching losses will be decreased significantly.

In order to verify the correctness of the control strategy, the simulation for a 5 MVA system is conducted. The multiple steps MPDCC has a good performance in both dynamic and steady state. A scaled down LV three-level NPC converter with LCL filter testbench (10 kVA) is used for experimental validation.

Finally, the advantage of using multiple steps is proved through comparing with single step MPDCC. At the same conditions, MS-MPDCC can achieve better current quality with low switching frequency compared to SS-MPDCC. SS-MPDCC has slightly better dynamics, though.

Additionally, a thermal analysis is conducted for MS-MPDCC. As MS-MPDCC can achieve a low switching frequency, compared to DPC and VOC, MS-MPDCC has the lowest switching losses and average junction temperature for the same operation point and same type of semiconductors.

7 Backstepping Control

The previous chapters have investigated the state of the art control algorithms, VOC and DPC, discussed in chapter 5. As an alternative, MPC is studied systematically in chapter 6, including the SS-MPC and MS-MPC. The later one can good excellent performance with extremely low switching frequency, e.g. lower than 500 Hz. This property can help MV power conversion systems to achieve better efficiency. The MS-MPC might be intensively developed in the next years.

However, there are also several drawbacks, for example, high computation effort, the steady state error, no systematic methods for weighting factor design and limited capability of disturbance rejection. Another issue is the fact that during operation, the real system parameters might change, which will causes a mismatch with the control model parameters used for prediction. Control errors might arise if the mismatch is too large. In order to overcome this drawback, this chapter presents a non-linear controller for the grid converter control based on Lyapunov function, so that zero steady-state error can be obtained for tracking the grid currents.

7.1 Overview of Backstepping Control

Backstepping control (BSC) was mainly introduced in the early 90s by Petar V. Kokotovic, and was considered as a breakthrough for nonlinear control. In reality, most of real physical systems are nonlinear and especially parameter uncertainties are inevitable. As described in reference [173], the ease that backstepping incorporated uncertainties and unknown parameters makes it instantly popular and rapidly accepted.

In the past decades, many nonlinear control design approaches, such as variable structure control (e.g., Sliding mode Control) [174], Lyapunov Redesign [175] and backstepping control [173] have been proposed. The backstepping approach is a recursive Lyapunov-based method, which has the flexibility to avoid cancellations of useful nonlinearities and implement regulation and tracking properties [176]. By employing this method, the construction of feedback control laws and Lyapunov functions are systematic, following a step by step controller design. The backstepping method is addressed by Krstic, Kanellakopoulos and Kokotovic in reference [177]. This backstepping design formulation was first applied to electrical machines in [178], where it was used to design a nonlinear feedback control for an induction machine without flux measurements and assuming that all the parameters of the system are known. Reference [179] presents the current tracking control via an adaptive backstepping approach for a three phase PWM AC-DC converter. Backstepping control adopted for an active power filter with LCL filter is presented in [180]. A combination of adaptive control, neural network control and backstepping control was introduced for three phase active power filters to improve the control performance [181]. In reference [182], the backstepping control combining direct power control without phase-locked loop is used for AC/DC converter control at

both balanced and unbalanced grid conditions.

With the power system becoming more complex, many system parameter uncertainty increases. It is necessary to develop robust and adaptive control approaches to deal with this issue. Among the variety of advanced nonlinear controls, backstepping is an attractive method since it does not ignore any high order nonlinear terms and maintains global system nonlinearity. Especially for the application of grid converter with LCL filters, no additional passive or active damping is needed. The high order frequency harmonics can be easily attenuated through the LCL filter. However, its attenuation for low order harmonics is weak. Especially for a low resonance frequency design of the LCL circuit, which is normally chosen in MV and high power applications due to the low converter switching frequency, low order harmonics are problematic and can cause resonance problems. Low order harmonics are existing commonly in the real grid due to nonlinear loads, so the reduction and suppression of low order harmonics needs to be solved. Reference [82] presents a novel harmonic impedance expression to study the effects of power supply distortion on the harmonic performance of the system. Full feedforward of the grid voltage is applied to eliminate the grid voltage effects on the grid currents [183,184]. Reference [185] proposes a feedforward scheme based on a band pass filter to revise the output admittance which can reduce the effects of the distorted grid voltage. Reference [186] presents an adaptive control based on backstepping to improve the dynamic performance of voltage source converters in high voltage direct current applications. However, the disturbance of grid voltage is not considered.

In summary, backstepping control is becoming a promising non-linear approach to control grid converter with LCL filter in balanced and unbalanced grid voltage applications, especially handling the system parameter uncertainties. Figure 7.1 shows the overview of backstepping control for grid converters with LCL-filter. The detailed design will be explained in the next subsections.

7.2 Controller Design of Backstepping Control

In this section, a backstepping controller will be designed for the LCL-based three-phase three-level NPC grid-connected inverter. The objective is to achieve that the grid current i_2 is tracking the grid current reference i_{2r} with zero steady-state error in the case of low order harmonics existing in the grid voltage. The system model is given by equation 7.1 [83], where $x_{1k} = i_{2k}$ is the grid side current; $x_{2k} = v_{ck}$ is the capacitor voltage; $x_{3k} = i_{1k}$ is the converter side current; u_k is the output voltage of the converter; and v_{gk} is the grid voltage. In the $\alpha\beta$ coordinate system, $k = \alpha, \beta$. The dynamic system (equation 7.1) is identical for α and β, so it is sufficient to design the current controller for $k = \alpha$, and use the same controller also for the β axis.

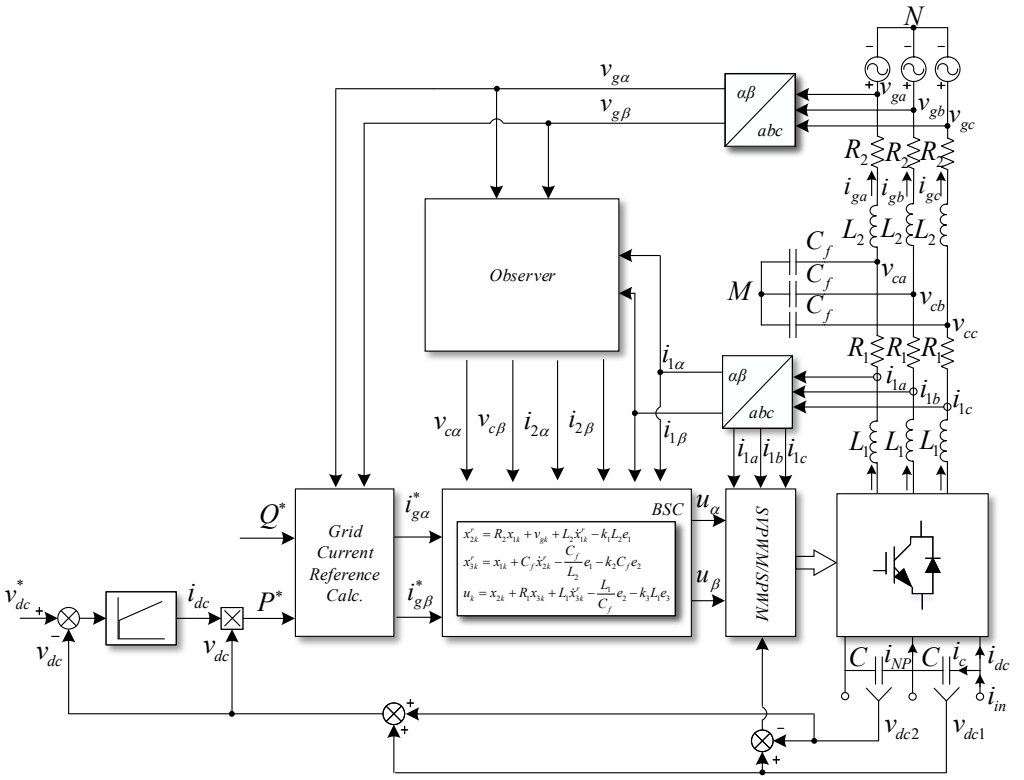

Figure 7.1: *Backstepping Control for Grid Converter with LCL-filter*

$$\begin{bmatrix} \dot{x}_{1k} \\ \dot{x}_{2k} \\ \dot{x}_{3k} \end{bmatrix} = \begin{bmatrix} -\frac{R_2}{L_2} & \frac{1}{L_2} & 0 \\ -\frac{1}{C_f} & 0 & \frac{1}{C_f} \\ 0 & -\frac{1}{L_1} & -\frac{R_1}{L_1} \end{bmatrix} \begin{bmatrix} x_{1k} \\ x_{2k} \\ x_{3k} \end{bmatrix} + \begin{bmatrix} 0 \\ 0 \\ \frac{1}{L_1} \end{bmatrix} u_k + \begin{bmatrix} -\frac{1}{L_2} \\ 0 \\ 0 \end{bmatrix} v_{gk} \tag{7.1}$$

In the following, a step-to-step procedure for the controller of the grid current tracking is given applying the backstepping theory [177]. First, we define the system errors as:

$$e_1 = x_{1k} - x^r_{1k} \tag{7.2}$$

$$e_2 = x_{2k} - x^r_{2k} \tag{7.3}$$

$$e_3 = x_{3k} - x_{3k}^r \tag{7.4}$$

where x_{1k}^r is the grid current reference; x_{2k}^r and x_{3k}^r are virtual control variables (similar with the references of capacitor voltage and converter current).

7.2.1 Controller Design

Step 1: Forming the derivative of both sides of equation 7.2 and applying equation 7.1, the dynamics of the grid current error e_1 can be deduced as equation 7.5, and a Lyapunov function V_1 is chosen according to equation 7.6:

$$\dot{e}_1 = \dot{x}_{1k} - \dot{x}_{1k}^r = -\frac{R_2}{L_2}x_{1k} + \frac{1}{L_2}x_{2k} - \frac{1}{L_2}v_{gk} - \dot{x}_{1k}^r \tag{7.5}$$

$$V_1 = \frac{e_1^2}{2} \tag{7.6}$$

We define the virtual control variable x_{2k}^r:

$$\begin{aligned} x_{2k}^r &= L_2\left(\tfrac{R_2}{L_2}x_{1k} + \tfrac{1}{L_2}v_{gk} + \dot{x}_{1k}^r - k_1 e_1\right) \\ &= R_2 x_{1k} + v_{gk} + L_2\dot{x}_{1k}^r - k_1 L_2 e_1 \end{aligned} \tag{7.7}$$

Using equation 7.3, 7.5, 7.6 and 7.7, the derivative of the Lyapunov function V_1 (equation 7.6) can be easily calculated as:

$$\begin{aligned} &\dot{V}_1 = e_1\dot{e}_1 = e_1\left(-\tfrac{R_2}{L_2}x_{1k} + \tfrac{1}{L_2}(e_2 + x_{2k}^r) - \tfrac{1}{L_2}v_{gk} - \dot{x}_{1k}^r\right) \\ &= -k_1 e_1^2 + \tfrac{1}{L_2}e_1 e_2 \end{aligned} \tag{7.8}$$

Step 2: Similar to step 1, the dynamics of the system error e_2 and a Lyapunov function V_2 can be derived:

$$\dot{e}_2 = \dot{x}_{2k} - \dot{x}_{2k}^r = -\frac{1}{C_f}x_{1k} + \frac{1}{C_f}x_{3k} - \dot{x}_{2k}^r \tag{7.9}$$

$$V_2 = \frac{e_1^2}{2} + \frac{e_2^2}{2} \tag{7.10}$$

Choose the virtual control variable x_{3k}^r as:

$$\begin{aligned} &x_{3k}^r = C_f\left(\tfrac{1}{C_f}x_{1k} + \dot{x}_{2k}^r - \tfrac{1}{L_2}e_1 - k_2 e_2\right) \\ &= x_{1k} + C_f\dot{x}_{2k}^r - \tfrac{C_f}{L_2}e_1 - k_2 C_f e_2 \end{aligned} \tag{7.11}$$

Based on 7.4, 7.8, 7.10 and 7.11, we find the derivative of the Lyapunov function V_2:

$$\begin{aligned}\dot{V}_2 &= e_1\dot{e}_1 + e_2\dot{e}_2 \\ &= -k_1e_1^2 + \tfrac{1}{L_2}e_1e_2 + e_2\left(-\tfrac{1}{C_f}x_{1k} + \tfrac{1}{C_f}(e_3 + x_{3k}^r) - \dot{x}_{2k}^r\right) \\ &= -k_1e_1^2 - k_2e_2^2 + \tfrac{1}{C_f}e_2e_3\end{aligned} \tag{7.12}$$

Step 3: Finally, based on 7.4 and the system equation 7.1, the derivative of the system error e_3 can be represented by equation 7.13. To prove the stability and analyze the steady-state accuracy, we introduce the Lyapunov function equation 7.14.

$$\dot{e}_3 = \dot{x}_{3k} - \dot{x}_{3k}^r = -\frac{1}{L_1}x_{2k} - \frac{R_1}{L_1}x_{3k} + \frac{1}{L_1}u_k - \dot{x}_{3k}^r \tag{7.13}$$

$$V_3 = \frac{e_1^2}{2} + \frac{e_2^2}{2} + \frac{e_3^2}{2} \tag{7.14}$$

Design the controller u_k as:

$$\begin{aligned}u_k &= L_1\left(\tfrac{1}{L_1}x_{2k} + \tfrac{R_1}{L_1}x_{3k} + \dot{x}_{3k}^r - \tfrac{1}{C_f}e_2 - k_3e_3\right) \\ &= x_{2k} + R_1x_{3k} + L_1\dot{x}_{3k}^r - \tfrac{L_1}{C_f}e_2 - k_3L_1e_3\end{aligned} \tag{7.15}$$

The designed controller output u_k is a function of physical variables (x_{1k}, x_{2k}, x_{3k}), reference variable (x_{1k}^r) and grid voltage (v_{gk}), including several derivatives of reference variable and grid voltage. Due to the complexity of the expression of u_k, the final expression is not given explicitly here. However, the stability of the controller is proved in the following section. Additionally, for the whole system, no PLL is used. Since the active and reactive power are the controlled objectives, the grid side current references are calculated through equations 7.16 and 7.17, where $V_{g,m}$ denotes the amplitude of the grid phase voltage.

$$\begin{cases} P = \frac{3}{2}(v_{g\alpha}i_{g\alpha} + v_{g\beta}i_{g\beta}) \\ Q = \frac{3}{2}(v_{g\beta}i_{g\alpha} - v_{g\alpha}i_{g\beta}) \end{cases} \tag{7.16}$$

$$\begin{cases} i_{g\alpha} = \frac{Pv_{g\alpha}+Qv_{g\beta}}{\frac{3}{2}(v_{g\alpha}^2+v_{g\beta}^2)} = \frac{Pv_{g\alpha}+Qv_{g\beta}}{\frac{3}{2}V_{g,m}^2} \\ i_{g\beta} = \frac{Pv_{g\beta}-Qv_{g\alpha}}{\frac{3}{2}(v_{g\alpha}^2+v_{g\beta}^2)} = \frac{Pv_{g\beta}-Qv_{g\alpha}}{\frac{3}{2}V_{g,m}^2} \end{cases} \tag{7.17}$$

7.2.2 Stability Analysis

In the view of equation 7.8, 7.13, 7.14 and 7.15, the derivative of the Lyapunov function V_3 can be deduced by:

$$\begin{aligned}\dot{V}_3 &= e_1\dot{e}_1 + e_2\dot{e}_2 + e_3\dot{e}_3 \\ &= -k_1e_1^2 - k_2e_2^2 + \tfrac{1}{C_f}e_2e_3 + e_3\left(-\tfrac{1}{L_1}x_{2k} - \tfrac{R_1}{L_1}x_{3k} + \tfrac{1}{L_1}u_k - \dot{x}_{3k}^r\right) \\ &= -k_1e_1^2 - k_2e_2^2 - k_3e_3^2\end{aligned} \tag{7.18}$$

According to the Lyapunov theorem [177] and equation 7.14 and 7.18, the system is asymptotically stable with positive k_1, k_2, and k_3. We achieve:

$$\lim_{t\to+\infty} e_1 = \lim_{t\to+\infty}(x_{1k} - x_{1k}^r) = 0 \tag{7.19}$$

$$\lim_{t\to+\infty} e_2 = \lim_{t\to+\infty}(x_{2k} - x_{2k}^r) = 0 \tag{7.20}$$

$$\lim_{t\to+\infty} e_3 = \lim_{t\to+\infty}(x_{3k} - x_{3k}^r) = 0 \tag{7.21}$$

From equation 7.19, 7.20 and 7.21, the error between the reference variables and physical variables becomes zero. The control objective is obtained.

In order to reduce the complexity of the controller and in the case of ensuring system stability, a modified backstepping controller is designed for the system. Equation 7.11 and 7.15 are simplified as (7.22) and (7.23),

$$x_{3k}^r = x_{1k} + C_f\dot{x}_{2k}^r - k_2C_fe_2 \tag{7.22}$$

$$u_k = x_{2k} + R_1x_{3k} + L_1\dot{x}_{3k}^r - k_3L_1e_3 \tag{7.23}$$

and the simplified system matrix in 7.24 is achieved. The system matrix is an upper triangular matrix. The controller parameters, k_1, k_2 and k_3 and can be easily tuned to get the system stable.

$$\begin{pmatrix}\dot{e}_1\\ \dot{e}_2\\ \dot{e}_3\end{pmatrix} = \begin{pmatrix}-k_1 & \frac{1}{L_2} & 0\\ 0 & -k_2 & \frac{1}{C_f}\\ 0 & 0 & -k_3\end{pmatrix}\begin{pmatrix}e_1\\ e_2\\ e_3\end{pmatrix} \tag{7.24}$$

These control parameters can also be obtained by solving the equation 7.24 considering the performance specification in the time domain. The system error state equation 7.24 is a linear time invariant (LTI) free motion without input control. The solution of the error system can be expressed as:

$$\mathbf{x}(t) = e^{At}\mathbf{x}(0) \tag{7.25}$$

where $\mathbf{x}$ represents the error state variables $\begin{bmatrix} e_1 & e_2 & e_3 \end{bmatrix}^T$. The matrix $sI - A$ and $(sI - A)^{-1}$ are derived as:

$$sI - A = \begin{vmatrix} s+k_1 & -1/L_2 & 0 \\ 0 & s+k_2 & -1/C_f \\ 0 & 0 & s+k_3 \end{vmatrix} \tag{7.26}$$

$$(sI-A)^{-1} = \begin{vmatrix} \frac{1}{s+k_1} & \frac{1}{L_2(s+k_1)(s+k_2)} & \frac{1}{L_2C_f(s+k_1)(s+k_2)(s+k_3)} \\ & \frac{1}{(s+k_2)} & \frac{1}{C_f(s+k_2)(s+k_3)} \\ & & \frac{1}{(s+k_3)} \end{vmatrix} \tag{7.27}$$

By employing inverse Laplace transformation, the state transition matrix can be achieved:

$$\begin{aligned} \Phi(t) &= \mathcal{L}^{-1}(sI-A)^{-1} \\ &= \begin{vmatrix} e^{-k_1t} & \frac{1}{L_2(k_2-k_1)}(e^{-k_1t}-e^{-k_2t}) & M \\ 0 & e^{-k_2t} & \frac{1}{C_f(k_3-k_2)}(e^{-k_2t}-e^{-k_3t}) \\ 0 & 0 & e^{-k_3t} \end{vmatrix} \end{aligned} \tag{7.28}$$

where

$$M = \frac{1}{L_2C_f(k_2-k_1)}\left[\frac{1}{k_3-k_1}e^{-k_1t} - \frac{1}{k_3-k_2}e^{-k_2t} - \left(\frac{1}{k_3-k_1} - \frac{1}{k_3-k_2}\right)e^{-k_3t}\right] \tag{7.29}$$

So the solution of the error system can be described as:

$$\mathbf{x}(t) = \Phi(t)\mathbf{x}(0) \tag{7.30}$$

If the convergence time of e_3 is set to 0.001 s for 5% error band of the initial error value $e_3(0)$, it can be obtained:

$$e_3(t) = e^{-k_3t}e(0) \Rightarrow \frac{e_3(0.001)}{e(0)} = e^{-k_3 \cdot 0.001} = 0.05 \tag{7.31}$$

So it can be derived that $k_3 = 2996$. Similarly, the other two controller parameters can be designed to $k_2 = 1210$ and $k_1 = 1049$.

7.3 Observer based Backstepping Control

The basic observer design method has been discussed in subsection 6.2.3. Since the BSC controller is identical for both α and β axis, the observer can be designed for one axis, and the same observer will be used for the other axis. From the system equation 7.1, the system is a third order system. The observer system matrix A_0, input matrix B_0, disturbance matrix P_0 and the feedforward matrix D_0 respectively are:

$$A_0 = \begin{vmatrix} -R_2/L_2 & 1/L_2 & 0 \\ -1/C_f & 0 & 1/C_f \\ 0 & -1/L_1 & -R_1/L_1 \end{vmatrix} \tag{7.32}$$

$$B_0 = \begin{vmatrix} 0 \\ 0 \\ 1/L_1 \end{vmatrix} \tag{7.33}$$

$$C_0 = eye(3) \tag{7.34}$$

$$D_0 = \begin{vmatrix} 0 & 0 & 0 \end{vmatrix}^T \tag{7.35}$$

Since the three state variables are needed for the feedback, the output matrix is designed as unity matrix. It should be noted that actually the converter side current is measured. However, the observed converter side current is preferred to use due to the inherent low pass filter function of the observer. The system should have three poles, and for simplicity, select two of them as dominant poles and the third one as non-dominant pole. The second order specification based calculation is as follows:

$$\sigma\% = e^{-\frac{\pi\xi}{\sqrt{1+\xi^2}}} \tag{7.36}$$

$$t_p = \frac{\pi}{\omega_n\sqrt{1-\xi^2}} \tag{7.37}$$

$$\omega_b = \omega_n\sqrt{1-2\xi^2+\sqrt{2-4\xi^2+4\xi^4}} \tag{7.38}$$

where ξ and ω_n are the damping ratio and natural frequency. $\sigma\%$ is the overshoot and t_p is the peak time. ω_b is the system bandwidth. If the system overshoot and peak time are designed to 5% and 0.001 s respectively, the damping ratio and natural frequency can be calculated by employing equations 7.36 and 7.37, which are $\xi = 0.69$ and $\omega_n = 4341\,\mathrm{rad\,s^{-1}}(690\,\mathrm{Hz})$. The bandwidth of the system can be achieved via equation 7.38, which is $\omega_b = 4453\,\mathrm{rad\,s^{-1}}(707\,\mathrm{Hz})$. The system closed loop dominant poles can be derived:

$$\lambda_{1,2} = -\xi\omega_n \pm j\omega_n\sqrt{1-\xi^2} = 2996 \pm 3142j \tag{7.39}$$

The non-dominant pole can be assigned to $\lambda_3 = -10\omega_n = -4.3\times10^4$. So the observer system poles can be expressed as:

$$Observer\_P = \begin{bmatrix} \lambda_1 & \lambda_2 & \lambda_3 \end{bmatrix} \tag{7.40}$$

According to equation 6.30, the eigenvalue of the observer system matrix can be further deduced as:

$$\lambda(A_o - LC_o) = \lambda[(A_o - LC_o)]^T = \lambda(A_o^T - C_o^T L^T) \tag{7.41}$$

By employing pole placement controller design, the observer output feedback matrix L can be deduced as:

$$L_T = acker(A_0', C_P', Observer\_P) \tag{7.42}$$

where $C_P = \begin{bmatrix} 0 & 0 & 1 \end{bmatrix}$, and "acker" is a pole placement design function for single-input systems in Matlab.

7.4 Simulation Results

First, the proposed controller is verified with a numerical simulation study using MATLAB/Simulink. The system parameters used in simulation can be found in the MV value column given in table 5.5 with the PU base values given in table 3.3. The following subsection will present the steady state, the transient performance of BSC control and the performance under non-ideal grid voltage.

The parameters for the proposed controller are based on the methods discussed in subsection 7.2.2. The sampling time is chosen as 20 µs, the switching frequency is 1050 Hz. Based on simulation studies, it is found that higher switching frequency (e.g., 10 kHz) or lower sampling period (e.g., 20 µs) can improve the BSC, e.g., achieving low harmonics. A zero steady state error can be easily obtained by average model in simulation. In order to reduce the sensors, a full state Luenberger observer is employed in the simulation.

7.4.1 Steady State Performance

At first, the nominal operation is selected for the BSC method validation. The simulation results with BSC for the MV 5 MVA wind turbine are presented in figure 7.2. Figure 7.2a shows that a pure sinusoidal grid voltage (PCC) is assumed. The three-phase converter current is shown in figure 7.2b, which is well regulated. The grid current is controlled in the $\alpha\beta$ frame. The FFT analysis of the converter current is shown in figure 7.2c. Since the modulator and the neutral point voltage control are used, the harmonics spectrum has clear characteristic at around 2000 Hz and its multiple values, which is similar to the VOC (figure 5.9c). The three-phase grid current and its FFT analysis are shown in figure 7.2d and figure 7.2e. It is obvious that the grid current is well regulated without any damping with a THD of 2.2%. Both α and β components of the grid current are well tracked. The tracking errors for both components are shown in figure 7.2g, which proves the controller parameter design. The active power and reactive power tracking are shown in figure 7.2h. Since the grid current is directly controlled, no reactive power compensation is needed, unlike the case of VOC and DPC, and active and reactive power can be accurately controlled. The three phase converter voltage

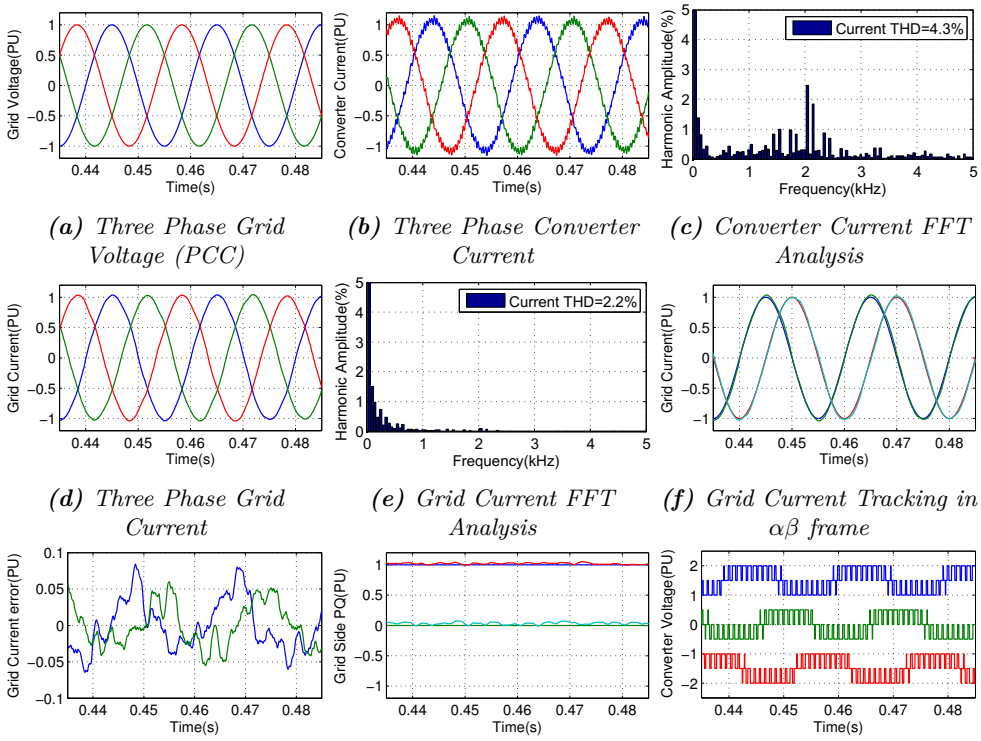

(a) Three Phase Grid Voltage (PCC) *(b) Three Phase Converter Current* *(c) Converter Current FFT Analysis*

(d) Three Phase Grid Current *(e) Grid Current FFT Analysis* *(f) Grid Current Tracking in $\alpha\beta$ frame*

(g) Grid Current Tracking error *(h) Grid Active and Reactive Power* *(i) Three Phase Converter Voltage*

Figure 7.2: *Backstepping Control under Nominal Operation Point*

is shown in figure 7.2i. It can be noted that the BSC method has similar switching transitions as the VOC (figure 5.9i).

The DC-link voltage balancing is shown in figure 7.3. The same balancing method is adopted as for the VOC. Both upper and lower capacitor voltage (v_{dc1} and v_{dc2}) are well limited within 0.5% of half the DC-link voltage. The average frequency is around 588 Hz, which is the same level as the VOC (figure 5.9h).

7.4.2 Transient Performance

The transient performance is further investigated for evaluation of the BSC algorithm. In order to test the BSC at different operation conditions, two cases are designed as following:

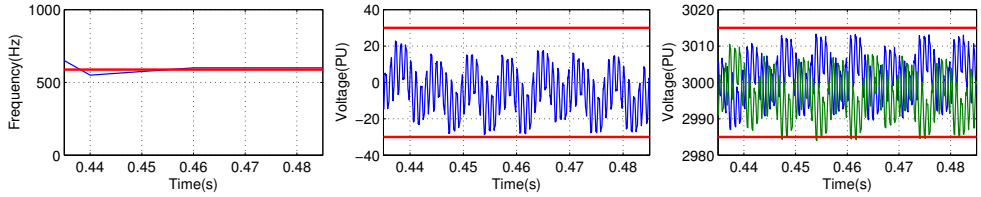

(a) *Average Frequency* ***(b)*** $v_{dc1} - v_{dc2}$ ***(c)*** v_{dc1} *and* v_{dc2}

Figure 7.3: *DC-link Voltage Balancing and Average Frequency of BSC at Nominal Operation Point*

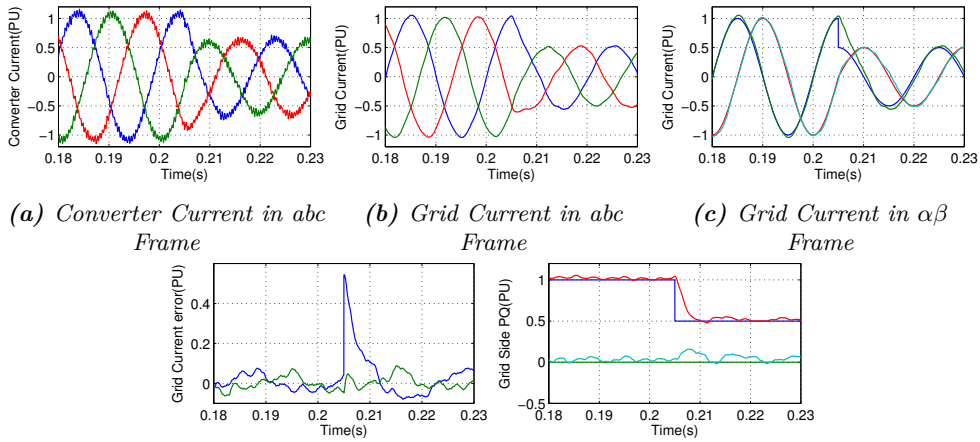

(a) *Converter Current in abc Frame* ***(b)*** *Grid Current in abc Frame* ***(c)*** *Grid Current in* $\alpha\beta$ *Frame*

(d) *Grid Current Tracking Error* ***(e)*** *Active and Reactive Power Tracking*

Figure 7.4: *BSC Case A-Active Power Drops to* 0.5 PU *and Reactive Power Is Zero*

- Case A: Active Power drops to 0.5 PU and reactive power is zero
- Case B: Active Power drops to 0 PU and recovers to nominal operation while reactive power is zero

The simulation results of case A are given in figure 7.4. The active power reference drops down to 50% of nominal power at 0.205 s, while the reactive power is zero. The grid voltage is still symmetrical and sinusoidal. Figure 7.4a shows the three phase converter current transients, which are well controlled and very fast. The grid current is directly controlled in $\alpha\beta$ frame. Figure 7.4b and figure 7.4c illustrate the grid current in abc frame and tracking performance in $\alpha\beta$ frame, respectively. It shows a very good

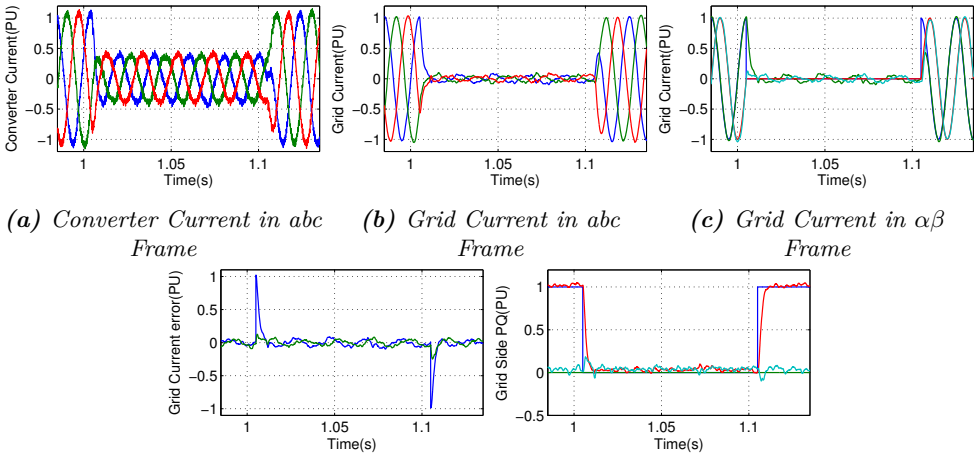

(a) Converter Current in abc Frame *(b) Grid Current in abc Frame* *(c) Grid Current in αβ Frame*

(d) Grid Current Tracking Error *(e) Active and Reactive Power Tracking*

Figure 7.5: *BSC Case B-Active Power Drops to* 0 PU *and Recovery to Nominal Point while Reactive Power Is Zero*

dynamics, which is fast and even without obvious overshoot. The rising time is 6.4 ms. The tracking error is shown in figure 7.4d. The system active and reactive power tracking (figure 7.4e) has a good dynamic performance.

In order to test the control algorithm during a severe scenario, case B is analysed verification. The active power drops to 0 PU and recovers to the nominal point while the reactive power is zero. Figure 7.5a shows the three phase converter side current. It can be noted that the converter current is not zero while the active and reactive power are set to zero, which is used for the capacitor reactive compensation. This is the same as for MS-MPDCC control figure **??**, where the converter current is controlled. Figure 7.5b shows the well controlled three phase grid current, and figure 7.5c the grid current in $\alpha\beta$ frame. At 1.005 s instant, there is a big step (1 PU) for $i_{1\alpha}$. However, the transition is very smooth. The falling time is 6.3 ms. At 1.105 s instant, the active power reference is set to nominal value again. It can be noted that the current does not have a big overshoot. The rising time is 6.6 ms. The grid current error is shown in figure 7.5d.

7.4.3 Thermal Analysis

Loss Analysis The loss analysis for different operation conditions is shown in figure 7.6. It is proved again that the loss distribution for three-level NPC converters is unbalanced. The conduction losses depend on the operation points, so they are almost

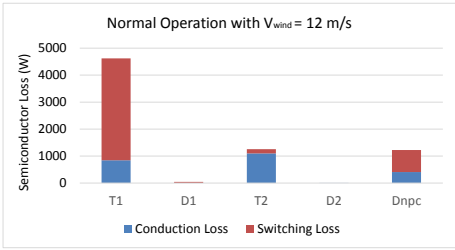

(a) *Case 1:* $P = 1.0$ *and* $Q = 0$

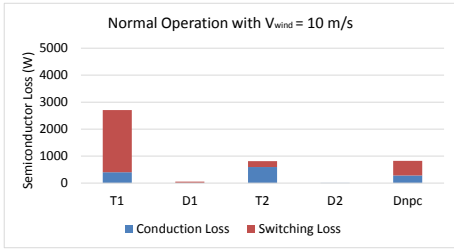

(b) *Case 2:* $P = 0.61$ *and* $Q = 0$

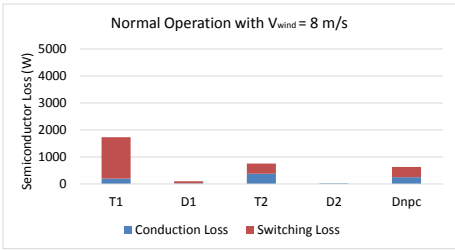

(c) *Case 3:* $P = 0.31$ *and* $Q = 0$

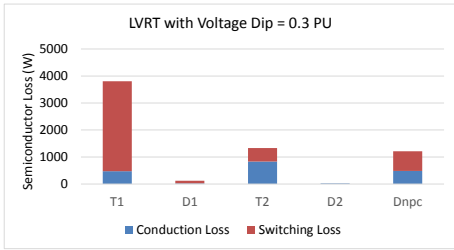

(d) *Case 4:* $P = 0.56$ *and* $Q = 0.42$

Figure 7.6: *Losses Analysis at Different Operation Points with BSC*

Table 7.1: *BSC Control with different Switching Frequencies at Nominal Operation*

$f_{\overline{SW}}$ (Hz)	THD (%)	P_{loss} (kW)	η (%)
957	2.16	70.10	98.60
749	2.38	54.37	98.91
598	3.80	42.89	99.14
501	7.03	34.61	99.31

the same as for the previous three methods. Compared to the VOC (figure 5.13), BSC has not achieved lower switching losses. Especially, for the LVRT with voltage dip 0.3 PU, the losses of outer switches are obviously increased compared to VOC. For the same operation point, e.g., nominal operation, loss analysis with different switching frequencies is also conducted, and shown in figure 7.7. Information on the switching frequencies is given in table 7.1. It can be noted that THD and losses are in the same range with VOC (table 5.9).

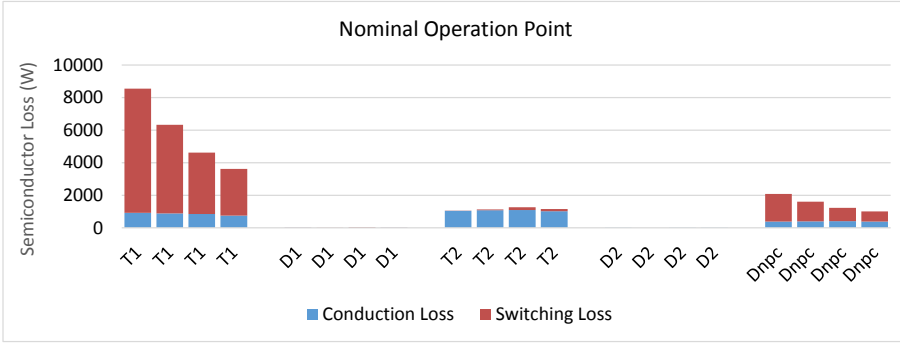

Figure 7.7: *Loss Distribution for Different Switching Frequencies at Nominal Operation Point with BSC (Refer to table 7.1)*

Temperature Estimation The average junction temperature estimation for different operation points is shown in figure 7.8. Corresponding to the loss distribution, the temperature estimation for the semiconductors is uneven either, and the BSC method has much higher temperature stress during the LVRT operation. The average junction temperature for different control parameters and nominal operation is shown in figure 7.9. In the first case, the average junction temperature of T_1 has already reached 115℃, which is near to the maximum operation value 125℃. From table 7.1, the average frequency for this case is around 957 Hz. This shows that the selected MV IGBT should operate below 1000 Hz.

7.4.4 Performance under Abnormal Grid Voltage

Balanced Grid Voltage Dips As designed in section 5.4.1, two cases with balanced grid voltage dip are also conducted for the BSC method. Case 3, three-phase grid voltage drops to 0.7 PU (at 0.66 s) is shown in figure 7.10. The converter and grid currents are shown in figure 7.10b and figure 7.10c, respectively. Both are well regulated. The dynamics can be seen from the grid side active and reactive power in figure 7.10d. The rising times of active and reactive power are 2.8 ms and 4.6 ms, indicating a good dynamics. The average switching frequency around 1031 Hz for case 3, is slightly increased compared to normal operation (figure 7.3a). The upper and lower capacitor voltage is well controlled in the boundary, 1% of half the DC-link voltage.

Case 4, three-phase grid voltage drops to 0.5 PU, is shown in figure 7.11. There is an overshoot of the converter and grid current (7.11b and 7.11c) which is around 1.5 PU phase current. The dynamic is very fast which can be seen clearly in the grid side injected power tracking (figure 7.11d). The rising time of the active power is around 4.3 ms and for the reactive power is around 6.2 ms. During the LVRT, the average

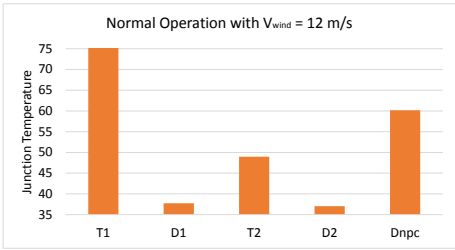

(a) Case 1: $P = 1.0$ and $Q = 0$

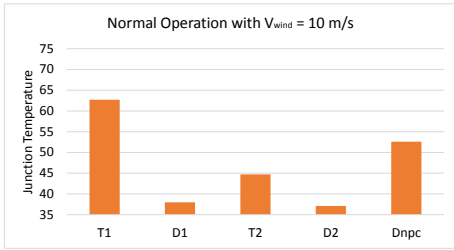

(b) Case 2: $P = 0.61$ and $Q = 0$

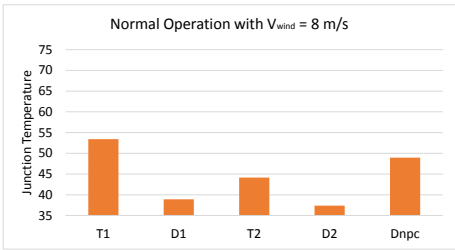

(c) Case 3: $P = 0.31$ and $Q = 0$

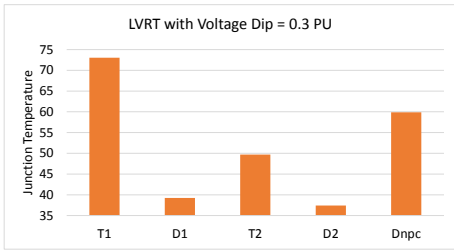

(d) Case 4: $P = 0.56$ and $Q = 0.42$

Figure 7.8: *Average Junction Temperature at Different Operation Points with BSC*

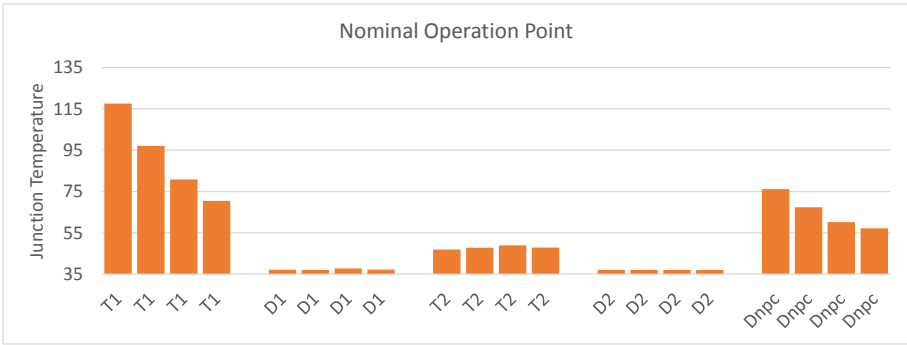

Figure 7.9: *Average Junction Temperature for Different Switching Frequencies at Nominal Operation Point with BSC (Refer to table 7.1)*

switching frequency is around 866 Hz lower than in case 3. Especially, the switching frequency for outer switch T_1 and inner switch T_2 are 725 Hz and 1000 Hz respectively. For compromise, the DC-link voltage balancing slightly leaves the boundary. However, the difference between upper and lower capacitor voltage is still under 2 % of half DC-link voltage.

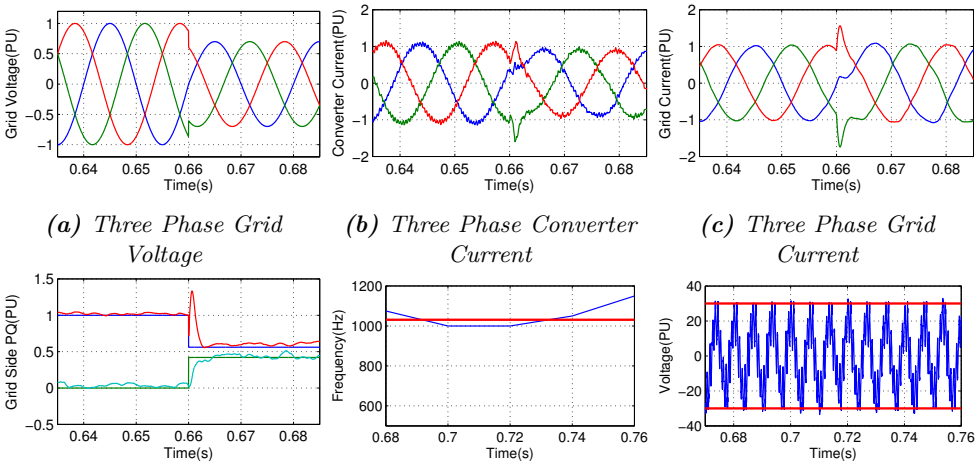

(a) Three Phase Grid Voltage *(b) Three Phase Converter Current* *(c) Three Phase Grid Current*

(d) Grid Active and Reactive Power *(e) Average Switching Frequency* *(f) Capacitor Voltage* $v_{dc1} - v_{dc2}$

Figure 7.10: *BSC Case 3 Three-phase Grid Voltage Drops to* 0.7 PU

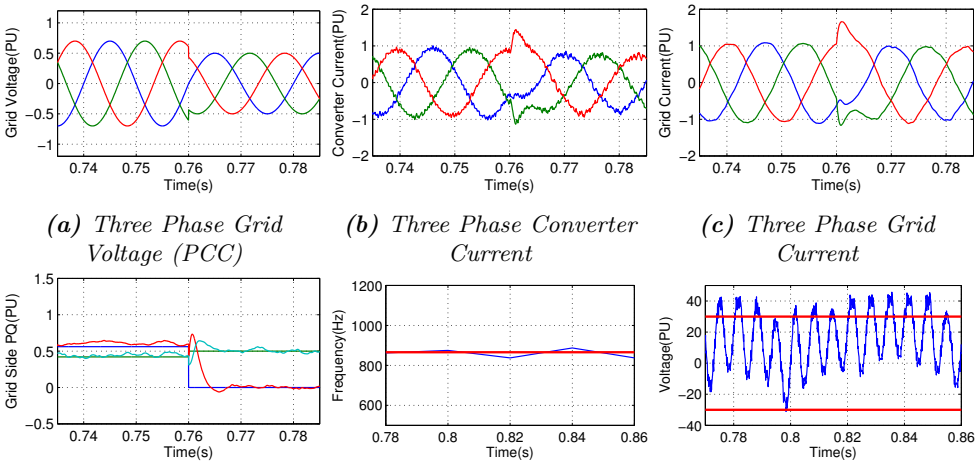

(a) Three Phase Grid Voltage (PCC) *(b) Three Phase Converter Current* *(c) Three Phase Grid Current*

(d) Grid Active and Reactive Power *(e) Average Switching Frequency* *(f) Capacitor Voltage* $v_{dc1} - v_{dc2}$

Figure 7.11: *BSC Case 4 Three-phase Grid Voltage Drops to* 0.5 PU

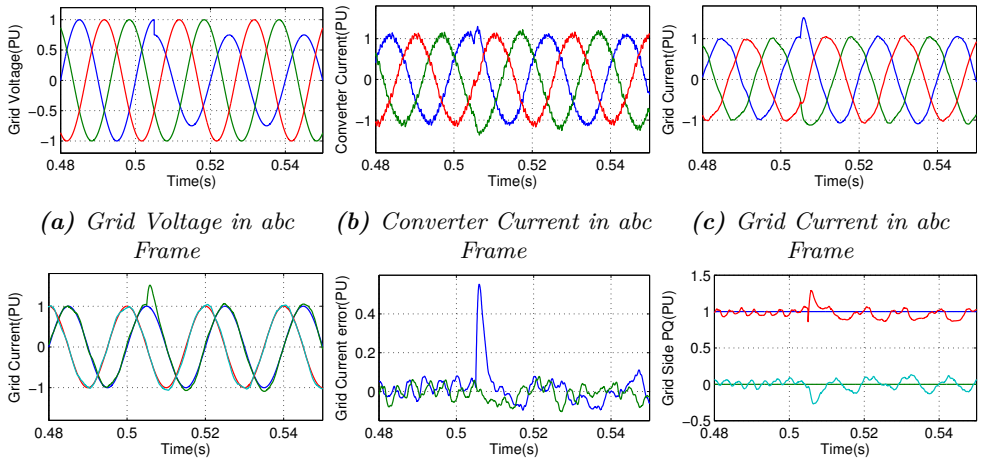

(a) *Grid Voltage in abc Frame*

(b) *Converter Current in abc Frame*

(c) *Grid Current in abc Frame*

(d) *Grid Current in $\alpha\beta$ Frame*

(e) *Grid Current Tracking Error*

(f) *Grid Active and Reactive Power*

Figure 7.12: *BSC Grid Voltage Phase B Drops to 75% of the Rated Value at* 0.505 s

Unbalanced Grid Voltage Dips In order to verify the robustness of the BSC method, an unbalanced grid voltage is analysed. Figure 7.12 shows the results with grid voltage phase B dropping to 75% of the rated value. It is assumed that the control objective during unbalanced grid voltage is to control the grid current to be still symmetrical. At non-ideal grid voltage, the grid current reference can not be calculated by employing equation 7.17. Here, the grid current reference is directly given as pure sinusoidal signal in $\alpha\beta$ frame. The two pure sinusoidal signals references can be found in figure 7.12d. The tracking error of the grid side current is shown in figure 7.12e. The steady state error is controlled inside of a 10% error band. Due the unbalanced grid voltage, the injected active and reactive power are oscillating as shown in figure 7.12f.

Distorted Grid Voltage Besides an unbalanced grid voltage which happens under grid faults, a distorted grid voltage is quite common in power systems. In order to evaluated the BSC during distorted grid voltage, the fifth and seventh order harmonics with an amplitude 5% of the rated value are injected in the grid voltage (figure 7.13a,7.13b). The most important advantage of BSC is that it can generally suppress the grid current harmonics without an additional control structure. The controlled grid current is shown in figure 7.13e, its FFT analysis in figure 7.13f. The low order harmonics are suppressed in the grid current, and the THD is only 2.1%. This means the BSC method can handle the grid current harmonics caused by a distorted grid voltage effectively. It should be noted that for a better performance, the controller parameter k_1,k_2 and k_3

have been increased with 1.5 margin. The current tracking in the $\alpha\beta$ frame is shown in figure 7.13g, the tracking error in figure 7.13h, which indicates the steady state error is well regulated in the 5% error band. The main reason for this is that the BSC method has considered the grid voltage in the nonlinear control design process. So the control variables ($u_{\alpha,\beta}$) contain the relevant information for the modulation process, which modulates the converter voltage so that the current contains relevant order harmonics, seen in figure 7.13c and figure 7.13d. From the FFT analysis it can be noted that besides the characteristic frequency spectrum around the switching frequency and its multiples, the fifth and seventh order harmonics appear. Due to the distorted grid voltage, the fifth and seventh order harmonics exist in the capacitor current. According to the Kirchhoff current law, $i_2 = i_1 - i_c$, the grid current will not contain relevant order harmonics. Due to the fifth and seventh order 5 % amplitude grid voltage injection, the reactive power has a ripple with 300 Hz.

7.4.5 Performance with Parameter Mismatch

Due to the power system becoming more complex, the grid impedance varies commonly, and a parameter mismatch is expected, i.e., that the parameters in the controller are different from the real physical values. This could be improved by adaptive control which can identify real values and adjust the controller parameters accordingly. However, this will make the controller more complicated. Another way to solve this problem is to improve the robustness of the controller for parameter mismatch. In order to verify the operation of BSC with parameter mismatch, two cases are studied. Keeping the controller parameters the same, the first case is to increase the L_2 to 150% of its original value, and the second one is to decrease L_2 to 50% of its original value. The results of both cases are shown in figure 7.14 and figure 7.15. It can be found that a 50% mismatch of parameter L_2 does not obviously affect the system performance. Only is the reactive power has a slight steady state error, which can be accepted.

7.5 Summary

In this chapter, the backstepping method is introduced and improved for grid converter control with LCL filter applications. BSC is a nonlinear controller based on the Lyapunov function, and zero steady state error can be achieved theoretically. First, an overview of the BSC method is described in subsection 7.1. The origin of BSC and the development and applications are discussed. Until now, there are few applications for power converter control. However, due to its advantages, e.g., general suppression of grid current harmonics, zero steady state error, nonlinear characteristics handling and good dynamic performance, BSC becomes an attractive control method for power converter control.

Second, backstepping controller design is discussed step by step. The stability analysis is conducted by employing the Lyapunov theorem. Since the BSC needs the full

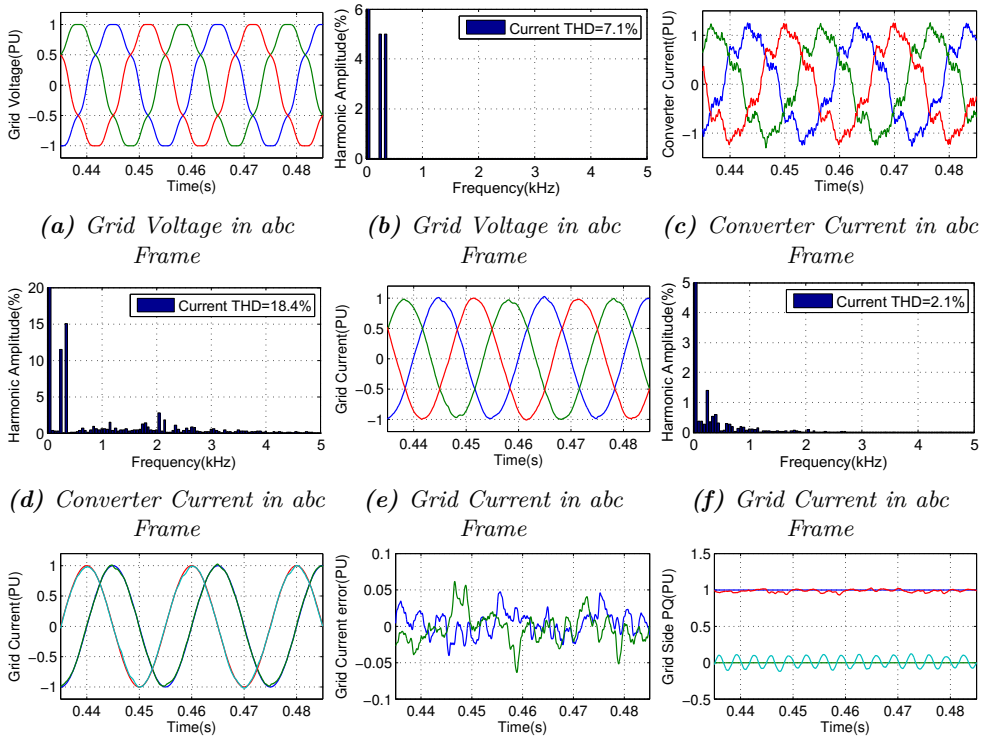

(a) *Grid Voltage in abc Frame*

(b) *Grid Voltage in abc Frame*

(c) *Converter Current in abc Frame*

(d) *Converter Current in abc Frame*

(e) *Grid Current in abc Frame*

(f) *Grid Current in abc Frame*

(g) *Grid Current in $\alpha\beta$ Frame*

(h) *Grid Current Tracking Error*

(i) *Grid Active and Reactive Power*

Figure 7.13: *BSC Grid Voltage Contains 5% of the Fundamental Amplitude Harmonics at 5th and 7th Order*

information of states, in order to reduce the measurement sensors, a full state Luenberg observer design including the feedback matrix selection is presented in subsection 7.3.

Finally, simulations have been conducted for the verification of BSC at different scenarios. The results prove that BSC has been implemented correctly and can be successfully applied for power converter control.

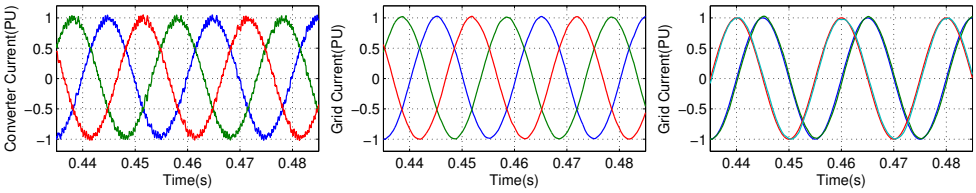

(a) Converter Current in abc Frame *(b) Grid Current in abc Frame* *(c) Grid Current in αβ Frame*

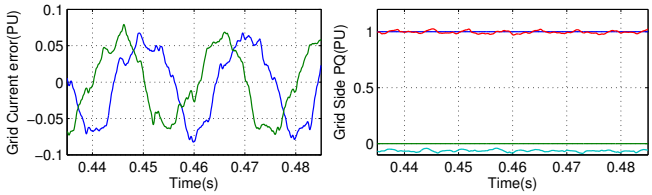

(d) Grid Current Tracking Error *(e) Active and Reactive Power Tracking*

Figure 7.14: *BSC Grid Impedance L_2 Mismatch with 50% more than Initial Value*

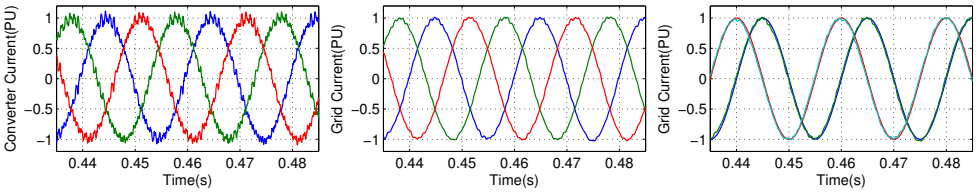

(a) Converter Current in abc Frame *(b) Grid Current in abc Frame* *(c) Grid Current in αβ Frame*

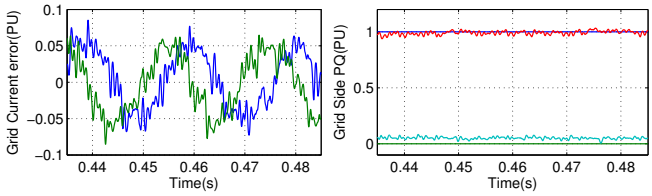

(d) Grid Current Tracking Error *(e) Active and Reactive Power Tracking*

Figure 7.15: *BSC Grid Impedance L_2 Mismatch with 50% less than Initial Value*

Part IV

Conclusions

8 Summary and Outlook

8.1 Summary and Contribution

With the development of renewable energy power generation all over the world, grid converters are becoming a key equipment between the power generation and the grid. This thesis focuses on MV grid current control of megawatt wind energy conversion systems. For the investigation, first, a megawatt wind energy conversion system is designed. Key parts of the system are modelled in Chapter 3, including the grid converter, the DC-link capacitor, the LCL filter and the PCC voltage. In order to verify the algorithms practically, a scaled down low voltage system setup is also designed and built in the laboratory. For controlling the grid side converters with the LCL filter, stability analysis is conducted regarding two current feedback options, which are grid current feedback control and converter current feedback control. The stability range considering sampling frequency and resonance frequency is derived. In order to damp the resonances of the LCL filter, both passive damping and active damping methods are analysed in detail, and active damping is implemented for MPC. For grid converter control, it is necessary to fulfil the grid code in different operation modes. The latest grid codes of different countries and areas are collected, and especially the German grid code regarding fault ride-through is studied. Besides stability and power quality, thermal performance is an aspect for evaluation of the system. Loss analysis and temperature estimation methods are introduced in Chapter 4. Based on the results of Chapter 3 and 4, grid converter control strategies are investigated in Chapter 5. Voltage Oriented Control (VOC) is the state of the art grid converter control method, which is a mature control strategy used in industry. However, it is difficult to improve the performance of the classic VOC. Due to this reason, several control strategies are investigated, i.e., Direct Power Control

(DPC), Model Predictive Control (MPC) and Backstepping Control (BSC). DPC and MPC are two direct control methods without modulation process, while BSC is implemented with modulation, and therefore belongs to the indirect control methods. For MPC, both single step MPDCC and multiple steps MPDCC are investigated.

Based on the analysis results of these control methods, a spider chart is exhibited in figure 8.1. Three specifications concerning steady state, average switching frequency, THD and efficiency, and two specifications concerning transients, rising time and overshoot are illustrated for a 0.7 PU Voltage Dip. It can be found that among the four methods, Multiple Steps MPDCC can achieve the best efficiency with the lowest average switching frequency considering the same level of THD. However, for the transients, MS-MPDCC might react a bit slower but still in a reasonable range.

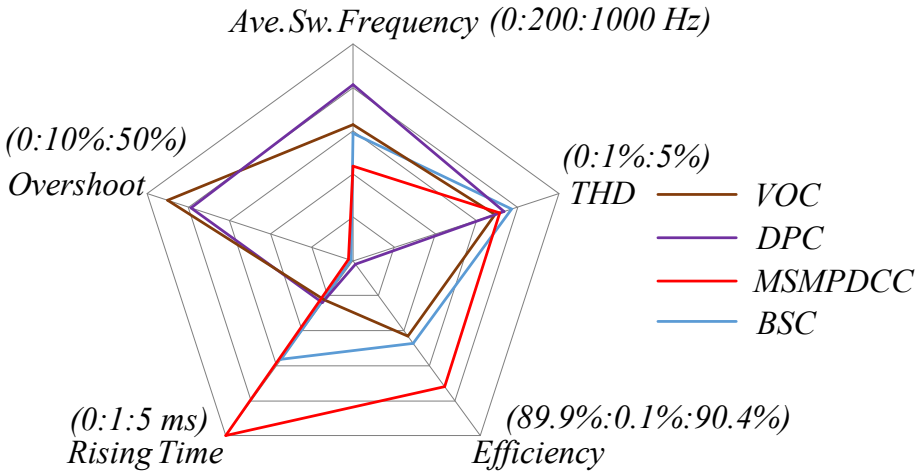

Figure 8.1: *Spider Chart Comparing the VOC, DPC, DPC and MSMPDCC in Terms of Average Switching Frequency (Ave.Sw.Frequency), THD, Efficiency, Step Response Rising Time and Overshoot with* 0.7 PU *Voltage Dip*

The objective of this thesis is to try to find a current control strategy to improve the efficiency of large wind energy conversion systems without sacrificing dynamic performance, steady state performance and power quality. In order to evaluate the four mentioned control strategies, both normal and abnormal operation at several typical operation points are investigated considering the dynamic, steady state, LVRT and thermal analysis. It can be found that MS-MPDCC can achieve the lowest switching frequency meanwhile the THD of the current is kept below 5% which complies with the grid code. The main contributions of this thesis to the state of the art can be summarized as follows:

– ***Power Electronics Design for Megawatt WECS with MV Multi-level Converter***

As reviewed in table 1.1, there are few MV multi-level converter WECS in the market. However, with the increasing of single wind turbine power rating, the MV converter WECS is a promising alternative for the next generation wind turbines. This thesis presents and discusses the most important power electronics parts of WECS in detail, and gives particular design methods from the electrical engineering perspective.

– ***Proposed Multiple Steps Prediction Control for Grid Converter***

The switching frequency of a MV converter is a limitation for the converter operation. The switching frequency is directly connected to the semiconductor losses, reliability, current quality and grid filter design. LCL filters have been proved a superior filter type for MV converters compared to a single L filter. In order to reduce the switching frequency further, multiple steps model predictive direct current control is proposed for the grid converter control. In order to reduce the sensor quantity, a full order observer is developed. Active damping is proposed for the system to eliminate damping losses. With these three approaches, the WECS performance can be noticeably improved in terms of efficiency.

– ***Proposed Advanced Non-linear Control for Grid Converter***

With the systems becoming more complex, the grid impedance and other system parameters might change all the time. This will cause a mismatch between the predictive model and the real system, which might lead to unexpected control errors. In order to solve these problems, an advanced non-linear control is proposed. The control performance has been verified in simulation for unsymmetrical faults, parameter mismatch and distorted grid voltage.

– ***Comprehensive Comparison of Grid Converter Control Strategies***

A comprehensive comparison among the state of the art, i.e., VOC, DPC, the emerging model predictive control including single step and multiple steps solutions and the advanced non-linear control, backstepping control has been conducted in terms of transient, steady state, LVRT, thermal performance and efficiency. This investigation forms a good base for further research.

8.2 Further Research Perspectives

Although several aspects regarding power electronics for megawatt WECS have been discussed and investigated in detail, there are still many open research points. Some of them are listed below:

- In this thesis, three-level NPC is chosen as the grid converter. Due to the voltage limit of the semiconductors, it is difficult to achieve a voltage level like 33 kV to directly connect the MV grid without a transformer. A transformer-less WECS could be implemented with other topologies, e.g., series-connected H-Bridges, or with new generation semiconductors with high blocking voltage. This is an interesting research point for future wind turbines.
- For the active damping implementation, a virtual resistor is a common concept which is adopted here. However, the optimal resistance for different operation points could be a research point for the active damping improvement. Also different active damping methods comparison is an interesting point.
- In the thesis, the LCL-filter is designed assuming the spectrum of space vector modulation, which is not optimal for other direct control without modulator, e.g., DPC and MPC. The LCL-filter optimization for these methods is an important research point.
- For the LVRT, only symmetrical grid faults are considered in the thesis. Unsymmetrical grid faults are definitively a crucial scenario which needs to be researched. Especially for the backstepping control, due to its superior robustness, unsymmetrical faults are not a big challenge. It is valuable to compare the control algorithms performance for the unsymmetrical faults.

Moreover, evaluating on the power converters based on the new generation power semiconductors, e.g., SiC, considering the thermal performance is an interesting point as well. Besides those technical topics, the development and implementation of MV wind energy conversion system from the cost view is very important and valuable for investigation.

Bibliography

[1] BP, "BP Statistical Review of World Energy 2016," [Online]. Available: http://www.bp.com, Jun. 2016.

[2] Federal Ministry of Economics and Technology, "Energy Concept for an Environmentally Sound, Reliable and Affordable Energy Supply," [Online]. Available: http://www.bmwi.de, Sep. 2010.

[3] A. Rudd, "Speech on a new direction for UK energy policy," [Online]. Available: https://www.gov.uk, Nov. 2015.

[4] REN21, "RENEWABLES 2017 - GLOBAL STATUS REPORT," [Online]. Available: http://www.ren21.net, Jun. 2017.

[5] M. V. O. Wind, "V164-8.0 MW breaks world record for wind energy production," [Online]. Available: http://www.mhivestasoffshore.com, Jan. 2014.

[6] Adwen, "8 MW PLATFORM," [Online]. Available: http://www.adwenoffshore.com, Jun. 2016.

[7] REN21, "Siemens expands portfolio with 8 MW offshore wind turbine," [Online]. Available: http://www.siemens.com/, Jul. 2016.

[8] V. Yaramasu, B. Wu, P. C. Sen, S. Kouro, and M. Narimani, "High-power wind energy conversion systems: State-of-the-art and emerging technologies," *Proceedings of the IEEE*, vol. 103, no. 5, pp. 740–788, 2015.

[9] F. Blaabjerg and K. Ma, "Future on Power Electronics for Wind Turbine Systems," *IEEE Journal of Emerging and Selected Topics in Power Electronics*, vol. 1, no. 3, pp. 139–152, 2013.

[10] N. Holtsmark, H. J. Bahirat, M. Molinas, B. A. Mork, and H. K. Hoidalen, "An All-DC Offshore Wind Farm With Series-Connected Turbines: An Alternative to the Classical Parallel AC Model?" *IEEE Transactions on Industrial Electronics*, vol. 60, no. 6, pp. 2420–2428, 2013.

[11] M. A. Bahmani, T. Thiringer, A. Rabiei, and T. Abdulahovic, "Comparative Study of a Multi-MW High-Power Density DC Transformer With an Optimized High-Frequency Magnetics in All-DC Offshore Wind Farm," *IEEE Transactions on Power Delivery*, vol. 31, no. 2, pp. 857–866, 2016.

[12] R. Cardenas, R. Pena, S. Alepuz, and G. Asher, "Overview of Control Systems for the Operation of DFIGs in Wind Energy Applications," *IEEE Transactions on Industrial Electronics*, vol. 60, no. 7, pp. 2776–2798, 2013.

[13] R. Pena, J. C. Clare, and G. M. Asher, "Doubly fed induction generator using back-to-back PWM converters and its application to variable-speed wind-energy generation," *IEE Proceedings - Electric Power Applications*, vol. 143, no. 3, pp. 231–241, 1996.

[14] M. Chinchilla, S. Arnaltes, and J. C. Burgos, "Control of permanent-magnet generators applied to variable-speed wind-energy systems connected to the grid," *IEEE Transactions on Energy Conversion*, vol. 21, no. 1, pp. 130–135, 2006.

[15] M. E. Haque, M. Negnevitsky, and K. M. Muttaqi, "A Novel Control Strategy for a Variable-Speed Wind Turbine With a Permanent-Magnet Synchronous Generator," *IEEE Transactions on Industry Applications*, vol. 46, no. 1, pp. 331–339, 2010.

[16] S. M. Muyeen, R. Takahashi, T. Murata, and J. Tamura, "A variable speed wind turbine control strategy to meet wind farm grid code requirements," *IEEE Transactions on Power Systems*, vol. 25, no. 1, pp. 331–340, 2010.

[17] M. Liserre, R. Cardenas, M. Molinas, and J. Rodriguez, "Overview of Multi-MW Wind Turbines and Wind Parks," *IEEE Transactions on Industrial Electronics*, vol. 58, no. 4, pp. 1081–1095, 2011.

[18] K. H. Tan, "Squirrel-Cage Induction Generator System Using Wavelet Petri Fuzzy Neural Network Control for Wind Power Applications," *IEEE Transactions on Power Electronics*, vol. 31, no. 7, pp. 5242–5254, 2016.

[19] M. G. Simoes, B. K. Bose, and R. J. Spiegel, "Fuzzy logic based intelligent control of a variable speed cage machine wind generation system," *IEEE Transactions on Power Electronics*, vol. 12, no. 1, pp. 87–95, 1997.

[20] H. Chen and D. C. Aliprantis, "Analysis of Squirrel-Cage Induction Generator With Vienna Rectifier for Wind Energy Conversion System," *IEEE Transactions on Energy Conversion*, vol. 26, no. 3, pp. 967–975, 2011.

[21] K. Ma, *Power Electronics For The Next Generation Wind Turbine System.* Springer, May 2015.

[22] L. H. Hansen, L. Helle, F. Blaabjerg, E. Ritchie, S. MunkNielsen, H. Bindner, P. Sørensen, and B. Bak-Jensen, "Conceptual survey of Generators and Power Electronics for Wind Turbines," Risø National Laboratory, Roskilde, Denmark, Dec. 2001.

[23] Y. Song and F. Blaabjerg, "Overview of DFIG-based Wind Power System Resonances under Weak Networks," *IEEE Transactions on Power Electronics*, vol. PP, no. 99, pp. 1–1, 2016.

[24] J. M. Carrasco, L. G. Franquelo, J. T. Bialasiewicz, E. Galvan, R. C. PortilloGuisado, M. A. M. Prats, J. I. Leon, and N. Moreno-Alfonso, "Power-Electronic Systems for the Grid Integration of Renewable Energy Sources: A Survey," *IEEE Transactions on Industrial Electronics*, vol. 53, no. 4, pp. 1002–1016, 2006.

[25] W. Erdman and M. Behnke, "Low Wind Speed Turbine Project Phase II: The Application of Medium-Voltage Electrical Apparatus to the Class of Variable Speed Multi-Megawatt Low Wind Speed Turbines," [Online]. Available: http://www.nrel.gov, Jun. 2005.

[26] H. Bevrani, T. Ise, and Y. Miura, "Virtual synchronous generators: A survey and new perspectives," *International Journal of Electrical Power and Energy Systems*, vol. 54, pp. 244 – 254, 2014.

[27] Standardization Administration of the P.R.C., "Standard voltages," *GB/T 156-2007*, Apr. 2007.

[28] J. Rodriguez, S. Bernet, B. Wu, J. O. Pontt, and S. Kouro, "Multilevel voltage-source-converter topologies for industrial medium-voltage drives," *IEEE Transactions on Industrial Electronics*, vol. 54, no. 6, pp. 2930–2945, 2007.

[29] J. Rodriguez, J.-S. Lai, and F. Z. Peng, "Multilevel inverters: a survey of topologies, controls, and applications," *IEEE Transactions on Industrial Electronics*, vol. 49, no. 4, pp. 724–738, 2002.

[30] A. Nabae, I. Takahashi, and H. Akagi, "A New Neutral-Point-Clamped PWM Inverter," *IEEE Transactions on Industry Applications*, vol. IA-17, no. 5, pp. 518–523, 1981.

[31] S. Ogasawara and H. Akagi, "Analysis of variation of neutral point potential in neutral-point-clamped voltage source PWM inverters," in *Conference Record of the 1993 IEEE Industry Applications Conference Twenty-Eighth IAS Annual Meeting*, 1993, pp. 965–970.

[32] C. Newton and M. Sumner, "Neutral point control for multi-level inverters: theory, design and operational limitations," in *Industry Applications Conference, 1997. Thirty-Second IAS Annual Meeting, IAS '97., Conference Record of the 1997 IEEE*, vol. 2, 1997, pp. 1336–1343.

[33] N. Celanovic and D. Boroyevich, "A comprehensive study of neutral-point voltage balancing problem in three-level neutral-point-clamped voltage source PWM inverters," *IEEE Transactions on Power Electronics*, vol. 15, no. 2, pp. 242–249, 2000.

[34] J. E. Espinoza, J. R. Espinoza, and L. A. Moran, "A systematic controller-design approach for neutral-point-clamped three-level inverters," *IEEE Transactions on Industrial Electronics*, vol. 52, no. 6, pp. 1589–1599, 2005.

[35] A. Bendre, G. Venkataramanan, D. Rosene, and V. Srinivasan, "Modeling and design of a neutral-point voltage regulator for a three-level diode-clamped inverter using multiple-carrier modulation," *IEEE Transactions on Industrial Electronics*, vol. 53, no. 3, pp. 718–726, 2006.

[36] T. Bruckner and S. Bemet, "Loss balancing in three-level voltage source inverters applying active NPC switches," in *Power Electronics Specialists Conference, 2001. PESC. 2001 IEEE 32nd Annual*, vol. 2, 2001, pp. 1135–1140.

[37] T. Bruckner, S. Bernet, and H. Guldner, "The active NPC converter and its loss-balancing control," *IEEE Transactions on Industrial Electronics*, vol. 52, no. 3, pp. 855–868, 2005.

[38] C. Dietrich, S. Gediga, M. Hiller, R. Sommer, and H. Tischmacher, "A new 7.2kV medium voltage 3-Level-NPC inverter using 6.5kV-IGBTs," in *2007 European Conference on Power Electronics and Applications*, 2007, pp. 1–9.

[39] O. S. Senturk, L. Helle, S. Munk-Nielsen, P. Rodriguez, and R. Teodorescu, "Medium voltage three-level converters for the grid connection of a multi-MW wind turbine," in *2009 13th European Conference on Power Electronics and Applications*, 2009, pp. 1–8.

[40] W. L. Erdman, J. Keller, D. Grider, and E. VanBrunt, "A 2.3-MW Medium-voltage, three-level wind energy inverter applying a unique bus structure and 4.5-kV Si/SiC hybrid isolated power modules," in *2015 IEEE Applied Power Electronics Conference and Exposition (APEC)*, March 2015, pp. 1282–1289.

[41] D. Krug, S. Bernet, S. S. Fazel, K. Jalili, and M. Malinowski, "Comparison of 2.3-kV Medium-Voltage Multilevel Converters for Industrial Medium-Voltage Drives," *IEEE Transactions on Industrial Electronics*, vol. 54, no. 6, pp. 2979–2992, Dec 2007.

[42] M. Hagiwara and H. Akagi, "Control and experiment of pulsewidth-modulated modular multilevel converters," *IEEE Transactions on Power Electronics*, vol. 24, no. 7, pp. 1737–1746, July 2009.

[43] P. W. Hammond, "A new approach to enhance power quality for medium voltage ac drives," *IEEE Transactions on Industry Applications*, vol. 33, no. 1, pp. 202–208, Jan 1997.

[44] H. Akagi, "Classification, Terminology, and Application of the Modular Multilevel Cascade Converter (MMCC)," *IEEE Transactions on Power Electronics*, vol. 26, no. 11, pp. 3119–3130, Nov 2011.

[45] M. Malinowski, K. Gopakumar, J. Rodriguez, and M. A. Perez, "A survey on cascaded multilevel inverters," *IEEE Transactions on Industrial Electronics*, vol. 57, no. 7, pp. 2197–2206, July 2010.

[46] N. Thitichaiworakorn, M. Hagiwara, and H. Akagi, "A Medium-Voltage Large Wind Turbine Generation System Using an AC/AC Modular Multilevel Cascade Converter," *IEEE Journal of Emerging and Selected Topics in Power Electronics*, vol. 4, no. 2, pp. 534–546, 2016.

[47] A. Lesnicar and R. Marquardt, "An innovative modular multilevel converter topology suitable for a wide power range," in *2003 IEEE Bologna Power Tech Conference Proceedings,*, vol. 3, June 2003, p. 6.

[48] M. Saeedifard and R. Iravani, "Dynamic Performance of a Modular Multilevel Back-to-Back HVDC System," *IEEE Transactions on Power Delivery*, vol. 25, no. 4, pp. 2903–2912, Oct 2010.

[49] S. Rohner, S. Bernet, M. Hiller, and R. Sommer, "Modulation, losses, and semiconductor requirements of modular multilevel converters," *IEEE Transactions on Industrial Electronics*, vol. 57, no. 8, pp. 2633–2642, Aug 2010.

[50] S. Allebrod, R. Hamerski, and R. Marquardt, "New transformerless, scalable Modular Multilevel Converters for HVDC-transmission," in *2008 IEEE Power Electronics Specialists Conference*, June 2008, pp. 174–179.

[51] M. Glinka and R. Marquardt, "A new AC/AC multilevel converter family," *IEEE Transactions on Industrial Electronics*, vol. 52, no. 3, pp. 662–669, June 2005.

[52] Q. Tu, Z. Xu, and L. Xu, "Reduced switching-frequency modulation and circulating current suppression for modular multilevel converters," *IEEE Transactions on Power Delivery*, vol. 26, no. 3, pp. 2009–2017, July 2011.

[53] J. Kucka, D. Karwatzki, and A. Mertens, "AC/AC modular multilevel converters in wind energy applications: Design considerations," in *2016 18th European Conference on Power Electronics and Applications (EPE'16 ECCE Europe)*, Sept 2016, pp. 1–10.

[54] E. dos Santos and E. R. da Silva, *Advanced Power Electronics Converters: PWM Converters Processing AC Voltages*. Wiley-IEEE Press, November 2014.

[55] D. Andler, "Experimental investigation of three-level active neutral point clamped voltage source converters using integrated gate-commutated thyristors," Ph.D. Thesis, Technische Universität Dresden, 2013.

[56] N. Iwamuro and T. Laska, "IGBT History, State-of-the-Art, and Future Prospects," *IEEE Transactions on Electron Devices*, vol. 64, no. 3, pp. 741–752, March 2017.

[57] K. Vechalapu, S. Bhattacharya, E. VanBrunt, S. H. Ryu, D. Grider, and J. Palmour, "Comparative Evaluation of 15 kV SiC MOSFET and 15 kV SiC IGBT for Medium Voltage Converter under Same dv/dt Conditions," *IEEE Journal of Emerging and Selected Topics in Power Electronics*, vol. PP, no. 99, pp. 1–1, 2016.

[58] K. Mainali, A. Tripathi, S. Madhusoodhanan, A. Kadavelugu, D. Patel, S. Hazra, K. Hatua, and S. Bhattacharya, "A Transformerless Intelligent Power Substation: A three-phase SST enabled by a 15-kV SiC IGBT," *IEEE Power Electronics Magazine*, vol. 2, no. 3, pp. 31–43, Sept 2015.

[59] H. Li and Z. Chen, "Overview of different wind generator systems and their comparisons," *IET Renewable Power Generation*, vol. 2, no. 2, pp. 123–138, 2008.

[60] J. Li, A. Q. Huang, S. Bhattacharya, and W. Jing, "Application of active NPC converter on generator side for MW direct-driven wind turbine," in *2010 Twenty-Fifth Annual IEEE Applied Power Electronics Conference and Exposition (APEC)*, Feb 2010, pp. 1010–1017.

[61] R. Teodorescu, M. Liserre, and P. Rodriguez, *Grid converters for photovoltaic and wind power systems.* Hoboken, NJ, USA: Wiley, 2011.

[62] G. Michalke, "Variable speed wind turbines modelling, control, and impact on power systems," Ph.D. Thesis, Technische Universität Darmstadt, 2008.

[63] L. Quéval and H. Ohsaki, "Back-to-back converter design and control for synchronous generator-based wind turbines," in *2012 International Conference on Renewable Energy Research and Applications (ICRERA)*, Nov 2012, pp. 1–6.

[64] B. M. Wilamowski and J. D. Irwin, *The Industrial Electronics Handbook, Second Edition.* CRC Press, March 2011.

[65] T. C. Y. Wang, Z. Ye, G. Sinha, and X. Yuan, "Output filter design for a grid-interconnected three-phase inverter," in *Power Electronics Specialist Conference, 2003. PESC '03. 2003 IEEE 34th Annual*, vol. 2, 2003, pp. 779–784 vol.2.

[66] A. A. Rockhill, M. Liserre, R. Teodorescu, and P. Rodriguez, "Grid-filter design for a multimegawatt medium-voltage voltage-source inverter," *IEEE Transactions on Industrial Electronics*, vol. 58, no. 4, pp. 1205–1217, 2011.

[67] R. Beres, X. Wang, F. Blaabjerg, C. L. Bak, and M. Liserre, "A review of passive filters for grid-connected voltage source converters," in *2014 IEEE Applied Power Electronics Conference and Exposition - APEC 2014*, 2014, pp. 2208–2215.

[68] Y. Jiao and F. C. Lee, "LCL Filter Design and Inductor Current Ripple Analysis for a Three-Level NPC Grid Interface Converter," *IEEE Transactions on Power Electronics*, vol. 30, no. 9, pp. 4659–4668, 2015.

[69] R. Meyer and A. Mertens, "Design of LCL filters in consideration of parameter variations for grid-connected converters," in *2012 IEEE Energy Conversion Congress and Exposition (ECCE)*, 2012, pp. 557–564.

[70] H. Yin, M. Dereschkewitz, D. Wagenitz, and S. Dieckerhoff, "A versatile test bench for grid integration investigations of back-to-back wind energy conversion systems," in *Renewable Energy Research and Application (ICRERA), 2014 International Conference on*, 2014, pp. 695–700.

[71] J. Brahmi, L. Krichen, and A. Ouali, "A comparative study between three sensorless control strategies for {PMSG} in wind energy conversion system," *Applied Energy*, vol. 86, no. 9, pp. 1565 – 1573, 2009.

[72] X. Wang, S. Yuvarajan, and L. Fan, "MPPT control for a PMSG-based grid-tied wind generation system," in *North American Power Symposium (NAPS), 2010*, 2010, pp. 1–7.

[73] S. Alepuz, A. Calle, S. Busquets-Monge, J. Bordonau, S. Kouro, and B. Wu, "Control scheme for low voltage ride-through compliance in back-to-back NPC converter based wind power systems," in *2010 IEEE International Symposium on Industrial Electronics*, 2010, pp. 2357–2362.

[74] T. Brückner, *The Active NPC Converter for Medium Voltage Drives.* Aachen, Germany: Shaker Verlag, 2006.

[75] F. B. M. P. Kazmierkowski, R. Krishnan, *Control in Power Electronics: Selected Problems.* Amsterdam, The Netherlans: Academic Press, 2002.

[76] M. Liserre, F. Blaabjerg, and S. Hansen, "Design and control of an LCL-filter-based three-phase active rectifier," *IEEE Transactions on Industry Applications*, vol. 41, no. 5, pp. 1281–1291, 2005.

[77] M. Liserre, F. Blaabjerg, and S. Hansen, "Design and control of an LCL-filter based three-phase active rectifier," in *Industry Applications Conference, 2001. Thirty-Sixth IAS Annual Meeting. Conference Record of the 2001 IEEE*, vol. 1, 2001, pp. 299–307.

[78] M. Liserre, R. Teodorescu, and F. Blaabjerg, "Stability of photovoltaic and wind turbine grid-connected inverters for a large set of grid impedance values," *IEEE Transactions on Power Electronics*, vol. 21, no. 1, pp. 263–272, 2006.

[79] M. Castilla, J. Miret, A. Camacho, J. Matas, and L. G. de Vicuna, "Reduction of current harmonic distortion in three-phase grid-connected photovoltaic inverters via resonant current control," *IEEE Transactions on Industrial Electronics*, vol. 60, no. 4, pp. 1464–1472, 2013.

[80] R. Teodorescu, F. Blaabjerg, M. Liserre, and A. Dell'Aquila, "A stable three-phase LCL-filter based active rectifier without damping," in *Industry Applications Conference, 2003. 38th IAS Annual Meeting. Conference Record of the*, vol. 3, 2003, pp. 1552–1557.

[81] X. Wang, F. Blaabjerg, and P. C. Loh, "Grid-Current-Feedback Active Damping for LCL Resonance in Grid-Connected Voltage-Source Converters," *IEEE Transactions on Power Electronics*, vol. 31, no. 1, pp. 213–223, 2016.

[82] E. Twining and D. G. Holmes, "Grid current regulation of a three-phase voltage source inverter with an LCL input filter," *IEEE Transactions on Power Electronics*, vol. 18, no. 3, pp. 888–895, 2003.

[83] Y. Jia, J. Zhao, and X. Fu, "Direct Grid Current Control of LCL-Filtered Grid-Connected Inverter Mitigating Grid Voltage Disturbance," *IEEE Transactions on Power Electronics*, vol. 29, no. 3, pp. 1532–1541, 2014.

[84] S. G. Parker, B. P. McGrath, and D. G. Holmes, "Regions of Active Damping Control for LCL Filters," *IEEE Transactions on Industry Applications*, vol. 50, no. 1, pp. 424–432, 2014.

[85] J. Yin, S. Duan, and B. Liu, "Stability Analysis of Grid-Connected Inverter With LCL Filter Adopting a Digital Single-Loop Controller With Inherent Damping Characteristic," *IEEE Transactions on Industrial Informatics*, vol. 9, no. 2, pp. 1104–1112, 2013.

[86] J. Dannehl, C. Wessels, and F. W. Fuchs, "Limitations of Voltage-Oriented PI Current Control of Grid-Connected PWM Rectifiers With LCL Filters," *IEEE Transactions on Industrial Electronics*, vol. 56, no. 2, pp. 380–388, 2009.

[87] Y. Tang, P. C. Loh, P. Wang, F. H. Choo, and F. Gao, "Exploring Inherent Damping Characteristic of LCL-Filters for Three-Phase Grid-Connected Voltage Source Inverters," *IEEE Transactions on Power Electronics*, vol. 27, no. 3, pp. 1433–1443, 2012.

[88] J. Wang, J. D. Yan, L. Jiang, and J. Zou, "Delay-Dependent Stability of Single-Loop Controlled Grid-Connected Inverters with LCL Filters," *IEEE Transactions on Power Electronics*, vol. 31, no. 1, pp. 743–757, 2016.

[89] J. Dannehl, M. Liserre, and F. W. Fuchs, "Filter-Based Active Damping of Voltage Source Converters With LCL Filter," *IEEE Transactions on Industrial Electronics*, vol. 58, no. 8, pp. 3623–3633, 2011.

[90] M. Liserre, A. Dell'Aquila, and F. Blaabjerg, "Genetic algorithm-based design of the active damping for an LCL-filter three-phase active rectifier," *IEEE Transactions on Power Electronics*, vol. 19, no. 1, pp. 76–86, 2004.

[91] P. C. Loh and D. G. Holmes, "Analysis of multiloop control strategies for LC/CL/LCL-filtered voltage-source and current-source inverters," *IEEE Transactions on Industry Applications*, vol. 41, no. 2, pp. 644–654, 2005.

[92] P.A.Dahono, "A control method to damp oscillation in the input LC filter," in *Power Electronics Specialists Conference, 2002. pesc 02. 2002 IEEE 33rd Annual*, vol. 4, 2002, pp. 1630–1635.

[93] M. Altin, . Göksu, R. Teodorescu, P. Rodriguez, B. B. Jensen, and L. Helle, "Overview of recent grid codes for wind power integration," in *Optimization of Electrical and Electronic Equipment (OPTIM), 2010 12th International Conference on*, 2010, pp. 1152–1160.

[94] C. P. Patrick Graichen, Mara Marthe Kleiner, "The energy transition in the power sector: State of affairs 2015," [Online]. Available: https://www.agora-energiewende.de, 2016.

[95] VDE, "Technical requirements for the connection and operation of customer installations to the high-voltage network (TCC High-Voltage)," [Online]. Available: https://www.vde.com/, 2015.

[96] Global Wind Energy Council, "Global wind report annual market update," [Online]. Available: http://www.gwec.net, 2015.

[97] K. Ma, M. Liserre, and F. Blaabjerg, "Operating and loading conditions of a three-level neutral-point-clamped wind power converter under various grid faults," *IEEE Transactions on Industry Applications*, vol. 50, no. 1, pp. 520–530, 2014.

[98] F. Blaabjerg, R. Teodorescu, M. Liserre, and A. V. Timbus, "Overview of control and grid synchronization for distributed power generation systems," *IEEE Transactions on Industrial Electronics*, vol. 53, no. 5, pp. 1398–1409, Oct 2006.

[99] X. Wang, S. Yuvarajan, and L. Fan, "MPPT control for a PMSG-based grid-tied wind generation system," in *North American Power Symposium 2010*, Sept 2010, pp. 1–7.

[100] S. Hu and H. Xu, "Research on sensorless control based back-to-back converter for direct-driven wecs," in *2009 Asia-Pacific Power and Energy Engineering Conference*, March 2009, pp. 1–4.

[101] S. Alepuz, S. Busquets, J. Bordonau, J. Pontt, C. Silva, and J. Rodriguez, "Comparison of Control Strategies to Meet Low Voltage Ride-Through Requirements in Distributed Power Generation Systems," in *2007 IEEE International Symposium on Industrial Electronics*, 2007, pp. 2619–2624.

[102] S. Alepuz, A. Calle, S. Busquets-Monge, S. Kouro, and B. Wu, "Use of Stored Energy in PMSG Rotor Inertia for Low-Voltage Ride-Through in Back-to-Back NPC Converter-Based Wind Power Systems," *IEEE Transactions on Industrial Electronics*, vol. 60, no. 5, pp. 1787–1796, May 2013.

[103] Asociación Empresarial Eólica (AEE), "Offprint From The Grid Code P.O. 12.2," [Online]. Available: https://http://www.aeeolica.org, 2008.

[104] J. Driesen and K. Visscher, "Virtual synchronous generators," in *Power and Energy Society General Meeting - Conversion and Delivery of Electrical Energy in the 21st Century, 2008 IEEE*, 2008, pp. 1–3.

[105] D. Andler, E. Hauk, R. Álvarez, J. Weber, S. Bernet, and J. Rodríguez, "New junction temperature balancing method for a three level active NPC converter," in *Power Electronics and Applications (EPE 2011), Proceedings of the 2011-14th European Conference on*, 2011, pp. 1–9.

[106] A. Schönung and H. Stemmler, "Geregelter drehstrom-umkehrantrieb mit gesteuertem umrichter nach dem unterschwingungsverfahren," *BBC Mitteilungen*, vol. 46, no. 12, pp. 699–721, 1964.

[107] F. Blaschke, *Das verfahren der feldorientierung zur regelung der drehfeldmaschine*. Siemens Forschungs-und Entwicklungsberichte, 1974.

[108] K. Hasse, "Zur dynamik drehzahlgeregelter antriebe mit stromrichtergespeiste. asynchron-kurzschlussläufer-maschinen," Ph.D. Thesis, Department of Electrical Engineering and Information Technology, Technische Universität Darmstadt, 1969.

[109] A. B. Plunkett, "A current-controlled PWM transistor inverter drive," in *IEEE-IAS fourteenth annual meeting*, October 1979, pp. 785–792.

[110] D. M. Brod and D. W. Novotny, "Current Control of VSI-PWM Inverters," *IEEE Transactions on Industry Applications*, vol. IA-21, no. 3, pp. 562–570, 1985.

[111] M. P. Kazmierkowski and M. A. Dzieniakowski, "Review of current regulation methods for VS-PWM inverters," in *Industrial Electronics, 1993. Conference Proceedings, ISIE'93 - Budapest., IEEE International Symposium on*, 1993, pp. 448–456.

[112] S. Buso, L. Malesani, and P. Mattavelli, "Comparison of current control techniques for active filter applications," *IEEE Transactions on Industrial Electronics*, vol. 45, no. 5, pp. 722–729, 1998.

[113] T. Noguchi and I. Takahashi, "Quick torque response control of an induction motor based on a new concept," in *IEEJ Tech. Meet. on Rotating Machine*, 1984, pp. 61–70.

[114] M. Depenbrock, "Verfahren und einrichtung zur regelung einer drehfeldmaschine," Patent DE3 438 504 A1, Apr, 1986.

[115] I. Takahashi and T. Noguchi, "A new quick-response and high-efficiency control strategy of an induction motor," *IEEE Transactions on Industry Applications*, vol. IA-22, no. 5, pp. 820–827, 1986.

[116] T. Ohnishi, "Three phase PWM converter/inverter by means of instantaneous active and reactive power control," in *Industrial Electronics, Control and Instrumentation, 1991. Proceedings. IECON '91., 1991 International Conference on*, Oct 1991, pp. 819–824 vol.1.

[117] M. Morari, C. Garcia, and D. M. Prett, "Model predictive control: Theory and practice—A survey," *Automatica*, vol. 25, no. 3, pp. 335–348, 1989.

[118] J. Rodriguez, J. Pontt, C. Silva, M. Salgado, S. Rees, U. Ammann, P. Lezana, R. Huerta, and P. Cortes, "Predictive control of three-phase inverter," *Electronics Letters*, vol. 40, no. 9, pp. 561–563, April 2004.

[119] P. C. Jose Rodriguez, *Predictive control of power converters and electrical drives.* Chichester West Sussex UK: Wiley-IEEE Press, 2012.

[120] V. Utkin, "Variable structure systems with sliding modes," *IEEE Transactions on Automatic Control*, vol. 22, no. 2, pp. 212–222, 1977.

[121] R. A. DeCarlo, S. H. Zak, and G. P. Matthews, "Variable structure control of nonlinear multivariable systems: a tutorial," *Proceedings of the IEEE*, vol. 76, no. 3, pp. 212–232, 1988.

[122] J. Y. Hung, W. Gao, and J. C. Hung, "Variable structure control: a survey," *IEEE Transactions on Industrial Electronics*, vol. 40, no. 1, pp. 2–22, 1993.

[123] K. D. Young, V. I. Utkin, and U. Ozguner, "A control engineer's guide to sliding mode control," *IEEE Transactions on Control Systems Technology*, vol. 7, no. 3, pp. 328–342, 1999.

[124] M. Liserre, A. Dell'Aquila, and F. Blaabjerg, "Design and control of a three-phase active rectifier under non-ideal operating conditions," in *Industry Applications Conference, 2002. 37th IAS Annual Meeting. Conference Record of the*, vol. 2, 2002, pp. 1181–1188.

[125] V. Blasko and V. Kaura, "A novel control to actively damp resonance in input LC filter of a three-phase voltage source converter," *IEEE Transactions on Industry Applications*, vol. 33, no. 2, pp. 542–550, 1997.

[126] T. Noguchi, H. Tomiki, S. Kondo, and I. Takahashi, "Direct power control of PWM converter without power-source voltage sensors," *IEEE Transactions on Industry Applications*, vol. 34, no. 3, pp. 473–479, 1998.

[127] G. Giglia, M. Pucci, C. Serporta, and G. Vitale, "Experimental comparison of three-phase distributed generation systems based on VOC and DPC control techniques," in *Power Electronics and Applications, 2007 European Conference on*, 2007, pp. 1–12.

[128] M. Schröder, S. Gierschner, and H. G. Eckel, "Comparison of different control techniques for grid side VSC in terms of losses and current harmonics," in *Power Electronics and Applications (EPE), 2013 15th European Conference on*, 2013, pp. 1–8.

[129] R. Zaimeddine and T. Undeland, "Direct power control strategies of a grid-connected three-level voltage source converter VSI-NPC," in *Power Electronics and Applications (EPE 2011), Proceedings of the 2011-14th European Conference on*, 2011, pp. 1–7.

[130] W. Chen, Y. Zou, and L. Xu, "Direct power control for Neutral-point-clamped three-level PWM rectifier," in *Industrial Technology, 2008. ICIT 2008. IEEE International Conference on*, 2008, pp. 1–6.

[131] N. Li, Y. Wang, S. Li, Y. Li, and Z. Wang, "Direct power control strategy used in three-level NPC converters," in *Power Electronics and Motion Control Conference (IPEMC), 2012 7th International*, vol. 3, 2012, pp. 1675–1679.

[132] J. Reese, R. Lohde, and F. W. Fuchs, "Frt capability of direct power controlled converters connected by an actively damped lcl-filter for wind power applications," in *Proceedings of the 2011 14th European Conference on Power Electronics and Applications*, Aug 2011, pp. 1–10.

[133] H. Yin and S. Dieckerhoff, "Experimental comparison of DPC and VOC control of a three-level NPC grid connected converter," in *2015 IEEE 6th International Symposium on Power Electronics for Distributed Generation Systems (PEDG)*, June 2015, pp. 1–7.

[134] J. Eloy-Garcia, S. Arnaltes, and J. L. RodriguezAmenedo, "Extended direct power control of a three-level neutral point clamped voltage source inverter with unbalanced voltages," in *2008 IEEE Power Electronics Specialists Conference*, 2008, pp. 3396–3400.

[135] ABB Switzerland Ltd, "IGBT Module 5SNA 1200G450350," [Online]. Available: www.abb.com/semiconductors, 2016.

[136] L. Malesani, P. Mattavelli, and S. Buso, "Robust dead-beat current control for PWM rectifiers and active filters," *IEEE Transactions on Industry Applications*, vol. 35, no. 3, pp. 613–620, May 1999.

[137] P. Cortes, M. P. Kazmierkowski, R. M. Kennel, D. E. Quevedo, and J. Rodriguez, "Predictive control in power electronics and drives," *IEEE Transactions on Industrial Electronics*, vol. 55, no. 12, pp. 4312–4324, Dec 2008.

[138] D. Clarke, C. Mohtadi, and P. Tuffs, "Generalized predictive control—part i. the basic algorithm," *Automatica*, vol. 23, no. 2, pp. 137 – 148, 1987.

[139] D. Clarke, C. Mohtadi, and P. Tuffs, "Generalized predictive control—part ii extensions and interpretations," *Automatica*, vol. 23, no. 2, pp. 149 – 160, 1987.

[140] D. Clarke and C. Mohtadi, "Properties of generalized predictive control," *Automatica*, vol. 25, no. 6, pp. 859 – 875, 1989.

[141] R. Kennel, A. Linder, and M. Linke, "Generalized predictive control (GPC)-ready for use in drive applications?" in *Power Electronics Specialists Conference, 2001. PESC. 2001 IEEE 32nd Annual*, vol. 4, 2001, pp. 1839–1844.

[142] J. Rodriguez, J. Pontt, C. A. Silva, P. Correa, P. Lezana, P. Cortes, and U. Ammann, "Predictive current control of a voltage source inverter," *IEEE Transactions on Industrial Electronics*, vol. 54, no. 1, pp. 495–503, Feb 2007.

[143] S. Kouro, P. Cortes, R. Vargas, U. Ammann, and J. Rodriguez, "Model predictive control-a simple and powerful method to control power converters," *IEEE Transactions on Industrial Electronics*, vol. 56, no. 6, pp. 1826–1838, June 2009.

[144] R. Vargas, P. Cortes, U. Ammann, J. Rodriguez, and J. Pontt, "Predictive control of a three-phase neutral-point-clamped inverter," *IEEE Transactions on Industrial Electronics*, vol. 54, no. 5, pp. 2697–2705, Oct 2007.

[145] P. Cortes, J. Rodriguez, C. Silva, and A. Flores, "Delay compensation in model predictive current control of a three-phase inverter," *IEEE Transactions on Industrial Electronics*, vol. 59, no. 2, pp. 1323–1325, Feb 2012.

[146] P. Cortes, A. Wilson, S. Kouro, J. Rodriguez, and H. Abu-Rub, "Model Predictive Control of Multilevel Cascaded H-Bridge Inverters," *IEEE Transactions on Industrial Electronics*, vol. 57, no. 8, pp. 2691–2699, Aug 2010.

[147] T. Geyer, G. Papafotiou, and M. Morari, "Model predictive direct torque control-part i: Concept, algorithm, and analysis," *IEEE Transactions on Industrial Electronics*, vol. 56, no. 6, pp. 1894–1905, June 2009.

[148] H. Miranda, P. Cortes, J. I. Yuz, and J. Rodriguez, "Predictive torque control of induction machines based on state-space models," *IEEE Transactions on Industrial Electronics*, vol. 56, no. 6, pp. 1916–1924, June 2009.

[149] G.Papafotiou, J. Kley, K. G. Papadopoulos, P. Bohren, and M. Morari, "Model predictive direct torque control-part ii: Implementation and experimental evaluation," *IEEE Transactions on Industrial Electronics*, vol. 56, no. 6, pp. 1906–1915, June 2009.

[150] P. Cortes, J. Rodriguez, D. E. Quevedo, and C. Silva, "Predictive current control strategy with imposed load current spectrum," *IEEE Transactions on Power Electronics*, vol. 23, no. 2, pp. 612–618, March 2008.

[151] H. Miranda, R. Teodorescu, P. Rodriguez, and L. Helle, "Model predictive current control for high-power grid-connected converters with output LCL filter," in *Industrial Electronics, 2009. IECON '09. 35th Annual Conference of IEEE*, Nov 2009, pp. 633–638.

[152] P. CortÉs, J. RodrÍguez, P. Antoniewicz, and M. Kazmierkowski, "Direct Power Control of an AFE Using Predictive Control," *IEEE Transactions on Power Electronics*, vol. 23, no. 5, pp. 2516–2523, Sept 2008.

[153] J. Rodriguez, M. P. Kazmierkowski, J. R. Espinoza, P. Zanchetta, H. Abu-Rub, H. A. Young, and C. A. Rojas, "State of the art of finite control set model predictive control in power electronics," *IEEE Transactions on Industrial Informatics*, vol. 9, no. 2, pp. 1003–1016, May 2013.

[154] "Predictive control in power converters and electrical drives-part i," *IEEE Transactions on Industrial Electronics*, vol. 63, no. 6, pp. 3834–3984, June 2016.

[155] "Predictive control in power converters and electrical drives-part ii," *IEEE Transactions on Industrial Electronics*, vol. 63, no. 7, pp. 4472–4641, July 2016.

[156] D. Andler, M. Perez, J. Rodríguez, and S. Bernée, "Predictive control of three-level active NPC converter with evenly energy losses distribution," in *Power Electronics Conference (IPEC), 2010 International*, June 2010, pp. 754–759.

[157] P. Cortes, G. Ortiz, J. I. Yuz, J. Rodriguez, S. Vazquez, and L. G. Franquelo, "Model Predictive Control of an Inverter With Output Filter for UPS Applications," *IEEE Transactions on Industrial Electronics*, vol. 56, no. 6, pp. 1875–1883, June 2009.

[158] S. Rivera, S. Kouro, B. Wu, S. Alepuz, M. Malinowski, P. Cortes, and J. Rodriguez, "Multilevel direct power control-a generalized approach for grid-tied multilevel converter applications," *IEEE Transactions on Power Electronics*, vol. 29, no. 10, pp. 5592–5604, Oct 2014.

[159] T. Geyer, *Low complexity model predictive control in power electronics and power systems*. Cuvillier Verlag, 2005.

[160] T. Geyer, "Generalized model predictive direct torque control: Long prediction horizons and minimization of switching losses," in *Decision and Control, 2009 held jointly with the*

2009 28th Chinese Control Conference. CDC/CCC 2009. Proceedings of the 48th IEEE Conference on, Dec 2009, pp. 6799–6804.

[161] T.Geyer, "Model predictive direct current control for multi-level converters," in *2010 IEEE Energy Conversion Congress and Exposition*, Sept 2010, pp. 4305–4312.

[162] B. S. Riar, T. Geyer, and U. K. Madawala, "Model predictive direct current control of modular multi-level converters," in *Industrial Technology (ICIT), 2013 IEEE International Conference on*, Feb 2013, pp. 582–587.

[163] S. Mariethoz, A. G. Beccuti, and M. Morari, "Analysis and optimal current control of a voltage source inverter connected to the grid through an LCL filter," in *2008 IEEE Power Electronics Specialists Conference*, June 2008, pp. 2132–2138.

[164] J. Lu, *Automatic Control Theory.* Northwestern Polytechnical University Press, 2009.

[165] T. Geyer and D. E. Quevedo, "Multistep direct model predictive control for power electronics-part 1: Algorithm," in *2013 IEEE Energy Conversion Congress and Exposition*, 2013, pp. 1154–1161.

[166] T. Geyer and D. E. Quevedo, "Multistep direct model predictive control for power electronics-part 2: Analysis," in *2013 IEEE Energy Conversion Congress and Exposition*, 2013, pp. 1162–1169.

[167] P. Karamanakos, T. Geyer, N. Oikonomou, F. D. Kieferndorf, and S. Manias, "Direct model predictive control: A review of strategies that achieve long prediction intervals for power electronics," *IEEE Industrial Electronics Magazine*, vol. 8, no. 1, pp. 32–43, 2014.

[168] X. Zhang, Y. Wang, C. Yu, L. Guo, and R. Cao, "Hysteresis Model Predictive Control for High-Power Grid-Connected Inverters With Output LCL Filter," *IEEE Transactions on Industrial Electronics*, vol. 63, no. 1, pp. 246–256, 2016.

[169] D. Wojciechowski, "Novel predictive control of 3-phase LCL-based active power filter," in *2009 Compatibility and Power Electronics*, 2009, pp. 298–305.

[170] J. M. Maciejowski, *Predictive control : with constraints.* Harlow England: Prentice Hall, 2001.

[171] T. Geyer, "Low complexity model predictive control in power electronics and power systems," Ph.D. Thesis, ETH Zurich, 2005.

[172] T. M. Blooming and D. J. Carnovale, "Application of IEEE STD 519-1992 Harmonic Limits," in *Conference Record of 2006 Annual Pulp and Paper Industry Technical Conference*, 2006, pp. 1–9.

[173] P. Kokotović and M. Arcak, "Constructive nonlinear control: a historical perspective," *Automatica*, vol. 37, no. 5, pp. 637 – 662, 2001.

[174] C. Edwards and S. k. Spurgeon, *Sliding Mode Control: Theory and Applications.* Taylor and Francis, 1998.

[175] H. K. Khalil, *Nonlinear Systems Third edition.* Prentice Hall, 2002.

[176] J. Zhou and C. Wen, *Adaptive Backstepping Control of Uncertain Systems.* Springer-Verlag Berlin Heidelber, 2008.

[177] M. Krstic, I. Kanellakopoulos, and P. Kokotovic, *Nonlinear and Adaptive Control Design.* Wiley Interscience, 1995.

[178] I. Kanellakopoulos, P. T. Krein, and F. Disilvestro, "Nonlinear flux-observer-based control of induction motors," in *1992 American Control Conference*, 1992, pp. 1700–1705.

[179] A. Allag, M. Y. Hammoudi, S. M. Mimoune, M. Y. Ayad, M. Becherif, and A. Miraoui, "Tracking control via adaptive backstepping approach for a three phase PWM AC-DC converter," in *2007 IEEE International Symposium on Industrial Electronics*, 2007, pp. 371–376.

[180] J. J. Ge, Z. M. Zhao, and J. J. Li, "Backstepping control for active power filter with LCL filter," in *2nd IET Renewable Power Generation Conference (RPG 2013)*, 2013, pp. 1–4.

[181] Y. Fang, J. Fei, and Z. Wang, "Adaptive neural backstepping control strategy of three-phase active power filter," in *2015 European Control Conference (ECC)*, 2015, pp. 380–385.

[182] D. Sun, X. Wang, and Y. Fang, "Backstepping direct power control without phase-locked loop of ac/dc converter under both balanced and unbalanced grid conditions," *IET Power Electronics*, vol. 9, no. 8, pp. 1614–1624, 2016.

[183] X. Wang, X. Ruan, S. Liu, and C. K. Tse, "Full Feedforward of Grid Voltage for Grid-Connected Inverter With LCL Filter to Suppress Current Distortion Due to Grid Voltage Harmonics," *IEEE Transactions on Power Electronics*, vol. 25, no. 12, pp. 3119–3127, 2010.

[184] W. Li, X. Ruan, D. Pan, and X. Wang, "Full-Feedforward Schemes of Grid Voltages for a Three-Phase LCL -Type Grid-Connected Inverter," *IEEE Transactions on Industrial Electronics*, vol. 60, no. 6, pp. 2237–2250, 2013.

[185] X. Wu, X. Li, X. Yuan, and Y. Geng, "Grid Harmonics Suppression Scheme for LCL-Type Grid-Connected Inverters Based on Output Admittance Revision," *IEEE Transactions on Sustainable Energy*, vol. 6, no. 2, pp. 411–421, 2015.

[186] S.-Y. Ruan, G.-J. Li, X.-H. Jiao, Y.-Z. Sun, and T. Lie, "Adaptive control design for VSC-HVDC systems based on backstepping method ," *Electric Power Systems Research*, vol. 77, no. 5–6, pp. 559 – 565, 2007.

[187] G. F. Reed, B. M. Grainger, A. R. Sparacino, R. J. Kerestes, and M. J. Korytowski, "Advancements in medium voltage DC architecture development with applications for powering electric vehicle charging stations," in *Energytech, 2012 IEEE*, 2012, pp. 1–8.

[188] dSPACE, *SCALEXIO Hardware Installation and Configuration*, 2013th ed. dSPACE GmbH, May 2013.

[189] D. Andler, S. Kouro, M. Perez, J. Rodriguez, and B. Wu, "Switching loss analysis of modulation methods used in neutral point clamped converters," in *2009 IEEE Energy Conversion Congress and Exposition*, 2009, pp. 2565–2571.

[190] X. Jing, J. He, and N. A. O. Demerdash, "Application and losses analysis of ANPC converters in doubly-fed induction generator wind energy conversion system," in *2013 International Electric Machines Drives Conference*, 2013, pp. 131–138.

[191] Infineon Technologies AG, "Thermal Equivalent Circuit Models," [Online]. Available: www.abb.com/semiconductors, 2008.

[192] ABB, "Semiconductors," [Online]. Available: http://new.abb.com/, Jan. 2017.

[193] HITACHI, "Semiconductors," [Online]. Available: http://www.hitachi.com/, Jan. 2017.

[194] INFINEON, "Semiconductors," [Online]. Available: https://www.infineon.com/, Jan. 2017.

[195] MITSUBISHI, "Semiconductors," [Online]. Available: http://www.mitsubishielectric.com/, Jan. 2017.

[196] WESTCODE, "Semiconductors," [Online]. Available: http://www.westcode.com/, Jan. 2017.

[197] TOSHIBA, "Semiconductors," [Online]. Available: http://www.toshiba.com/, Jan. 2017.

Appendix

A Scaled Low Voltage Setup

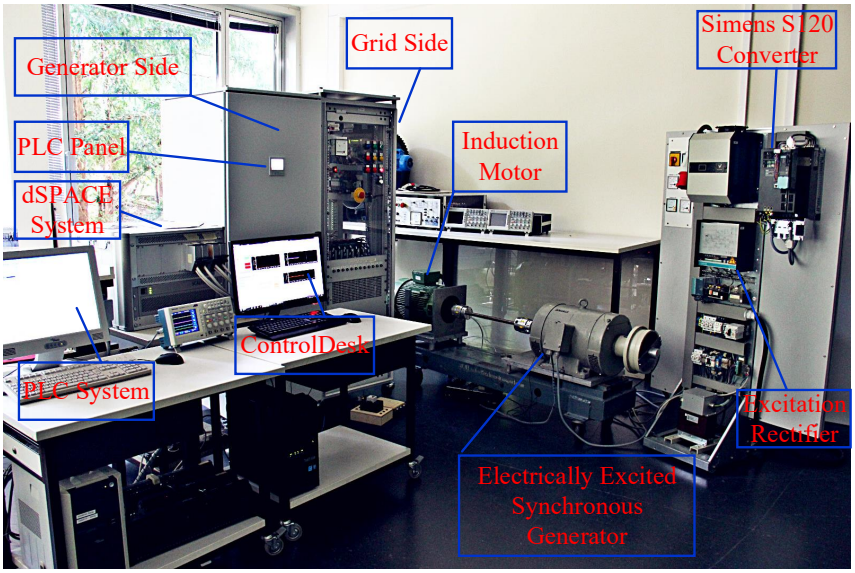

Figure A.1: *10KVA Three Phase Three-level (A)NPC Back-to-back Power Conversion System Test Bench*

A.1 Control System

The PLC is the connecting link between the dSPACE control system and the drive train. It is designed to implement a basic but yet extendable model of a wind turbine.

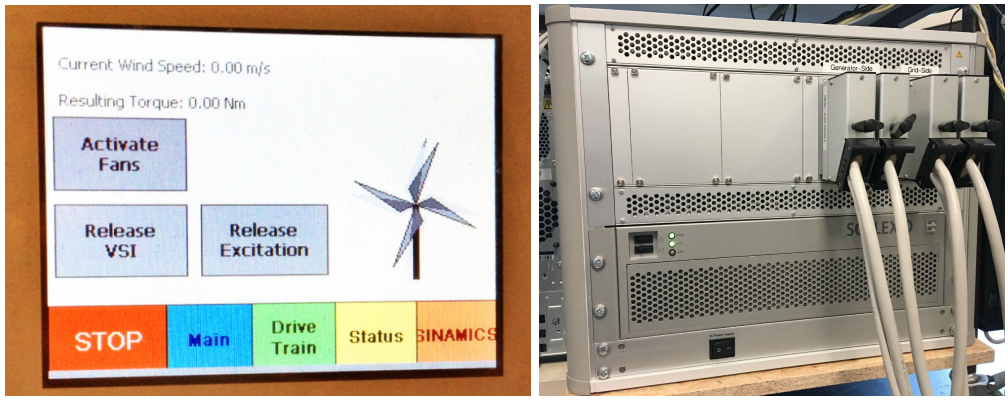

(a) Human-machine-interface *(b) dSPACE SCALEXIO System*

Figure A.2: *PLC Touch-enabled Display and dSPACE Control System*

Principally, with this PLC, not only the characteristic curves of wind profiles and wind turbines but also curves of other generators with a multi-dimensional characteristics can be provided. The curves can be changed online during the operation e.g. to represent effects of pitch control.

The control hardware allows to implement several independent PWM carriers for the multilevel converters. Due to the two FPGAs, it is possible to realize different control algorithms, e.g., a standard cascaded control or a model predictive control scheme independently for each converter. This allows a detailed investigation of the grid compliance including fault cases [16, 97, 101]. The outside view of the dSAPCE SCALEXIO system is shown in figure A.2b. There are two DS2655 FPGA Base Module, and each of them has two DS2655M1 I/O Modules. Two I/O modules are used for generator side converter control and the other two are used for grid side converter control.

The internal structure of the FPGA module and I/O module are shown in figure A.3a and figure A.3b respectively [188].

A.2 Power Converter

The grid side power converter including IGBT modules, drivers and heat sinks is shown in figure A.4a.

A.3 LCL Filter

The grid side LCL filter is shown in figure A.4b.

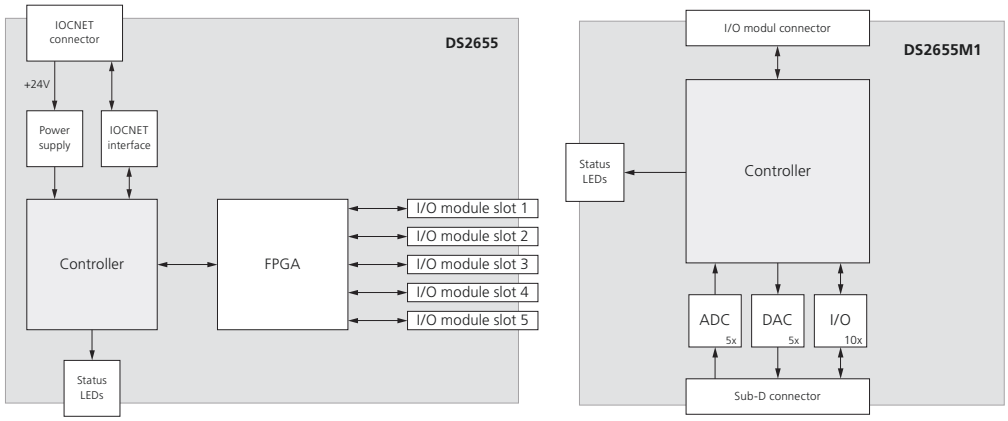

(a) *DS2655 FPGA Base Module* ***(b)*** *DS2655M1 I/O Module*

Figure A.3: *Internal Structure of dSAPCE SCALEXIO System*

(a) *IGBT Modules, Drivers and Heat Sinks* ***(b)*** *LCL Filter*

Figure A.4: *Power Converter and LCL Fitler*

B Switching Matrix for MPC

$$M_{sc} = \left|\begin{array}{cc|ccccccccccccc}
13 & 0 & 3 & 5 & 7 & 9 & 11 & 13 & 16 & 18 & 20 & 22 & 24 & 26 \\
4 & 1 & 4 & 8 & 12 & 0 & 0 & 0 & 0 & 0 & 0 & 0 & 0 & 0 \\
4 & 2 & 6 & 10 & 14 & 0 & 0 & 0 & 0 & 0 & 0 & 0 & 0 & 0 \\
6 & 3 & 0 & 6 & 14 & 16 & 26 & 0 & 0 & 0 & 0 & 0 & 0 & 0 \\
5 & 4 & 1 & 5 & 13 & 15 & 0 & 0 & 0 & 0 & 0 & 0 & 0 & 0 \\
6 & 5 & 0 & 4 & 8 & 16 & 18 & 0 & 0 & 0 & 0 & 0 & 0 & 0 \\
5 & 6 & 2 & 3 & 7 & 17 & 0 & 0 & 0 & 0 & 0 & 0 & 0 & 0 \\
6 & 7 & 0 & 6 & 10 & 18 & 20 & 0 & 0 & 0 & 0 & 0 & 0 & 0 \\
5 & 8 & 1 & 5 & 9 & 19 & 0 & 0 & 0 & 0 & 0 & 0 & 0 & 0 \\
6 & 9 & 0 & 8 & 12 & 20 & 22 & 0 & 0 & 0 & 0 & 0 & 0 & 0 \\
5 & 10 & 2 & 7 & 11 & 21 & 0 & 0 & 0 & 0 & 0 & 0 & 0 & 0 \\
6 & 11 & 0 & 10 & 14 & 22 & 24 & 0 & 0 & 0 & 0 & 0 & 0 & 0 \\
5 & 12 & 1 & 9 & 13 & 23 & 0 & 0 & 0 & 0 & 0 & 0 & 0 & 0 \\
6 & 13 & 0 & 4 & 12 & 24 & 26 & 0 & 0 & 0 & 0 & 0 & 0 & 0 \\
5 & 14 & 2 & 3 & 11 & 25 & 0 & 0 & 0 & 0 & 0 & 0 & 0 & 0 \\
4 & 15 & 4 & 16 & 26 & 0 & 0 & 0 & 0 & 0 & 0 & 0 & 0 & 0 \\
6 & 16 & 0 & 3 & 5 & 15 & 17 & 0 & 0 & 0 & 0 & 0 & 0 & 0 \\
4 & 17 & 6 & 16 & 18 & 0 & 0 & 0 & 0 & 0 & 0 & 0 & 0 & 0 \\
6 & 18 & 0 & 5 & 7 & 17 & 19 & 0 & 0 & 0 & 0 & 0 & 0 & 0 \\
4 & 19 & 8 & 18 & 20 & 0 & 0 & 0 & 0 & 0 & 0 & 0 & 0 & 0 \\
6 & 20 & 0 & 7 & 9 & 19 & 21 & 0 & 0 & 0 & 0 & 0 & 0 & 0 \\
4 & 21 & 10 & 20 & 22 & 0 & 0 & 0 & 0 & 0 & 0 & 0 & 0 & 0 \\
6 & 22 & 0 & 9 & 11 & 21 & 23 & 0 & 0 & 0 & 0 & 0 & 0 & 0 \\
4 & 23 & 12 & 22 & 24 & 0 & 0 & 0 & 0 & 0 & 0 & 0 & 0 & 0 \\
6 & 24 & 0 & 11 & 13 & 23 & 25 & 0 & 0 & 0 & 0 & 0 & 0 & 0 \\
4 & 25 & 14 & 24 & 26 & 0 & 0 & 0 & 0 & 0 & 0 & 0 & 0 & 0 \\
6 & 26 & 0 & 3 & 13 & 15 & 16 & 0 & 0 & 0 & 0 & 0 & 0 & 0
\end{array}\right| \tag{B.1}$$

C Losses Analysis

C.1 Conduction Losses

The conduction losses can be estimated by the device voltage, device current and the junction temperature. Normally these data can be taken from typical on-state characteristics of the datasheet. The on-state characteristics of selected IGBT Module, 5SNA 1200G450350 is shown in appendix figure C.2.

It can be easily obtained that the average conduction losses of an IGBT is:

$$P_{con,IGBT} = \frac{1}{T_{con}} \int u_{on} \cdot i_{con} dt \tag{C.1}$$

where u_{on} represents the on-state voltage drop. The i_{con} indicates the device current. The average conduction losses can be calculated from equation C.2, where u_{T0} and r_{T0} are the additional dc voltage between collector and emitter when the IGBT is conducting and the equivalent differential resistance of the device. $\overline{I}_{con}$ and $I^2_{con,rms}$ are the average value and RMS value of the IGBT conduction current. Similarly, the average conduction losses of a diode can be expressed according to equation C.3.

$$\begin{aligned} P_{con,IGBT} &= \tfrac{1}{T_{con}} \int_0^{T_{con}} (u_{T0} \cdot i_{con} + r_{T0} \cdot i^2_{con})\, dt \\ &= u_{T0} \cdot \overline{I}_{con} + r_{T0} \cdot I^2_{con,RMS} \end{aligned} \tag{C.2}$$

$$P_{con,Diode} = u_{F0} \cdot \overline{I}_{F,con} + r_{F0} \cdot I^2_{F,RMS} \tag{C.3}$$

C.2 Switching Losses

The switching losses contain two processes, which are the turn-on and turn-off, specifically IGBT turn-on, IGBT turn-off and Diode turn-off. For the modern fast recovery diodes used with IGBTs, the turn-on losses are less than 1% of its turn-off losses, which is negligible and not considered in the losses analysis [189]. The switching losses can be estimated by the device current, commutation voltage and the junction temperature during the switching process. The switching energy can be obtained by integration of switching losses during the transient processes, which normally can be found from the datasheet. The selected IGBT average switching losses for a fundamental time period (0.02s) can be estimated by employing [190]:

$$P_{sw,IGBT} = \frac{u_c}{U_{rated}} \frac{i_c}{I_{rated}} (E_{on,IGBT} + E_{off,IGBT}) f_{sw} \tag{C.4}$$

where $E_{on,IGBT}$ and $E_{off,IGBT}$ are the turn-on and turn-off energy, which are considered constants in this simplified equation, and can be obtained from the datasheet. U_{rated} and I_{rated} are the reference commutation voltage and current respectively. u_c and i_c represent the actual commutation voltage and current, respectively. The average switching losses of a diode can be expressed according to equation C.5. For the selected IGBT and Diode, the relevant switching losses are shown in appendix figure C.3.

$$P_{sw,Diode} = \frac{u_c}{U_{rated}} \frac{i_c}{I_{rated}} (E_{rec,Diode}) f_{sw} \tag{C.5}$$

C.3 Temperature Estimation

The thermal characteristics can be modelled with electrical quantities, e.g., loss sources represented with current sources, temperature represented with voltage. The thermal behaviour of semiconductor components can be described either using Cauer model (T model) or using Foster model (PI model). Compared to Cauer model, for the Foster

model, the individual RC elements do not represent any physical meaning, while the individual RC elements of Cauer model can be assigned to the individual layers of the module (chip, chip solder, substrate, substrate solder, base plate) [191]. The Foster equivalent thermal network of junction to ambient for one switch and inverse diode is shown in figure C.1.

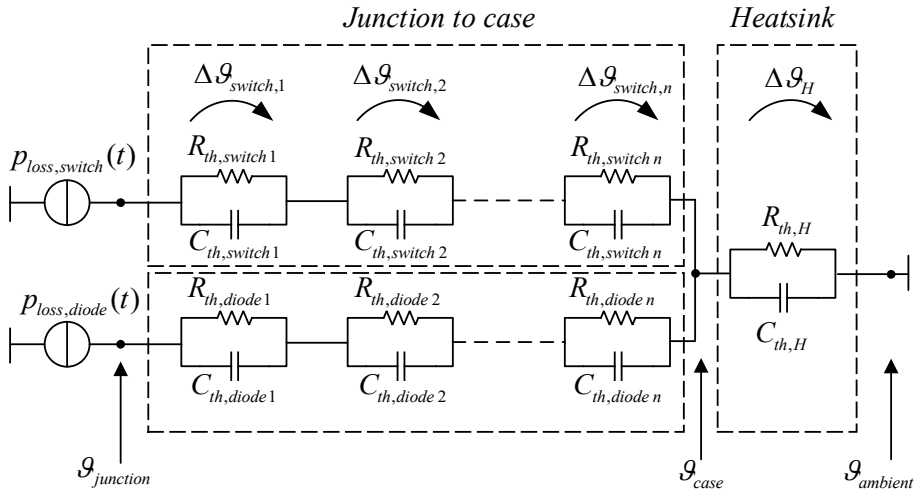

Figure C.1: *Equivalent Thermal Network (Foster Network) of Junction to Ambient for one Switch and Inverse Diode*

Here R_{th} and C_{th} represent the thermal resistance and thermal capacitance, respectively. Normally, the thermal resistance and a time constant τ are given in the datasheet. The parameters of thermal impedance of selected IGBT and Diode are shown in table C.1.

Table C.1: *The Parameters of Thermal Impedance for Selected IGBT and Diode [135]*

Thermal Impedance	$Z_{IGBT/Diode,jc}$		
	$i=1$	$i=2$	$i=3$
$R_{th,switch\,i}(K/kW)$	6.4	2.1	1.04
$\tau_{th,switch\,i}(s)$	0.193	0.0214	0.00278
$R_{th,diode\,i}(K/kW)$	12.5	4.4	2.16
$\tau_{th,diode\,i}(s)$	0.192	0.0226	0.0031

The thermal impedance from junction to case for one switch or reverse diode can be calculated as:

$$Z_{th,jc}(t) = \sum_{i=1}^{n} R_{th,i} \cdot (1 - e^{-\frac{t}{\tau_i}}) \tag{C.6}$$

Similarly, the heatsink impedance $Z_{th,H}(t)$ can be also calculated. The average junction temperature can be calculated with:

$$\vartheta_{j,s}(t) = P_{loss,s}(t) \cdot Z_{th,jc,s}(t) + (P_{loss,s}(t) + P_{loss,d}(t)) \cdot Z_{th,H}(t) + \vartheta_a \tag{C.7}$$

$$\vartheta_{j,d}(t) = P_{loss,d}(t) \cdot Z_{th,jc,d}(t) + (P_{loss,s}(t) + P_{loss,d}(t)) \cdot Z_{th,H}(t) + \vartheta_a \tag{C.8}$$

where the subscript s represents switch and d represents diode.

Since the losses are time dependent and periodic over the fundamental frequency $f_1(50\,\mathrm{Hz})$, the junction temperature will contain the same frequency ripple. In this thesis, the losses calculation and temperature estimation will be done by employing the numerical simulation, PLECS thermal modelling with Foster Network, which is sufficient for the evaluation of different control methods.

D Multi-Level Converters and Switches

[1]Under development
[2]Asymmetric IGCTs
[3]Reverse conducting IGCTS

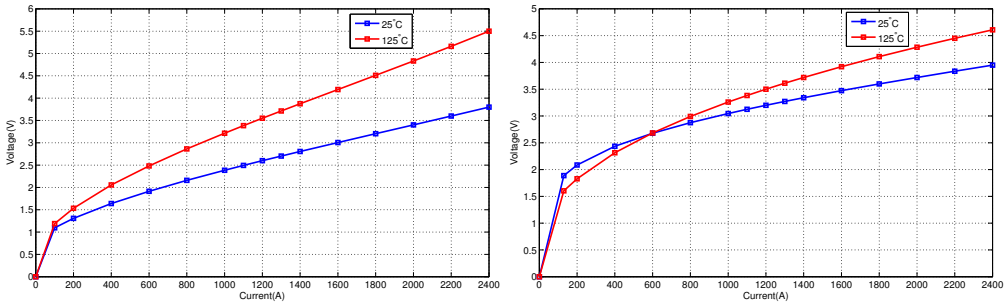

(a) *IGBT on-state Characteristics* ***(b)*** *Diode Forward Characteristics*

Figure C.2: *Selected IGBT and Diode*

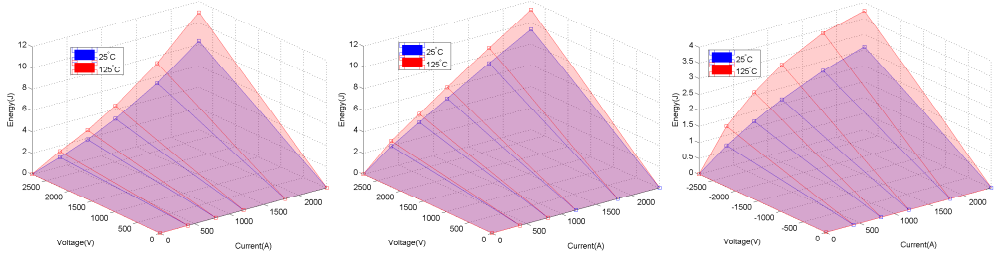

(a) *Selected IGBT Turn-on Energy* ***(b)*** *Selected IGBT Turn-off Energy* ***(c)*** *Selected Diode Turn-off Energy*

Figure C.3: *Switching Losses for Selected IGBT and Diode*

Table D.1: *Market Overview MV Multi-level Converter*

Manufacture	Model Name	Power (MVA)	Voltage (kV)	Topology	Semi.
ABB	PCS6000 Wind	4 - 12	3.3,4.16	3L-NPC-VSC	IGCT
ABB	ACS1000	Air 0.315 - 2 Water 1.8 - 5	6.0 to 11	3L-NPC-VSC	IGCT
ABB	ACS2000	0.25 - 3.2	4.0 to 6.9	5L-NPC-VSC	IGBT
ABB	ACS5000	Air 2 - 7 Water 5 - 36	6.0 to 13.8	5L-NPC-HB-VSC	IGCT
ABB	ACS6000	5 - 36	2.3 to 3.3	3L-NPC-VSC	IGCT
Siemens	P-HARMONY GH150	4 - 30	4 to 7.2	ML-CHB-VSC	IGBT
Siemens	P-HARMONY GH180	0.18 - 24.4	2.3 to 11	ML-CHB-VSC	IGBT
Siemens	SINAMICS SM120 CM	6.3 - 13.7	3.3 to 7.2	3L-NPC-VSC MMC	IGBT/IGCT
Siemens	SINAMICS GM150	1 - 30	2.3 to 4.16	3L-NPC-VSC	IGBT/ IGCT
Siemens	SINAMICS SM150	3.4 - 40	3.3 to 4.16	3L-NPC-VSC	IGBT/ IGCT
GE	MV6 Series	0.16 - 6.5	2.3 to 6.9	3L-NPC-VSC	IGBT
GE	MV7000	3 - 81	3.3 to 10	3L-NPC-VSC	IGBT
TOSHIBA	T300MV2™	300 - 1100 HP	4.16	5L-NPC-VSC	IGBT
TOSHIBA	MTX2™	500 - 1500 HP	4.16	5L-NPC-VSC	IGBT
TOSHIBA	MTX2™-60	3500 - 6000 HP	4.16	5L-NPC-VSC	IGBT
WEG	MVW01	400 - 16	2.3 to 6.9	3/5L-NPC-VSC	IGBT
Eaton	SC9000 EP	300 - 6000 HP	2.4 to 4.16	3L-NPC-VSC	IGBT
YASKAWA	MV1000	175 - 16000 HP	2.4 to 11	9L-CHB-VSC	IGBT
Rockwell	PowerFlex 6000	0.137 - 5.6	2.3 to 10	ML-CHB-VSC	IGBT
Rockwell	PowerFlex 7000	Air 0.15 - 6 Water 2.24 - 5.595	2.3 to 6.6	ML-CHB-VSC	IGBT

Table D.2: *Market Overview MV Power Semiconductor Switches [55, 192–197]*

Type	Manufacture	Voltage Ratings (kV) V_{CES} (IGBT/IEGT) V_{DRM} (IGCT)	Current Ratings (A) I_C (IGBT/IEGT) I_{TGQM} (IGCT)	Package
IGBT	ABB	1.7	150-3600	module
		2.5	1500	module
		3.3	250-1500	module
		4.5	150-1200	module
		6.5	400-750	module
IGBT	HITACHI	1.7	1200-3600	module
		2.5	400-1200	module
		3.3	400-1800	module
		4.5	600-1500	module
		6.5	500-750	module
IGBT	INFINEON	1.7	400-3600	module
		3.3	400-1500	module
		4.5	800-1200	module
		6.5	250-750	module
IGBT	MITSUBISHI	1.7	500-1000	module
		3.3	1000-1500	module
		4.5	800-1200	module
		6.5	750	module
IGBT	WESTCODE	2.5	360-2250	press-pack
		4.5	160-2400	press-pack
IEGT	TOSHIBA	1.7[1]	1200	module
		3.3	400-1500	module
		3.3	1200	press-pack
		4.5	900-1200	module
		4.5	750-2100	press-pack
IGCT	ABB	4.5	3600-5000[2]	press-pack
		4.5	2200[3]	press-pack
		5.5	3600[2]	press-pack
		5.5	1800[3]	press-pack
		6.5	3800	press-pack
IGCT	MITSUBISHI	6.5	400-1500	press-pack

Table D.3: *Grid Codes of Wind Power Generation in Different Countries and Areas*

Country	Organization	Title	Date	Source
UK	NGET	THE GRID CODE (ISSUE 5)	Sep. 2016	www2.nationalgrid.com
China	SGCC	GB/T 19963-2011 Technical rule for connecting wind farm to power system	Dec. 2011	www.cec.org.cn
Germany	VDE FNN	VDE-AR-N 4120 Technical requirements for the connection and operation of customer installations to the high voltage network (TAB high voltage)	Jan. 2015	www.vde.com/fnn
Denmark	Energinet.dk	Technical regulation 3.2.5 for wind power plants with a power output above 11 kW	Jun. 2015	www.energinet.dk
USA	NERC	Standard PRC-024-1 Generator Frequency and Voltage Protective Relay Settings	Mar. 2014	www.nerc.com
	NERC	Standard PRC-024-2	Pending	www.nerc.com
EU	ENTSOe	COMMISSION REGULATION (EU) 2016/631 establishing a network code on requirements for grid connection of generators	Apr. 2016	www.entsoe.eu

Selected Papers

- H. Yin, M. Dereschkewitz, D. Wagenitz, and S. Dieckerhoff, *"A Versatile Test Bench for Grid Integration Investigations of Back-to-Back Wind Energy Conversion Systems"*, 2014 IEEE International Conference on Renewable Energy Research and Application (ICRERA), 2014, pp. 695-700.

- H. Yin and S. Dieckerhoff, *"Experimental comparison of DPC and VOC control of a three-level NPC grid connected converter"*, 2015 IEEE 6th International Symposium on Power Electronics for Distributed Generation Systems (PEDG), 2015, pp. 1-7.

- M. Norambuena and H. Yin and S. Dieckerhoff and J. Rodriguez, *"Improved Finite Control Set Model Predictive Control with Fixed Switching Frequency for Three Phase NPC Converter"*, PCIM Europe 2016, VDE International Exhibition and Conference for Power Electronics, Intelligent Motion, Renewable Energy and Energy Management, 2016, pp. 1-8.